ÇUKUROVA UNIVERSITY
INSTITUTE OF NATURAL AND APPLIED SCIENCES

**PhD THESIS**

**Ünal YILMAZ**

# INVESTIGATION OF HIGH EFFICIENT DC-DC CONVERTERS FOR ON-BOARD BATTERY CHARGING SYSTEM IN ELECTRIC VEHICLES

**DEPARTMENT OF ELECTRICAL AND ELECTRONICS ENGINEERING**

**ADANA-2020**

ÇUKUROVA UNIVERSITY
INSTITUTE OF NATURAL AND APPLIED SCIENCES

**INVESTIGATION OF HIGH EFFICIENT DC-DC CONVERTERS FOR ON-BOARD BATTERY CHARGING SYSTEM IN ELECTRIC VEHICLES**

**Ünal YILMAZ**

**PhD THESIS**

**DEPARTMENT OF ELECTRICAL AND ELECTRONICS ENGINEERING**

We certify that the thesis titled above was reviewed and approved for the award of degree of the Doctor of Philosophy by the board of jury on 27/08/2020.

| | | |
|---|---|---|
| ………………………… | ……………………………… | ……………………………… |
| Assoc. Prof. Dr. Ahmet TEKE | Assoc. Prof. Dr. Turgay İBRİKÇİ | Assoc. Prof. Dr. Murat AKSOY |
| SUPERVISOR | MEMBER | MEMBER |
| ………………………… | ……………………………… | |
| Assoc. Prof. Dr. Lütfü SARIBULUT | Asst. Prof. Dr. Murat FURAT | |
| | MEMBER | |

This PhD Thesis is written at the Department of Electrical and Electronics Engineering of Institute of Natural and Applied Sciences of Çukurova University.
**Registration Number**:

**Prof. Dr. Mustafa GÖK**
**Director**
**Institute of Natural and Applied Sciences**

# ABSTRACT

**PhD THESIS**

**INVESTIGATION OF HIGH EFFICIENT DC-DC CONVERTERS FOR ON-BOARD BATTERY CHARGING SYSTEM IN ELECTRIC VEHICLES**

**Ünal YILMAZ**

**ÇUKUROVA UNIVERSITY**
**INSTITUTE OF NATURAL AND APPLIED SCIENCES**
**DEPARTMENT OF ELECTRICAL AND ELECTRONICS ENGINEERING**

Supervisor : Assoc. Prof. Dr. Ahmet TEKE
Year: 2020, Pages: 201
Jury : Assoc. Prof. Dr. Ahmet TEKE
: Assoc. Prof. Dr. Turgay İBRİKÇİ
: Assoc. Prof. Dr. Murat AKSOY
: Assoc. Prof. Dr. Lütfü SARIBULUT
: Assist. Prof. Dr. Murat FURAT

Due to the limited interior space in electric vehicles, two-stage battery chargers should meet some requirements such as high power density and high efficiency. The efficiency and power density of two-stage on-board battery chargers largely depend on isolated DC-DC converters. In this thesis, two different topologies are proposed for on-board battery charging systems in electric vehicles. A control method, based on artificial neural networks (ANN), is developed for soft switched (ZVS) LLC resonance converter in Topology-I and it was compared with the traditional method at different load conditions. Thanks to the proposed control method, improvement in steady state error and transient response time was observed. Both the grid and photovoltaic (PV) panel fed, two-stage battery charging unit proposed in the Topology-II. For the proposed topology, a maximum power point tracking (MPPT) method with high speed and high accuracy has been developed and compared to traditional methods. In addition, a LLC resonance DC-DC converter is designed to allow the high-power and low-power battery to be charged on a single circuit. Thus, the proposed Topology-II is intended to allow the electric vehicle to travel more miles with a single charge process. The proposed topologies have been analyzed at different load ranges to measure efficiency system according to European efficiency standard.

**Key Words**: Electric Vehicles, Battery Chargers, DC-DC Converters, Soft Switching, ANN.

## ÖZ

### DOKTORA TEZİ

**ELEKTRİKLİ ARAÇLARDA DÂHİLİ BATARYA ŞARJ SİSTEMİ İÇİN YÜKSEK VERİMLİ DA-DA DÖNÜŞTÜRÜCÜLERİN İNCELENMESİ**

**Ünal YILMAZ**

**ÇUKUROVA ÜNİVERSİTESİ**
**FEN BİLİMLERİ ENSTİTÜSÜ**
**ELEKTRİK – ELEKTRONİK MÜHENDİSLİĞİ ANABİLİM DALI**

Danışman : Doç. Dr. Ahmet TEKE
Yıl: 2020, Sayfa: 201
Jüri : Doç. Dr. Ahmet TEKE
: Doç. Dr. Turgay İBRİKÇİ
: Doç. Dr. Murat AKSOY
: Doç. Dr. Lütfü SARIBULUT
: Dr. Öğr. Üyesi Murat FURAT

Elektrikli araçlarda sınırlı iç hacim nedeniyle, batarya şarj ünitelerinin yüksek güç yoğunluğu ve yüksek verimlilik gibi gereksinimleri karşılaması gerekmektedir. İki aşamalı dâhili batarya şarj ünitelerinin verimliliği ve güç yoğunluğu büyük ölçüde yalıtımlı DA-DA dönüştürücülere bağlıdır. Bu tezde, iki-aşamalı batarya şarj ünitesi için iki farklı çalışma önerilmektedir. Topoloji-I'de yapay sinir ağları (YSA) kullanılarak tasarlanan kontrol metodu yumuşak anahtarlamalı (ZVS) LLC rezonans dönüştürücüye farklı yük durumlarında uygulanarak geleneksel yöntem ile karşılaştırılmıştır. Ani yük değişiminde geleneksel yönteme göre kararlı durum hatasında ve geçici tepki süresinde iyileştirme olduğu gözlemlenmiştir. Topoloji-II'de ise hem şebeke hem de PV panel beslemeli, iki-aşamalı batarya şarj ünitesi önerilmiştir. Önerilen topoloji için geleneksel yöntemlere göre yüksek hızda ve yüksek doğruluk oranına sahip maksimum güç noktası izleme (MPPT) metodu geliştirilmiştir. Ayrıca, yüksek güçlü ve düşük güçlü bataryanın tek bir devre üzerinde şarj edilmesine olanak sağlaması için bir LLC rezonans DA-DA dönüştürücü tasarlanmıştır. Önerilen batarya şarj mimarisi sayesinde tek bir şarj işlemi ile elektrikli aracın daha fazla yol alabilmesine olanak sağlaması amaçlanmıştır. Önerilen topolojilerde Avrupa verimlilik standardına göre hesaplama yapılmıştır.

**Anahtar Kelimeler:** Elektrikli Araçlar, Batarya Şarj Sistemi, DA-DA Dönüştürücüler, Yumuşak Anahtarlama, YSA.

## EXTENDED SUMMARY

The decrease in fossil fuels, rising oil prices, carbon emissions caused by vehicles with conventional internal combustion engines, and greenhouse gases, causing serious damage to human and nature health, has caused an increase in interest in electric vehicles on a global scale. Research topics are intensively researched by the scientific world, such as improving the performance of electric vehicles, enabling them to be charged in less time and enabling them to travel more with a single charge process. Since all power components (motor, auxiliary loads, lighting, etc.) in electric vehicles are powered by batteries, battery chargers create a large part of research on electric vehicle technology.

The main function of battery chargers is to provide high efficiency and reliable power transmission between the energy source (grid) and the battery. In the Literature, battery charging units are basically examined under two main titles which are on-board and off-board battery chargers. Off-board battery chargers are designed to exemplify the functionality of conventional gas filling stations. Charging units are located outside the vehicle, allowing the battery to charge in a shorter time at high power. However, off-board battery chargers have problems such as high power demand, complex battery charge management and battery warming problems. These problems are considered as research topics for the Literature.

On the other hand, on-board battery chargers are examined under two main titles as single-stage and two-stage battery chargers. Although, there are advantages such as low number of circuit elements, low cost, easy installation, high efficiency provided by single-stage battery chargers, these battery chargers are generally preferred at low powers (≤1 kw) since there is a high electrical stress on power circuit elements. They also need a high capacity output capacitor to reduce output voltage fluctuations.

On the other hand, well-designed, two-stage on-board battery chargers can accommodate desired features such as high energy transmission efficiency, high power factor and low total harmonic distortion (THD). The two-stage on-board battery chargers consist of an AC-DC converter to convert the alternating current (AC) to direct current (DC) and a DC-DC converter to regulate direct current to the desired level. AC-DC converters are used in conjunction with a power factor regulator (PFC) circuit to regulate the power factor for the battery charger and reduce the total harmonic distortions occurring in the grid current. However, DC-DC converters, provide galvanic insulation between the battery and grid, while enabling safer charging, and also the efficiency of the battery charging unit largely depends on the efficiency of the DC-DC converters. Thus, DC-DC converters are very important for battery chargers.

DC-DC converters designed to be used in battery chargers are expected to have features such as high energy conversion efficiency, reduction of switching losses and electromagnetic interference (EMI) by applying soft switching methods. In addition, they should be avoided additional circuit elements as much as possible and also they should show performance in a wide load range and narrow frequency change band. There are studies proposed in the Literature focusing on resonance converter and soft switching methods to increase the efficiency of dc-dc converters designed for battery chargers. There are studies proposed in the Literature which have simple and feasible or complex and difficult-to-understand control methods to increase performance of DC-DC converters. At the same time, topological innovations have been proposed in the Literature, so that they can be fed from high power density and environmentally friendly alternative energy sources.

In this Thesis, two different topologies are proposed for the two-stage on-board battery charging unit. A design consisting of an AC-DC boost power factor correction circuit and half bridge LLC resonance converter for two stage battery charger topology is proposed in Topology-I. A control method capable of soft switching (ZVS) with artificial neural networks (ANN) support has been developed for the LLC Resonance converter circuit. The voltage characteristics of LLC resonance converter with the developed control method in different load range (5% -100% load range) are compared with the traditional method. An improvement in steady-state error and transient response time compared to the traditional method has been observed under sudden load change. In addition, by applying soft switching method, it is aimed to reduce switching losses and electromagnetic interference (EMI) at high frequency. According to European efficiency standards, efficiency analysis was performed by obtaining performance results in six different load cases (5%, 10%, 20%, 30%, 50%, 100%). Thanks to soft switching (ZVS), switching losses are reduced and efficiency increase is achieved. In addition, by applying AC-DC converter average current mode control method (ACM), high power factor and low phase angle were obtained, while total harmonic distortion was observed to comply with IEC 61000-3-2 THD standards. Computer applications of the proposed method were carried out using Matlab / Simulink program.

In Topology-II, a two-stage battery charging architecture is proposed. In the proposed battery charging architecture, the grid powered high power battery and the auxiliary battery feeding the low power loads with PV panel connection are on the same circuit. For the PV panel side, in order to operate the PV panel at the maximum power point under variable radiation and temperature conditions, a two-stage maximum power point tracking (MPPT) method has been developed. The improved MPPT method consists of a soft calculation function, created according to the current-voltage characteristics, and fuzzy logic for regulating PWM signal. The developed MPPT method has been compared with traditional methods in terms of accuracy and the convergence time and maximum power point capture performance under variable atmospheric conditions. It has been observed that the convergence time and accuracy rate are improved compared to traditional MPPT methods. In addition, the low power battery that feeds auxiliary loads in conventional battery chargers is powered by high power battery. In the proposed method, the battery feeding the auxiliary loads is fed from the PV panel. In this way, the high power battery transmits the charged energy only to the electric motor, allowing the electric vehicle to travel more with a single charge process. In the grid supply side, high power factor and low harmonic distortion were obtained by operating the bridgeless ac-dc power factor regulating average current mode control method. In the dc-dc step, LLC Resonance transducer was designed to operate the system as a two-input and two-output structure. The voltage and current characteristics of the proposed topology under different load conditions are analyzed. In addition, according to European efficiency standards, efficiency analysis was performed by obtaining performance results in six different load situations (5%, 10%, 20%, 30%, 50%, 100%). In addition, by applying ac-dc converter average current mode control method, high power factor and low phase angle were obtained, while total harmonic distortion was observed to comply with IEC 61000-3-2 THD standards. Computer applications of the proposed method were carried out using Matlab / Simulink program.

The proposed Topology-I can be a serious candidate for a two-stage battery charge topology, both in terms of the control method being higher performance and easier to apply than the traditional method, as well as low switching losses and high efficiency due to the resonant converter and soft switching application. In addition, Topology-II can be an important candidate for two-stage battery charging topology in order to allow the electric vehicle to travel more with a single charge process and to reduce the energy usage cost by using renewable energy in the short term.

## GENİŞLETİLMİŞ ÖZET

Fosil yakıtların azalması, artan petrol fiyatları, geleneksel içten yanmalı motorlara sahip araçların sebep olduğu karbon salınımı ve sera gazlarının, insan ve doğa sağlığı üzerinde ciddi zararlar oluşturması, elektrikli araçlara olan ilginin küresel ölçekte artmasına yol açmıştır. Elektrikli araçların performansını artırmak, daha kısa sürede şarj edilebilmelerini sağlamak ve tek bir şarj işlemiyle daha fazla yol alabilmesine olanak sağlamak gibi araştırma konuları, bilim dünyası tarafından yoğun bir şekilde araştırılmaktadır. Elektrikli araçların sahip olduğu güç bileşenleri (motor, yardımcı yükler, aydınlatma vb.) elektrikli araçlardaki bataryalardan beslendikleri için, batarya şarj üniteleri elektrikli araç teknolojisi ile ilgili araştırmaların büyük bir bölümünü oluşturmaktadır.

Batarya şarj ünitelerinin temel fonksiyonu, enerji kaynağı (şebeke) ile batarya arasında yüksek verimlilikte ve güvenilir bir şekilde güç aktarımı sağlamaktır. Literatürde, batarya şarj üniteleri temel olarak; dâhili (On-board) ve harici (Off-board) olmak üzere iki ana başlık altında incelenmektedir. Harici batarya şarj üniteleri, geleneksel benzin dolum istasyonlarının işlevselliğini örnek alacak şekilde tasarlanmıştır. Şarj üniteleri aracın dışında bulunur ve bataryanın yüksek güçte daha kısa sürede şarj işleminin gerçekleşmesine olanak sağlar. Fakat harici batarya şarj ünitelerinde yüksek güç talebi, karmaşık batarya şarj yönetimi ve bataryalarda ısınma gibi problemler bulunmaktadır. Bu problemler, Literatür için araştırma konuları olarak ele alınmaktadır.

Dâhili batarya şarj üniteleri, tek-aşamalı ve iki-aşamalı olmak üzere iki ana başlık altında incelenmektedir. Tek aşamalı batarya şarj ünitelerinin sağlamış olduğu az devre eleman sayısı, düşük maliyet, kolay kurulum, yüksek verimlilik gibi avantajları olmasına rağmen bu batarya şarj ünitelerinde yüksek güçlerde güç devre elemanları üzerinde elektriksel stres fazla olduğu için genellikle düşük güçlerde (≤1 kW) tercih edilmektedir. Aynı zamanda, çıkış gerilim dalgalanmalarını azaltmak için yüksek kapasiteye sahip çıkış kondansatörüne ihtiyaç duymaktadırlar.

İyi tasarlanmış, iki-aşamalı dâhili batarya şarj üniteleri, yüksek enerji iletim verimliliği, yüksek güç faktörü ve düşük toplam harmonik bozunum (THD) gibi arzulanan özellikleri barındırabilmektedirler. İki-aşamalı dâhili batarya şarj ünitelerinin ilk aşaması alternatif akımı (AA) doğru akıma (DA) dönüştürmek için bir AA-DA dönüştürücü ve ikinci aşaması ise doğru akımı istenilen düzeye getirebilmek için bir DA-DA dönüştürücüden oluşmaktadır. AA-DA dönüştürücüler batarya şarj ünitesi için güç faktörünü düzenlemek ve şebeke akımında meydana gelen toplam harmonik bozunumları azaltmak için bir güç faktörü düzenleyici (PFC) devresi ile birlikte kullanılır. DA-DA Dönüştürücüler ise batarya ile şebeke arasında galvanik yalıtım sağlayarak daha güvenli bir şarj işlemine olanak sağlarken aynı zamanda batarya şarj ünitesinin verimliliği büyük oranda DA-DA dönüştürücülerin verimliliğine bağlıdır. Dolayısıyla, DA-DA dönüştürücüler batarya şarj üniteleri için oldukça önem arz etmektedirler.

Batarya şarj ünitelerinde kullanılmak üzere tasarlanan DA-DA dönüştürücülerin verimliliğinin yüksek olması, yumuşak anahtarlama metotları uygulanarak anahtarlama kayıplarının ve elektromanyetik girişimlerin azaltılması (EMI), mümkün olduğunca ek devre elemanlarından kaçınılması, geniş yük aralığında performans gösterebilmesi, frekans değişim bandının dar olması gibi özelliklere sahip olması beklenir. Literatürde yapılan çalışmalarda, batarya şarj üniteleri için tasarlanan DA-DA dönüştürücülerin verimliliğini artırmak için, rezonans dönüştürücü ve yumuşak anahtarlama metotları üzerinde yoğunlaşırken, geniş yük aralığında yüksek performans göstermek için ise basit ve uygulanabilir veya karmaşık ve anlaşılması zor kontrol metotları üzerinde durulmuştur. Aynı zamanda yüksek güç yoğunluğu ve çevre dostu alternatif enerji kaynaklarından beslenebilmeleri için topolojik yenilikler Literatürde önerilmiştir.

Bu tez çalışmasında, iki aşamalı batarya şarj ünitesi için iki farklı topoloji önerilmiştir. Topoloji-I'de iki aşamalı batarya şarj topolojisi için AA-DA artırıcı güç faktörü düzenleyici devresi ve yarım köprü LLC rezonans dönüştürücüden oluşan bir tasarım yapılmıştır. LLC rezonans dönüştürücü devresi için yapay sinir ağları (YSA) destekli yumuşak anahtarlama yapabilen bir kontrol yöntemi geliştirilmiştir. Geliştirilen kontrol yöntemi farklı yük Aralığında (5%-100% Yük aralığı) çıkış akım ve gerilim karakteristikleri geleneksel yöntem ile karşılaştırılmıştır. Ani yük değişiminde geleneksel yönteme göre kararlı durum hatasında ve geçici tepki süresinde iyileştirme olduğu gözlemlenmiştir. Ayrıca, yumuşak anahtarlama metodu uygulanarak yüksek frekansta, anahtarlama kayıplarının ve elektromanyetik girişimlerin (EMI) azaltılması amaçlanmıştır. Avrupa verimlilik standartlarına göre altı farklı yük durumunda (%5, %10, %20, %30, %50, %100) performans sonuçları alınarak verimlilik analizi yapılmıştır. Yumuşak anahtarlama sayesinde anahtarlama kayıpları azaltılarak verimlilik artışı sağlanmıştır. Ayrıca AA-DA dönüştürücü ortalama akım kontrol metodu uygulanarak, yüksek güç faktörü ve düşük faz açısı elde edilirken, toplam harmonik bozunumun ise IEC 61000-3-2 THD standartlarına uygun olduğu gözlemlenmiştir. Önerilen yöntemin bilgisayar uygulamaları Matlab/Simulink programı kullanılarak gerçekleştirilmiştir.

Topoloji-II'de ise şebeke ve fotovoltaik (PV) beslemesi olan yüksek güçlü batarya ve düşük güçlü yükleri beslemek için yardımcı bataryanın aynı devre üzerinde şarj olabileceği iki aşamalı bir batarya şarj mimarisi modellenmiştir. PV besleme basamağı için farklı ışınım ve sıcaklık durumlarında PV paneli maksimum güç noktasında çalıştırabilmek için PV panelin akım ve gerilim karakteristiklerine göre yumuşak hesaplama ve bulanık mantıktan oluşan iki aşamalı bir maksimum güç noktası izleme (MGNİ) metodu geliştirilmiştir. Geliştirilen MGNİ metodu farklı atmosferik koşullarda maksimum güç noktasına yakınsama hızı ve maksimum güç noktasını yakalama performansı olarak doğruluk oranı bakımından geleneksel yöntemlerle karşılaştırılmıştır. Geleneksel MGNİ metotlara göre yakınsama hızında ve doğruluk oranında iyileştirme sağlandığı gözlemlenmiştir. Geleneksel batarya şarj ünitelerinde yardımcı yükleri besleyen düşük güçlü batarya, yüksek güçlü bataryadan beslenmektedir. Önerilen yöntemde ise yardımcı yükleri besleyen batarya PV panelden beslenmektedir. Böylece yüksek güçlü batarya şarj edilen enerjiyi sadece elektrik motoruna ileterek elektrikli aracın tek bir şarj işlemi ile daha fazla yol alabilmesine olanak sağlayabilmektedir.

Şebeke besleme basamağında ise köprüsüz AA-DA güç faktörü düzenleyici ortalama akım kontrol metodu ile çalıştırılarak, yüksek güç faktörü ve düşük harmonik bozunum elde edilmiştir. DA-DA basamağında ise sistemin iki girişli ve iki çıkışlı yapı olarak çalıştırılabilmesi için LLC rezonans dönüştürücü tasarlanmıştır. Önerilen topoloji farklı yük durumlarında, gerilim ve akım karakteristikleri analiz edilmiştir. Önerilen sistem, Avrupa verimlilik standartlarına göre altı farklı yük durumunda (%5, %10, %20, %30, %50, %100) performans sonuçları alınarak verimlilik analizi yapılmıştır. Ayrıca AA-DA dönüştürücü ortalama akım mod kontrol metodu uygulanarak, yüksek güç faktörü ve düşük faz açısı elde edilirken, toplam harmonik bozunumun ise IEC 61000-3-2 THD standartlarına uygun olduğu gözlemlenmiştir. Önerilen yöntemin bilgisayar uygulamaları Matlab/Simulink programı kullanılarak gerçekleştirilmiştir.

Önerilen Topoloji-I, gerek kontrol yönteminin geleneksel yönteme göre daha yüksek performanslı ve kolay uygulanabilir olması gerekse rezonans dönüştürücü ve yumuşak anahtarlama uygulamasından dolayı düşük anahtarlama kayıplarına ve yüksek verimliliğe sahip olması açısından iki-aşamalı batarya şarj topolojisi için ciddi bir aday olabilir. Topoloji-II ise tek bir şarj işlemi ile elektrikli aracın daha fazla yol alabilmesine olanak sağlaması ve yenilenebilir enerji kullanılarak kısa vadede enerji kullanım maliyetini düşürebilmesi açısından iki aşamalı batarya şarj topolojisi için önemli bir aday olabilir.

**ACKNOWLEDGEMENTS**

First of all, I express my gratitude to my superior Assoc. Prof. Dr. Ahmet TEKE for his expertise and help during this thesis, as well as his full support and patience. His knowledge, scientific experience and perspective have enabled me to complete this thesis study.

In addition, I would like to thank PhD thesis progress committee members Assoc. Prof. Dr. Turgay İBRİKÇİ and Asst. Prof. Dr. Murat FURAT for their academic perspective and valuable time.

Besides, I would like to thank my dear friend Ömer TÜRKSOY for both his spiritual support and his interest and helpfulness.

I would also like to express my gratitude to Prof. Dr. Ali KIRÇAY for his scientific perspective, support and encouragement. Additionally, I express my gratitude for the financial support of Harran University Scientific Research Project Unit (Project Number: 19012).

Finally, I would like to thank all my family members for their endless support and love throughout my life.

**CONTENTS** **PAGE**

**LIST OF TABLES** **PAGE**

**LIST OF FIGURES** **PAGE**

XXIX

## LIST OF ABBREVIATIONS

AC : Alternative Current
ANN : Artificial Neural Networks
BCU : Battery Charge Unit
DAB : Dual Active Bridge
DC : Direct Current
EMI : Electromagnetic Inference
EV : Electric Vehicle
FB : Full Bridge
FLC : Fuzzy Logic Control
HB : Half Bridge
HEV : Hybrid Electric Vehicle
Hz : Hertz
IC : Incremental Conductance
IEC : International Electrotechnical Commission
LM : Levenberg-Marquardt
MPPT : Maximum Power Point Tracking
MSE : Mean square Error
OBC : On-board Charger
P : Real Power
P&O : Perturbation and Observation
PFC : Power Factor Correction
PI : Proportional Integrator
PS : Phase Shift
PV : Photovoltaic
PWM : Pulse Width Modulation
Q : Quality factor
SAE : Society of Automotive Engineers

THD : Total Harmonic Distortion
VCO : Voltage Controlled Oscillator
ZCS : Zero Current Switching
ZCT : Zero Current Transition
ZVS : Zero Voltage Switching
ZVT : Zero Voltage Transition

# 1. INTRODUCTION

In this section, battery charging methods for plug-in electric vehicles, charging standards and codes, on-board single-stage and two-stage battery charging methods with specifications and challenges encountered, AC-DC PFC converters general structures and specifications and finally isolated DC-DC converters, benefits and challenges to provide is presented. In addition, the research objectives, contributions and organization of the thesis are given at the end of this section.

## 1.1. Background and Motivation

Researches show that vehicles with conventional internal combustion motors used in transportation account for about 20% of the first energy consumed, while 23% of $CO_2$ emissions and about 14% of emitted greenhouse gases. In addition, if the current consumption rate is continued, fossil fuels are predicted to be run out in the next 50 years (Özbay et al., 2020). The fact that the traditional internal combustion vehicles are nearing their exhaustion life and the damage they give to the environment have increased the popularity of electric vehicle technology (Ronanki et al., 2019, Restrepo et al., 2018, Lee et al., 2017).

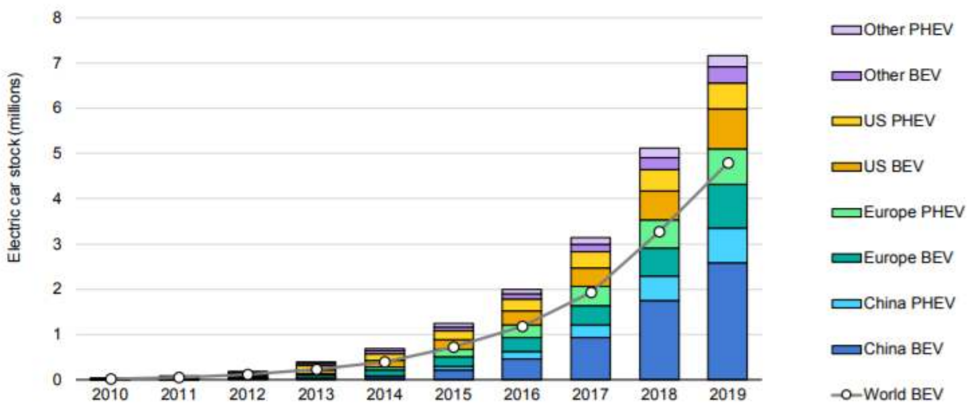


Figure 1.1 Global electric car stock (IEA, 2020).

The supporting data that electric vehicles increase in popularity every year worldwide is presented in Figure 1.1.

Research subjects such as improving the performance of electric vehicles, making them charge in less time and driving more miles with a single charge process are intensively researched by the scientific world. Since all components (electric motor, auxiliary loads, lighting ...) are powered by batteries in electric vehicles, battery chargers constitute a large part of the researches on electric vehicle technology. Among the main functions of battery chargers are used to achieve high efficiency and reliable power transmission between the energy source (grid) and the battery (Bai et al., 2012, Iyer et al., 2019, Lee et., 2017). As shown in Figure 1.2, in general structure, battery charging units are examined under two main headings. The first one is the off-board and the second one is on-board battery charger (OBC).

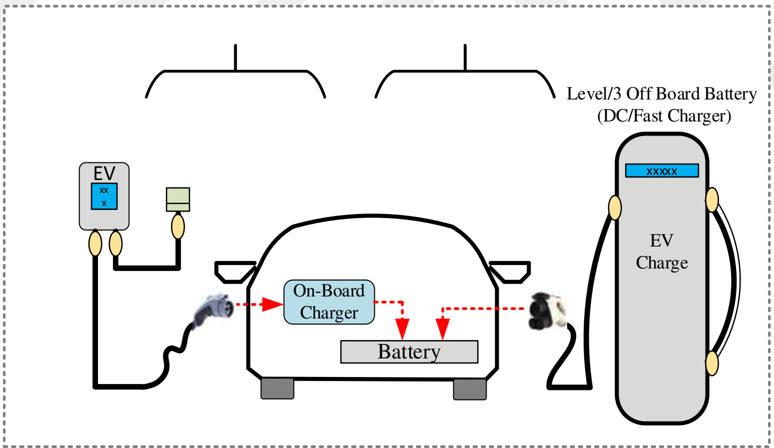


Figure 1.2 General structure of battery chargers

Off-board chargers are the infrastructure that can mimic the functionality of a petrol refueling station, the battery charger is located outside the EVs and allows the battery to be charged in high power, in a shorter time (Ronanki et al., 2019). However, off-board battery chargers have problems such as having a complex battery management system, high power demand, and battery heating problem (Wirtz et al., 2011). Since have the serious drawbacks as mentioned, off-board battery chargers demand rates are quite low compared to on-board battery chargers.

On-board battery chargers (OBC) operate at relatively low powers, less concerning about heating problem and battery management systems are easier to implement. However, they are embedded in electric vehicles so that they create a bit more weight and take up more space (Wirtz et al., 2011). The internal structure of a plug-in EV and the on-board battery charger design are shown in Figure 1.3.

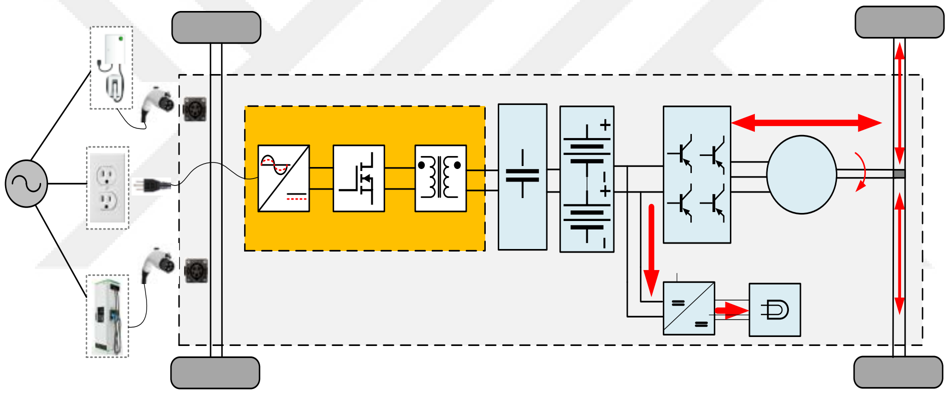

Figure 1.3 The internal structure of a plug-in EV and on-board battery chargers.

In order to perform battery charging process safely and to perform high quality charging, different standards have been defined in the literature for the charging of the battery in electric vehicles. The most widely used standard is the J1772 standard, prepared by Society of Automotive Engineers (SAE). According to SAE J1772 standard, the charging speed is expressed in certain levels as shown in Table 1.1. In Level 1 and Level 2 charging methods, alternating current is provided to the on-board AC-DC rectifier and the direct current required for battery charging is obtained from the output of this rectifier. In the other type DC fast charging, the conversion of the alternating current to direct current is done at the charging station and direct current is given to the battery of the vehicle. The average time of DC charging, varies between 20 minutes and 20 hours depending on the type of battery, energy capacity and charger (Polat et al., 2015) Motor rating power (kw), battery capacities and range (mil) information of commercially produced electric vehicles are presented in (Ronanki et al., 2019, Kongjeen et al., 2018).

Table 1.1 SAE J1772 standard (Kongjeen et al., 2018)

| Type of Charge | Grid Connection | Voltage | Current | Type of Charge |
|---|---|---|---|---|
| AC Level 1 | 1 phase | 120 V | 12-16 A | Slow |
| AC Level 2 | 1 phase | 240 V | < 80 A | Slow |
| AC Level 3 | 1,3 phase | 240 V | > 80 A | Slow |
| DC Level 1 | - | 200-450 V | 80 A | Slow |
| DC Level 2 | - | 200-450 V | 200 A | Medium |
| DC Level 3 | - | 200-600 V | 400 A | Fast |

The 61851 standard, defined by the International Electrotechnical Commission (IEC), is mostly used in Europe and China. Charging methods in the IEC 61851 standard and maximum current and voltage values specified in these methods are given in Table 1.2 (Polat et al., 2015).

Table 1.2 IEC 61851 charging standard

| | Charging Mode | Phase-Number | Rated Voltage (V) | Max. Current (A) |
|---|---|---|---|---|
| AC | Mode 1 | 1 | ≤250 | ≤16 |
| | | 3 | ≤480 | |
| | Mode 2 | 1 | ≤250 | ≤32 |
| | | 3 | ≤480 | |
| | Mode 3 | 1 | ≤250 | ≤250 |
| | | 3 | ≤480 | |
| DC | Mode 4 | --- | ≤1000 | ≤400 |

In order to reduce charging time (fast charging), CHAdeMO standards used in Europe and USA as well as in Japan. The electrical characteristics of the method is shown in Table 1.3 (Polat et al., 2015).

Table 1.3 CHAdeMO charging standards

| Charging Type | Rated Voltage (Vdc) | Max. Current (A) | Max. Power- (kW) |
|---|---|---|---|
| CHAdeMO | 500 | 125 | 62.5 |

On-board battery chargers are generally presented in the literature in two different topologies which are single-stage and two-stage OBC.

General structure of single-stage battery charger topology is given in Figure 1.4. Single-stage OBC topologies provide high efficiency in low power stages, since the number of circuit elements is low, they can be realized with high reliability and low cost. On the other hand, since the electrical stress on the circuit elements is high, they are generally preferred for low power stages (≤1 kW). The main drawback of the single-stage OBC is that they need a high capacity output electrolyte capacitor to minimize output voltage ripples. (Li, et al., 2013, Oh, et al., 2013, Jeong, et al., 2019).

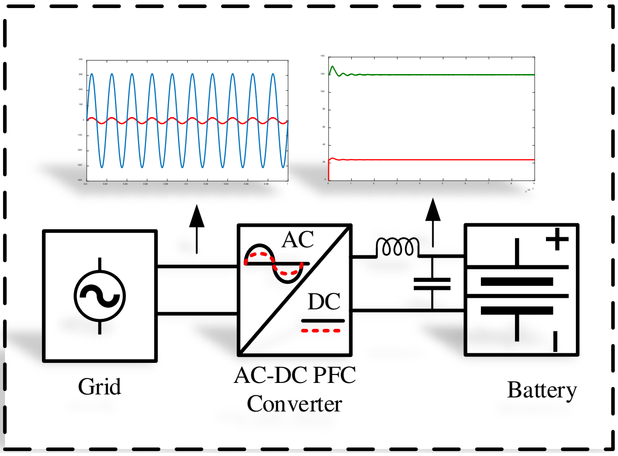


Figure 1.4 General structure of single-stage battery charger.

On the other hand, well-designed two-stage OBC should have desired features like performing at high power density, high power conversion efficiency, high power factor, and low total harmonic distortion (THD). A conventional two-stage battery charger topology consist of an AC-DC PFC converter as a first stage, followed by isolated DC-DC converter as a second stage (Kim et al., 2015, Shi et al., 2017, Yilmaz et al., 2019, Shi et al., 2018). The configuration of two stage battery OBC is given in Figure 1.5.

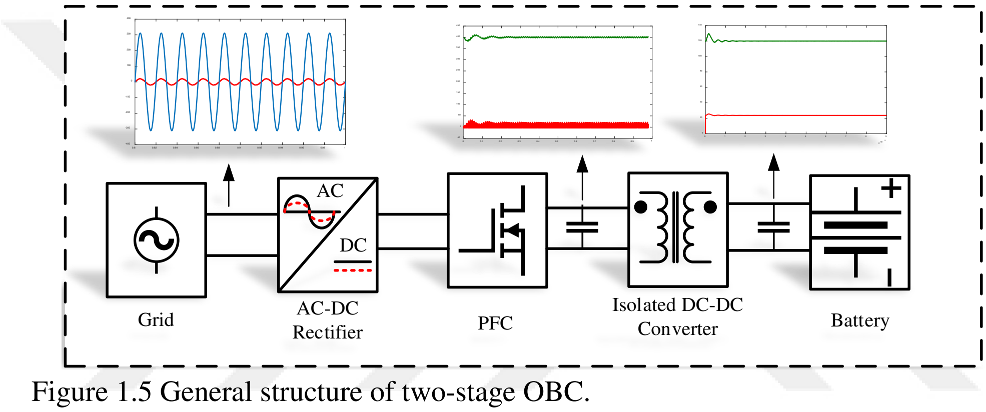

Figure 1.5 General structure of two-stage OBC.

The AC-DC PFC converter is used to convert the alternating current received from the power source (grid) into direct current in high efficiency and high power factor, because low power factor causes extra electrical stress and reduce system efficiency. PFC converter also provides stable dc-link voltage (Das et al., 2013, Shi et al., 2016, Musavi et al., 2010). The effect of AC-DC PFC converter in OBC is shown in Figure 1.6.

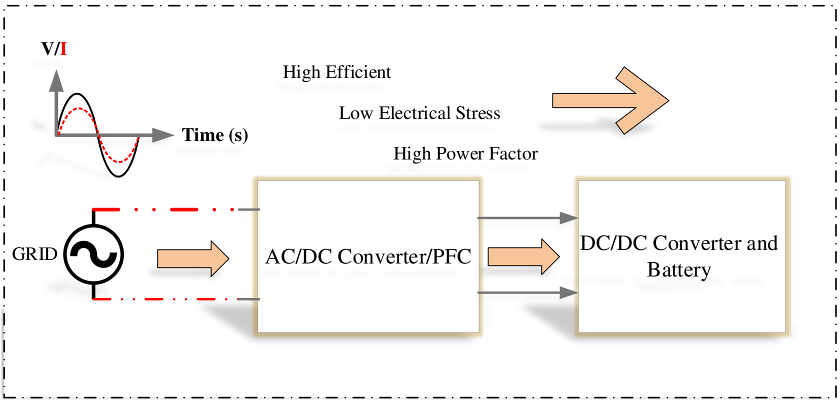


Figure 1.6 The effect of AC-DC PFC converter in OBC

There are some features that AC-DC PFC converters designed for OBC should provide. AC-DC PFC converters must meet The first of these challenges is the high power factor. The power factor, in its most basic definition, is found by the ratio of the real power $P$ to the apparent power ($S$). Real power is the factor that does the actual work in energy transfer. Apparent power is found by the rms values of the current $I_{rms}$ and voltage $V_{rms}$. If the real power and apparent power are equal, the load is called completely resistive. However, if the actual power is not equal to the apparent power, the system has energy storage circuit elements such as an inductor and capacitor. In this case, they store and release energy during the energy transfer process, resulting in low energy transfer efficiency (Alam., 2017).

The pf appears between ‘0’ and ‘1’ depending on the system designed. The value expected from the pf is unity ‘1’ but even if this is done theoretically, 0.99 and above is considered to be good, since it is not possible to realize unity ‘1’ pf, in circuits that do not have a fully resistive load. Pf is also directly related to total harmonic distortion (THD) which is given in eqs.1 (Alam., 2017).

$$PF = \left( \frac{1}{\sqrt{1+(THD)^2}} \right) \cos(\phi_V - \phi_i) \tag{1.1}$$

Phase voltage, current and harmonic relationship of power factor are shown in Figure 1.7.

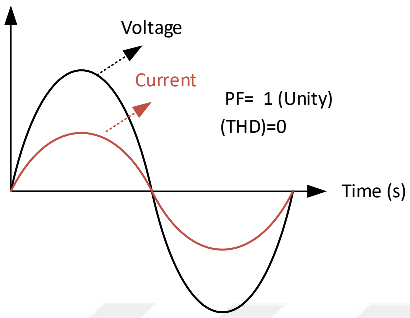


Figure 1.7 Voltage, current and THD relationship of power factor (Alam., 2017)

Another challenge to be overcome in PFC converter design is to reduce total harmonic distortion. Power electronics circuits perform the conversion of alternating current to direct current while battery charging is performed in EVs. Harmonic distortions in current and voltage occur during this process. Harmonic distortion and low power factor that occur in current and voltage increase power loss in electrical cables and limit cable capacity (Büyük., 2019). For the sustainable use of electrical energy, a standard is recommended by IEC61000-3-2 (D class) (Musavi et al., 2011).

Total harmonic distortions (THD) can be defined as the ratio of the rms value of the distortions occurring in individual signals (current and voltage) to the rms value of the fundamental signal.

$$THD_k = \frac{\sqrt{\sum_{n=2} k^2{}_n}}{k_1} \tag{1.2}$$

Where $k$ can be defined as voltage or current, $k_1$ is the fundamental signal (Büyük., 2019).

The limits of individual harmonic distortions occurring in current/watt is specified in the standards. Table 1.4 presents the individual current harmonics and percentages determined according to IEC61000-3-2 standards (Musavi et al., 2011).

Table 1.4 IEC61000-3-2 standards

| Individual odd Harmonic order h | Maximum permissible harmonic current per watt (mA/W) | Maximum permissible harmonic current (A) |
|---|---|---|
| 3 | 3.4 | 2.3 |
| 5 | 1.9 | 1.14 |
| 7 | 1.0 | 0.77 |
| 9 | 0.5 | 0.4 |
| 11 | 0.35 | 0.33 |
| 13 | 0.3 | 0.21 |
| $15 \leq n \leq 39$ Odd harmonics only | 3.85/n | 0.15*15/n |

In the second stage of OBC, using an isolated dc-dc converter in order to provide high power density, high efficiency (important for EVs to travel more with a single charge process), galvanic isolation between battery and grid (for reliable energy transfer), enabling battery charger to operate in a wide load range (charger operation, under light load to full load condition) which are specified in Figure 1.8 (Lee et al., 2016, Gautam et al., 2013, Deng et al., 2014, He et al., 2017).

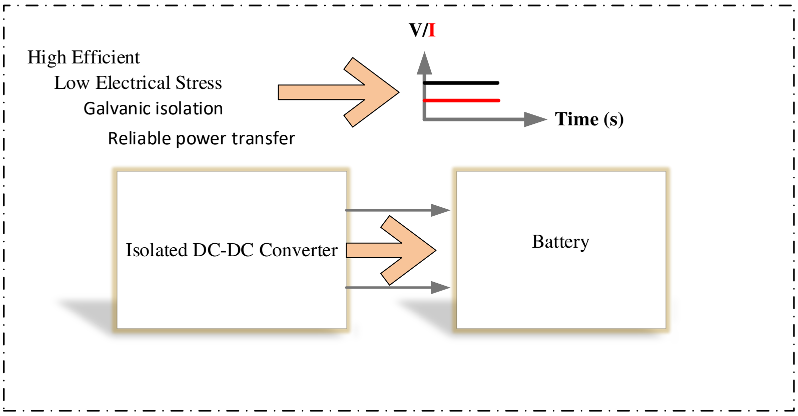


Figure 1.8 The effect of isolated DC-DC PFC converter in OBC.

Increasing the efficiency of OBC is a very important issue for EVs since the efficiency of BCUs is directly related to the mileage that the electric vehicle can travel. Efficiency of two-stage OBC largely depends on the efficiency of the isolated dc-dc converter, and the well-designed dc-dc converter also positively contributes to battery lifespan. The isolated DC-DC converters to be used in battery chargers are generally expected to provide the following challenges (Lee et al., 2016, Gautam et al., 2013, Deng et al., 2014, He et al., 2017).

- Wide load and output voltage range (light load-full load).
- Application of soft switching under wide load range.
- Avoiding using snubber circuit in order to reduce power loss.
- Narrow switching frequency variation.
- High energy transmission efficiency

Due to the limited interior space in electric vehicles, the proposed OBCs must meet some requirements. These requirements are; high power density, high efficiency and good heat dissipation. The efficiency and high power density of OBCs largely depend on the designed isolated DC-DC converters. In the isolated

DC-DC converters, which are generally designed and operated at high frequencies, the size of the circuit elements decreases, while the switching losses increase. In order to prevent this situation, soft switching methods (Bai et al., 2012, Kim et al., 2015, Whitaker et al., 2014, Lee et al., 2017, Praneeth et al. 2019, Tao et al., 2019), resonance converters (Guatam et al., 2013, Pandey et al., 2019, Deng et al., 2014, Wang et al., 2014, Lin et al., 2018), control methods (Choi et al., 2018, Iyer et al., 2019, Liu et al., 2017, Alhamrouni et al., 2016, Hsieh et al., 2011) and topological improvements (Kim et al., 2017, Lee., 2015, Lee et al., 2015, Shi et al., 2018, Lee et al., 2017) are proposed in the Literature.

Isolated DC-DC converters proposed for on-board battery chargers in the Literature are mainly focused on similar issues as described above. These issues are; soft switching for high efficiency, resonant converters, either complex and difficult to understand or simple but deficient control methods or topological improvements for high power density.

## 1.2. Research Objectives and Contributions

Two-stage on-board battery chargers used in electric vehicles still suffer from high production costs, conversion efficiency ratios and low power quality conditioning. For this reason, it is very important to increase the efficiency of the two-stage on-board battery chargers, improve the controller structures and use renewable energy sources with topological developments. Since the effectiveness of OBCs topologies largely depends on the efficiency of the DC-DC converter, it is very important to support the DC-DC converter with different controller structures and soft switching methods to increase efficiency. In addition, ensuring the use of renewable energy sources with topological changes in the DC-DC converter will save energy in a short time and help reduce energy production cost. Based on the important issues described above, the aims of the presented research are to overcome the shortcomings and expected developments.

The objectives of the thesis are given below;

- Detailed investigation of the characteristics, design, control parameters of isolated DC-DC topologies for EVs two processing stages battery chargers.
- Performing computer applications in different load ranges (light load-to-full load) of isolated DC-DC converter topologies and controller structures and presenting their results.
- Investigation of soft switching method for isolated DC-DC converters in order to reduce switching losses and catch high efficiency.
- Design and analysis of two different AC-DC PFC converters and controller structure, as well as realization of computer application for two-stage battery charging unit.
- Presenting a detailed design approach based on theoretical analysis and simulation studies for two-stage battery charger.
- Presenting of the designing, theoretical infrastructure and computer application of two-stage battery charging unit with a maximum rated power of 3.3 kw (Level-2) for the implementation of the control and soft switching method (ZVS) designed for the LLC resonant converter.
- A LLC resonance converter for the proposed PV powered two-stage battery charger architecture; design, working principle and circuit element selection in detail.
- Investigation of maximum power point tracking (MPPT) methods for the proposed PV powered two-stage battery charger architecture and also comparison of accuracy and convergence rates.
- Development of an MPPT method for the proposed PV powered two-stage battery charger architecture, and also comparison with traditional methods in terms of accuracy and convergence rate.

- Presentation of battery charging architecture, design, theoretical infrastructure and computer application with a PV powered two-stage, maximum 3.3 kw (Level-2) power with LLC resonance converter.

The original contributions of the researches carried out in this thesis can be summarized as follows;

- ANN based controller, which can perform soft switching (ZVS) in a wide load range, is proposed for isolated HBLLC resonant converter (Topology-I).
- The ANN based soft switching (ZVS) control method for LLC resonant converter, applied two-stage battery charger topology, and operated in variable load cases according to European efficiency standards (Topology-I).
- The system was investigated in terms of efficiency, grid current harmonics (IEC61000-3-2, Class D- standards), load voltage ripples ($\Delta V$) under different operating cases (Topology-I)
- A two-stage battery charging topology with two inputs (PV system, Grid) and two outputs (high and low voltage batteries), isolated LLC resonant which can operate wide load range is proposed (Topology-II).
- MPPT control method has been improved and applied PV system used in the proposed system (Topology-II).
- The proposed MPPT control method was compared with conventional methods under variable weather conditions. Under all operating conditions performed at higher accuracy and speed than traditional methods (Topology-I).
- In the proposed topology, the auxiliary battery that feeds low powers is fed by the photovoltaic panel, so the load on the high power battery is reduced.

Thus allowing the electric vehicle to drive more miles with a single charge process (Topology-II).

- In the proposed Topology-II, it provides energy saving in a short time period by using clean reliable and environmentally friendly energy, thanks to the PV panel and MPPT method.
- The designed two LLC resonant converter, applied proposed two-stage battery charger topology, and operated in variable load cases according to European efficiency standards (Topology II).
- The system was investigated in terms of efficiency, grid current harmonics (IEC61000-3-2, Class D- standards), load voltage ripples ($\Delta V$) under different operating cases (Topology-II).

### 1.3. The Organization of Thesis

The organization of the thesis is arranged as follows;

**Chapter 1** Overview of battery chargers for electric vehicles, presentation of standards and codes, features of single-stage and two-stage battery chargers and deficiencies in the Literature, features and conditions to meet of AC-DC and DC-DC converters are summarized. It also explains the main objectives and contributions of the thesis.

**Chapter 2** The properties and deficiencies of isolated DC-DC converters with the control methods for two-stage battery charger, are presented in detail and analyzed together with the simulation results of the presented converters in the Literature. The results obtained are given as a summary.

**Chapter 3** Describes the soft switching methods in order to reduce switching losses, reduce electromagnetic inference (EMI), and increase efficiency of the isolated DC-DC converters used in two-stage battery charger.

**Chapter 4** HBLLC resonant converter with ANN based soft switching (ZVS) control method applied a 3.3 kw powered (Level-2) two stage battery charger topology. The results obtained by operating under variable load conditions from the proposed system were presented by analyzing them according to IEC61000-3-2, Class D- standards and European efficiency standards.

**Chapter 5** HBLLC resonant converter for proposed 3.1 kw powered (Level-2) two-stage battery charger topology with PV system is designed and also MPPT control method developed for the proposed topology has been compared with traditional methods under different weather conditions (temperature and irradiance). The results obtained by operating under variable load conditions from the proposed system were presented by analyzing them according to IEC61000-3-2, Class D- standards and European efficiency standards.

**Chapter 6** Conclusion and Future Work

The Organization of thesis detailed illustrated in Figure 1.9

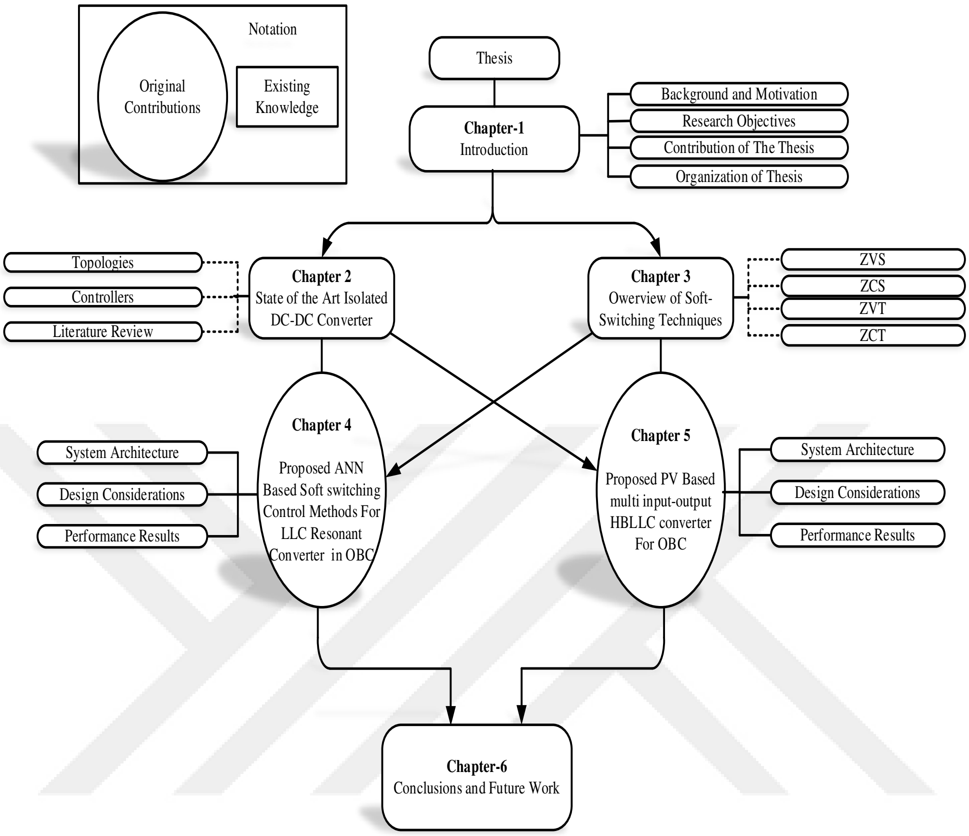


Figure 1.9 Organization of Thesis.

# 2. DC-DC CONVERTER TOPOLOGIES

In this section, isolated DC-DC converters in the Literature are examined one by one and their performances were evaluated by computer applications (Matlab / Simulink). In addition, detailed analysis was carried out by operating the converters in different load conditions (5%, 10%, 20%, 30%, 50%, 100% load cases). Furthermore, all isolated DC-DC converters analyzed were run at the same output power (3.3-kw, Level-2). Finally, at the end of this section, isolated DC-DC converters used for battery charging unit in electric vehicles in the Literature are given in detail.

## 2.1. Flyback Converter

Many isolated DC-DC converter structures for switching power supplies are available in the Literature. Flyback converter has the simplest structure among the existing isolated DC-DC converters. Output filter coil using only transformer (coupled coil) as a magnetic element, using only one semiconductor switch which simplifies the converter. On the other hand, due to limitations of the magnetic core It is preferred for low power applications. However, by adding additional circuit elements the flyback converter can be operated under high power demanded circuits (Tarzamni et al., 2017, Abdelmessih et al., 2018, Connaughton et al., 2019, Thangavelu et al., 2016, Wi et al., 2019, Shitole et al., 2018, Chen et al., 2015, Kang et al., 2012, Wang et al., 2008). The traditional flyback converter with control structure is shown in Figure 2.1.

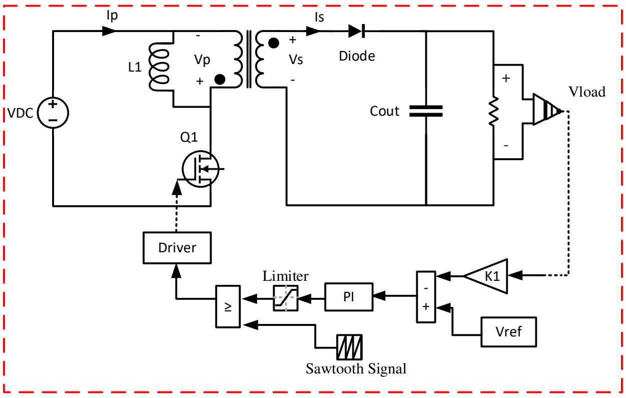


Figure 2.1 Flyback converter with controller

In order to analysis the switching operations of flyback converter the following steps are given;

Analysis for switch on state;

$$\left[\begin{array}{l} V_{DC} = V_p = L_m.\dfrac{\Delta iLm}{d(t)} \\ \dfrac{\Delta iLm}{d(t)} = \dfrac{\Delta iLm}{\Delta(t)} = \dfrac{\Delta iLm}{DT} = \dfrac{Vs}{Lm} \\ \text{The magnetic inductance current change for switch on state is following} \\ (\Delta iLm)_{Closed} = \dfrac{V_s DT}{L_m} \end{array}\right] \quad (2.1)$$

Analysis for switch off state;

$$\left[\begin{array}{l} V_P = V_S \cdot (\dfrac{N1}{N2}) = -V_{Load} \cdot (\dfrac{N1}{N2}) \\ L_m.\dfrac{\Delta iLm}{d(t)} = -V_{Load} \cdot (\dfrac{N1}{N2}) \Leftrightarrow \dfrac{\Delta iLm}{d(t)} = \dfrac{\Delta iLm}{(1-D)\cdot T} = \dfrac{-V_{Load}}{Lm} \cdot (\dfrac{N1}{N2}) \\ \text{The magnetic inductance current change for switch on state is following} \\ (\Delta iLm)_{Open} = \dfrac{-V_{Load}(1-D)T}{Lm} \cdot (\dfrac{N1}{N2}) \end{array}\right] \quad (2.2)$$

$$\begin{bmatrix} \text{The net magnetic inductance current change is zero so that} \\ (\Delta iLm)_{Closed} + (\Delta iLm)_{Open} = 0 \Leftrightarrow V_{Load} = V_{DC} \cdot (\frac{(D)}{1-D}) \cdot (\frac{N1}{N2}) \end{bmatrix} \tag{2.3}$$

Where $V_{Load}$ is the load current, $L_m$ is the magnetizing inductance, $V_{DC}$ is the source current *D* is the duty cycle, *T* is the switching period (Tarzamni et al., 2017, Abdelmessih et al., 2018, Connaughton et al., 2019, Zavare et al., 2015, Kushwaha et al., 2018, Singh et al., 2019).

In order to design control structure, the output voltage is subtracted from the reference voltage and the resulting error signal is damped by the pi controller. The reference signal obtained at the output of the pi controller is compared with the frequency-specified carrier signal so that the desired frequency PWM is generated for the switching element (mosfet) (Figure 2.1).

### 2.1.1. Performance Results

At this stage, the performance results of the computer application in pi controlled isolated flyback DC-DC converter Matlab/Simulink are presented. Figure 2.2 shows in detail the input-output voltage and output current of the flyback converter, tested at different load conditions.

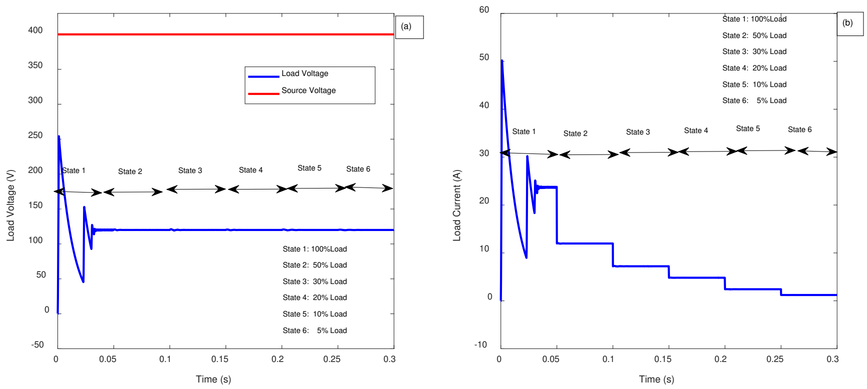


Figure 2.2 Source and load voltage (a), Load current under variable load conditions (b)

Transformer primary current and magnetizing current of the pi controlled flyback converter tested in different load cases are given in Figure 2.3.

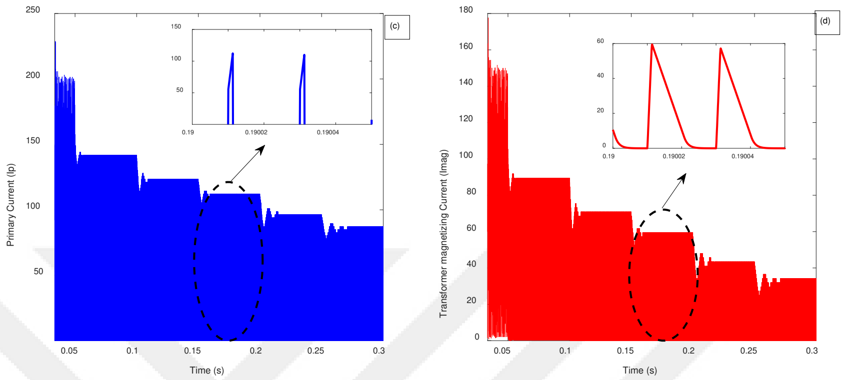


Figure 2.3 Transformer primary side current (a), Transformer magnetizing current (b)

The electrical characteristics of the pi controlled flyback converter with computer application in Matlab / Simulink are given in Table 2.1.

Table 2.1 Electrical characteristics of flyback converter

| **Variables** | **Electrical Characteristics** |
|---|---|
| $V_{in}$ (dc) | 400 V |
| $V_{out}$ (dc) | 120 V |
| $R_{load}$ | 4.965 to 99.3Ω |
| $N_p$:$N_s$ | 10:4 |
| $f_s$ | 100 kHz |
| $C_{out}$ | 2500µF |
| $P_{max}$ | 3.3-Kw (Level-2) |
| Controller | |
| $K_p$ | 2.283 |
| $K_i$ | 6.328 |

## 2.2. Full-Bridge Converter

In industrial applications, full-bridge isolated DC-DC converters are generally used at high power and frequencies. In the full-bridge converter performance, the parasitic oscillations between the switching losses and the parasitic capacitance of the power switches and the leakage inductance of the transformer reach unacceptable levels. However, by applying soft switching method, current and voltage stress on power circuit elements can be reduced, efficiency can be increased by reducing switching losses and it can perform in lower electromagnetic interference. The isolated full-bridge converter with conventional voltage control structure is shown in the Figure 2.4 (Kanamarlapudi et al., 2018, Gautam et al., 2013, Safaee et al., 2015, Kanamarlapudi et al., 2017, Shi et al., 2013., Safaee et al., 2016., Kathiresan et al., 2017., Lee et al., 2015., Lai et al., 2013., Saeed et al., 2018).

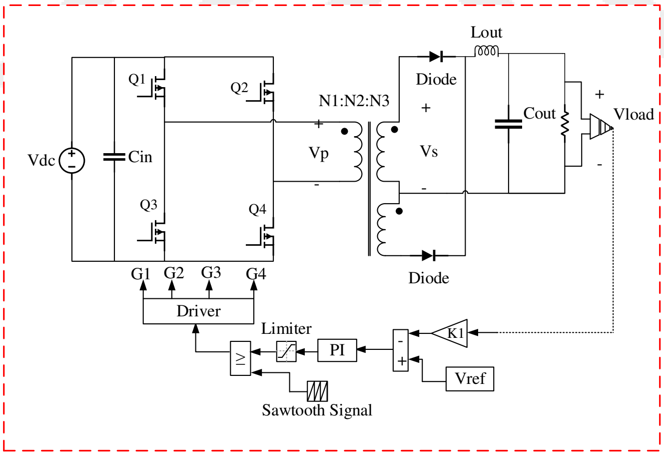


Figure 2.4 Full-bridge DC-DC converter with control structure

When the turn-on and off states of the switches are analyzed, two different situations occur. The Q2 and Q3 switches are turned off while the Q1 and Q4 switches are on. When the circuit is analyzed according to the switching state, the following equation is obtained (Gautam et al., 2013).

$$\left[ V_{Load} = 2 \cdot V_{DC} \cdot (\frac{N2}{N1}) \cdot D \right]$$

(2.4)

Where $V_{Load}$ is load voltage $V_{DC}$ is input voltage, D is duty cycle, $N_1$ and $N_2$ are primary and secondary turn number (Gautam et al., 2013, Yang et al., 2015, Whitaker et al., 2014, Tao et al., 2019, Kanamarlapudi et al., 2018).

In order to design control structure, the output voltage is subtracted from the reference voltage and the resulting error signal is damped by the pi controller. The reference signal obtained at the output of the pi controller is compared with the frequency-specified carrier signal so that the desired frequency PWM is generated for the switching element (Mosfet) (Figure 2.4).

### 2.2.1. Performance Results

At this stage, the performance results of the computer application in pi controlled isolated full-bridge DC-DC converter Matlab/Simulink are presented. Figure 2.5 shows in detail the input and output voltage and output current of the isolated full-bridge DC-DC converter, tested at different load cases.

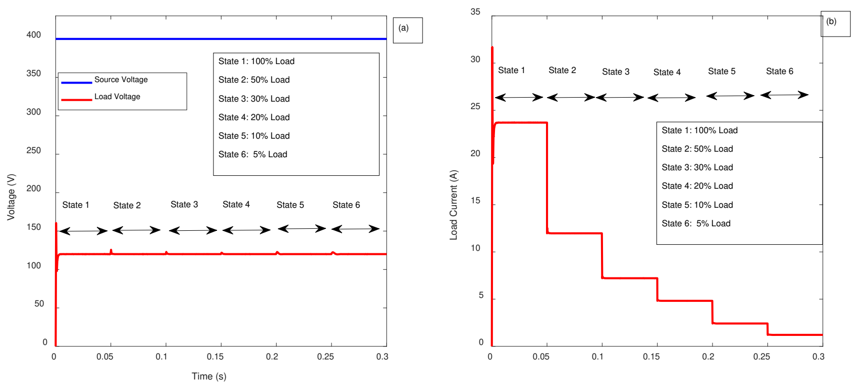


Figure 2.5 Source and load voltages (a), Load current under variable load conditions (b)

Figure 2.6 shows the transformer primary and secondary side voltages and currents of the pi controlled full-bridge isolated DC-DC converter, tested in different load cases.

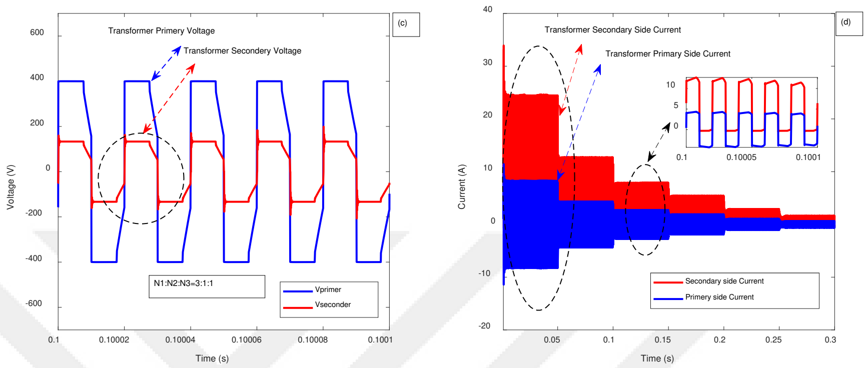


Figure 2.6 The transformer primary-secondary voltages (c) and current (d)

The electrical characteristics of the pi controlled isolated full-bridge DC-DC converter with computer application in Matlab / Simulink are given in Table 2.2.

Table 2.2 Electrical characteristics of the isolated full-bridge converter

| **Variables** | **Electrical Characteristics** |
|---|---|
| $V_{in}$ (dc) | 400 V |
| $V_{out}$ (dc) | 120 V |
| $R_{load}$ | 4.965 to 99.3Ω |
| $N_1$:$N_2$:$N_3$ | 3:1:1 |
| $f_s$ | 100 kHz |
| $C_{out}$ | 220 µF |
| $L_{out}$ | 100 µH |
| $P_{max}$ | 3.3-Kw (Level-2) |
| Controller | |
| $K_p$ | 2.283 |
| $K_i$ | 6.328 |

### 2.3. Half-Bridge Converter

Half-bridge isolated DC-DC converter has fewer switching elements than full-bridge converter, so that switching losses are less. However, the current and voltage stress on the power circuit elements is high. By applying soft switching method, current and voltage stress on power circuit elements can be reduced, efficiency can be increased by reducing switching losses and it can perform in lower electromagnetic interference (Rathore et al., 2013, Yeon et al., 2016, Ye et al., 2013, Liu et al., 2014., Mishima et al., 2009). In industrial applications, half-bridge isolated DC-DC converters are generally used at medium power and high frequencies required systems. The conventional isolated half-bridge converters with voltage control structure is given in Figure 2.7.

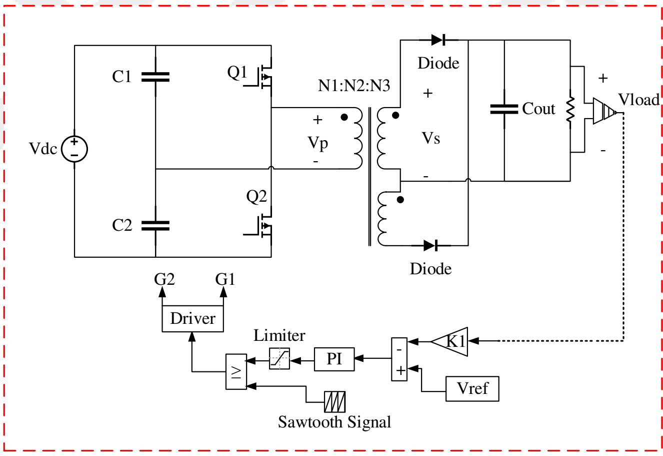


Figure 2.7 Half bridge DC-DC converter with control structure

When the turning on and off states of the switches are analyzed, two different situations occur. The Q2 switch is turned off while the Q1 switch is on. If the circuit is analyzed according to the switching state, the following equation is determined (Rathore et al., Yeon et al., 2016, Ye., 2014).

$$\left[ V_{Load} = V_{DC} \cdot (\frac{N2}{N1}) \cdot D \right] \tag{2.5}$$

Where $V_{Load}$ is load voltage $V_{DC}$ is input voltage, D is duty cycle, $N_1$ and $N_2$ are primary and secondary turn number (Lee et al., 2013, Duan et al., 2015, Xie et al., 2018, Cunha et al. 2019).

In order to design control structure, the output voltage is subtracted from the reference voltage and the resulting error signal is damped by the pi controller. The reference signal obtained at the output of the pi controller is compared with the frequency-specified carrier signal so that the desired frequency PWM is generated for the switching element (Mosfet) (Figure 2.7).

### 2.3.1. Performance Results

At this stage, the performance results of the computer application in pi controlled isolated half-bridge DC-DC converter Matlab/Simulink are presented. Figure 2.8 shows in detail the input-output voltage and output current of the isolated half-bridge converter, tested at different load cases.

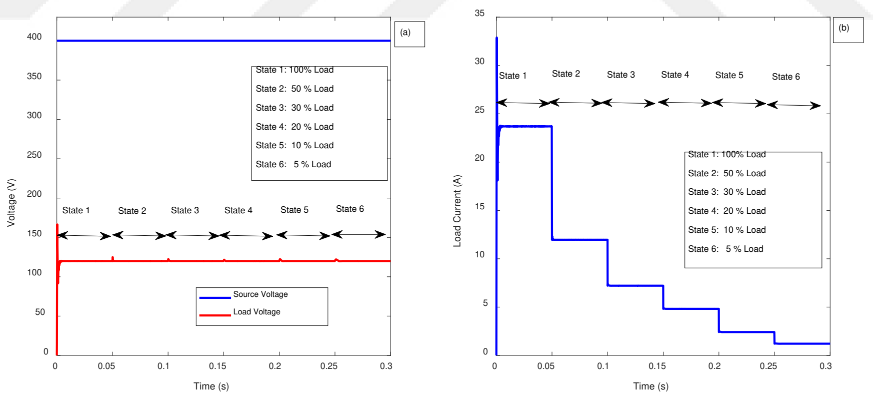


Figure 2.8 Half-bridge isolated DC-DC converter source and load voltage (a), load current under variable load conditions (b)

In order to design control structure, the output voltage is subtracted from the reference voltage and the resulting error signal is damped by the pi controller. The reference signal obtained at the output of the pi controller is compared with the frequency-specified carrier signal so that the desired frequency PWM is generated for the switching element (Mosfet).

Figure 2.9 shows the transformer primary-secondary voltages and currents of the pi controlled half-bridge DC-DC converter tested in different load cases.

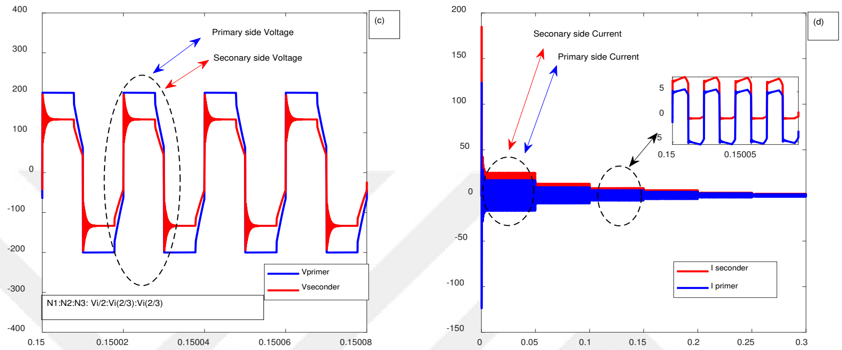


Figure 2.9 Pi controlled half-bridge DC-DC converter transformer primary-secondary side voltages (c) and current (d)

The electrical characteristics of the pi controlled isolated half-bridge converter with computer application in Matlab / Simulink are given in Table 2.3.

Table 2.3 Electrical characteristics of the isolated half-bridge converter

| **Variables** | **Electrical Characteristics** |
|---|---|
| $V_{in}$ (dc) | 400 V |
| $V_{out}$ (dc) | 120 V |
| $R_{load}$ | 4.965 to 99.3Ω |
| $N_1$:$N_2$:$N_3$ | 3:2:2 |
| $f_s$ | 100 kHz |
| $C_{out}$ | 220 µF |
| $L_{out}$ | 100 µH |
| $P_{max}$ | 3.3 kw (Level-2) |
| Controller | |
| Kp | 2.283 |
| Ki | 6.328 |

### 2.4. LLC Resonant Converter

LLC resonant converters are of interest for two-stage battery charging units used in electric vehicles, due to their high efficiency, low electromagnetic interference (EMI), wide load and voltage operating range, as well as their ability to operate under high power density. However, LLC resonant converters have some problems at high frequency operations, these are higher susceptibility to parasitic capacitance and leakage inductance, higher stress in switching devices, and increased EMI. The isolated LLC resonant DC-DC converter with control structure is shown in the Figure 2.10 (Jovanovic et al., 2016, Lin et al., 2018, Vu et al., 2018, Noah et al., 2018, Park et al. 2016 Kang et al., 2016, Kundu et al., 2017, Wang et al., 2018, Hua et al., 2019).

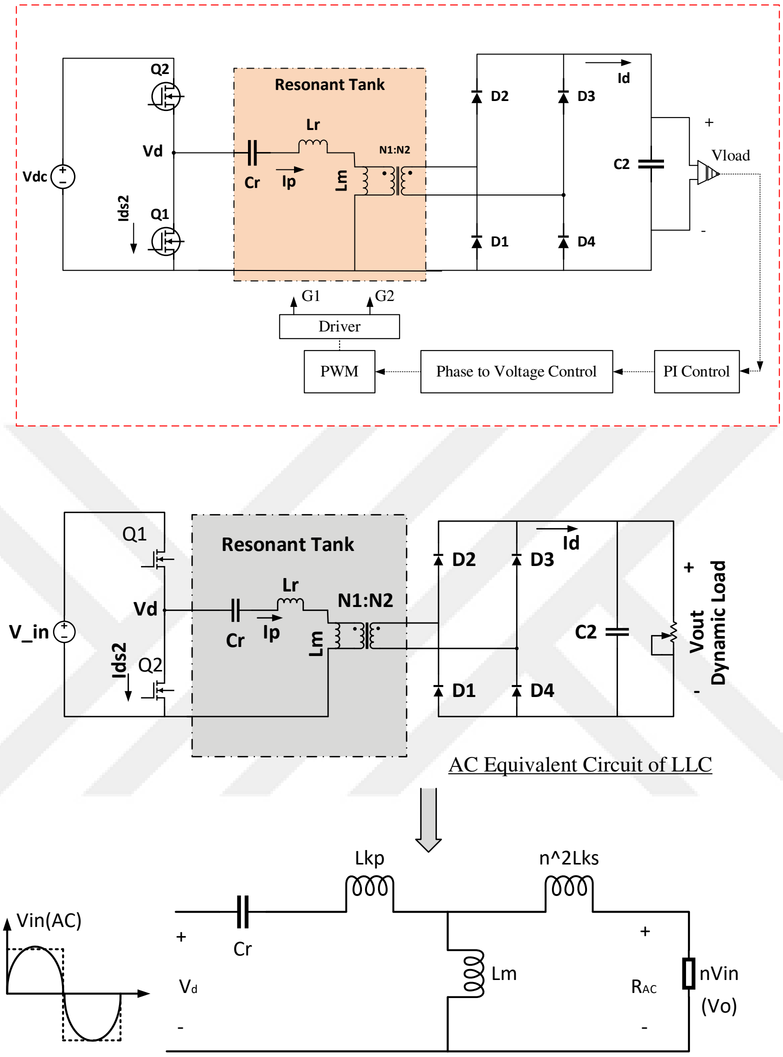


Figure 2.10 LLC resonant converter and AC equivalent circuit

In order to analysis and determine the circuit parameters of LLC resonant converter the following steps are given;

Current and voltage values of the AC equivalent circuit is shown;

$$\begin{bmatrix} \mathrm{I}_{\mathrm{AC}} = \dfrac{\Pi \cdot I_0}{2}\sin(wt) \\ \mathrm{VR}_{\mathrm{H}} = +V_0 \Rightarrow if\ \sin(wt) > 0 \\ \mathrm{VR}_{\mathrm{H}} = -V_0 \Rightarrow if\ \sin(wt) < 0 \\ \mathrm{VR}_{\mathrm{H}}{}^{F} = \dfrac{4 \cdot V_0}{\Pi}\sin(wt) \end{bmatrix} \tag{2.6}$$

AC load value has been determined by following equations;

$$\begin{bmatrix} \mathrm{R}_{\mathrm{AC}} = \dfrac{VR_H{}^F}{I_{AC}} = \dfrac{8}{\Pi^2}\dfrac{V_0}{I_0} = \dfrac{8}{\Pi^2}R_{LOAD} \\ n = \dfrac{N_P}{N_S}, \\ \mathrm{R}_{\mathrm{AC}} = \dfrac{8 \cdot n^2}{\Pi^2}R_{LOAD} \end{bmatrix} \tag{2.7}$$

The voltage gain is determined by the following equations

$$\begin{bmatrix} \mathrm{M} = \dfrac{2\mathrm{n} \cdot \mathrm{V}_0}{\mathrm{V}_{\mathrm{in}}} = \left| \dfrac{\mathrm{w}^2 \mathrm{L}_{\mathrm{m}} \mathrm{R}_{\mathrm{AC}} \mathrm{C}_{\mathrm{R}}}{\mathrm{jw}(1 - \dfrac{\mathrm{w}^2}{\mathrm{w}_0{}^2}) \cdot (\mathrm{L}_{\mathrm{m}} + \mathrm{n}^2 \mathrm{L}_{\mathrm{ks}}) + \mathrm{R}_{\mathrm{AC}}(1 - \dfrac{\mathrm{w}^2}{\mathrm{w}_{\mathrm{p}}{}^2})} \right| \\ \text{Where}, \quad \mathrm{w}_0 = \dfrac{1}{\sqrt{\mathrm{L}_{\mathrm{r}}\mathrm{C}_{\mathrm{r}}}}, \qquad \mathrm{w}_{\mathrm{p}} = \dfrac{1}{\sqrt{\mathrm{L}_{\mathrm{P}}\mathrm{C}_{\mathrm{r}}}} \end{bmatrix} \tag{2.8}$$

Finally, voltage gain can be regulated as following equation;

$$\left[\begin{array}{l} M = \dfrac{2n \cdot V_0}{V_{in}} = \left| \dfrac{\dfrac{w^2}{{w_p}^2}(\dfrac{k}{k+1})}{j(\dfrac{w}{w_0}) \cdot (1-\dfrac{w^2}{{w_0}^2}) \cdot Q \cdot \dfrac{(k+1)^2}{2k+1} + (1-\dfrac{w^2}{{w_p}^2})} \right| \\ \\ \text{Where, } k = \dfrac{L_m}{L_{kp}}, \qquad Q = \dfrac{\sqrt{L_r / C_r}}{R_{AC}} \\ \end{array}\right] \quad (2.9)$$

Where, $V_o$ is output voltage $V_{in}$ is input voltage, $V_{RH}$ is transformer secondary side voltage, $R_{AC}$ is ac load value, $n$ is turn ratio of transformer, $M$ is gain w is switching frequency, $w_o$ is resonant frequency $W_p$ primary resonant frequency, $L_m$ magnetizing inductance, $L_r$ is resonant inductance, $C_r$ resonant capacitance (Jovanovic et al., 2016, Lin et al., 2018, Vu et al., 2018, Noah et al., 2018).

In order to design control structure, the output voltage is subtracted from the reference voltage and the resulting error signal is damped by the pi controller. With the signal at the output of the pi controller, the reference frequency conversion is made and sent to the PWM regulator so that the PWM signal produced at the desired frequency is sent to the switching element (Figure 2.10).

### 2.4.1. Performance Results

At this stage, the performance results of the computer application in voltage controlled isolated half-bridge LLC resonant DC-DC converter Matlab/Simulink are presented Figure 2.11.

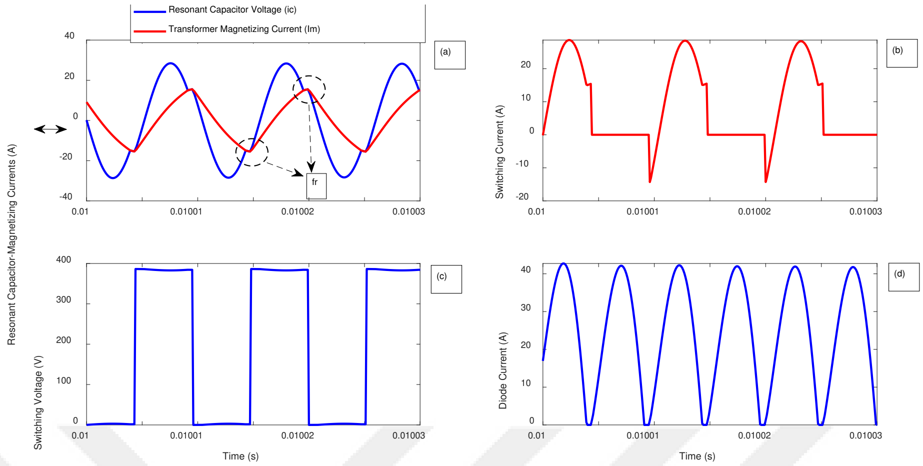


Figure 2.11 Resonant capacitor and transformer magnetizing current (a), Switching current (Is2) (b), Switching voltage (Vs2) (c), Diode current (d)

Figure 2.12 shows in detail the output voltage, current and switching frequency of the isolated half-bridge LLC resonant converter, tested at different load cases.

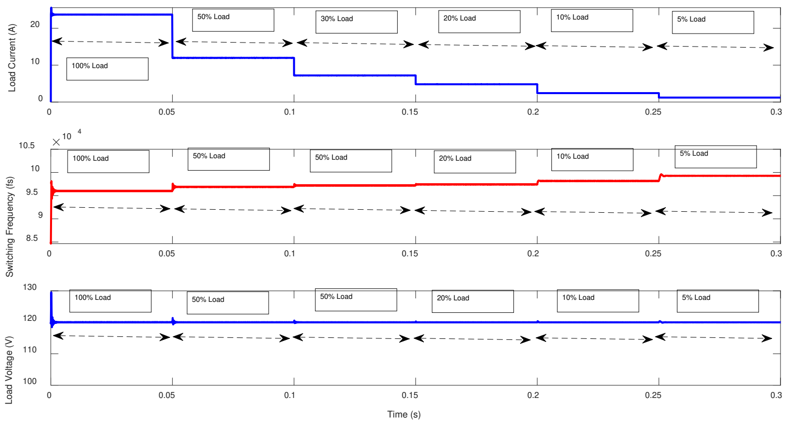


Figure 2.12 Load current (a), Switching frequency (b), Load voltage (c),

The electrical characteristics of the voltage-controlled isolated half-bridge LLC resonant DC-DC converter with computer application in Matlab / Simulink are given in Table 2.4.

Table 2.4 Electrical characteristics of the isolated LLC resonance converter

| Variables | Electrical Characteristics |
|---|---|
| $V_{in}$ (dc) | 400 V |
| $V_{out}$ (dc) | 120 V |
| $R_{load}$ | 4.965 to 99.3Ω |
| $N_1$:$N_2$ | 74:39 |
| $f_s$ | 65-120 kHz |
| $L_r$ | 9.45 µH |
| $C_r$ | 268.033 nF |
| $L_m$ | 35.84 µH |
| $f_r$ | 100 kHz |
| $P_{max}$ | 3.3-Kw (Level-2) |

## 2.5. Phase Shift Full Bridge Converter.

Phase shifted full-bridge dc-dc converter (PSFB) is similar to the conventional full-bridge dc-dc converter. However, the (PSFB) converter can be operated at high switching frequencies and also has advantages such as low EMI; low switching losses and also doesn’t require additional snubber circuits to reduce losses. PSFB converters are preferred for high power applications such as renewable energy systems, battery charging systems, and etc. The switching operations of PSFB converter is given in Figure 2.14. Conventional phase shift isolated DC-DC converter with control structure is given in Figure 2.13 (Li et al., 2015, Lo et al., 2011, Li et al., 2017 Liu et al., 2017, Hou et al., 2016, Mallik et al., 2017, Safaee et al., 2016, Baek et al., 2018).

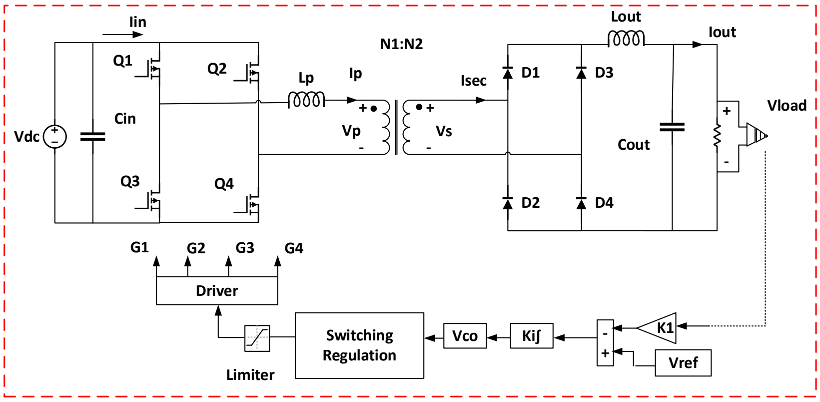


Figure 2.13 Conventional PSFB DC-DC converter with control structure

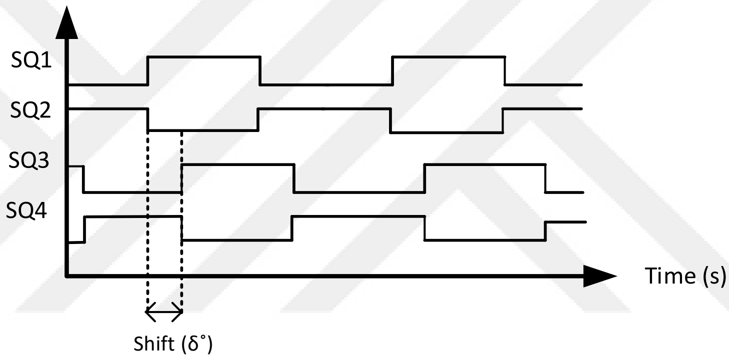


Figure 2.14 Switching operations for PSFB converter

The following equations can be used to find the electrical characteristics of the phase shifted full-bridge DC-DC converter;

$$P = \frac{V_1 \cdot V_2 \cdot N}{W \cdot L} \cdot (\delta - \frac{\delta^2}{\Pi}) \tag{2.10}$$

$$C_{input} = \frac{\Delta I_L \cdot T_{SW}}{8 \Delta V_o} \tag{2.11}$$

$$C_{output} = \frac{I_o \cdot D \cdot T_{SW}}{\Delta V_o} \tag{2.12}$$

Where $V_1$ and $V_2$ are the input and output dc voltage, N is the turn ratio of transformer, $\delta$ is the phase angle, D is the duty cycle, $T_{sw}$ is switching period, $I_L$ is the inductance current (Koroglu et al., 2019).

In order to design control structure, the output voltage is subtracted from the reference voltage and the resulting error signal is damped by the integrator. The signal obtained from the output of the integrator is converted to a signal in the appropriate frequency range (100kHz-150kHz) by the voltage controlled oscillator (VCO) and sent to the PWM generator. It is transmitted to the switching elements by applying phase shifting between the produced PWM signals (Figure 2.13).

### 2.5.1. Performance Results

At this stage, the performance results of the computer application in voltage controlled isolated full-bridge phase shifted DC-DC converter Matlab/Simulink are presented.

Figure 2.15 shows in detail the input-output voltage and output current of the isolated phase shifted full-bridge dc-dc converter, tested at different load cases.

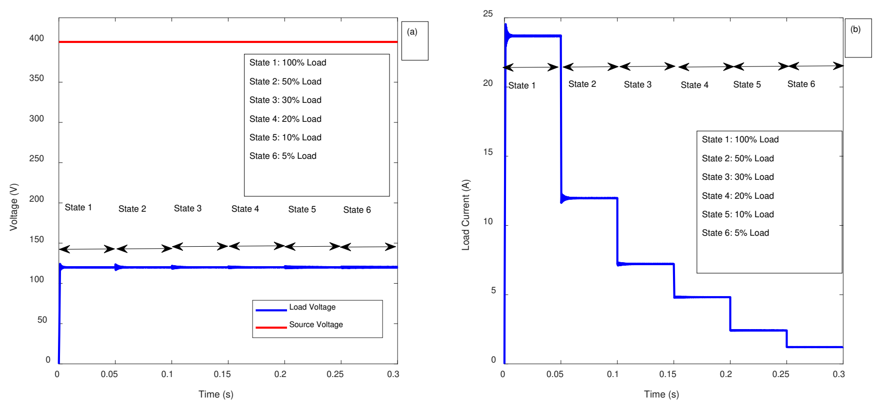


Figure 2.15 PHFB isolated DC-DC converter source and load voltage (a), Load current under variable load conditions (b)

Figure 2.16 shows the transformer primary and secondary side voltages and currents of the voltage controlled phase shifted full-bridge isolated converter.

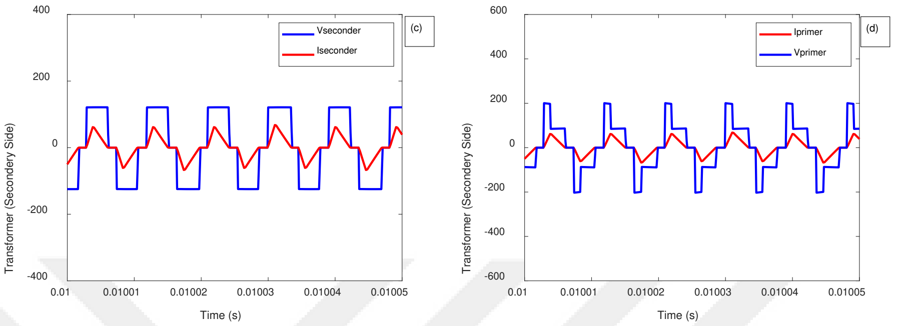


Figure 2.16 PHFB isolated DC-DC converter transformer secondary side voltage-current (a), primary side voltage-current (b)

Figure 2.17 shows the switching operations of voltage controlled phase shift full-bridge isolated DC-DC converter tested in different load cases.

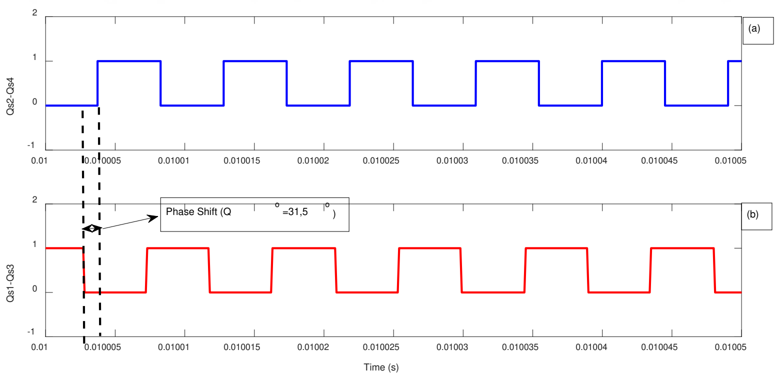


Figure 2.17 PHFB converter switching signals (Qs2-Qs4) (a), (Qs1-Qs3) (b)

The electrical characteristics of the voltage-controlled isolated PSFB DC-DC converter with computer application in Matlab / Simulink are given in Table 2.5.

Table 2.5 Electrical characteristics of the isolated PSFB DC-DC converter

| Variables | Electrical Characteristics |
|---|---|
| $V_{in}$ (dc) | 400 V |
| $V_{out}$ (dc) | 120 V |
| $R_{load}$ | 4.965 to 99.3Ω |
| $N_1$:$N_2$ | 1:1 |
| $C_{out}$ | 26.6 µF |
| $C_{in}$ | 1.33 µF |
| $L_1$/$L_2$ | 3/1.2 µH |
| fs | 100-150 kHz |
| Phase Shift ($\theta^o$) | $31.5^o$ |
| Rated Power (Pmax) | 3.3-Kw (Level-2) |

### 2.6. Dual Active Bridge Isolated DC-DC Converter

Dual active bridge isolated DC-DC converter can be preferred in many power ranges due to its advantages such as high power density, easy application and design suitable for soft switching (ZVS).

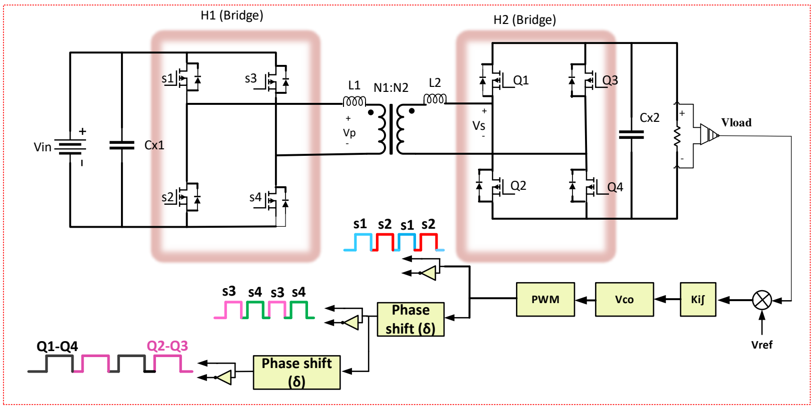


Figure 2.18 Dual active bridge isolated DC-DC converter with EPS control structure

Several different control methods for the DAB converter have been proposed in the literature. One of these control methods is the traditional PWM control method shown in Figure 2.18. In this method, while the DAB is operating, the cross-connected switches ($s_1$-$s_2$-$s_3$-$s_4$) in the primary side ($H_1$-bidge) are in the conduction state, on the other hand the H2-bridge connected switches in the secondary side (Q1-Q2-Q3-Q4) act out of the transmission and the current flows through the diodes connected parallel to the switches (Wang et al., 2013, Liu et al., 2014, Kondo et al., 2016, Assadi et al., 2018, Mishra et al., 2018). Although this method is easy to implement, it is insufficient in terms of dynamic performance. Also, it causes voltage limitation because the dc-input voltage has to be higher than the ac-output voltage (transformer). The other control method is traditional phase shift PWM control method, In the traditional phase shift PWM method, a phase shifts (δ) is given between the PWM modulations produced for switches connected to $H_1$-$H_2$ bridges. Thanks to this method, the power flow direction and magnitude can be changed by the voltage induced on the transformer leakage inductor. So that this method allows the dynamic performance of the converter to be increased and the soft switching method to be applied more easily. However, in the traditional phase shift PWM method, efficiency not reach the desired levels since current stress and power losses on the circuit elements are high. In order to overcome this situation, extended phase shift (EPS) PWM method has been developed in the literature (Zhao et al., 2012). Thus, efficiency is increased by reducing power losses and also reduce current stress the circuit elements.

In order to simplify DAB load voltage, control the relationship between power and voltages ($V_{in}$ and $V_{out}$.), The following equations are used.

$$\mathrm{P} = \frac{\mathrm{V_{in}} \cdot V_{out.} \cdot n}{wL}\left(\delta - \frac{\delta^2}{\Pi}\right) \tag{2.13}$$

Where P is the transmission power rate, $V_{in}$, represent source voltage, $V_{out}$. represent the load-voltage, *n* is the transformer turn ratio, w is angular frequency ($w=2pf_{switch}$), δ is the phase shift, L is the sum of transformer inductance and auxiliary inductances ($L_1$, $L_2$)

The following equations are used to determine the capacitor values at the input and output ($C_{x1}$, $C_{x2}$).

$$C_{x1}=\frac{\Delta i_L T_{switch}}{8\Delta V_{dc-link}} \tag{2.14}$$

capacitor value on the battery side;

$$C_{x2}=\frac{I_{out} D T_{switch}}{\Delta V_{Load.}} \tag{2.15}$$

Where $\Delta i_L$ is the peak-peak ripple current ($L_1$) $T_{switch}$ is switching period ($1/f_s$), $\Delta V_{dc\text{-}link}$ is the voltage output ripple, $I_{load}$. is the load current, $\Delta V_{Load.}$ is the load voltage ripple, D is duty cycle.

In order to design control structure, the output voltage is subtracted from the reference voltage and the resulting error signal is damped by the integrator. The signal obtained from the output of the integrator is converted to a signal in the appropriate frequency range (100 kHz-150 kHz) by the voltage controlled oscillator (VCO) and sent to the PWM generator. It is transmitted to the switching elements by applying phase shifting between the produced PWM signals (Figure 2.18).

### 2.6.1. Performance Results

At this stage, the performance results of the computer application in voltage controlled isolated full-bridge phase shifted DC-DC converter Matlab/Simulink are presented.

Figure 2.19 shows in detail the input and output voltage and output current of the isolated DAB DC-DC converter with extended phase shifted control, tested at different loads cases.

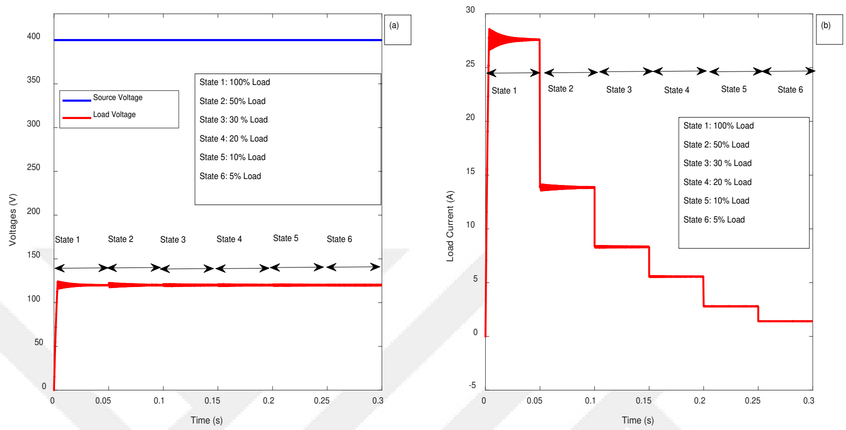


Figure 2.19 DAB isolated DC-DC converter source voltage and load voltage (a), load current under variable load conditions (b)

Figure 2.20 shows the transformer Primary-Secondary voltages and primary side inductor ($L_1$) voltages and currents of the EPS controlled DAB isolated dc-dc converter

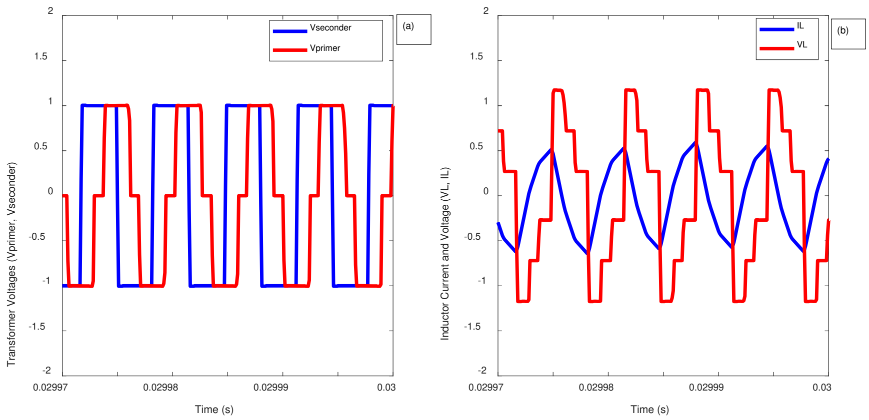


Figure 2.20 DAB isolated DC-DC converter transformer primary-secondary side voltages (a), primary side inductor ($L_1$) voltage-current (b)

The switching signals of EPS PWM controlled DAB converter are shown in Figure 2.21.

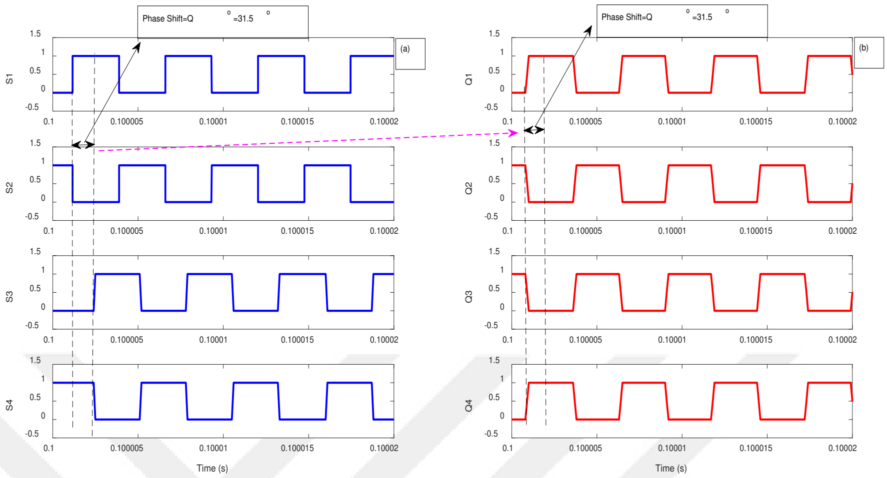

Figure 2.21 DAB converter switching signals ($s_1$-$s_2$-$s_3$-$s_4$) (a), ($Q_1$-$Q_2$-$Q_3$-$Q_4$) (b)

The electrical characteristics of the voltage-controlled isolated EPS DAB converter with computer application in Matlab / Simulink are given in Table 2.6.

Table 2.6 Electrical characteristics of the isolated EPS DAB DC-DC converter

| **Variables** | **Electrical Characteristics** |
|---|---|
| $V_{in}$ (dc) | 400 V |
| $V_{out}$ (dc) | 120 V |
| $R_{load}$ | 4.965 to 99.3Ω |
| $N_1$:$N_2$ | 1:1 |
| $C_{out}$ | 26.6 μF |
| $C_{in}$ | 1.33 μF |
| $L_1$/$L_2$ | 6.152 μH /15.85 μH |
| fs | 100-150 kHz |
| Phase $Shift_1$ ($\theta^o$) | 31.5$^o$ |
| Phase $Shift_2$ ($\theta^o$) | 31.5$^o$ |
| Rated Power (Pmax) | 3.3 kw (Level-2) |

## 2.7. Control Methods for DC-DC Converters

In two-stage battery chargers, batteries are connected to the output of isolated dc-dc converters. Since different charging states (SoC%) affect the load state of the battery, in the Literature, a dynamic load is generally, connected to the output of the isolated DC-DC converters instead of the battery and a performance analysis is done (from light load to full load). The current or voltage value measured over the dynamic load must be operated by driving at a reference current or voltage value. The current or voltage signal measured at the output of the DC-DC converters is compared with the defined reference signal, and the resulting error signal is passed through a controller to ensure the module operates at optimal value. The converter switches are triggered at the specified switching frequency to perform the control at the optimum value and reduce the error between the measured and the reference value. DC-DC converters can be controlled in two main control modes: current mode control and voltage mode control methods (Çelik., 2019).

### 2.7.1. Current Mode Control

The current mode control consists of the current loop inside and the voltage loop outside, as shown in Figure 2.22. The current mode control can be expressed as a revised version of the voltage mode control as a sampling holding circuit. The outer voltage loop generates a reference signal for the current loop, while the current loop generates the signal to regulate the duty cycle of the PWM signal sent to the switching elements. While current mode control offers advantages such as fast dynamic response, stable feedback and high bandwidth, on the other hand, operating both current and voltage control on the same structure makes the control of the system complex and difficult (Çelik., 2019).

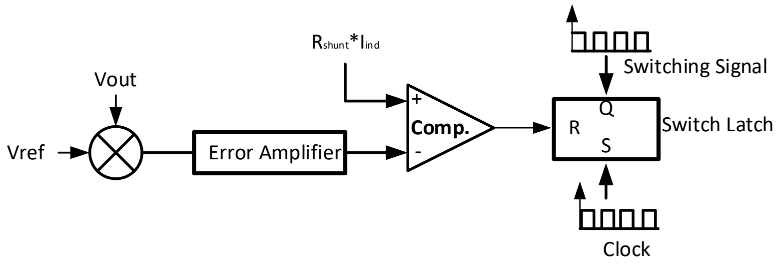


Figure 2.22 Current mode control

### 2.7.2. Voltage Mode Control

Voltage mode control as shown in the figure; The output voltage (Load-Voltage) of the isolated dc-dc converter is subtracted from the specified reference voltage, the resulting error signal is suppressed by the controller and compared to the carrier signal, the resulting signal is the PWM signal sent to the switches of the converter. The main purpose of this controller is to set the duty cycle of the PWM signal sent to the switches of the converter which is presented in Figure 2.23 (Çelik., 2019).

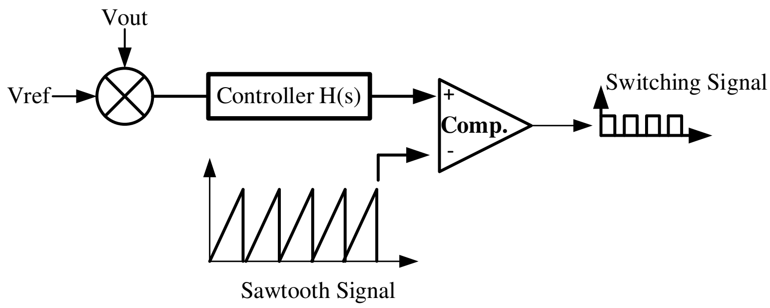


Figure 2.23 Voltage mode control

Voltage mode control has easier applicability compared to current mode control, and circuit analysis is easier in voltage mode control. In addition, ensuring stable modulation and high noise tolerance can be shown as promising aspects of this control mode. However, the dynamic response of this control mode is slower than current mode control.

### 2.8. DC-DC Converter for Bi-Directional Battery Charger

While bidirectional isolated DC-DC converters are used on-board battery chargers in electric vehicles, it usually creates an interface between the dc-link at the output of the ac-dc pfc converter and the battery. Dual active bridge (DAB) DC-DC converters can provide high power density, high energy efficiency, wide gain range, galvanic isolation and bidirectional power flow, and therefore have potential applications as DC-DC converters for bidirectional EV charging systems. In this study, the extended phase shift (EPS) PWM technique and soft switching method were applied to the bi-directional DAB converter (as shown in Figure 2.24). This method aimed to reduce switching losses and current-voltage stress on power circuit elements.

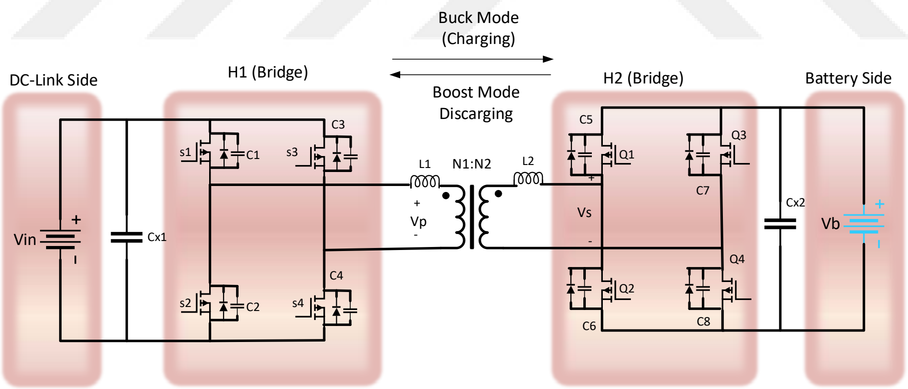


Figure 2.24 Bidirectional isolated DAB DC-DC Converter

In order to simplify IBDC voltage control the relationship between power and voltages (Vdc-link and $V_{bat}$.), The following equations are used.

$$\mathrm{P} = \frac{\mathrm{V_{in}} \cdot V_{bat.} \cdot n}{wL}(\delta - \frac{\delta^2}{\Pi}) \tag{2.16}$$

Where *P* is the transmission power rate, $V_{in}$, represent dc-link voltage (buck mode), $V_{bat}$. represent the battery voltage (boost mode), n is the transformer turn ratio, w is angular frequency ($w=2pf_{switch}$), $\delta$ is the phase shift, *L* is the sum of transformer inductance and auxiliary inductances ($L_1$, $L_2$)

The following equations are used to determine the capacitor values at the input and output ($C_{x1}$, $C_{x2}$).

$$C_{x1} = \frac{\Delta i_L T_{switch}}{8\Delta V_{dc-link}} \tag{2.17}$$

capacitor value on the battery side;

$$C_{x2} = \frac{I_{bat} D T_{switch}}{\Delta V_{bat.}} \tag{2.18}$$

Where $\Delta i_L$ *is the peak-peak ripple current* ($L_1$) $T_{switch}$ is switching period ($1/f_s$), $\Delta V_{dc\text{-}link}$ is the voltage output ripple (boost mode), Ibat. is the load current (buck mode), $\Delta V_{bat.}$ is the load voltage ripple (buck), *D* is duty cycle.

### 2.8.1. Extended Phase Shift PWM Method

Two different PWM methods are generally used to control bi-directional isolated dc-dc converters. These are traditional and phase shift PWM methods. In the traditional PWM method, while the IBDC is operating in the buck mode, the cross-connected switches ($s_1$-$s_2$-$s_3$-$s_4$) in the primary side ($H_1$-bidge) are in the conduction state, on the other hand the $H_2$-bridge connected switches in the secondary side ($Q_1$-$Q_2$-$Q_3$-$Q_4$) act out of the transmission and the current flows through the diodes connected parallel to the switches.

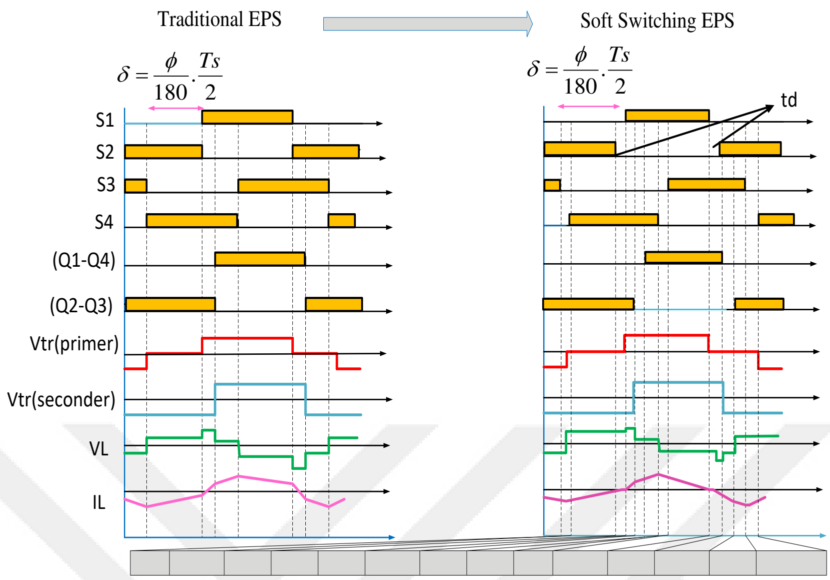


Figure 2.25 Operation states and wave form of the EPS and soft switching EPS.

This process is in the opposite when the converter is running in boost mode. Although this method is easy to implement, it is insufficient in terms of dynamic performance. Also, it causes voltage limitation because the dc-input voltage has to be higher than the ac-output voltage. In the traditional phase shift PWM method, a phase shifts (δ) is given between the PWM modulations produced for switches connected to $H_1$-$H_2$ bridges. Thanks to this method, the power flow direction and magnitude can be changed by the voltage induced on the transformer leakage inductor (Eqs. 2.16.). So that this method allows the dynamic performance of the converter to be increased and the soft switching method to be applied more easily. however, in the traditional phase shift PWM method, efficiency not reach the desired levels since current stress and power losses on the circuit elements are high. In order to overcome this situation, extended phase shift PWM method has been developed in the literature. Thus, efficiency is increased by reducing power losses and also reduce current stress the circuit elements. In this study, a soft switching EPS control method is proposed to reach high efficiency in both buck-boost modes and also it is easy to apply the proposed method to IBDC.

### 2.8.2. Operation Modes of the EPS Method

In order to make the control method easy and understandable, the waveforms of the operation modes are given in Figure 2.25. In addition, the variable operation states are detailed for different time intervals.

State 1(t0'≤t≤t1): On the primary side of DC-DC converter the $s_2$ and $s_4$ switches are on state $s_1$ and $s_3$ switches are off state, the inductor current is increase linearly, on the secondary side $Q_2$ and $Q_3$ switches are on states where $Q_1$ and $Q_4$ switches are off state, the voltage across primary side inductor is nearly zero and secondary side voltage is –n*Vout, the inductor current is;

$$iL_1(t) = iL_1(t0') + \frac{n \cdot Vout}{L_1}(t - t0') \tag{2.19}$$

State 2 (t1≤t≤t1'): $s_1$ is turned on state while the switching voltage is zero the capacitor $C_1$ discharged and $s_2$ turned off while the switching current is zero the $C_2$ capacitor is charged the inductor current increase linearly and the primary voltage ($V_{pri}$) is turn to input voltage ($V_{in}$). In order to provide soft switching method the dead time must be;

$$tdead \geq \frac{(C1 + C2).Vin}{iL_{pk}} \tag{2.20}$$

(*(tdead<Ts/4),* Where $T_s$ is switching frequency, $C_1=C_2=C_3=C_4$)

State3. (t1'≤t≤t2): On the primary side $s_1$ and $s_4$ switches are on state while Q2 and Q3 switches on the secondary side conduction mode the inductor current increase linearly and transformer secondary voltage turns to $n*V_{out}$. The primary side inductor current is calculated as;

$$iL(t) = iL(t1') + \frac{Vin + n*Vout}{L}(t - t1') \tag{2.21}$$

State 4(t2 ≤t≤t2'): On the secondary side $Q_1$-$Q_4$ turned on while switches voltages are zero and $Q_2$-$Q_3$ turned off while switches currents are zero $s_1$ and $s_4$ switches are conduction mode. In order to provide soft switching method the dead time must be;

$$tdead \geq \frac{(C5 + C8) \cdot n \cdot V_{out}}{iL_{pk}} \tag{2.22}$$

(*(tdead<Ts/4),* Where $T_s$ is switching frequency, $C_5=C_6=C_7=C_8$)

State 5 (t2' ≤t≤t3): The switches conditions are continuing as state 4, primary side transformer voltage is $V_{in}$-$n*V_{out}$, and the inductor current is calculated as;

$$iL(t) = iL(t2') + \frac{Vin - n*Vout}{L}(t - t2') \tag{2.23}$$

State 6 (t3 ≤t≤t3') $s_3$ is turned on state while the switching voltage is zero the capacitor $C_3$ discharged and $s_4$ turned off while the switching current is zero the $C_4$ capacitor is charged the inductor current starts to decrease;

State 7 (t3'≤t≤t4) On the primary side $s_1$ and $s_3$ switches are on state while $Q_2$ and $Q_3$ switches on the secondary side conduction mode the inductor current decrease linearly and transformer secondary voltage turns to -n*$V_{out}$. The primary side inductor current is calculated as;

$$iL_1(t) = iL_1(t3') - \frac{n*Vout}{L_1}(t - t3') \tag{2.24}$$

State 8 (t4≤t≤t4'): $s_1$ is turned off state while the switching current is zero the capacitor $C_1$ charged and $s_2$ turned on while the switching voltage is zero the $C_2$ capacitor is discharged the inductor current decrease as;

State 9 (t4'≤t≤t5): On the primary side $s_2$ and $s_3$ switches are on state while $Q_2$ and $Q_3$ switches on the secondary side conduction mode the inductor current decrease linearly and transformer secondary voltage turns to $n*V_{out}$. The primary side inductor current is calculated as;

$$iL(t) = iL(t4') + \frac{-Vin - n*Vout}{L}(t - t4')$$

(2.25)

State 10 (t5≤t≤t5'): $Q_1$-$Q_4$ turned off switching currents are zero while $Q_2$-$Q_3$ turned on and the switching voltages are zero the inductor current is decreasing linearly.

State 11 (t5'≤t≤t6) On the primary side $s_2$ and $s_3$ switches are on state while $Q_2$ and $Q_3$ switches on the secondary side conduction mode the inductor current increase linearly and transformer secondary voltage turns to $-n*V_{out}$. The primary side inductor current is calculated as;

$$iL(t) = iL(t5') + \frac{-Vin + n*Vout}{L}(t - t5') \tag{2.26}$$

State 12 (t6≤t≤t6') s3 is turned off state while the switching current is zero the capacitor C3 is charged and s4 turned on state while the switching voltage is zero the C4 capacitor is charged the inductor current increase as;

$$iL(t) = iL(t2) + \frac{-V1 + n*Vout}{L}(t - t6') \tag{2.27}$$

The operation states of the method proposed in Figure 5 and the transmission states of the switching elements are shown on the IBDC circuit diagram.

### 2.8.3. Control Strategy for Bidirectional DAB DC-DC Converter

In this study, a controller designed for bi-directional on-board battery chargers, which enables soft switching with the extended phase shift PWM method, applied to the bi-directional dual active bridge DC-DC converter. The designed controller is shown in detail in Figure 2.26. The first step of the controller is to define the operating mode of the system (buck mode (charging), boost mode (discharging)). PWM is then produced with the help of voltage controlled oscillator (VCO) by taking the difference of reference voltage and measured output voltage. Dead-time interval is determined for the produced PWM modulation and phase shifting is placed between the switching signals, and the generated signals are applied to the bi-directional DAB converter circuit performed for the operation of the switches.

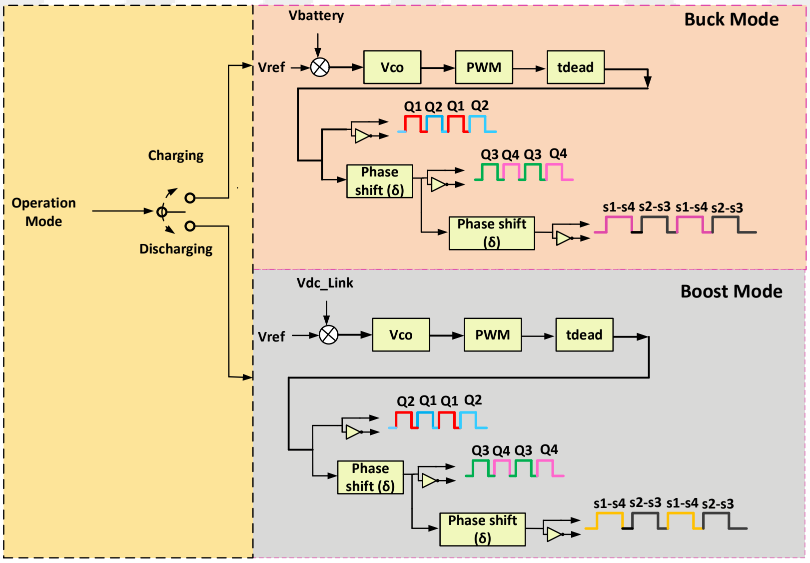


Figure 2.26 Control method for extended phase shift DAB DC-DC converter.

### 2.8.4. Performance Results

The bi-directional DAB converter has been tested for six different load cases as shown in Table 2.7.

Table 2.7 Operating cases of bi-directional DC-DC converter

| **States** | State 1 | State 2 | State 3 | State 4 | State 5 | State 6 |
|---|---|---|---|---|---|---|
| **Loads** | 100% | 50% | 30% | 20% | 10% | 5% |

The system has been examined in two different situations: discharging (boost mode) and charging (buck mode). Switching signals for boost mode are shown in Figure 2.27.

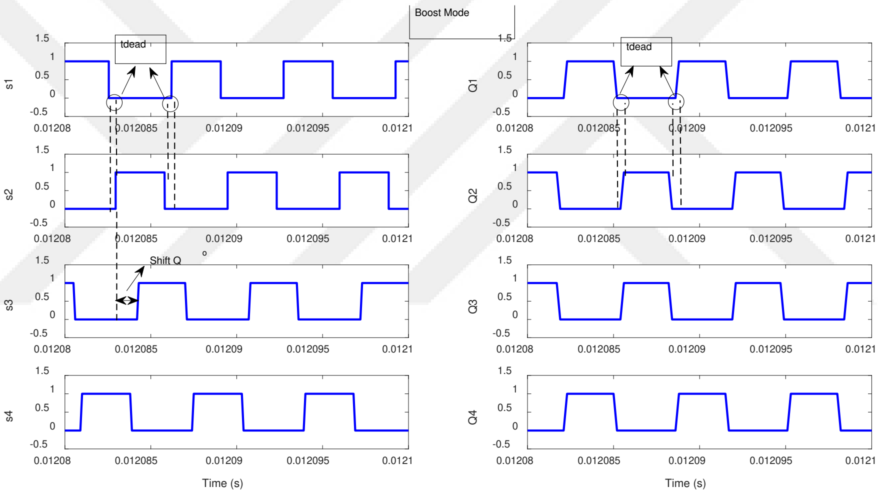


Figure 2.27 Switching signals for boost mode

While the system is operating in boost mode, the output current, input and output voltages for different load situations are shown in detail in Figure 2.28. Thanks to the proposed controller, the output voltage is kept constant over a wide load range.

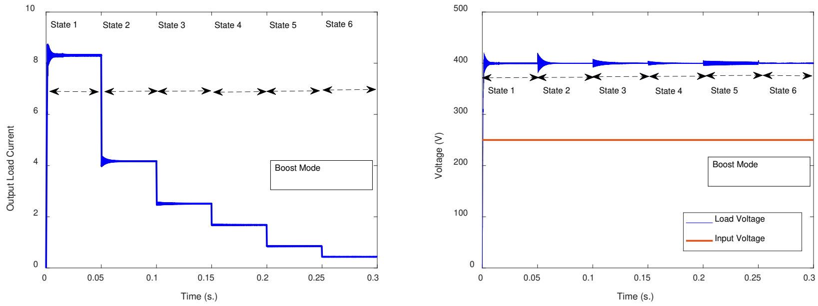


Figure 2.28 Current and voltage characteristics of DAB converter for boost mode

While the system is operating in boost mode, the voltage and current values of the switches s2 and s4 are shown in Figure 2.29. It has also been verified that the proposed controller performs soft switching.

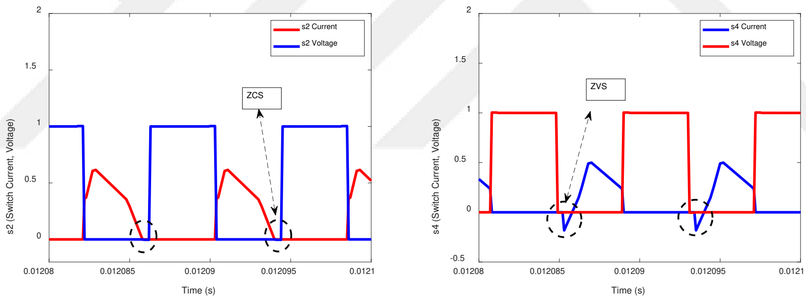


Figure 2.29 Current and voltage characteristics of $s_2$, $s_4$ switches (boost mode)

While the system is operating in boost mode, the voltage and current values of the switches $Q_2$ and $Q_4$ are shown in Figure 2.30. It has also been verified that the proposed controller performs soft switching.

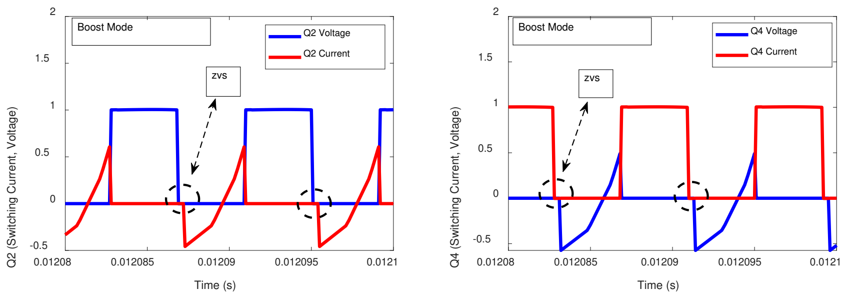


Figure 2.30 Current and voltage characteristics of $Q_2$, $Q_4$ switches (boost mode)

While the system is operating in boost mode, the voltage and current values characteristics of transformer is shown in Figure 2.31.

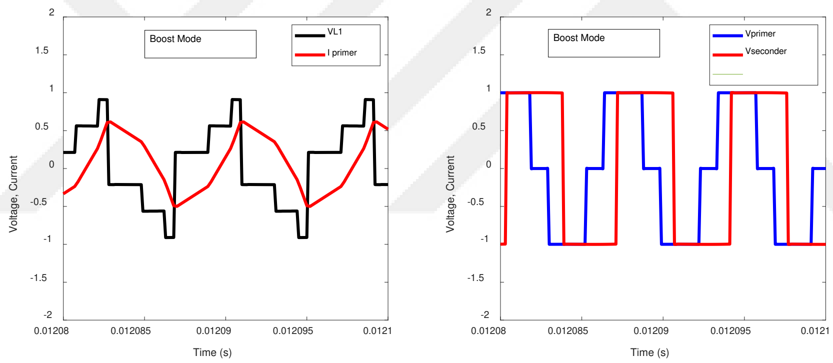


Figure 2.31 Current and voltage characteristics of transformer (boost mode)

The system has been examined in two different situations: discharging (boost mode) and charging (buck mode). Switching signals for buck mode are shown in Figure 2.32.

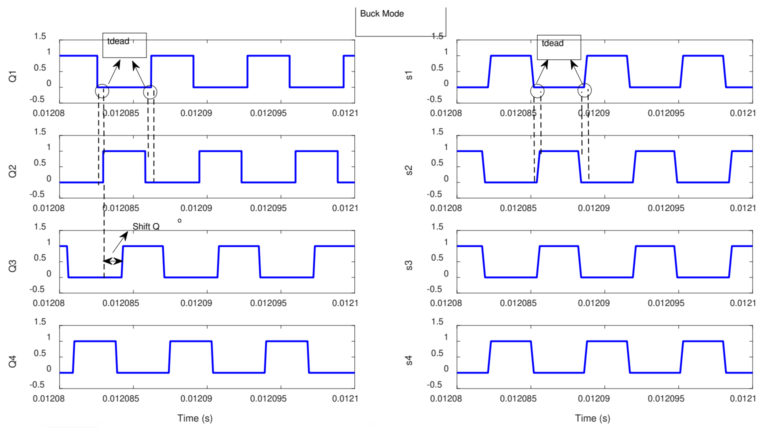


Figure 2.32 Switching signals for buck mode

While the system is operating in buck mode, the output current, input and output voltages for different load situations are shown in detail in Figure 2.33. Thanks to the proposed controller, the output voltage is kept constant over a wide load range.

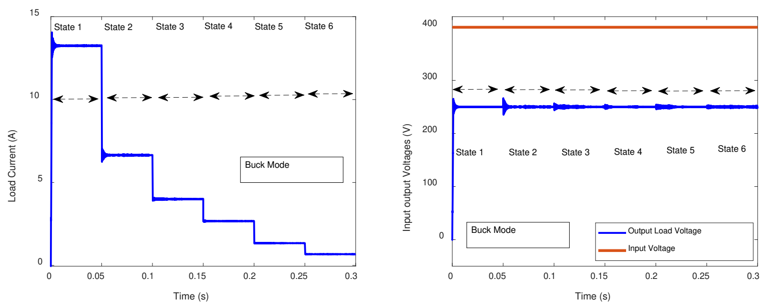


Figure 2.33 Current and voltage characteristics of DAB converter for buck mode

While the system is operating in boost mode, the voltage and current values of the switches $Q_2$ and $Q_4$ are shown in Figure 2.34. It has also been verified that the proposed controller performs soft switching.

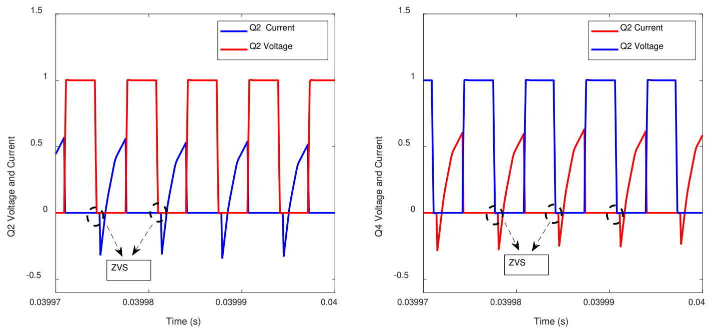


Figure 2.34 Current and voltage characteristics of $Q_2$, $Q_4$ switches (boost mode)

While the system is operating in boost mode, the voltage and current values of the switches $Q_2$ and $Q_4$ are shown in Figure 2.35. It has also been verified that the proposed controller performs soft switching.

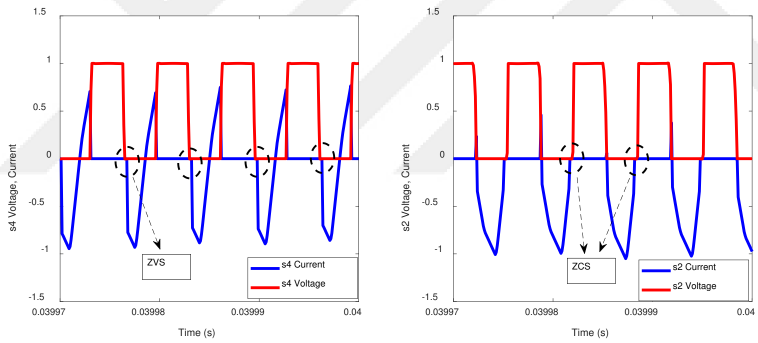


Figure 2.35 Current and voltage characteristics of s2, s4 Switches (buck mode)

While the system is operating in buck mode, the voltage and current values characteristics of transformer is shown in Figure 2.36.

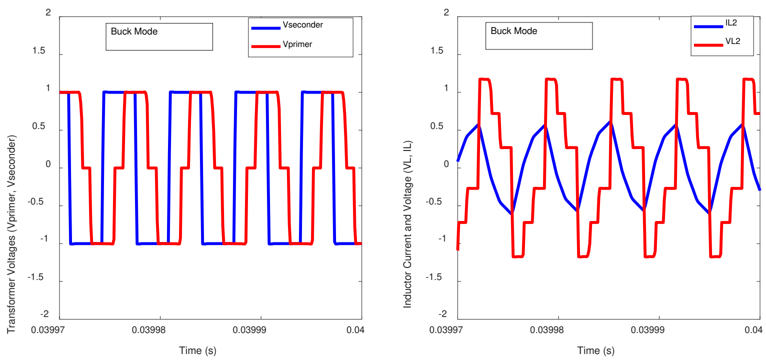


Figure 2.36 Current and voltage characteristics of transformer (buck mode)

## 2.9. Literature Overview

Isolated DC-DC converter topologies proposed for battery charging unit of electric vehicles in the literature are presented in detail in this section. The isolated DC-DC converter topologies and electrical performances used in the Literature are summarized in Table 2.7.

Table 2.8 Isolated DC-DC topologies used for battery charging unit in the Literature.

| References | Topology | Power | Freq. | Eff. (η) |
|---|---|---|---|---|
| Yang et al., 2015 | Full-bridge | 1-kW | -- | 95% |
| Whitaker et al., 2014 | Full-Bridge | 6.1-kW | 200 kHz | 95% |
| Tao et al., 2019 | Full-Bridge | ≈600 W | 100 kHz | 95% |
| Kanamarlapudi et al., 2018 | Full-bridge | 1.2-kW | 100 kHz | ≈95% |
| Zavare et al., 2015 | Flyback | 84-W | 125-kHz | 89% |
| Kushwaha et al., 2018 | Flyback | 850-W | 50-kHZ | 82% |
| Singh et al., 2019 | Flyback | 850-W | 20-kHz | ≈90% |
| Lee et al., 2013 | Half-bridge | 1.2-kW | 100 kHz | 95.1% |
| Duan et al., 2015 | Half-Bridge | 2.5-kW | 90-200 kHz | 93.2% |
| Xie et al., 2018 | Half-Bridge | 400-W | 100-kHz | --- |
| Cunha et al. 2019 | Half-bridge | 3-kW | 30-kHz | --- |
| Asa et al., 2013 | LLC Resonant | 1.2-kW | --- | 97% |
| Wang et al., 2014 | LLC Resonant | 3.3-kW | 200-kHz | 97.4% |
| Saket et al., 2016 | LLC Resonant | 1.2-kW | --- | 96.1% |
| Gumera et al., 2017 | LLC Resonant | 345-W | 90-200 kHz | 96.3% |
| Li et al., 2019 | LLC Resonant | 6.6-kW | 270-315 KhZ | 95.3% |
| Akamatsu et al., 2012 | Phase Shift FB | 1-kW | 50-kHz | ≈90% |
| Lu et al., 2017 | Phase Shift FB | 7.2-kW | 500-kHz | ≈97% |
| Lim et al., 2019 | Phase Shift FB | 3.3-kW | 50-kHz | 97.3% |
| Lee et al., 2019 | Phase Shift FB | 3.3-kW | 100-kHz | 97.9% |
| Feizi et al., 2020 | Phase Shift FB | 1.37-kW | 200-kHz | 95.5% |
| Wang et al., 2013 | DAB | 525-W | 20-kHz | 84% |
| Liu et al., 2014 | DAB | 3.5-kW | 60-90 kHz | ≈97% |
| Kondo et al., 2016 | DAB | 3.5-kW | 20-kHz | 93.3% |
| Assadi et al., 2018 | DAB | 6.6-kW | 125-kHz | --- |
| Mishra et al., 2018 | DAB | 3.5-kW | 25-kHz | --- |

Yang et al. proposed asymmetric PWM technique applied soft switched full-bridge DC-DC converter for battery charging unit in electric vehicles. The aim of the study is to design a high efficiency battery charging unit. The maximum efficiency of the converter, designed as a 1 kW prototype, has reached 95% (Yang et al. 2015).

Whitaker et al. proposed on-board battery charger unit architecture for electric vehicles. It aimed to achieve high power density and high efficiency at high frequencies by using silicon carbide power elements for the dc-dc converter. A 6.1 kW prototype was created for the dc-dc converter, which was applied in the soft switching technique, and was able to reach 96% efficiency (Whitaker et al., 2014).

Tao et al. studied on a full-bridge DC-DC converter with two clamp diodes and synchronous rectification is recommended for on-board battery charging unit in electric vehicles. Clamp diodes are used to suppress the voltage oscillation of the secondary side of the transformer and provide the commutation energy of the lagging leg. A prototype with an output power of about 600-w was designed and the maximum efficiency of the DC-DC converter with 100-khz switching frequency reached 95% (Tao et al., 2019).

Kanamarlapudi et. Studied on a full-bridge DC-DC converter capable of soft switching for two-stage on-board battery charging unit in electric vehicles. For the study, passive auxiliary circuit elements used to apply soft switching technique and also dampen voltage fluctuations on rectifier diodes in the secondary part. It also aimed to achieve high efficiency by using asymmetric PWM control technique. It has proposed a 1.2-kw prototype and has been reported to achieve a maximum efficiency of 95% (Kanamarlapudi et al., 2018).

Zavare et al. Studied on isolated flyback DC-DC converter for low size and low weight electric vehicle battery charger topology, the proposed battery charger topology has 84-watt rated power and 14-volt dc output voltage, the peak efficiency has reached 89% (Zavare et al., 2015).

Kushwaha et al. Proposed a battery charger topology for electric vehicle with isolated flyback converter. The rated power of proposed topology is 850-W and 48-volt dc output voltage, efficiency of proposed topology is measured as 82% (Kushwaha et al., 2018).

Singh et al. Proposed a battery charger topology with flyback DC-DC converter. The proposed topology has 850-w rated power and voltage conversion rate is 300V-to 65-V. The proposed topology has achieved approximately 90% efficiency (Singh et al. 2019).

Lee et al. proposed a 4-transformer half-bridge DC-DC converter for battery charging unit in electric vehicles. By applying soft switching technique to the proposed converter, it aimed to reduce switching losses and increase efficiency. A 1.2 k-w prototype has been made and has reached an efficiency of about 95% with 100-kHz switching frequency (Lee et al., 2013).

Duan et al. proposed half bridge DC-DC converter for on-board battery charging unit in electric vehicles. A new synchronous rectification control method used for the proposed dc-dc converter. It reached 93.2% efficiency by using 2.5-kw prototype and 12-V Li-ion battery (Duan et al., 2015).

Xie et al. proposed a current-fed half bridge DC-DC converter, which can make soft switching for battery charging unit in electric vehicles. The purpose of the proposed method is to reduce cost and increase power transfer efficiency by reducing switching losses. A 400-w prototype has been proposed to prove the reliability of the proposed converter (Xie et al., 2018).

Cunha et al. Proposed a boost half-bridge DC-DC converter for battery charging unit in Hybrid- electric vehicles. In the proposed method, semiconductor circuit elements are reduced and soft switching method is applied with asynchronous PWM. A 3-kW prototype was analyzed to increase the reliability of the proposed method (Cunha et al. 2019).

Asa et al. proposed a LLC locked loop controlled loop resonant converter for battery charger in electric vehicles. It is aimed to reduce switching losses and increase efficiency by applying soft switching method to the proposed dc-dc converter. To prove the reliability of the proposed method, the 1.2-kw prototype was analyzed and claimed to achieve a maximum efficiency of 97% at full load (Asa et al., 2013).

Wang et al. proposed LLC resonance converter for the on-board battery charger in electric vehicles. By applying soft switching (ZVS) method to the proposed dc-dc converter, it is aimed to reduce switching losses and increase efficiency. To prove the reliability of the proposed method, the 3.3-kw prototype was analyzed and claimed to achieve a maximum efficiency of 97.4% at full load (Wang et al., 2014).

Saket et al. LLC has proposed an LLC resonant converter for the on-board battery charger in electric vehicles. The main purpose of the proposed dc-dc converter is reducing parasitic capacitances to avoid overlapping faces between PCB traces. To prove the reliability of the proposed method, the 1.2-kw prototype was analyzed and claimed to achieve a maximum efficiency of 96.1% (Saket et al., 2016).

Gumera et al. proposed LLC resonant converter for the on-board battery charger in light electric vehicles. The 345-kw prototype was analyzed and claimed to achieve a maximum efficiency of 96.3% (Gumera et al., 2017).

Li et al. proposed resonance converter with SiC mosfet for on-board battery charger in electric vehicles. It is aimed to reduce switching losses and increase efficiency by applying soft switching method to the proposed converter. To prove the reliability of the designed circuit, the 6.6-kw prototype was analyzed and claimed to achieve a maximum charging efficiency of 95.3% (Li et al., 2019).

Akamatsu et al. proposed a secondary side phase shifted full-bridge DC-DC converter for the on-board battery charger in electric vehicles. It is aimed to reduce switching losses and increase efficiency by applying soft switching method to the proposed converter. To prove the reliability of the designed circuit, the 1-kw prototype was analyzed and claimed to measure the maximum efficiency at about 90% (Akamatsu et al., 2012).

Lu et al. proposed a phase shifted dual active bridge DC-DC converter for the on-board battery charger in electric vehicles. It is aimed to reduce switching losses and increase efficiency by applying soft switching method to all switches of the proposed converter. To prove the reliability of the designed circuit, the 7.2-kw prototype was analyzed and claimed to measure the maximum efficiency at about 97% (Lu et al., 2017).

Lim et al. proposed a phase shifted full-bridge DC-DC converter with employing a new center-tapped clamp circuit for on-board battery charging unit of electric vehicles. The main purpose of the proposed converter is to reduce conduction losses and increase efficiency. To prove the reliability of the designed circuit, the 3.3-kw prototype was analyzed and claimed to measure the maximum efficiency at about 97.3% (Lim et al., 2019).

Lee et al. proposed a novel clamping circuit with phase shifted full-bridge DC-DC converter, for the on-board battery charging unit of electric vehicles. The main purpose of the proposed converter is to increase the diode performance by using a simple clamping circuit, thereby reducing the output filter to increase efficiency. To prove the reliability of the designed circuit, the 3.3-kw prototype was analyzed and claimed to measure the maximum efficiency at about 97.5% (Lee et al., 2019).

Feizi et al. proposed a novel phase shifted full-bridge DC-DC converter with current doubler rectifier, for on-board battery charging unit of electric vehicles. By applying extended soft switching method to the proposed converter, it is aimed to reduce switching losses, reduce voltage stress in the secondary part and increase efficiency. To prove the reliability of the designed circuit, the 1.37-kw prototype was analyzed and claimed to achieve maximum efficiency of about 95.5% (Feizi et al., 2020).

Wang et al. proposed a dual active bridge DC-DC converter for on-board battery charging unit of electric vehicles. It is aimed to increase the performance of the converter by applying a dual-active-phase shift control method to the proposed converter. In order to prove the reliability of the designed circuit, the 525-w prototype was analyzed and claimed to achieve maximum efficiency of about 84% (Wang et al., 2013).

Liu et al. proposed a dual active bridge with boost series resonance converter for on-board battery charging unit of hybrid electric vehicles. It is aimed to increase efficiency by applying soft switching method to the proposed DC-DC converter. In order to prove the reliability of the designed circuit, the 3.5-kw prototype was analyzed and claimed to achieve maximum charging/discharging efficiency of 97% (Liu et al., 2014).

Kondo et al. proposed a dual active bridge isolated DC-DC converter for battery charging unit of electric vehicles. It is aimed to increase efficiency by applying a new phase shift control and soft switching method to the proposed dc-dc converter. In order to prove the reliability of the designed circuit, the 3.5-kw prototype was analyzed and claimed to achieve maximum charging-discharging efficiency at 93.3% (Kondo et al., 2016).

Assadi et al. proposed a dual active bridge isolated DC-DC converter for battery charging unit of electric vehicles. It is aimed to increase the performance by applying non-linear active transformer saturation mitigation technique to the proposed dc-dc converter. A 6.6-kw prototype was analyzed to prove the reliability of the designed circuit (Assadi et al., 2018).

Mishra et al. proposed a dual active bridge isolated DC-DC converter for Level-1 on board-battery charger in electric vehicles. It is aimed to increase efficiency by applying modified phase shift control method to the proposed isolated dc-dc converter. A 3.5-kw prototype was analyzed to prove the reliability of the designed circuit (Mishra et al., 2018).

## 2.10. Summary of the Section

In this section, the isolated DC-DC converter topologies used in two-stage on-board battery charger designed for electric vehicles are given with their controller structures. In addition, computer application results of DC-DC converters are presented. Literature research and Matlab / Simulink simulation results showed that in conventional isolated DC-DC converter topologies; The LLC resonance converter seems to be more advantageous because the number of circuit elements is low, its efficiency is high, and it performs in the narrow frequency range in the wide load (light load-to-full load) range. In addition, due to its features such as easy applicability, facilitating system analysis, ensuring stable modulation and high noise tolerance, voltage mode control has been preferred for the control of isolated dc-dc converters.

# 3. SOFT SWITCHING METHODS FOR DC-DC CONVERTERS

Isolated pulse width modulation (PWM) DC-DC converters are widely used in battery chargers of electric vehicles because of their high power density, fast transition response and ease of control. As the power demanded for battery charging increases, the power density of the converters needs to be increased, so that the isolated DC-DC converters need to be operated at high frequencies. However, as the switching frequency increases, switching losses and electromagnetic interference (EMI) noise increase. Therefore, soft switching methods have been proposed in the literature to solve these problems occurring in traditional hard switching converters (Saygı et al., 2017, Akamatsu et al., 2017, Altıntaş., 2007, Choi et al., 2014, Sayed et al., 2020, Mehedy et al., 2018). The electrical and economic features provided by hard switching and soft switching to the applied DC-DC converter are presented in Table 3.1.

Table 3.1 Electrical and economical property of hard switching and soft switching.

| **Electrical specifications** | **Hard Switching** | **Soft Switching** |
|---|---|---|
| Switching Loss | High | Almost none. |
| Efficiency | Low | Probably high |
| Circuit element numbers. | Ordinary | More |
| Power Density | Ordinary | Probably high |
| Electromagnetic Inference (EMI) | High | Less |
| Maturity | Developed | Developing |
| Cost | Standard | More |
| Applicability | Easy | More complex |

The switching loss response between hard and soft switching can basically be explained as follows; In hard switching during the 'on' state of the switch, the switching (MOSFET) voltage increases at least to be equal to the supply voltage, the current tends to flow from the drain to the source, causing the switch and high 'on' state losses. In soft switching, the current during the 'on' state of the switch is discharged over the output capacitance ($C_{oss}$) of the mosfet before turning on the device, so that it is diverted from the source, which eliminates the switching OPEN losses Shown in Figure 3.1. Initially, the parasitic mosfet transmits the body diode, and when MOSFET is activated, the current is connected to the channel (Zuk et al., 2014, Altıntaş., 2007, Iyer et al., 2017).

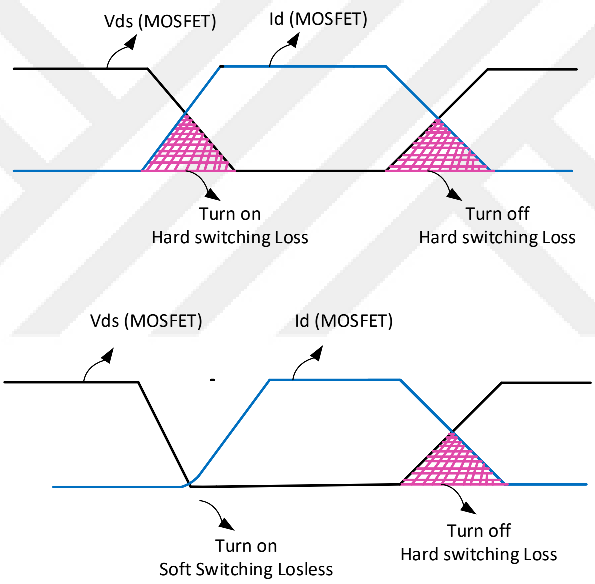


Figure 3.1 Switching loss analysis of hard-soft switching

Different methods are proposed and examined in the literature for soft switching techniques. These methods are; switching at zero current switching (ZCS), zero voltage switching (ZVS), transition at zero current (ZCT), transition at zero voltage (ZVT).

### 3.1. Zero Current Switching

Zero current switching (ZCS) is the technique that is performed during the time the power switch element turns on. A small value of inductance is connected in series to the power switch element, thus limiting the rate of increase of the current passing through the circuit element in the transmission process. As a result, the power loss is reduced by preventing the coincidence of current and voltage during the switching operation. In fact, the switching energy in the transmission process is transferred to the inductance. This energy in inductance is spent at a resistance in classical cells, but in modern cells it is recovered by transferring it to a voltage source or load with a short-term partial resonance. (Altıntaş., 2007, Dobi et al., 2018). The conventional basic zero current switching technique and waveform is shown in Figure 3.2.

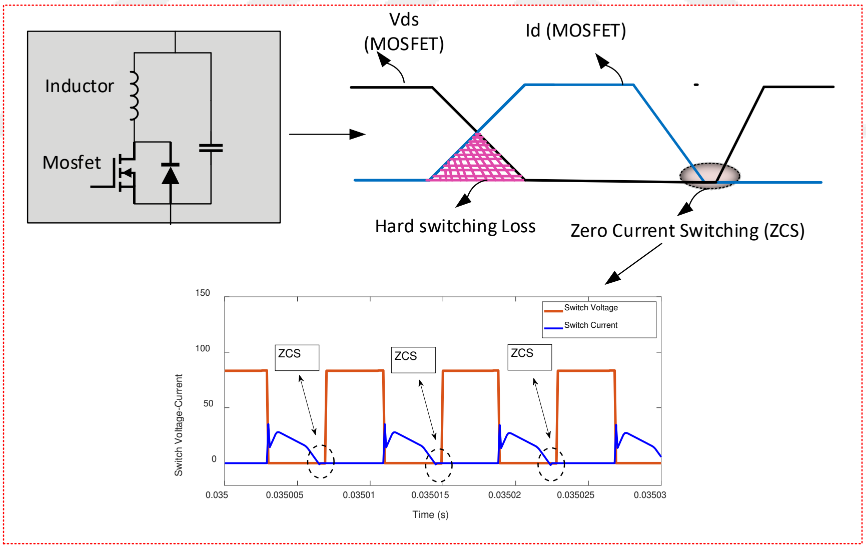


Figure 3.2 Conventional basic zero current switching technique and waveform.

### 3.2. Zero Voltage Switching (ZVS)

Zero Voltage Switching (ZVS) is a soft switching technique performed when entering the switch in the off-state time frame. In this technique, basically a small value capacitor is connected in parallel to the power switch (mosfet) of the DC-DC converter, limiting the rate of rise of the voltage at the ends of the element in the process of transmitting. Thus, in the process of exiting the transmission, the switching energy loss is reduced and the switching energy is transferred to the capacitor (Zuk et al., 2014, Altıntaş., 2007, Iyer et al., 2017, Dobi et al., 2018). The conventional basic zero voltage switching technique and waveform is shown in Figure 3.3.

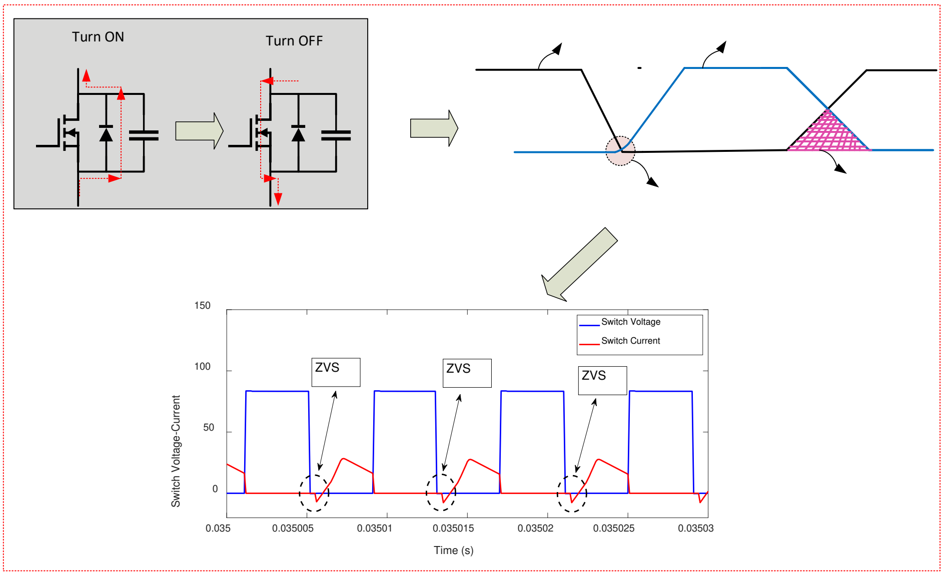


Figure 3.3 Conventional basic zero voltage switching technique and waveform.

### 3.3. Zero Current Transition (ZCT)

Zero Current Transition (ZCT) is a soft switching technique that is performed when the power switch turns off. In the literature, it is generally, preferred for low rated power and non-isolated DC-DC converters, it increases the number of circuit elements considerably, the cost increases, it is complicated and difficult to apply. However, in the ZCT technique, the current passing through the power switch is reduced to zero as a result of a short partial resonance process, then the control signal is cut off by keeping the current at zero. Thus, overlapping current and voltage and switching energy loss are completely eliminated. It can be said that both ZCS and ZVS are provided here. As a result, this process is a soft switching technique performed by reducing the current to zero (Saygı et al., 2017, Altıntaş., 2007, Dobi et al., 2018). The basic converter circuit where the ZCT method is applied is shown in Figure 3.4.

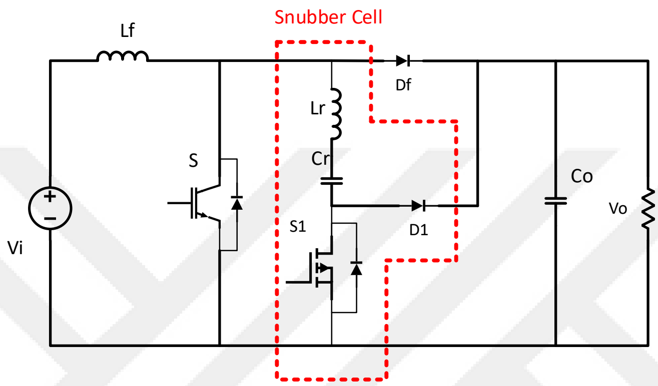


Figure 3.4 ZCT method applied basic converter (Saygı et al., 2017)

### 3.4. Zero Voltage Transition (ZVT)

Zero Voltage Transition (ZVT) is a soft switching technique applied when the power switch goes into the transmission state. In the literature, it is generally a preferred switching technique in low rated power and non-isolated DC-DC converters. The number of circuit elements increases considerably, production cost is high, implementation is complicated and difficult. However, in this technique, the voltage at the power switch ends is reduced to zero with a short-term partial resonance and the control signal is applied while keeping this voltage at zero. Thus, switching energy loss is completely eliminated. It can be said that both ZVS and ZCS provide this technique, which is carried out by taking the tension down to zero. This technique, in which switching energy is recovered, is also achieved with modern cells and requires an additional switch (Saygı et al., 2017, Altıntaş 2007, Dobi et al., 2018). The basic converter circuit where the ZVT method is applied is shown in Figure 3.5.

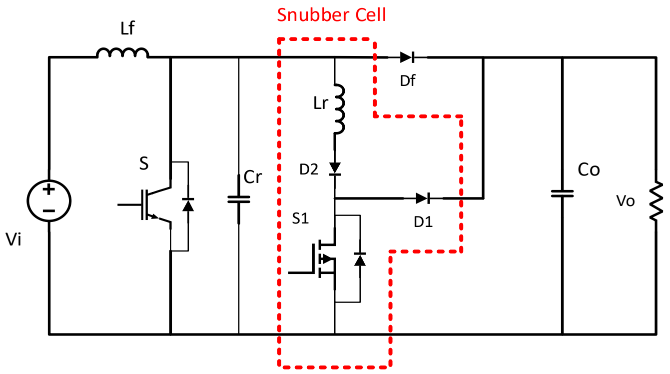


Figure 3.5 ZVT method applied basic converter (Saygı et al., 2017)

In the Literature, when the isolated DC-DC converters used for battery charging unit of electric vehicles are examined, it is seen that generally, ZVS, ZCS soft switching methods are used. It seems that the ZVT and ZCT methods are generally common in DC-DC converters with non-isolated and low power switch count. It has been observed that electric vehicles are not preferred in battery charging units, as they increase the number of circuit elements and thus the cost of production, and are also difficult and complex to apply. In the Literature, some of the proposed soft switched DC-DC converters for the battery charging unit of electric vehicles are shown in Table 3.2.

Table 3.2. The soft switched DC-DC converters for OBC in EVs

| **Reference** | **Power** | **Frequency** | **Method** | **Peak Efficiency** |
| --- | --- | --- | --- | --- |
| Akamatsu et al., 2012 | 1-kW | 50-kHz | ZCS-ZVS | --- |
| Iyer et al., 2017 | 3.3-kW | 50-kHz | ZVS | 97.5% |
| Yang et al., 2015 | 1-kW | 50-kHz | ZVS-ZCS | 95% |
| Li et al., 2012 | 2-kW | ---- | ZVS-ZCS | ---- |
| Wang et al., 2019 | 3.3-kW | 150-kHz | ZVS | --- |
| Sayed et al., 2020 | 3.2-kW | 40-kHz | ZVS-ZCS | --- |

Akamatsu et al. proposed a novel soft switching secondary side phase shift PWM techique for full bridge DC-DC converter and suitable for electric vehicle battery charger. a 1-kw dc-dc converter prototype proposed, where it applies soft switching methods (ZVS-ZCS). Graphically explained that the converter's peak efficiency is around 90% (Akamatsu et al., 2012).

Iyer et al. proposed a dual active bridge DC-DC converter for two-stage battery charging unit in electric vehicles. ZVS method has been applied as soft switching to the proposed dc-dc converter. In order to verify the suitability of the proposed method, a 3.3-kW prototype designed and stated that it reached 97.5% peak efficiency (Iyer et al., 2017).

Yang et al. proposed a highly efficient soft-switched PWM technique and applied the proposed technique to the isolated full bridge DC-DC converter. By applying the asymmetric PWM technique, it aimed to achieve zero current switching and zero voltage switching (ZVS-ZCS). To verify the suitability of the proposed method, he designed a 1-kw prototype and reached a peak efficiency of 95% (Yang et al., 2015).

Li et al. proposed and analyzed a high power DC-DC converter and active clamping circuit for battery chargers in electric vehicles. applied soft switching to reduce voltage stress on power switches and reduce switching losses (ZVS-ZCS). To verify the suitability of the proposed method, an insulated dc-dc converter with 2-kw rated power was analyzed (Li et al., 2012).

Wang et al. proposed a high power phase shifting full-bridge DC-DC converter for battery chargers in electric vehicles. applied soft switching (ZVS) to reduce voltage stress on the power switches, increase the power density of the converter and reduce switching losses. To verify the suitability of the proposed method, an isolated dc-dc converter with 3.3-kw rated power and 150-kHz switching frequency was analyzed (Wang et al., 2019).

Sayed et al. proposed a new circuit topology for battery chargers in electric vehicles. For the proposed topology, a high-power phase shifting, full-bridge DC-

DC converter with a current doubler circuit is used in the secondary part. The proposed dc-dc converter was applied soft switching (ZVS-ZCS) method to reduce voltage stress on the power switches, increase the power density of the converter and reduce switching losses. To verify the suitability of the proposed method, it was analyzed on a prototype with a 2-kw rated output power and it was stated that it reached over 92% efficiency (Sayed et al. 2020).

### 3.5. Summary of the Section

In this section, soft switching methods applied to isolated DC-DC converters recommended for two stage on-board battery charging unit in electric vehicles are examined. These methods are; Zero voltage switching (ZVS), zero current switching (ZCS), zero voltage transition (ZVT) and zero current transition (ZCT) methods. In isolated dc-dc converters recommended for electric vehicles, ZVS and ZCS soft switching methods are generally preferred to reduce switching current, increase the power density of the DC-DC converter, and reduce current and voltage stress on power switches. ZVT and ZCT methods are generally preferred for single-switch and non-isolated DC-DC converters. The main reasons for this situation can be explained as follows; The ZVT and ZCT methods need extra circuit elements, the production cost increases and the implementation is difficult and complex.

# 4. THE PROPOSED SYSTEM AND CONTROL

Since the internal volume of electric vehicles is limited, the on-board battery chargers recommended for electric vehicles must meet some requirements. These requirements are described in the Literature as follows: high power density, high efficiency, good heat dissipation, low harmonic distortion and high power factor. The power density and efficiency of on-board battery chargers largely depend on the design of the isolated dc-dc converters. In addition, low total harmonic distortions (THD) occurring in the grid current during the charging process improves both power conversion performance and electrical quality, the harmonic distortions occurring in the current should be within the range specified in IEC 61000-3-2 THD standards. In order to carry out charging under different load conditions, pi-based controller is used in conventional grid-connected on-board battery charging units. However, the pi based controller is generally; has problems such as slow dynamic response, steady state errors and complex structure. In order to improve dynamic response, reduce steady state error and also to simplify control structure in this study artificial neural network (ANN) based controller is designed. In addition, in the isolated DC-DC converters operated at high frequencies, circuit element sizes decrease while electromagnetic interference (EMI) and switching losses increase. In the proposed study, soft-switched (ZVS) half-bridge LLC resonance converter is designed for high efficiency, high power density and low EMI. Besides, it is aimed to capture low harmonic distortion and high power factor by using AC-DC boost PFC converter, easy to use, highly efficient and effective in harmonic damping, the AC-DC boost PFC converter is designed and controlled with the average current mode control (ACM). The two-stage OBC topology and controller structures proposed for the battery charging unit of electric vehicles are shown in detail in Figure 4.1.

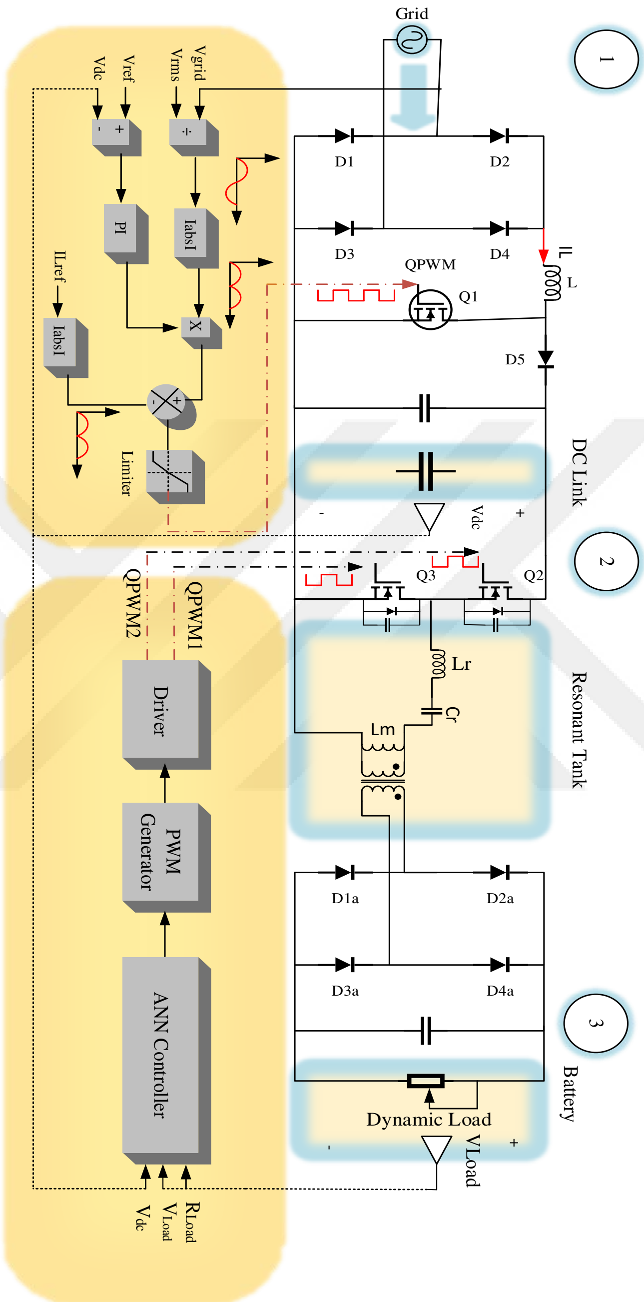


Figure 4.1 ANN Controller for two stage battery charger for HEVs/EVs.

## 4.1. AC-DC PFC Converter Part of OBC

In proposed two stage OBC; ac-dc boost pfc converter is preferred for the first stage, because it is easy to apply, highly efficient, high power factor and effective performance in harmonic damping (Kupati et al., 2015, De Gusseme et al., 2007, Karaarslan et al., 2011). The circuit structure of the ac-dc boost PFC converter and the path followed by the current according to the operating mode are shown in Figure 4.2.

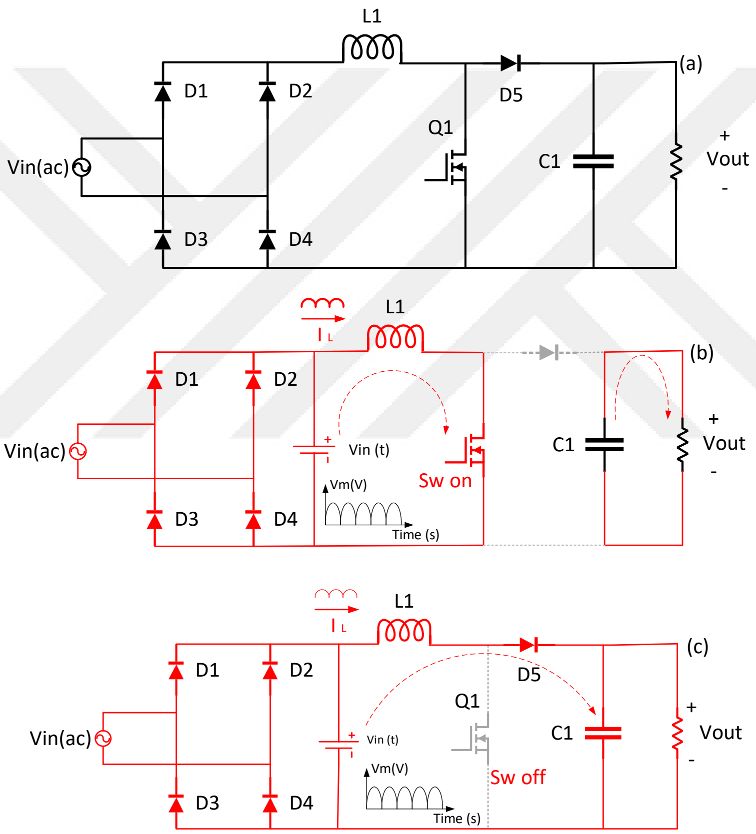


Figure 4.2 Switching operations of Boost PFC circuit

When the power switches turn on and off states are analyzed separately, the following equations can be derived (Kupati et al., 2015, De Gusseme et al., 2007, Karaarslan et al., 2011).

$$\begin{cases} \dfrac{di_L}{dt} = \dfrac{|V_{in}(t)|}{dt}, (t \in [0, DTs]) \\ V_{in}(t) = \sqrt{2}V_{in}\sin(wt) = \sqrt{2}V_{in}\sin\left(\dfrac{2\Pi}{T_0}t\right) \\ \dfrac{di_L}{dt} = \dfrac{V_0 - |V_{in}|}{L}, (t \in [DTs, Ts]) \end{cases} \tag{4.1}$$

The following equations are used in the Literature to determine the critical values of the capacitor and inductor of the AC-DC boost PFC converter.

The minimum inductance value of the boost PFC converter can be calculated with the following equation.

$$L_{\min} \geq \frac{D(1-D)^2}{2f_s}R_{load} \tag{4.2}$$

The minimum capacitance value of the boost PFC converter can be calculated with the following equation.

$$C_{\min} \geq \frac{D}{R_{load}.f_s.\Delta V} \tag{4.3}$$

The mathematical models used in the equations are named as follows; $I_L$ is inductor current, inductor, *fs* is switching frequency, D is duty ratio, Vo is load voltage, $V_{in}$ is grid voltage (Kupati et al., 2015, De Gusseme et al., 2007, Karaarslan et al., 2011).

Table 4.1 Operation parameters of boost PFC

| Vgrid | Frequency | Vload | Rload | C | L |
|---|---|---|---|---|---|
| 220*1.414 | 50 Hz | 400 V | (400*400)/3300 | 500e-6 | 0.6e-3 H |

The electrical properties of the designed boost PFC converter, such as total harmonic distortions (THD), phase angle between grid current and voltage and power factor are shown in Figure 4.3.

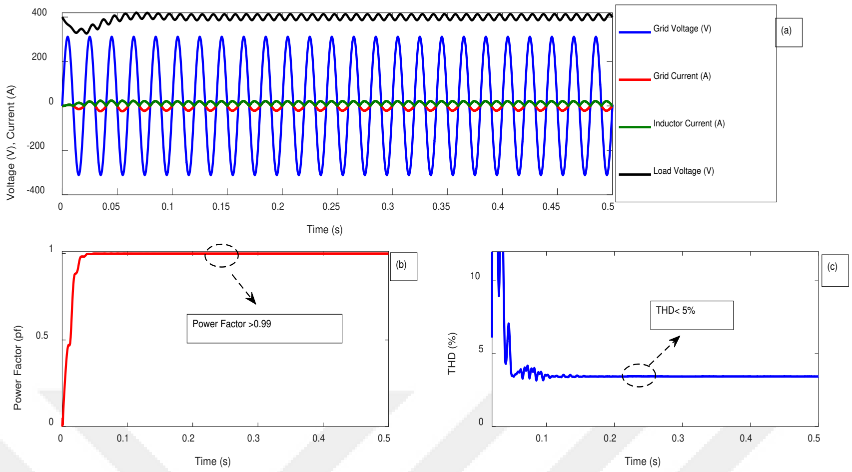


Figure 4.3 Grid current and voltages (a), Power factor (b), THD (c)

The average current mode controller structure used for current and voltage control of the AC-DC boost PFC converter is shown in Figure 4.4.

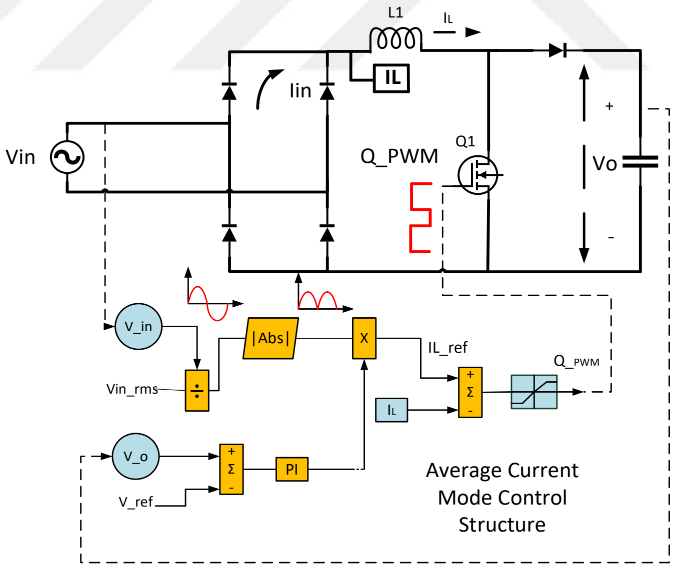


Figure 4.4 ACM controlled AC-DC boost PFC

Average current mode control method is widely preferred and effective control method for ac-dc PFC converters. In this controller; the output voltage is subtracted from a reference voltage signal. The resulting error signal is given to the input of the pi controller. While doing this, at the same time, the input voltage and the rms value of the input voltage are divided and the absolute value of the signal obtained is found. A reference signal for the inductance current is obtained by multiplying the output signal of the pi controller and the input voltage signal whose absolute value is taken. the inductance current is subtracted from the reference value generated for the inductance current. the obtained signal limits are given to the input of the specified relay. At the output of the relay, a PWM signal is generated for the power switch.

## 4.2. Designing and consideration of isolated DC-DC part for OBC

LLC resonance converter has become the most remarkable topology due to its high efficiency, low electromagnetic interference (EMI), wide load and voltage operation range and also the ability perform under high power density. For the second stage of OBC, a half-bridge LLC resonance converter with soft switched (ZVS) and ANN based controller structure is proposed. The LLC resonance converter and ac equivalent circuits are shown in Figure 4.5.

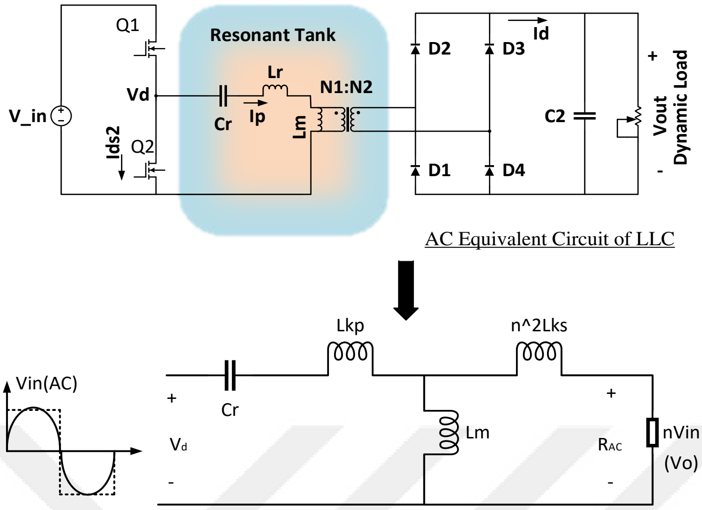


Figure 4.5 HBLLC resonant converter and equivalent circuit.

In order to analysis and determine the circuit parameters of LLC resonant converter the following steps are given;

Current and voltage calculation of AC equivalent circuit is specified in the following equations;

$$\begin{bmatrix} \mathrm{I}_{AC} = \dfrac{\Pi \cdot I_0}{2}\sin(wt) \\ \mathrm{VR}_{H} = +V_0 \Rightarrow if\ \sin(wt) > 0 \\ \mathrm{VR}_{H} = -V_0 \Rightarrow if\ \sin(wt) < 0 \\ \mathrm{VR}_{H}{}^{F} = \dfrac{4 \cdot V_0}{\Pi}\sin(wt) \end{bmatrix} \tag{4.4}$$

The calculation of the load value in the AC equivalent circuit is specified in the following equations.

$$\begin{bmatrix} \mathrm{R}_{AC} = \dfrac{VR_H{}^{F}}{I_{AC}} = \dfrac{8}{\Pi^2}\dfrac{V_0}{I_0} = \dfrac{8}{\Pi^2}R_{LOAD} \\ n = \dfrac{N_P}{N_S}, \\ \mathrm{R}_{AC} = \dfrac{8 \cdot n^2}{\Pi^2}R_{LOAD} \end{bmatrix} \tag{4.5}$$

The mathematical expression and equation of the voltage gain are indicated by the equation below.

$$\left[ M = \frac{2n \cdot V_0}{V_{in}} = \left| \frac{w^2 L_m R_{AC} C_R}{jw(1-\frac{w^2}{{w_0}^2}) \cdot (L_m + n^2 L_{ks}) + R_{AC}(1-\frac{w^2}{{w_p}^2})} \right| \quad \text{Where}, \quad w_0 = \frac{1}{\sqrt{L_r C_r}}, \quad w_p = \frac{1}{\sqrt{L_P C_r}} \right] \tag{4.6}$$

When the voltage gain is regulated, the following mathematical equation can be derived.

$$\left[ M = \frac{2n \cdot V_0}{V_{in}} = \left| \frac{\frac{w^2}{{w_p}^2}(\frac{k}{k+1})}{j(\frac{w}{w_0}) \cdot (1-\frac{w^2}{{w_0}^2}) \cdot Q \cdot \frac{(k+1)^2}{2k+1} + (1-\frac{w^2}{{w_p}^2})} \right| \quad \text{Where}, \ k = \frac{L_m}{L_{kp}}, \quad Q = \frac{\sqrt{L_r / C_r}}{R_{AC}} \right] \tag{4.7}$$

The mathematical values above can be explained as follows; $V_o$ is load voltage $V_{in}$ dc-link voltage, $V_{RH}$ is transformer secondary side voltage, $n$ is transformer's turn ratio, $M$ is voltage gain, w is angular frequency, $f_o$ is resonant frequency, $f_p$ primary resonant frequency, $L_m$ magnetizing inductance of the transformer, $L_r$ is resonant inductance, $C_r$ is resonant capacitance.

The effect of changing the quality factor (Q) and k index on the gain (M) is shown in Figure 4.6.

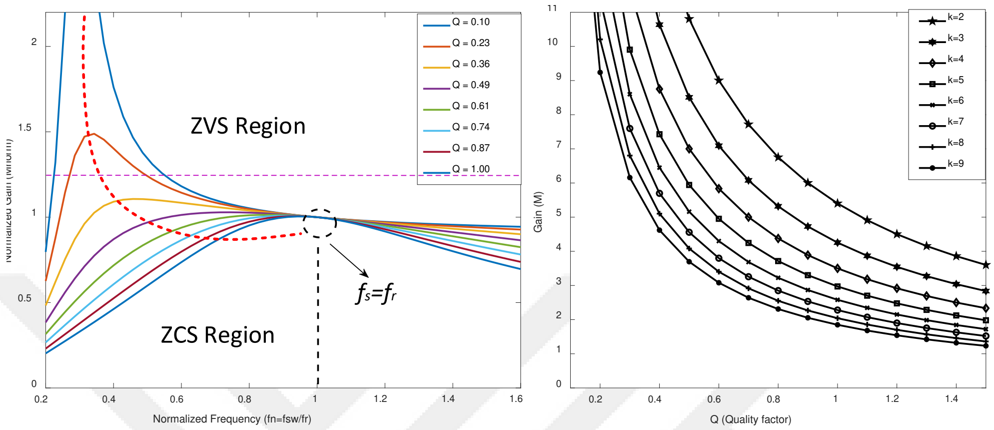


Figure 4.6 Effects of quality factor (Q) and inductance ratio (k) on the voltage gain in the LLC resonance converter.

### 4.2.1. Selection of LLC resonance converter circuit elements

The steps to be followed when choosing the circuit elements of the LLC resonance converter are presented below in equations.

In order to determine resonant capacitor (Cr);

$$\left[ C_r = \frac{1}{2\Pi Q \cdot f_o \cdot R_{ac}} = 302.82\text{nF} \right] \tag{4.8}$$

In order to determine resonant inductor (Lr);

$$\left[ L_r = \frac{1}{(2\Pi \cdot f_o)^2 \cdot C_r} = 11.57\mu H \right] \tag{4.9}$$

In order to determine Primary resonant inductor;

$$\left[ L_p = \frac{(k+1)^2}{(2k+1)}(L_r) = 37.887\mu H \right] \tag{4.10}$$

The relationship between primary resonant inductor, Magnetizing inductor and transformer primary side inductor is;

$$L_p = L_m + L_{pri};\ k = \frac{L_m}{L_{pri}} \Rightarrow L_p = (k+1)\cdot L_{pri}$$
$$\Rightarrow L_{pri} = 6.314\mu H \qquad (4.11)$$
$$\Rightarrow L_m = 31.573\mu H$$

In order to determine the winding turn numbers of the transformer;

$$\left[ n = \frac{Np}{Ns} = \frac{V_{in\ (\max)}}{2(V_o + 2V_d)} \cdot M_{(\min)} = \frac{400}{2(120+1)} \cdot (1.18) = 1.951 \right] \qquad (4.12)$$

Primary side minimum turn number can be determined as;

$$\left[ \begin{array}{l} N_{p(\min)} = \dfrac{n \cdot (V_o + 2V_d)}{2 \cdot f_p \cdot \Delta B \cdot A_e} \Rightarrow \\ \Rightarrow N_p = n \cdot N_s > N_{p(\min)} \end{array} \right] \qquad (4.13)$$

$$\left[ \begin{array}{l} N_{p(\min)} = \dfrac{1.951 \cdot (121)}{2 \cdot 4.6 \cdot 10^3 \cdot 0.3 \cdot 107 \cdot 10^{-6}} \Rightarrow 79.937 \\ \Rightarrow N_p = n \cdot N_s > N_{p(\min)} = 79.937 \\ \Rightarrow N_p = 80 \\ \Rightarrow N_s > N_{s(\min)} = 40.972 \\ \Rightarrow N_s = 41 \end{array} \right] \qquad (4.14)$$

To define the variables of the formulas above; $A_e$ is the transformers cross-sectional area in $m^2$ ($Ae = 107\ mm^2$, EER3541), $\Delta B$ is the maximum flux density swing in tesla; to prevent excessive hysteresis losses and heat generation, $\Delta B$ should be lower than 0.8T ($\Delta B$ in this study is chosen as 0.3T) (Park et al., 2016). $V_d$ is the diode voltage, $f_p$ is the minimum switching frequency, Np is the primary side turn number, Ns is the secondary side turn number, and n is the turn ratio.

### 4.2.2. Steady-state analysis for soft switched LLC resonance converter

In the switching operations of the LLC resonance converter, the switching signals (PWM) ($V_{GSQ1}$, $V_{GSQ2}$), the voltage on the power switches ($V_{DSQ1}$, $V_{DSQ2}$), current flowing through the power switch ($I_{Q1}$, $I_{Q2}$), and diode bridge current ($I_d$) in the secondary part, waveforms It is shown in Figure 4.7 (Toshiba., 2019). According to these waveforms, eight different operation modes are formed.

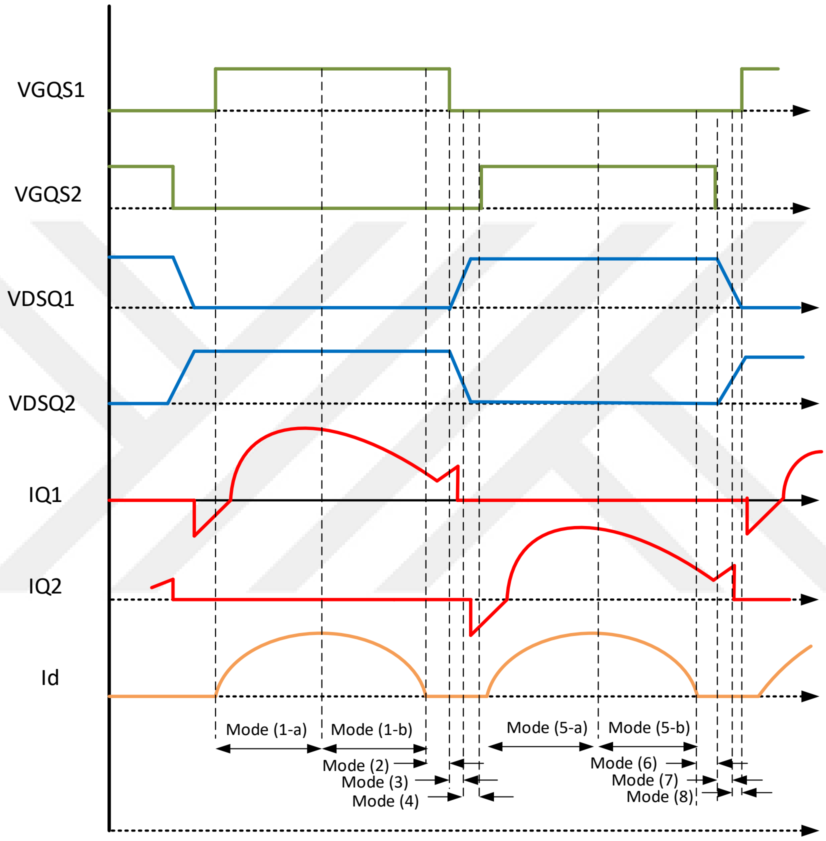


Figure 4.7 LLC resonance converter waveforms.

**Operation Mode 1-b ($Q_1$ is on state $Q_2$ is off state)**

In this operating mode, the first power switch ($Q_1$) is on ($Q_2$) while the power switch is in the off state. The primary part of the transformer consists of the current ($I_r$) flowing over the resonant tank ($L_r$ and $C_r$), the output current of the secondary part (Io) and the magnetic inductance current ($I_m$) of the transformer ($I_r = I_o + I_m$). In the secondary part of the transformer, the output current ($I_o$) flows over the filter capacitor ($C_o$) and the load. The voltage formed at the output provides a voltage up to (($N_1$ / $N_2$) * $V_o$) according to the number of turns (n) in the primary part of the transformer. Flow diagrams of the current in this operating mode and the activity status of the circuit elements are shown in Figure 4.8 (a).

**Operation Mode 2 ($Q_1$ is on state $Q_2$ is off state)**

In this mode of operation, the first power switches maintain the operation mode, while ($Q_1$) is on, ($Q_2$) is on the power switch. In this mode, the output current (Io) circulated in the primary part drops to zero. This mode continues until the resonance state between $L_r$ and $C_r$ ends. In the primary part, only the inductance current ($I_m$) of the transformer continues to flow and at the output, the energy induced on the capacitor ($C_o$) tries to discharge over the load. At the end of this mode, the $Q_1$ power switch turns off. Flow diagrams of the current in this operating mode and the activity status of the circuit elements are shown in Figure 4.8(b).

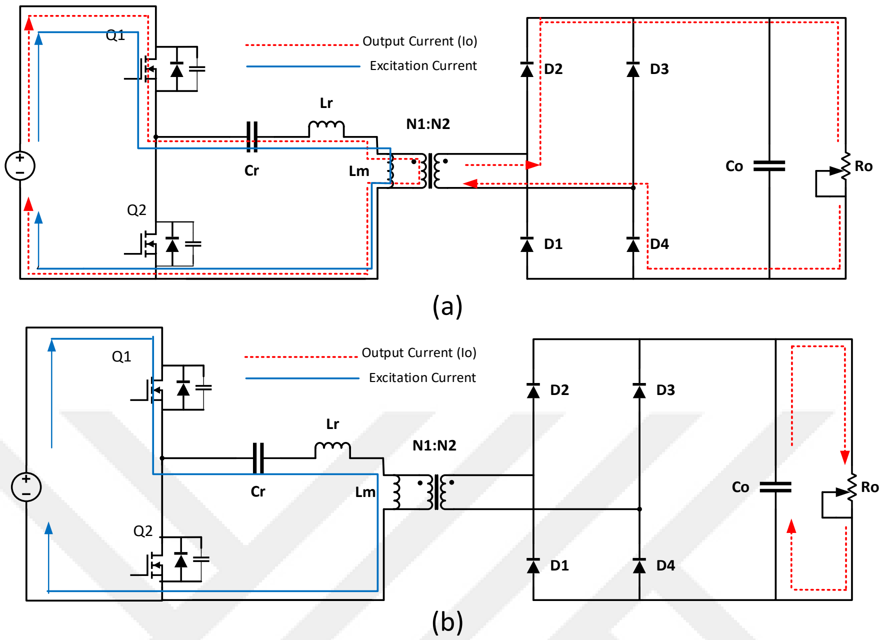


Figure 4.8 LLC resonance converter operation modes; (a) mode 1-b, (b) mode 2

**Operation Mode 3 ($Q_1$ is off state $Q_2$ is off state)**

In this mode of operation, both power switches ($Q_1$, $Q_2$) are off state. The magnetic inductance current ($I_m$) of the transformer continues to flow in the primary part. In this operating mode, since the switches are off state, current continues to flow through the parasitic capacitors ($C_{Q1}$ and $C_{Q2}$) of the switches. In this case, $C_{Q2}$ goes into discharge state while $C_{Q1}$ is charging. Thus, while the voltage of switch $Q_1$ increases, the voltage of switch $Q_2$ decreases. This mode of operation continues until the charge and discharge states of the parasitic capacitors are completed. Flow diagrams of the current in this operating mode and the activity status of the circuit elements are shown in Figure 4.9 (a).

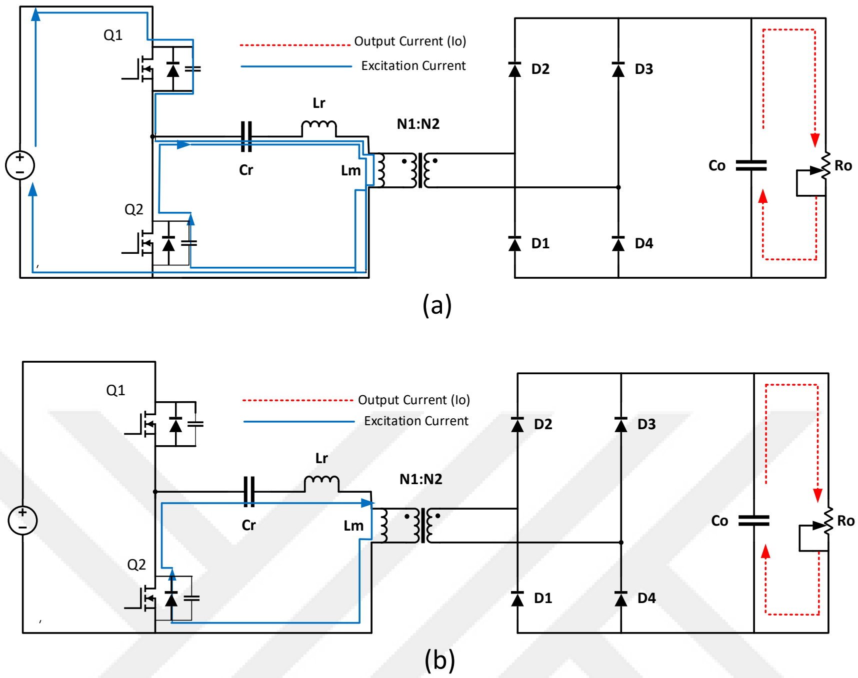


Figure 4.9 LLC resonance converter operation modes; (a) mode 3, (b) mode 4

**Operation Mode 4 (Q1 is off state Q2 is off state)**

In this operation mode, both power switches ($Q_1$, $Q_2$) are off. The magnetic inductance current ($I_m$) of the transformer continues to flow in the primary part of the parasitic capacitors even after the charge and discharge states are completed. In this mode, the transformer's magnetic current ($I_m$) flows through the body diode of the $Q_2$ switch, and the energy induced on the output capacitor (Co) is discharged through the load. At the end of this operating mode, switch $Q_2$ goes on. Flow diagrams of the current in this operating mode and the activity status of the circuit elements are shown in Figure 4.9 (b).

**Operation Mode 5-a ($Q_1$ is off state $Q_2$ is on state)**

The power switch $Q_1$ off state, while $Q_2$ turns on. The $Q_2$ switch turns on at zero switching voltage (ZVS) when the body diode is freewheeling. When the $Q_2$ switch turns on, the resonant capacitor ($C_r$) acts as a power source and causes current to flow in the primary part of the transformer. In the secondary part, the load current flows through diodes $d_1$ and $d_3$, creating Vo voltage on the load. The output voltage causes a voltage ($-(N_1 / N_2) * V_o$) on the magnetic inductance ($L_m$). This voltage causes the magnetic current ($I_m$) to be decayed. Flow diagrams of the current in this operating mode and the activity status of the circuit elements are shown in Figure 4.10 (a).

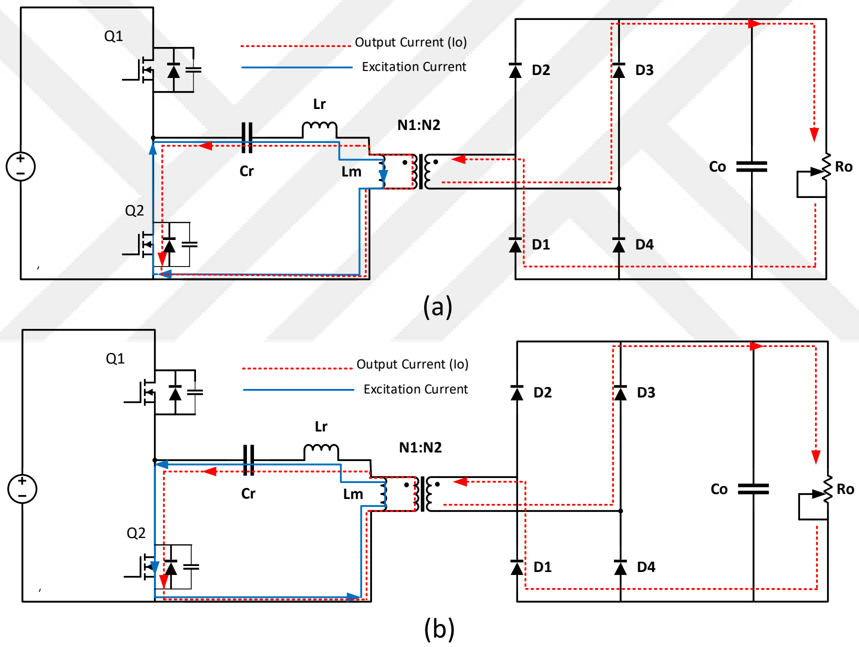


Figure 4.10 LLC resonance converter operation modes; (a) mode 5-a, (b) mode 5-b.

**Operation Mode 5-b ($Q_1$ is off state $Q_2$ is on state)**

In this operating mode, the power switch ($Q_1$) remains off state, while $Q_2$ is on state. The magnetizing current ($I_m$) starts to increase negatively. The resonance between $L_r$ and $C_r$ ends. This operation mode is completed when the output current ($I_o$) becomes zero and goes to the next operating mode. Flow diagrams of the current in this operating mode and the activity status of the circuit elements are shown in Figure 4.10 (b).

**Operation Mode 6 ($Q_1$ is off state $Q_2$ is on state)**

In this operating mode, the power switch ($Q_1$) remains off state, while $Q_2$ is on state. The magnetizing current ($I_m$) continues to flow through the transformer, $L_r$ and $C_r$ tanks. The $C_r$ resonance capacitor acts like a power source. At the end of this operating mode, the $Q_2$ switch turns off and the next operating mode starts. Flow diagrams of the current in this operating mode and the activity status of the circuit elements are shown in Figure 4.11 (a).

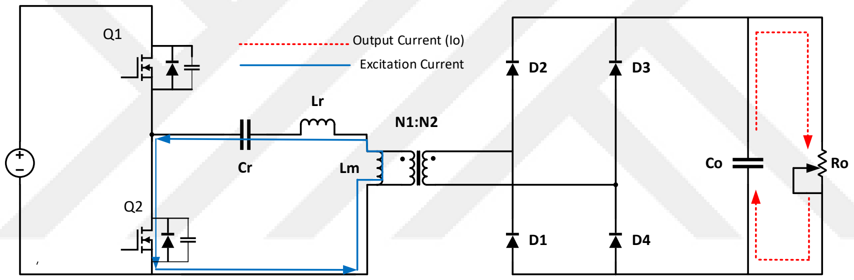


(a)

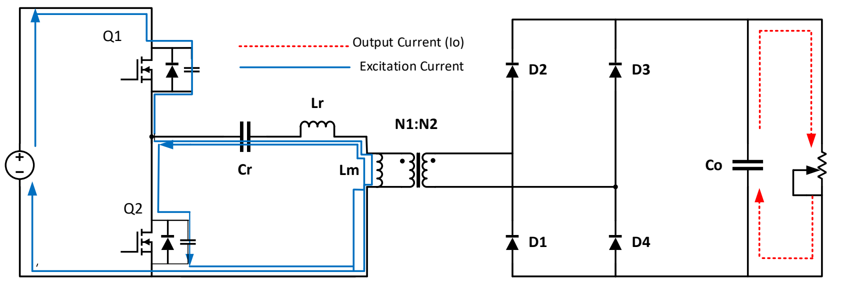


(b)

Figure 4.11 LLC resonance converter operation modes; (a) mode 6, (b) mode 7.

**Operation Mode 7 ($Q_1$ is off state $Q_2$ is off state)**

In this mode of operation, both power switches ($Q_1$, $Q_2$) are off state. The magnetic inductance current ($I_m$) of the transformer continues to flow in the primary part. In this operating mode, since the switches are off state, current continues to flow through the parasitic capacitors ($C_{Q1}$ and $C_{Q2}$) of the switches. In this case, $C_{Q2}$ goes into charge state while $C_{Q1}$ is discharging. Thus, while the voltage of switch $Q_1$ decrease, the voltage of switch $Q_2$ increases. This mode of operation continues until the charge and discharge states of the parasitic capacitors are completed. Flow diagrams of the current in this operating mode and the activity status of the circuit elements are shown in Figure 4.11 (b).

**Operation Mode 8 ($Q_1$ is off state $Q_2$ is off state)**

In this operation mode, both power switches ($Q_1$, $Q_2$) are off. The magnetic inductance current ($I_m$) of the transformer continues to flow in the primary part of the parasitic capacitors even after the charge and discharge states are completed. In this mode, the transformer's magnetic current ($I_m$) flows through the body diode of the $Q_1$ switch, and the energy induced on the output capacitor (Co) is discharged through the load. Flow diagrams of the current in this operating mode and the activity status of the circuit elements are shown in Figure 4. 12 (a).

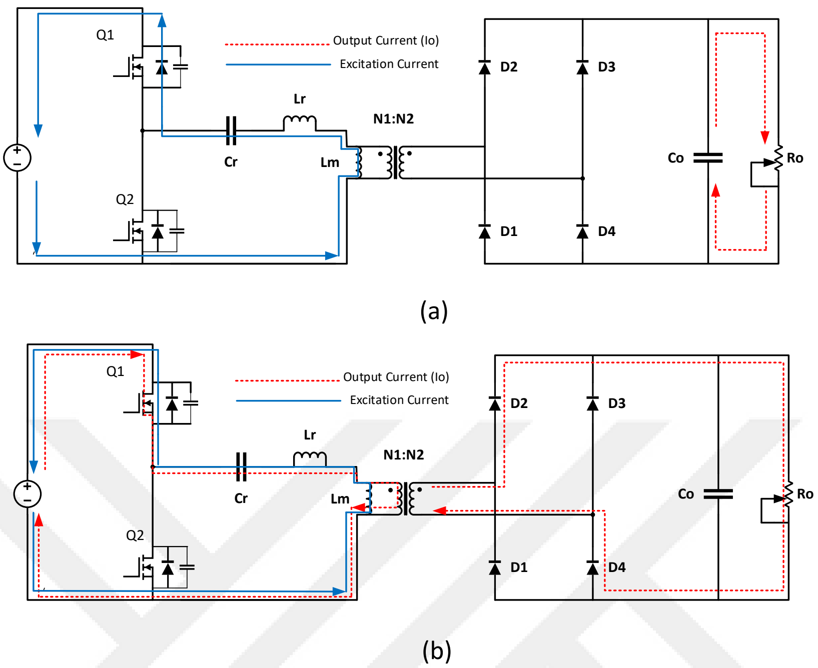


Figure 4.12 LLC resonance converter operation modes; (a) mode 8, (b) mode 1-a.

**Operation Mode 1-a (Q1 is on state Q2 is off state)**

The power switch $Q_1$ on state, while $Q_2$ turns off. The $Q_1$ switch turns on at zero switching voltage (ZVS) when the body diode is freewheeling. When the $Q_1$ switch turns on, the resonant capacitor ($C_r$) acts as a power source and causes current to flow in the primary part of the transformer. In the secondary part, the load current flows through diodes d2 and d4, creating Vo voltage on the load. The output voltage causes a voltage $((N_1 / N_2) * V_o)$ on the magnetic inductance ($L_m$). This voltage causes the magnetic current ($I_m$) to be decayed. Flow diagrams of the current in this operating mode and the activity status of the circuit elements are shown in Figure 12b.

### 4.2.3. Losses Analysis

Mosfet's power losses are calculated as the sum of three different power losses; switching losses, conduction losses and body diode losses of MOSFET.

$$P_{mosf} = P_{sw} + P_{Cond.} + P_{diode} \tag{4.15}$$

The switching losses are calculated as the sum of two different power losses, $P_{on}$ while the switch turn ON and $P_{off}$ when the switch turn OFF.

Mosfet's body diode losses are examined in sum of two power losses: conduction losses and turn-off losses. However, in case of reverse recovery of the body diode, the voltage across the body diode is approximately zero, so the turn of loss of the body diode is eliminated. Therefore, equation 1 can be extended as follows (Daş et al., 2019, Frivaldsky et al., 2013, Ali et al., 2017).

$$P_{mosf} = P_{on} + P_{off.} + P_{cond.} + P_{diode-cond.} \tag{4.16}$$

The relationship between power losses and energy can be defined as follows;

$$\begin{Bmatrix} P_{on} = E_{sw-on} \cdot fsw \\ P_{off} = E_{sw-off} \cdot fsw \end{Bmatrix} \tag{4.17}$$

Here $E_{sw-on}$ is the switch turn-on energy, $E_{sw-off}$ is the switch turn-off energy.

In this case, for the calculation of power losses;

$$E_{sw-on} = \int_0^{ton} v(t) \cdot i(t) \cdot dt \tag{4.18}$$

In this case;

$$i(t) = I_{\max}(\frac{t}{t_{on}}); v(t) = V_{bus}(1-(\frac{t}{t_{on}})) \tag{4.19}$$

Finally;

$$E_{sw-on} = \frac{V_{bus} I_{nax} \cdot t_{on}}{6} \tag{4.20}$$

For the switch turn-off losses

$$E_{sw-off} = \int_{0}^{toff} v(t) \cdot i(t) \cdot dt \tag{4.21}$$

In this case;

$$v(t) = V_{bus} (\frac{t}{t_{off}}); i(t) = I_{\max} (1 - (\frac{t}{t_{off}})) \tag{4.22}$$

Finally;

$$E_{sw-off} = \frac{V_{bus} I_{nax} \cdot t_{off}}{6} \tag{4.23}$$

For the conduction losses calculation;

$$P_{cond.} = I^2{}_{mosf(rms)} \cdot R_{ds-on} \tag{4.24}$$

Here $I_{mosf(rms)}$ represents the rms value of the drain-source current and Rds-on represents the resistance drain-source during on state.

$$P_{diode,cond.} = I_{diode(mean)} \cdot V_f \tag{4.25}$$

Here the $I_{diode\ (mean})$ represents mean value of the body diode current $V_f$ is the forward voltage of the diode.

As a result; Since soft switching (ZVS) is applied to the LLC resonance converter, Esw-on is eliminated and in the last case the loss analysis is calculated as follows;

$$P_{mosf} = P_{off.} + P_{cond.} + P_{diode-cond.} \tag{4.26}$$

## 4.3. ANN Control Method

The operating logic and basic features of artificial neural networks are just like biological neurons. In the most basic way, an artificial neural network algorithm consists of the input layer, the weight part, the summing node, activation function and the output layer. While a simple artificial neural network diagram is shown on the left side of Figure 4.13, the diagram of the artificial neural network designed for this study is shown on the right side.

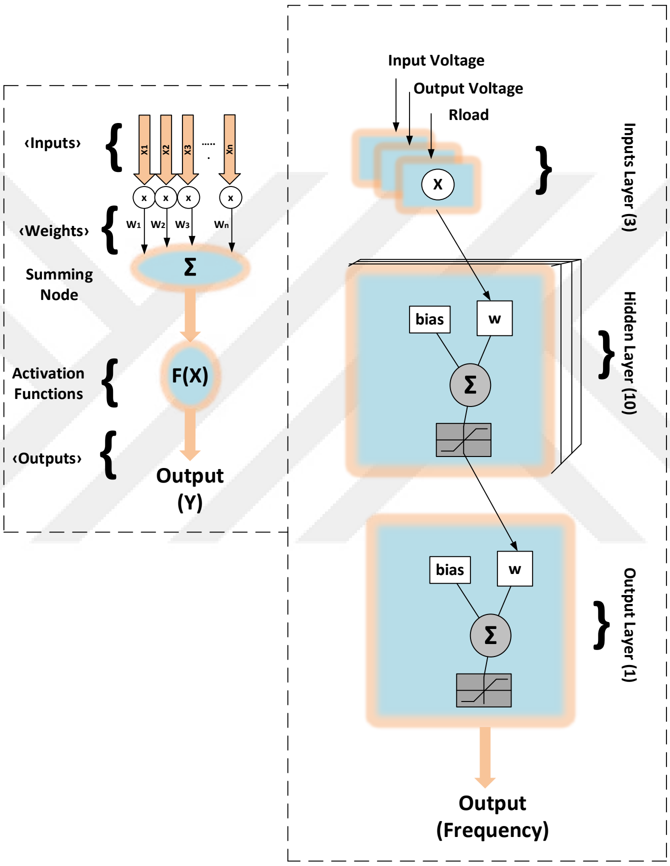


Figure 4.13 Structure of ANN and algorithm for proposed study

In this study, an artificial neural network is designed and applied to control the load voltage of the high efficiency two stage battery charging unit. Levenberg-Marquardt (LM) was used as the activation algorithm of the artificial neural network. Performance indicator for ANN structure is accepted as Mean square error (MSE). If every target desired to be reached in the output layer of the ANN is realized with an equal probability, MSE is expressed as the sum of the squares of the errors on the targets (Q) in the training sets, this situation is detailed with the following mathematical expressions. (Chamjangali et al., 2007, Çelik et al., 2016, Singh et al., 2007).

$$F(x)=\sum_{q=1}^{Q}(t_q-a_q)^T\cdot(t_q-a_q)$$
$$=\sum_{q=1}^{Q}e_q^T\cdot e_q=\sum_{q=1}^{Q}\sum_{j=1}^{S^M}(e_{j,q})^2=\sum_{i=1}^{N}vi^2 \tag{4.27}$$

Where $tq$ is $q$th target value of the function. $a$q is desired $q$th output of the function. $e_{j,q}$ represents $j$th element of the error, for the $q$th input/target pair.

The calculation of the Jacobian matrix in the LM algorithm is a very important step, the backpropagation algorithm is used in this step. While calculating the Jacobian matrix, the operation is performed by taking the derivatives of the errors instead of the derivative of the squares of the errors. (Chamjangali et al., 2007, Çelik et al., 2016, Singh et al., 2007).

$$V^T=[v1,v2,v3...vn]=\left[e_{1,1},e_{2,1}e_{3,1}e_{s^m},..Q\right] \tag{4.28}$$

The parameter vector can be defined as;

$$X^T=[x1,x2,x3...xn]=\left[w^1{}_{1,1},w^1{}_{2,1}w_{3,1}..w^2{}_{s,R},b_1{}^1,b_S{}^1,b_{S^M}{}^M\right] \tag{4.29}$$

Where $w^i_j$ represents the weight and $b_j^i$ represent the bias in order to reduce the error rate between targets and output values, $V$ represents the weight vector of hidden layers.

In order to calculate the backpropagation algorithm following equation is used,

$$\frac{\partial F(x)}{\partial x_1}=\frac{\partial e_q^T e_q}{\partial x_1} \tag{4.30}$$

Calculation of LM is needed for the Jacobian matrix as;

$$[J]_{h,l} = \frac{\partial v_h}{\partial x_1} = \frac{\partial e_{k,q}}{\partial x_1} \tag{4.31}$$

The detailed performance analysis of the Jacobian matrix can be shown in the following mathematical model.

$$\left[\begin{array}{l}
[J]_{h,l} = \dfrac{\partial v_h}{\partial x_1} = \dfrac{\partial e_{k,q}}{\partial w^{m}{}_{i,j}} = \dfrac{\partial e_{k,q}}{\partial n^{m}{}_{ii,q}} \cdot \dfrac{\partial n^{m}{}_{ii,q}}{\partial w^{m}{}_{i,j}} = s^{m}_{i,h} \dfrac{\partial \tilde{\tilde{n}}^{m}{}_{ii,q}}{\partial w^{m}{}_{i,j}} = S^{m}_{i,h} a^{m-1}_{j,q} \\
\text{if } x_1 \text{ is bias;} \\
n^{m}_{i} = \displaystyle\sum_{j=1}^{s^{m-1}} w^{m}_{ij} + b^{m}_{i} \quad \text{So that } \dfrac{\partial n^{m}{}_{i}}{\partial w^{m}{}_{i,j}} = a^{m-1}_{j} \quad \text{and } \dfrac{\partial n^{m}{}_{i}}{\partial b^{m}_{i}} = 1; \\
\text{Finally Marquardt sensitivity layer is;} \\
[J]_{h,l} = \dfrac{\partial v_h}{\partial x_1} = \dfrac{\partial e_{k,q}}{\partial w^{m}{}_{i,j}} = \dfrac{\partial e_{k,q}}{\partial n^{m}{}_{ii,q}} \cdot \dfrac{\partial n^{m}{}_{ii,q}}{\partial w^{m}{}_{i,j}} = S^{m}_{i,h} \dfrac{\partial \tilde{\tilde{n}}^{m}{}_{ii,q}}{\partial w^{m}{}_{i,j}} = S^{m}_{i,h} \\
\text{The Total Marquardt sensitivity is;} \\
S^{m} = \left[ \mathrm{S}^{\mathrm{m}}_{1} \middle| S^{m}_{2} \ldots \middle| S^{m}_{Q} \right]
\end{array}\right] \tag{4.32}$$

Where J(x) is the Jacobian matrix, $e_{k,q}$ is the $q$th error between target and output $k$th element (Chamjangali et al., 2007, Çelik et al., 2016, Singh et al., 2007).

In this study, an artificial neural network controller consisting of three inputs ($R_{Load}$, $V_{dc\text{-}Link}$, $V_{Load}$), single output (switching frequency) and 10 neurons was designed. In addition, Levenberg-Marquardt activation algorithm was used for the designed ANN controller. A two-stage battery charging unit was operated to create a table of 8000 samples. 15% of the samples were used for training and 15% for validation.

The flowchart of the designed ANN controller is shown in detail in figure 7. As stated in the flow diagram, firstly, dc-link voltage, load voltage and dynamic load values should be measured. Then, the measured values should be compared with the reference values. If the reference load voltage is greater than the measured value, the dynamic load and dc-link voltages are compared with the reference values and regulate the switching frequency with the help of the ANN controller activation function and Levenberg-Marquardt algorithm ($fs = fs + \Delta fs$). If the reference load voltage is smaller than the measured value, the dynamic load and dc-link voltages are compared with the reference values and regulate the switching frequency with the help of the ANN controller activation function and Levenberg-Marquardt algorithm ($fs = fs\text{-}\Delta fs$). If the measured load voltage value is equal to the reference value, the controller returns to the top to repeat the operations. The flowchart for the design of the proposed two stage on-board battery charger topology and ANN control based soft switched half-bridge LLC resonance converter is shown in Figure 4.14.

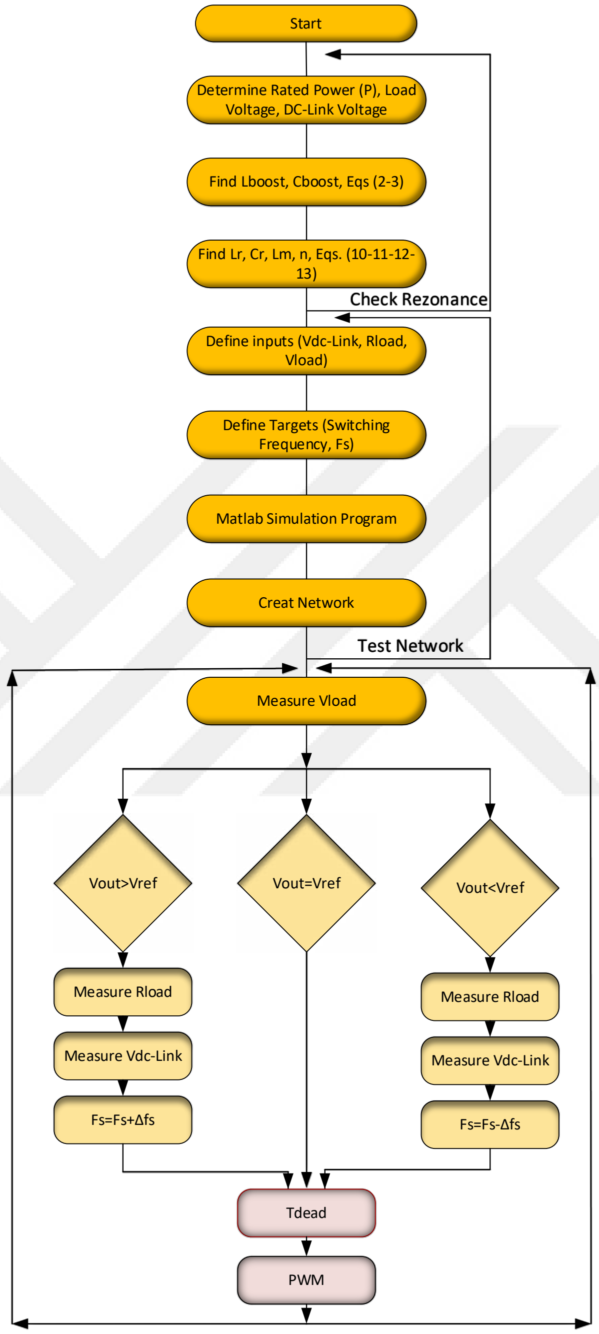


Figure 4.14 Flowchart of the proposed two-stage OBC

The internal structure of the artificial neural network created in the NNtool and GenSim sections of the Matlab simulation program is shown in Figure 4.15. The input layer (Figure 4.15(a)), dc-link voltage, output voltage and variable load (Rload) values are multiplied by weights (Figure 4.15 (b)) and collected with the appropriate bias values (Figure 4.15 (c)) and sent to the second layer. In the second layer (figure 4.15 (d)), the obtained data is multiplied by new weight values and the result added with appropriate bias values and finally switching frequency (fs) is generated at the output.

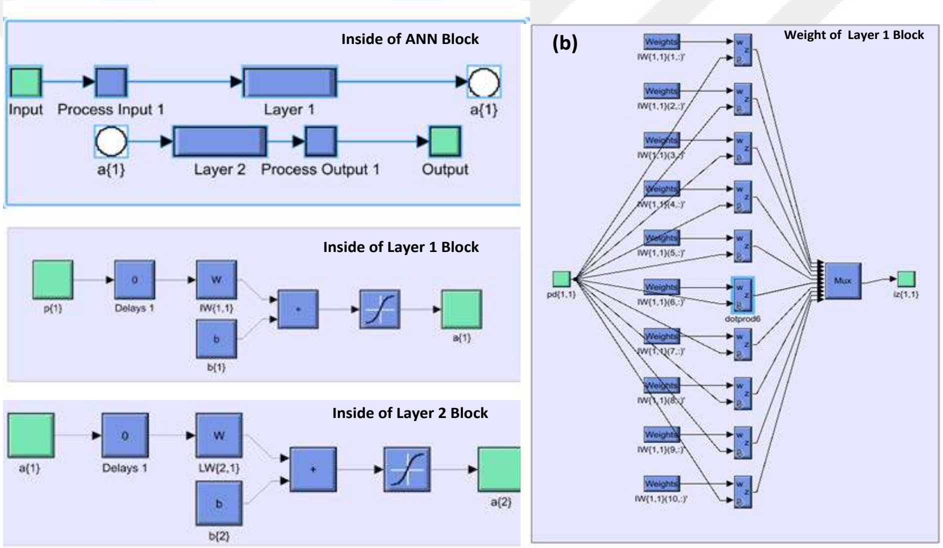


Figure 4.15 ANN block created in Matlab. (a) Network (b) Weight operation (b), (c) Layer 1, (d) Layer 2.

In order to operate the system with ZVS, a dead time is required between the primary side power switches. During this dead-time, the drain-source capacitors of the power switches are charged and discharged. At the same time, the transformer's magnetic inductance current ($I_{Lm}$) circulates between the drain-source capacitors of the power switches and the resonance tank (Alemdar., 2016, Jung et al., 2007).

$$Lm \le \frac{tdead}{16 \cdot Cs(eq) \cdot fsw} \tag{4.33}$$

$$tdead \ge 16 \cdot Lm \cdot Cs(eq) \cdot fsw \Leftrightarrow tdead \ge 16 * 31.536 * 10^{-6} * 12 * 10^{-9} * 85 * 10^{3}$$

$$\Rightarrow tdead \ge 5.146 * 10^{-7}$$

The dead-time interval placed between the PWM signals produced for primary side power switches was created in Matlab / Simulink as shown in figure 4.16.

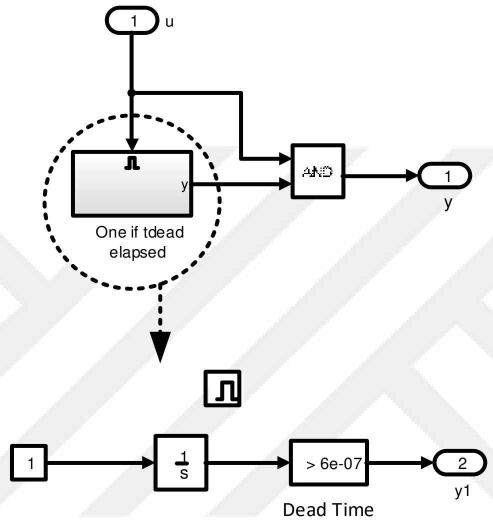


Figure 4.16 Internal structure of Tdead block

### 4.4. Performance Analysis

The proposed two-stage battery charger was operated in six different load states to calculate efficiency according to European efficiency standards.

Table 4.2 operation states of proposed system

| States | State 1 | State 2 | State 3 | State 4 | State 5 | State 6 |
|---|---|---|---|---|---|---|
| Values | %100 Load | %50 Load | %30 Load | %20 Load | %10 Load | %5 Load |

#### 4.4.1. State 1: (100% Load)

The grid voltage and current at full load (100% load) are shown in Figure 4.17. Phase angle ($Q_v$-$Q_i$) between grid voltage and current, power factor and dc-link voltage are shown in Figure 4.18. Switching frequency ($F_s$), load voltage and current of the LLC resonance converter are shown in Figure 4.19. Resonance capacitor current and magnetizing current ($I_{cr}$, $I_m$) of transformer, current of power switch ($I_{DSQ1}$), voltage of power switch ($V_{DSQ1}$), diode current ($I_d$) are shown in Figure 4.20. PWM signals of power switches ($V_{GSQ1}$-$V_{GSQ2}$), switching currents and ZVS operation are presented in Figure 4.21. The harmonic performance of proposed topology and (IEC-3-2-Class D) standards are compared in Figure 4.22.

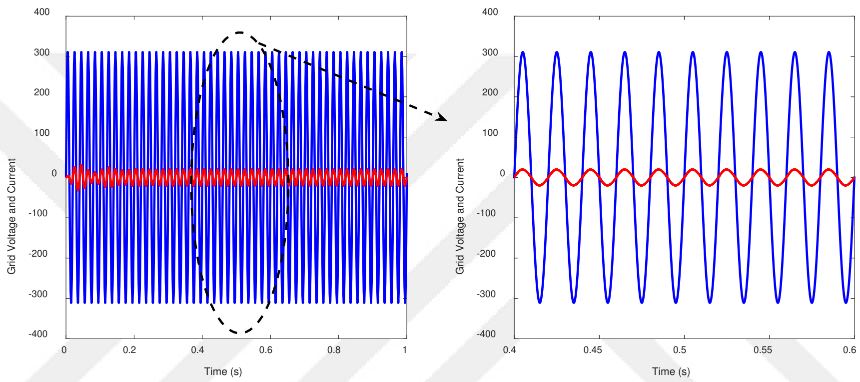


Figure 4.17 Grid voltage and current (100% load)

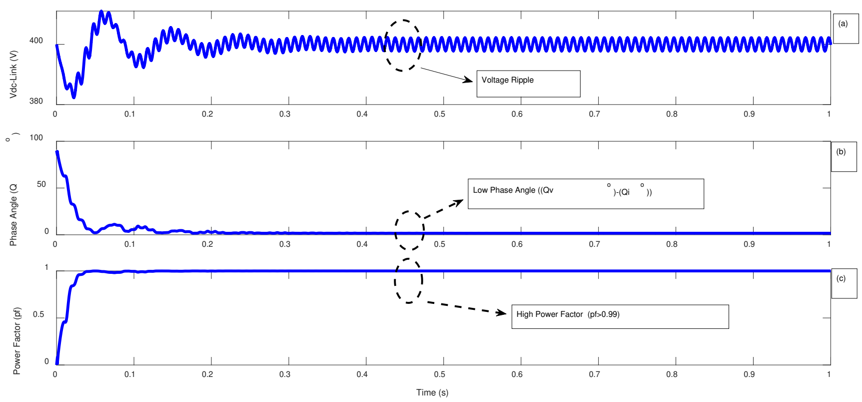


Figure 4.18 DC-Link voltage (a), Phase angle (b), Power factor (c), (100% load)

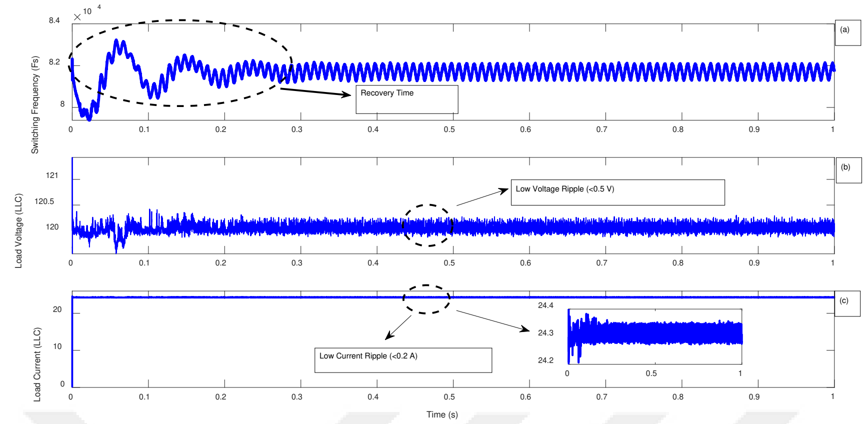


Figure 4.19 Switching frequency (a), Load voltage (b), Load current (c) (100% load)

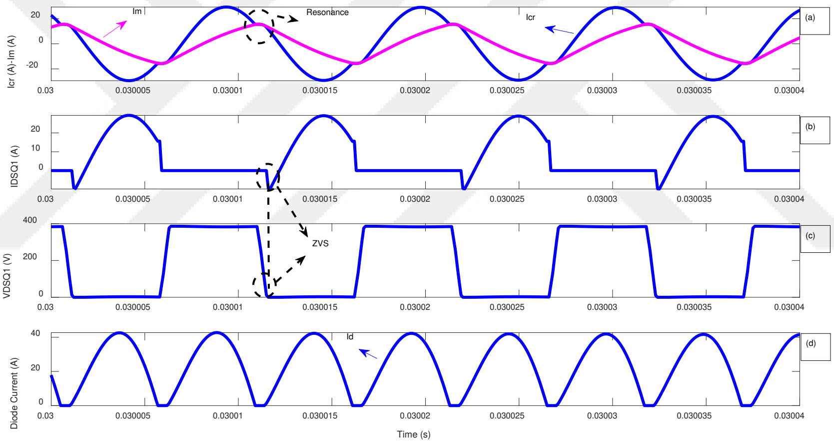


Figure 4.20 Icr and Im (a), IDSQ1 (b), VDSQ1 (c), Idiode (d), (100% load)

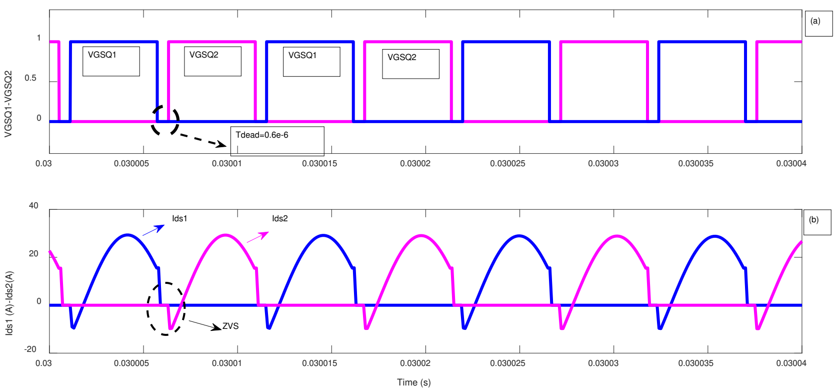


Figure 4.21 VGSQ1-VGSQ2 (a), IDSQ1 and IDSQ2 (b), (100% load)

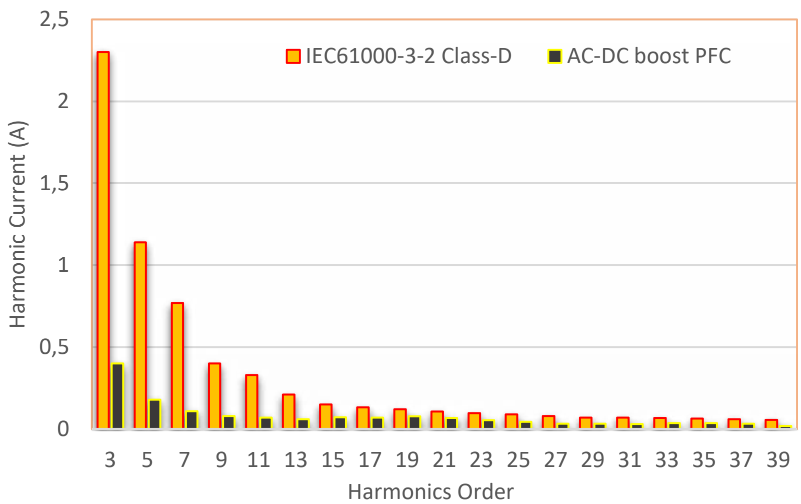


Figure 4.22 Grid current harmonics order (IEC-3-2-Class-D and proposed topology) (100% load)

The electrical properties obtained when the proposed two-stage battery charger is operated at full load are shown in Table 4.3.

Table 4.3. Electrical properties of proposed two stage battery charger (full load)

| State 1 | pf | THD | ΔV(ripple) | Efficiency |
|---|---|---|---|---|
| Full Load | ≥0.99 | ≤IEC61000-3-2-D-Class | <0.5 V | 96.8% |

### 4.4.2. State 2: (50% Load)

The grid voltage and current at 50% Load are shown in Figure 4.23. Phase angle ($Q_v$-$Q_i$) between grid voltage and current, power factor and dc-link voltage are shown in Figure 4.24. Switching frequency (Fs), load voltage and current of the LLC resonance converter are shown in Figure 4.25. Resonance capacitor current and magnetizing current ($I_{cr}$, $I_m$) of transformer, current of power switch ($I_{DSQ1}$), voltage of power switch ($V_{DSQ1}$), diode current ($I_d$) are shown in Figure 4.26. PWM signals of power switches ($V_{GSQ1}$-$V_{GSQ2}$), switching currents and ZVS operation are presented in Figure 4.27. The harmonic performance of proposed topology and (IEC-3-2-Class D) standards are compared in Figure 4.28.

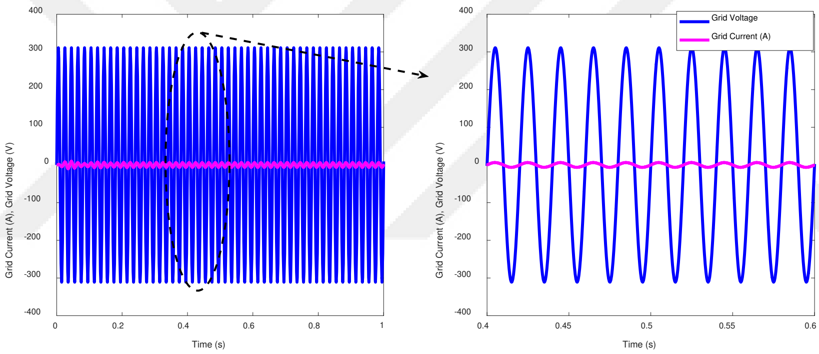


Figure 4.23 Grid voltage and current (50% load)

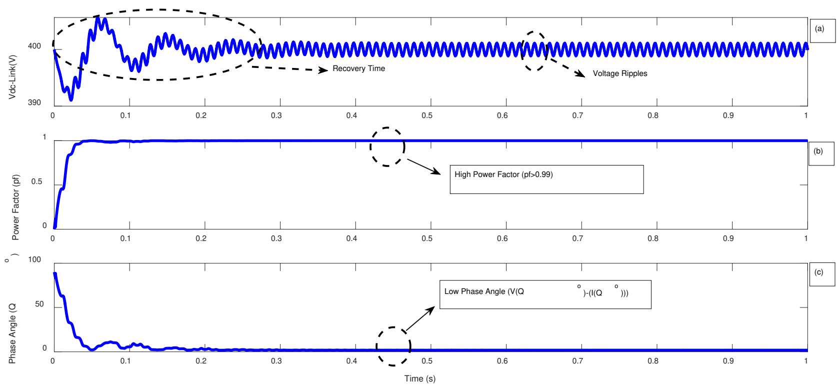


Figure 4.24 DC-Link voltage (a), Power factor (b), Phase angle (c), (50% load)

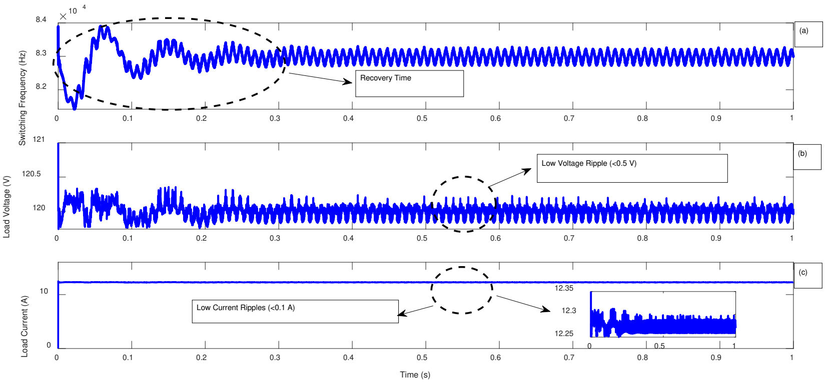


Figure 4.25 Switching frequency (a), Load voltage (b), Load current (c) (50% load)

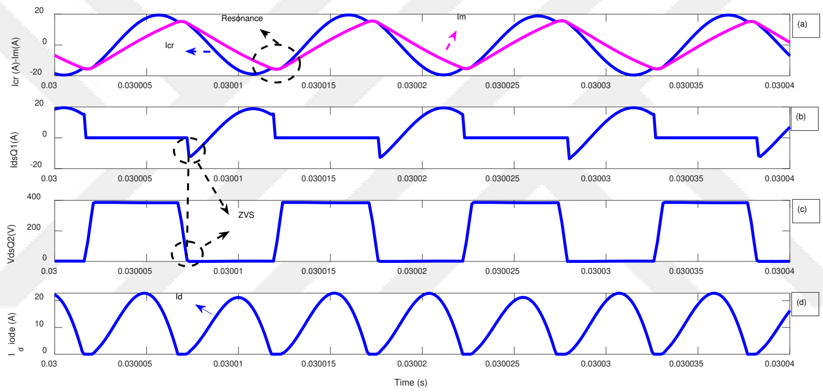


Figure 4.26 Icr and Im (a), IDSQ1 (b), VDSQ1 (c), Idiode (d), (50% load)

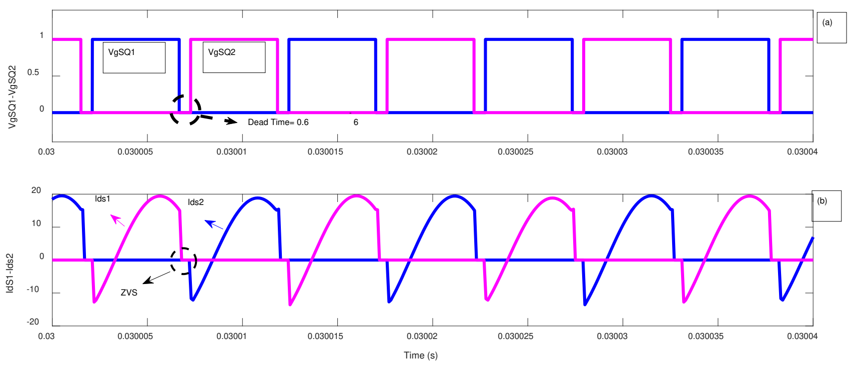


Figure 4.27 VGSQ1-VGSQ2 (a), IDSQ1 and IDSQ2 (b), (50% load)

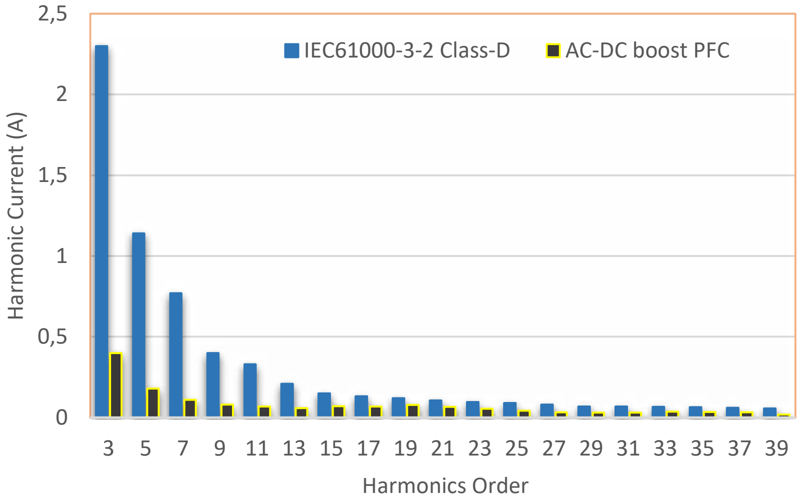


Figure 4.28 Grid current harmonics order (IEC-3-2-Class D and proposed topology) (50% load)

The electrical properties obtained when the proposed two-stage battery charger is operated at 50% load are shown in Table 4.4.

Table 4.4 Electrical properties of proposed two stage battery charger (50% load)

| State 2 | pf | THD | ΔV(ripple) | Efficiency |
|---|---|---|---|---|
| 50% Load | ≥0.99 | ≤IEC61000-3-2-D Class | <0.5 V | 94.1% |

### 4.4.3. State 3: (30% Load)

The grid voltage and current at 30% Load are shown in Figure 4.29. Phase angle ($Q_v$-$Q_i$) between grid voltage and current, power factor and dc-link voltage are shown in Figure 4.30. Switching frequency (Fs), load voltage and current of the LLC resonance converter are shown in Figure 4.31. Resonance capacitor current and magnetizing current ($I_{cr}$, $I_m$) of transformer, current of power switch ($I_{DSQ1}$), voltage of power switch ($V_{DSQ1}$), diode current ($I_d$) are shown in Figure 4.32. PWM signals of power switches ($V_{GSQ1}$-$V_{GSQ2}$), switching currents and ZVS operation are presented in Figure 4.33. The harmonic performance of proposed topology and (IEC-3-2-Class D) standards are compared in Figure 4.34.

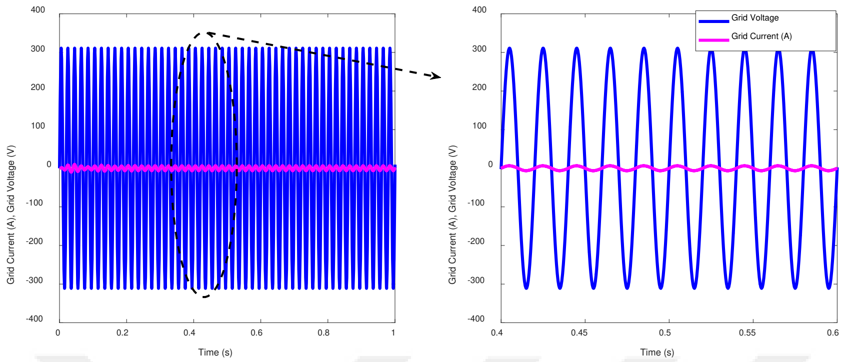


Figure 4.29 Grid voltage and current (30% load)

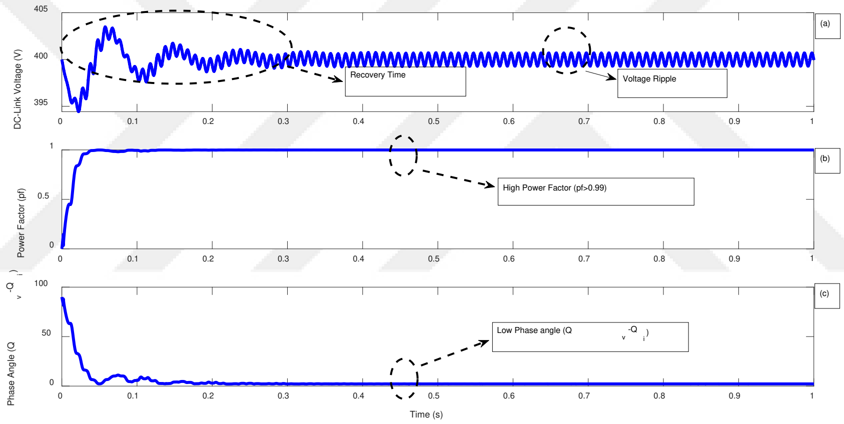


Figure 4.30 DC-Link Voltage (a), Power factor (b), Phase angle (c), (30% load

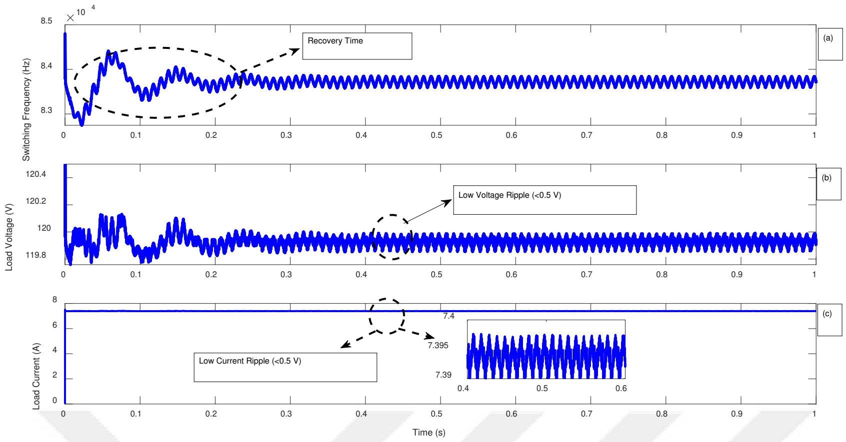


Figure 4.31 Switching frequency (a), Load voltage (b), Load current (c) (30% load)

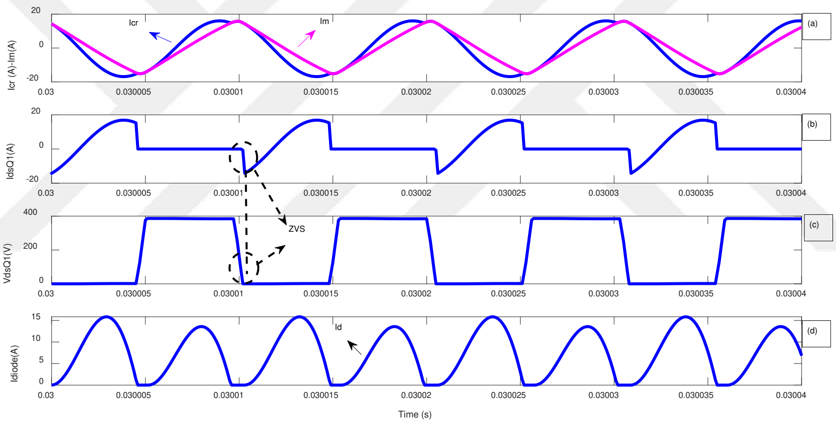


Figure 4.32 Icr and Im (a), IDSQ1 (b), VDSQ1 (c), Idiode (d), (30% load)

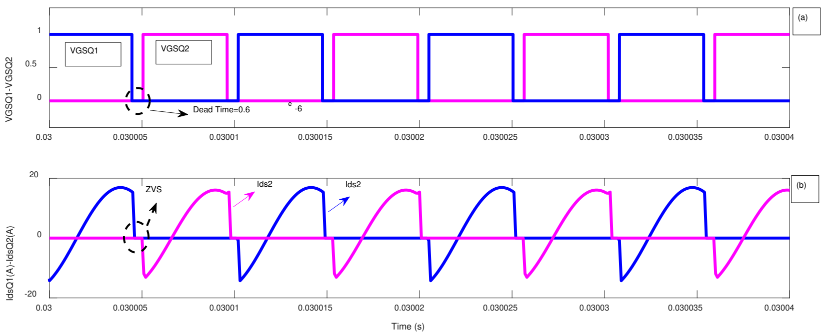


Figure 4.33 VGSQ1-VGSQ2 (a), IDSQ1 and IDSQ2 (b), (30% load)

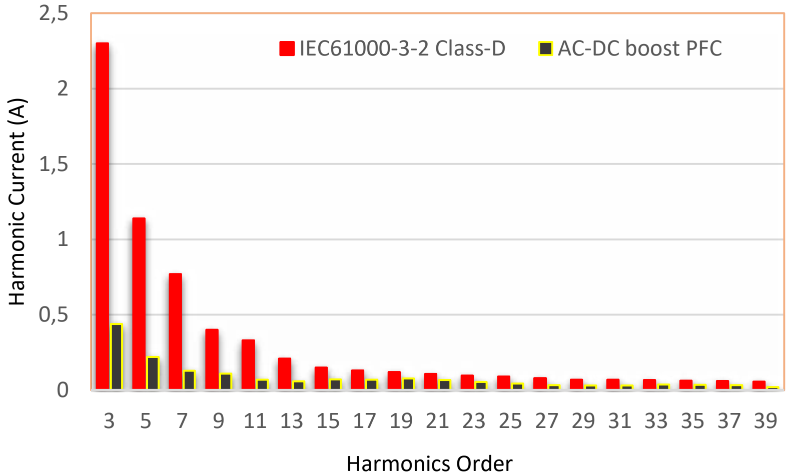


Figure 4.34 Grid Current Harmonics order (IEC-3-2-Class D and proposed topology) (30% load)

The electrical properties obtained when the proposed two-stage battery charger is operated at 30% load are shown in Table 4.5.

Table 4.5. Electrical properties of proposed two stage battery charger (30%-load)

| State 3 | pf | THD | ΔV(ripple) | Efficiency |
|---|---|---|---|---|
| 30% Load | ≥0.99 | ≤IEC61000-3-2-D-Class | <0.5 V | 92.6% |

### 4.4.4. State 4 (20% Load)

The grid voltage and current at 20% load are shown in Figure 4.35. Phase angle ($Q_v$-$Q_i$) between grid voltage and current, power factor and dc-link voltage are shown in Figure 4.36. Switching frequency (Fs), load voltage and current of the LLC resonance converter are shown in Figure 4.37. Resonance capacitor current and magnetizing current ($I_{cr}$, $I_m$) of transformer, current of power switch ($I_{DSQ1}$), voltage of power switch ($V_{DSQ1}$), diode current ($I_d$) are shown in Figure 4.38. PWM signals of power switches ($V_{GSQ1}$-$V_{GSQ2}$), switching currents and ZVS operation are presented in Figure 4.39. The harmonic performance of proposed topology and (IEC-3-2-Class D) standards are compared in Figure 4.40.

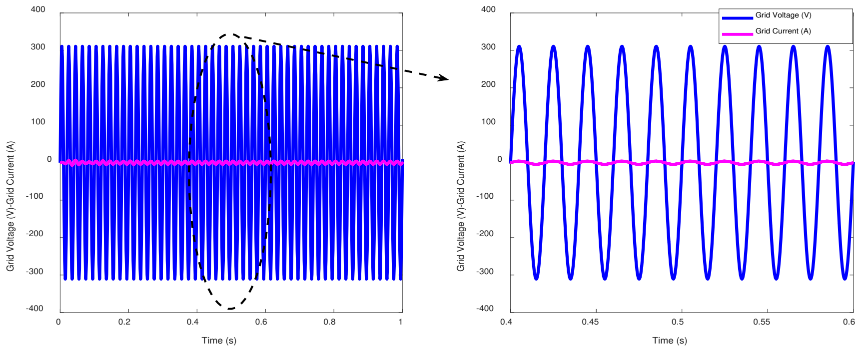


Figure 4.35 Grid Voltage and current (20% load)

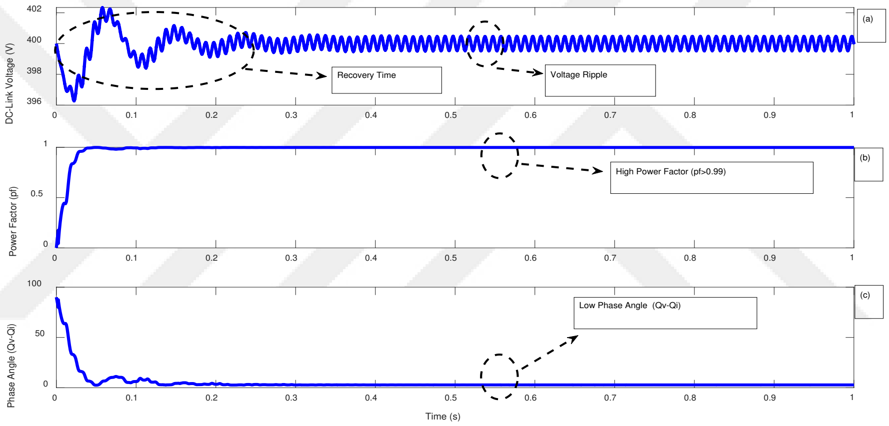


Figure 4.36 DC-Link Voltage (a), Power factor (b), Phase angle (c), (20% load)

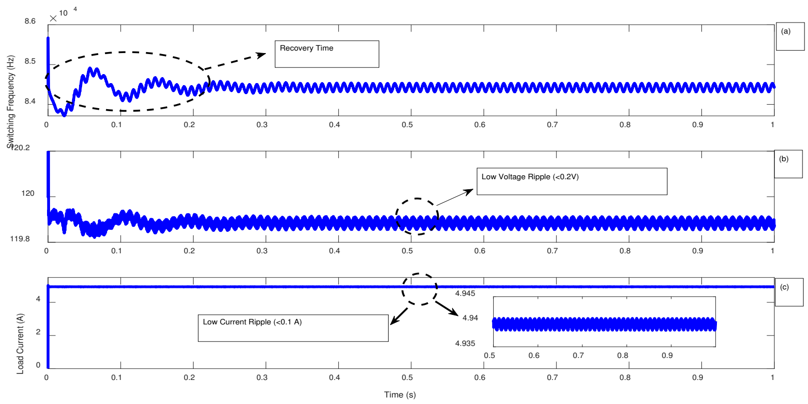


Figure 4.37 Switching frequency (a), Load voltage (b), Load current (c) (20% load)

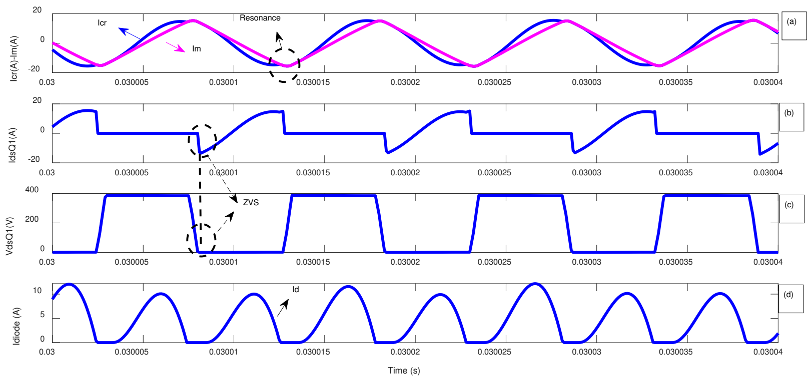


Figure 4.38 Icr and Im (a), IDSQ1 (b), VDSQ1 (c), Idiode (d), (20% load)

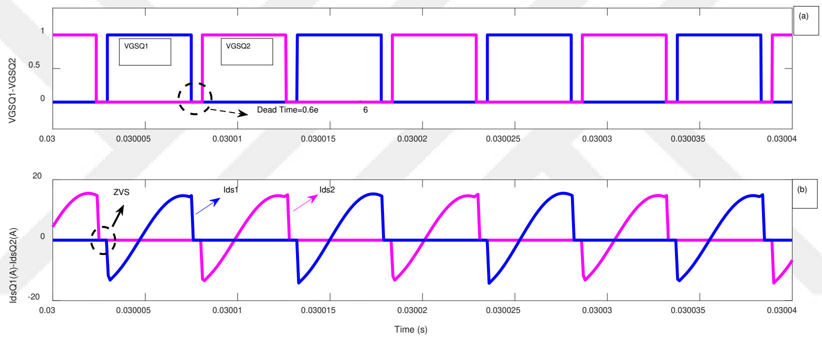


Figure 4.39 VGSQ1-VGSQ2 (a), IDSQ1 and IDSQ2 (b), (20% load)

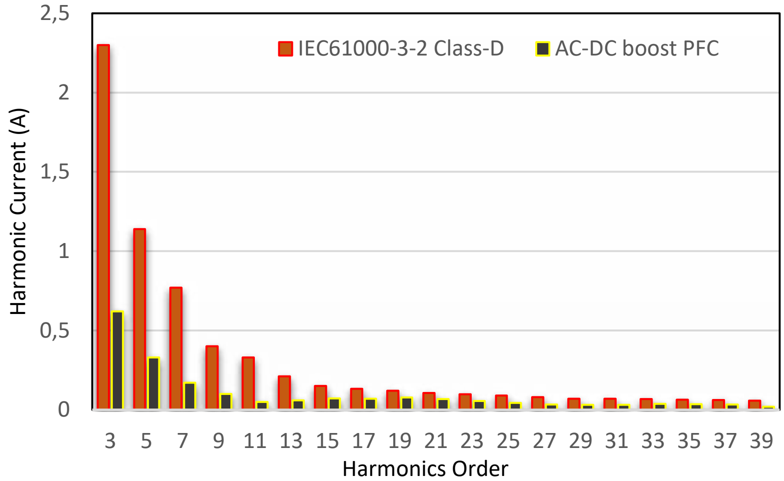


Figure 4.40 Grid current harmonics order (IEC-3-2-Class D and proposed topology) (20% load)

The electrical properties obtained when the proposed two-stage battery charger is operated at 20% load are shown in Table 4.6.

Table 4.6 Electrical properties of proposed two stage battery charger (20%-load)

| State 4 | pf | THD | ΔV(ripple) | Efficiency |
|---|---|---|---|---|
| 20% Load | ≥0.99 | ≤IEC61000-3-2-D-Class | <0.5 V | 91.3% |

### 4.4.5. State 5 (10% Load)

The grid voltage and current at 10% load are shown in Figure 4.41. Phase angle ($Q_v$-$Q_i$) between grid voltage and current, power factor and dc-link voltage are shown in Figure 4.42. Switching frequency (Fs), load voltage and current of the LLC resonance converter are shown in Figure 4.43. Resonance capacitor current and magnetizing current ($I_{cr}$, $I_m$) of transformer, current of power switch ($I_{DSQ1}$), voltage of power switch ($V_{DSQ1}$), diode current ($I_d$) are shown in Figure 4.44. PWM signals of power switches ($V_{GSQ1}$-$V_{GSQ2}$), switching currents and ZVS operation are presented in Figure 4.45. The harmonic performance of proposed topology and (IEC-3-2-Class D) standards are compared in Figure 4.46.

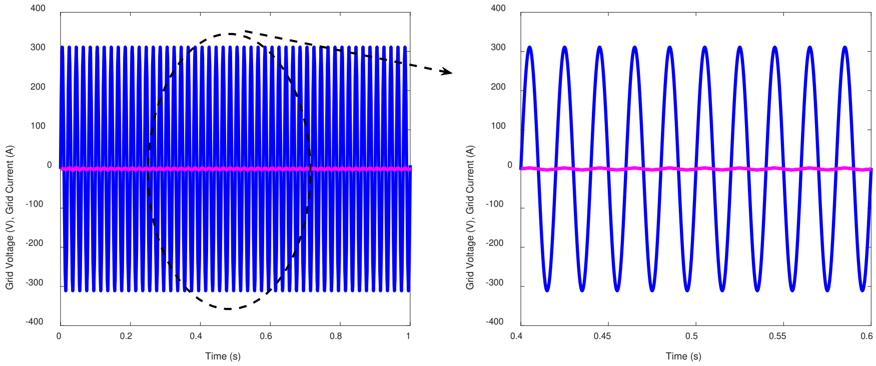


Figure 4.41 Grid voltage and current (10% load)

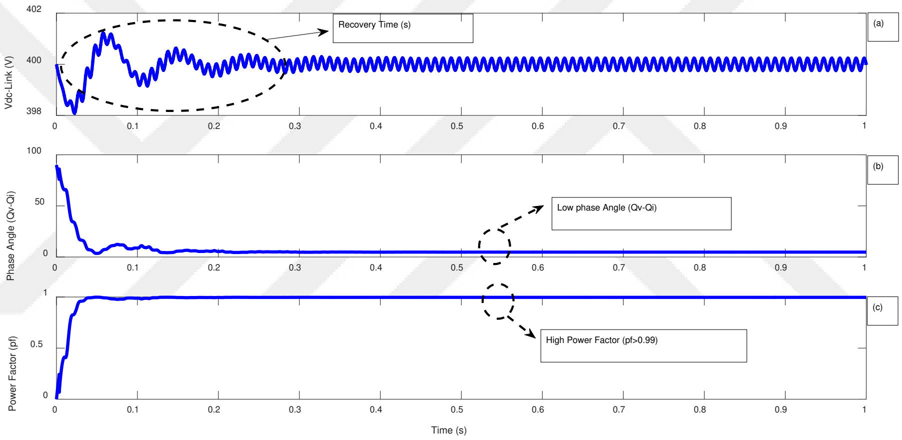


Figure 4.42 DC-Link voltage (a), Phase angle (c), Power factor (b), (10% load)

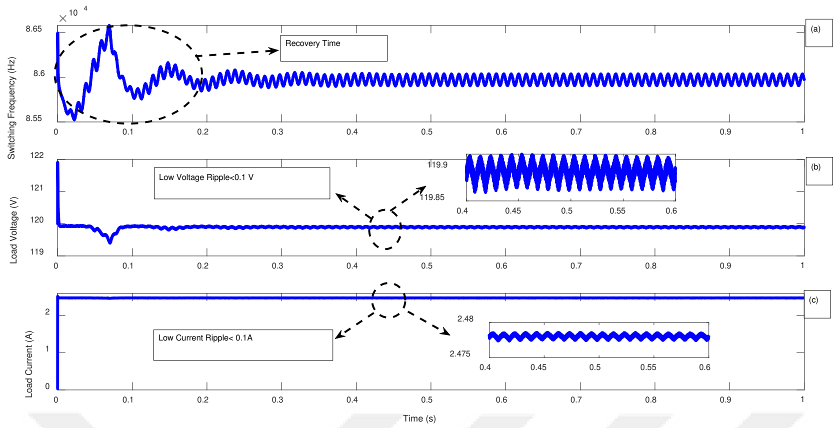


Figure 4.43 Switching frequency (a), Load voltage (b), Load current (c) (10% load)

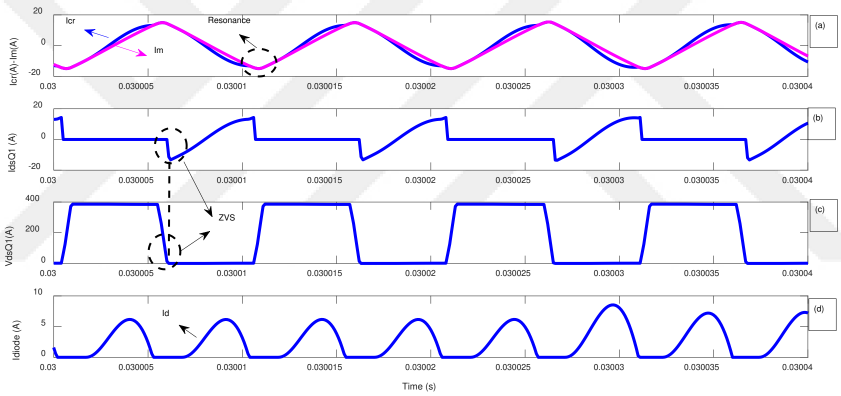


Figure 4.44 Icr and Im (a), IDSQ1 (b), VDSQ1 (c), Idiode (d), (10% load)

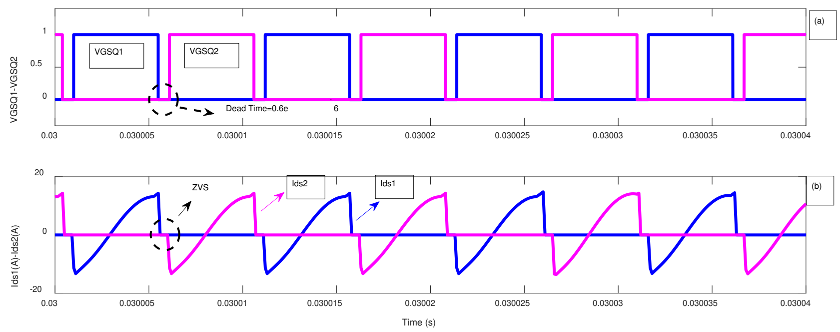


Figure 4.45 VGSQ1-VGSQ2 (a), IDSQ1 and IDSQ2 (b), (10% load)

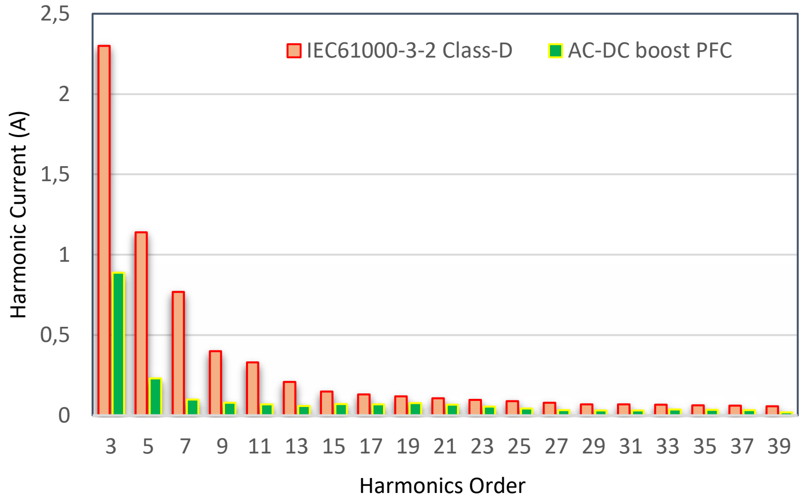


Figure 4.46 Grid current harmonics order (IEC-3-2-Class D and proposed topology) (10% load)

The electrical properties obtained when the proposed two-stage battery charger is operated at 10% load are shown in Table 4.7.

Table 4.7. Electrical properties of proposed two stage battery charger (10%-load)

| State 5 | pf | THD | ΔV(ripple) | Efficiency |
|---|---|---|---|---|
| 10 % Load | ≥0.99 | ≤IEC61000-3-2-D-Class | <0.5 V | 87.6% |

### 4.4.6. State 6 (5% Load)

The grid voltage and current at 5% Load are shown in Figure 4.47. Phase angle ($Q_v$-$Q_i$) between grid voltage and current, power factor and dc-link voltage are shown in Figure 4.48. Switching frequency (Fs), load voltage and current of the LLC resonance converter are shown in Figure 4.49. Resonance capacitor current and magnetizing current ($I_{cr}$, $I_m$) of transformer, current of power switch ($I_{DSQ1}$), voltage of power switch ($V_{DSQ1}$), diode current ($I_d$) are shown in Figure 4.50. PWM signals of power switches ($V_{GSQ1}$-$V_{GSQ2}$), switching currents and ZVS operation are presented in Figure 4.51. The harmonic performance of proposed topology and (IEC-3-2-Class D) standards are compared in Figure 4.52.

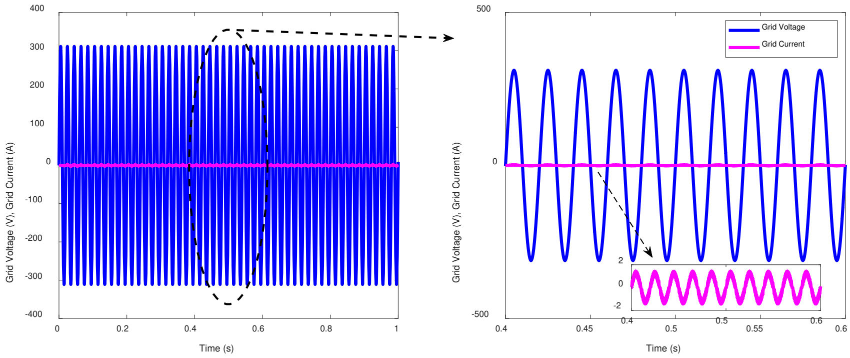


Figure 4.47 Grid voltage and current (5% load)

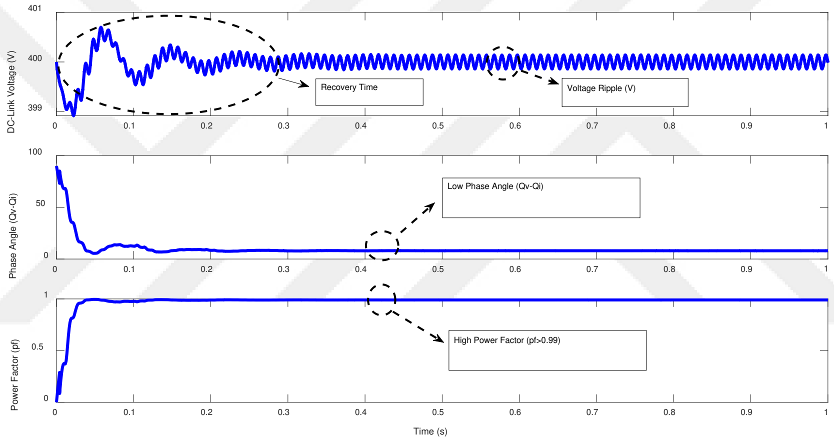


Figure 4.48 DC-Link voltage (a), Phase angle (c), Power factor (b), (5% load)

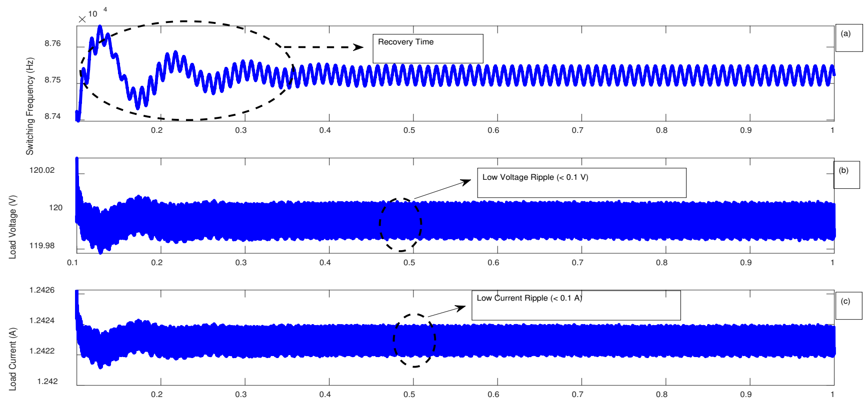


Figure 4.49 Switching frequency (a), Load voltage (b), Load current (c) (5% load)

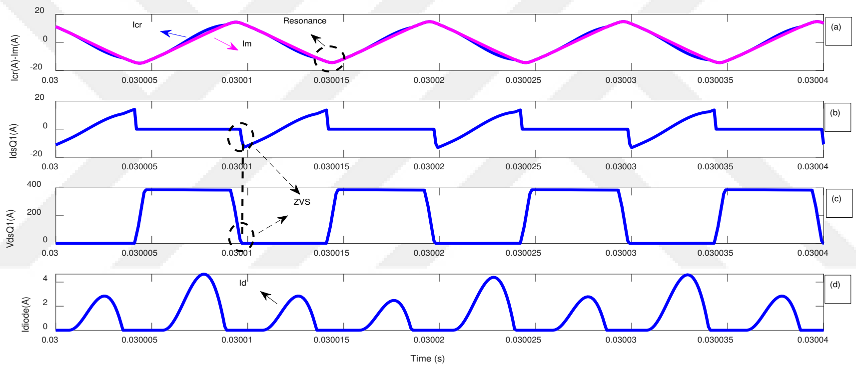


Figure 4.50 Icr and Im (a), IDSQ1 (b), VDSQ1 (c), Idiode (d), (5% load)

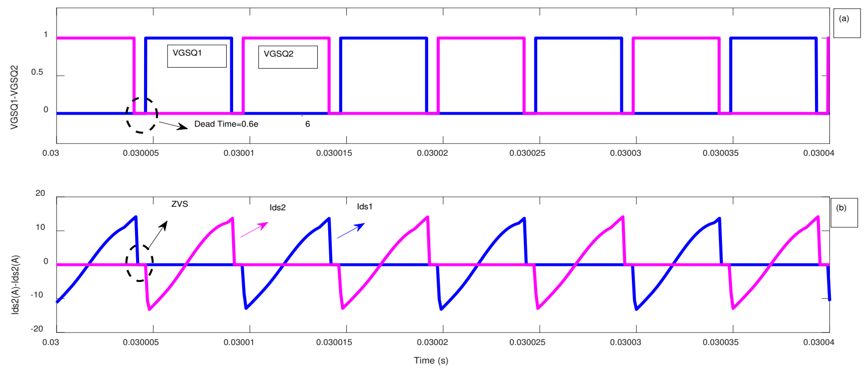


Figure 4.51 VGSQ1-VGSQ2 (a), IDSQ1 and IDSQ2 (b), (5% load)

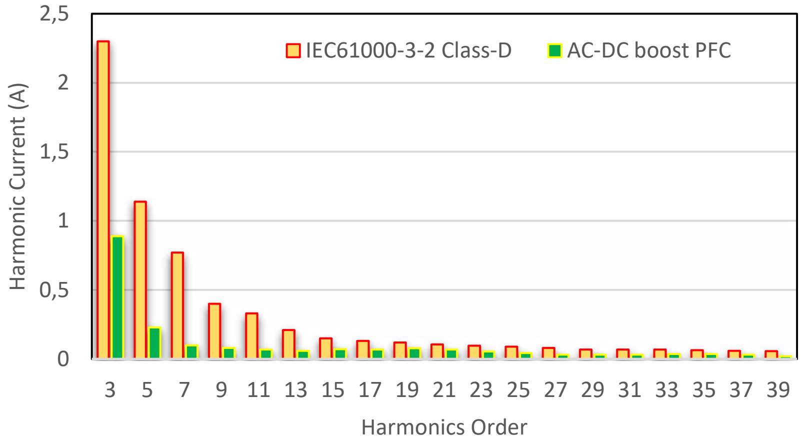


Figure 4.52 Grid current harmonics order (IEC-3-2-class D and proposed topology) (5% load)

The electrical properties obtained when the proposed two-stage battery charger is operated at 5% load are shown in Table 4.8.

Table 4.8 Electrical properties of proposed two stage battery charger (5% load)

| State 6 | pf | THD | ΔV(ripple) | Efficiency |
|---|---|---|---|---|
| 5 % Load | ≥0.9 | ≤IEC61000-3-2-D-Class | <0.5 V | 84.2% |

ANN-controlled two-stage battery charging unit, where all the situations are examined at the same time, and the load voltage, current and switching frequency are shown in Figure 4.53.

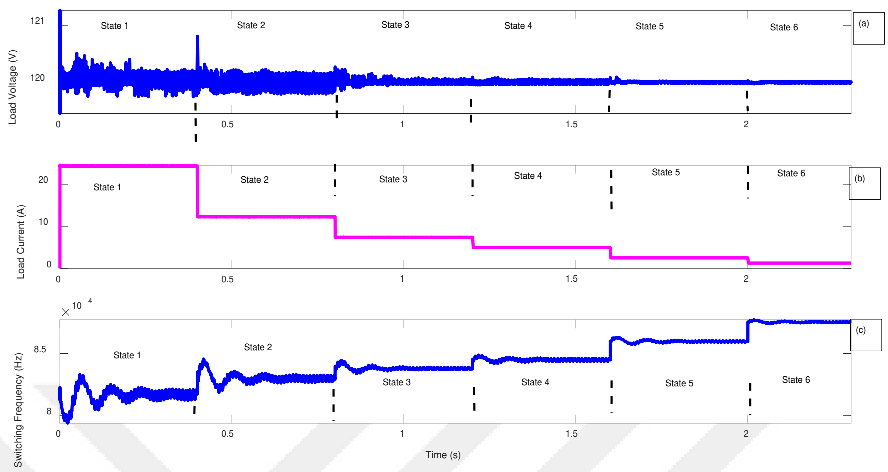


Figure 4.53 Load voltage (a), load current (b), switching frequency (c)

ANN control and conventional pi control were applied to the proposed topology, and when examined for all cases, ANN control's dynamic response and steady-state error were observed to be better than conventional pi control. The findings are presented in Figure 4.54.

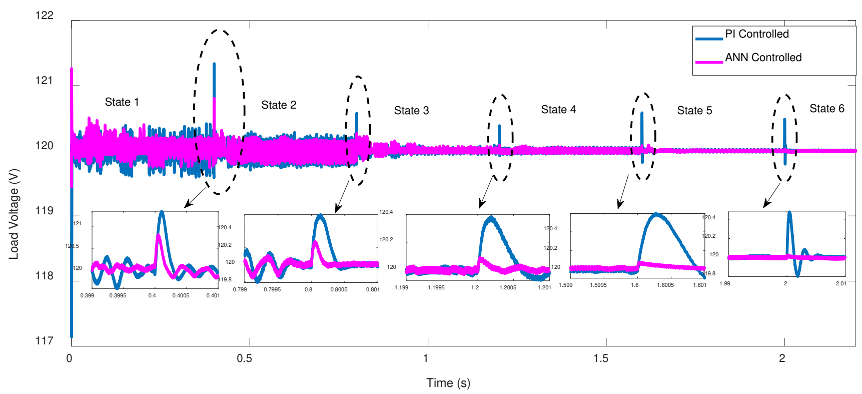


Figure 4.54 Dynamic response of ANN control and traditional pi control and steady-state error

ANN-controlled two-stage battery charging unit, where all the situations are examined at the same time, and the dc-link voltage and current are shown in figure 4.55.

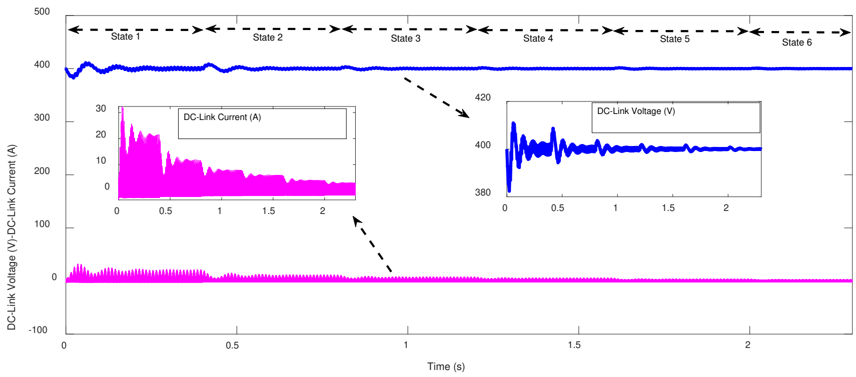


Figure 4.55 DC-link voltage and current for all states.

ANN-controlled two-stage battery charging unit, where all the situations are examined at the same time, and the grid voltage and current are shown in figure 4.56.

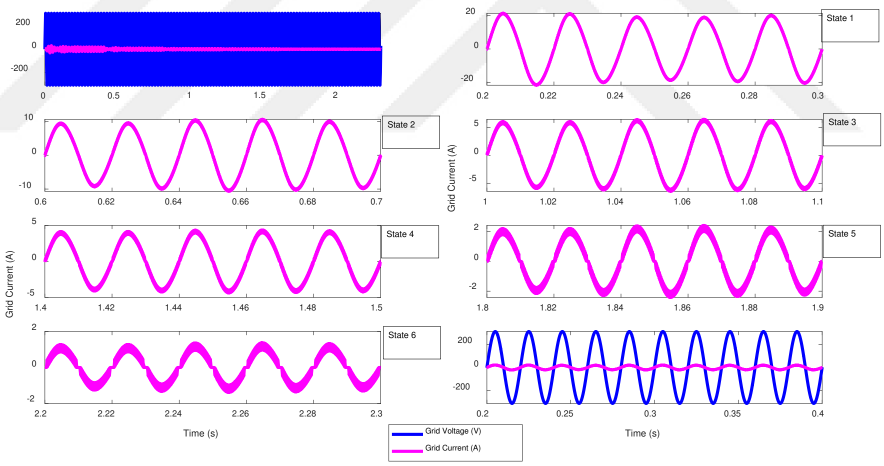


Figure 4.56 Grid voltage-current for all states

For proposed two-stage battery charger topology, load voltage controller, the designed ANN with feed-forward back propagation and Levenberg-Marquardt activation algorithm performance is demonstrated in Figure 4.57, by 99% accuracy.

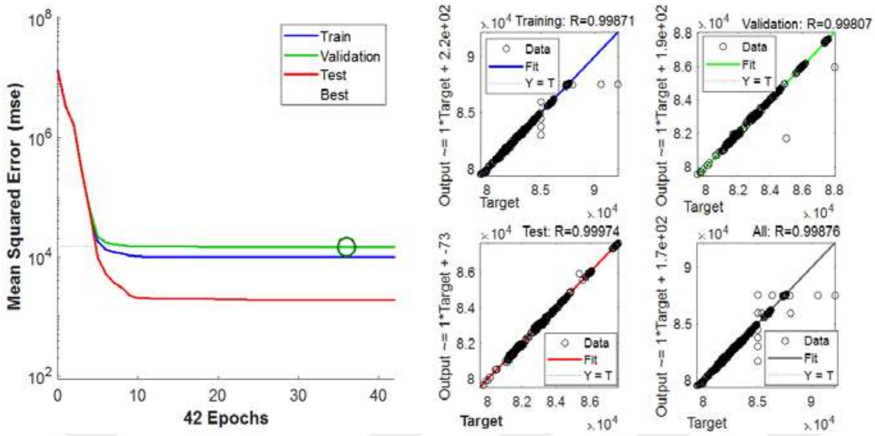


Figure 4.57 MSE and regression performance of the ANN controller

The efficiency, load voltage ripples, dc-link voltage ripples, of the system are given in Figure 4.58, under six different states. The peak efficiency of the two stage battery charger is measured as 96.8% and the maximum load voltage ripple is measured as lower than 1-volt and the maximum dc-link voltage ripples is measured as lower than 10-Volt. According to European efficiency standards, the system operated under six variable states (5%, 10%, 20%, 30%, 50%, 100%) and the peak efficiencies of each state are calculated separately. Efficiency is obtained by the ratio of output power to input power;

$$E\eta = \frac{P_{OUT}}{P_{IN}} * 100 \tag{4.34}$$

The European efficiency of the system calculated by the following equation.

$$\begin{aligned} EU\eta &= 0.03\eta_{\%5} + 0.06\eta_{\%10} + 0.13\eta_{\%20} + 0.1\eta_{\%30} + 0.48\eta_{\%50} + 0.2\eta_{\%100} \\ EU\eta &= 84.2*0.03 + 87.6*0.06 + 91.3*0.13 + 92.6*0.1 + 94.1*0.48 + 0.2*96.8 \\ EU\eta &= 93{,}4\% \end{aligned} \tag{4.35}$$

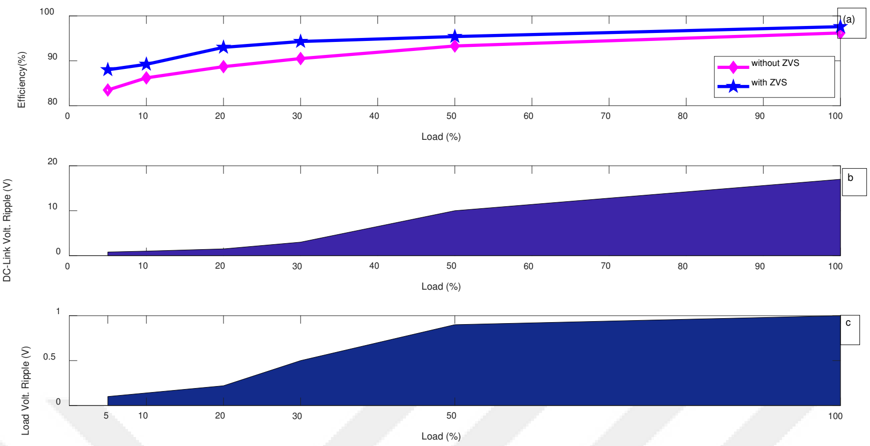


Figure 4.58 Two stage battery charger efficiency (a), DC-link voltage ripple, load voltage ripple (c),

The system designing parameters values and ANN control characteristics are given in Table 4.9 and Table 4.10.

Table 4.9 System parameters and values

| **Parameters** | **Values** | **Parameters** | **Values** |
|---|---|---|---|
| Vin (PFC) | 240 V | $R_{load}$ | 4.84Ω-96.96Ω |
| Frequency (PFC) | 50 Hz | $V_{out}$ | 120 V |
| Vin (LLC) | 365-420 V | Kp | 0.33 |
| Power (kW) | 3.3 kW (Level-2) | Ki | 74.66 |
| Lr | 11.57 µH | THD | <5% |
| Cr | 302.82nF | pf | >0.99 |
| Lm | 31.573 µH | fp | 57 KHz |
| fr | 85 KHz | Lboost | 0.6 mH |
| Cboost | 500 µF | Cdc-link | 984 µF |

Table 4.10 ANN control characteristics

| **Parameters** | **Values** |
|---|---|
| Network Type | Feed-Forward Backprop. |
| Input Data | $V_{Load}$, $R_{Load}$, $V_{dc\text{-}Link}$ |
| Target Data | $F_{switching}$ |
| Training Function | TrainLM |
| Adaption Learning Function | LEARNGDM |
| Performance Function | MSE |
| Number of Layers | 3 |
| Number of Neurons | 10 |
| Trasfer Function | TANSIG |
| Mu | 0.001 |
| Mu_dec | 0.1 |
| Mu_inc | 10 |
| Logging Data Decimation | 4000 |
| Epoch | 1000 (42) |

### 4.5. Discussion

In this study, a two-stage battery charging unit topology is designed. The LLC resonance transducer capable of soft switching (ZVS) for the proposed system has been controlled with a controller designed with artificial neural networks. It has been determined that problems such as dynamic response of traditional pi controller and steady state error are reduced (Figure 4.56. In addition, it is anticipated that the system can perform at higher power density, less switching losses and lower EMI conditions by designing a soft switched LLC resonance converter. Maximum efficiency of the proposed system was measured as 96.8%. In addition, when analyzed according to European efficiency standards, the efficiency of the system was calculated as 92.3%. It has been observed that the proposed system complies with the recommended IEC-3-2-Class D harmonic standards for the battery charging unit of electric vehicles, from light load to full load.

# 5. PROPOSED BATTERY CHARGER ARCHITECTURE

In this study, a two-stage battery charger architecture that can be powered both from the grid and a renewable energy source, was developed. A half-bridge LLC resonance (HBLLC) DC-DC converter is designed for the proposed battery charger and has been tested in a wide load range (5% load to 100% load). The first input of the HBLLC resonant converter is powered from the bridgeless PFC converter connected to the grid, while the other input is powered from the photovoltaic (PV) system. Moreover, in this study, for PV system, a maximum power point tracking (MPPT) method with higher accuracy and lower convergence time than traditional methods, was developed. On the other hand, the first output of the HBLLC resonance converter connected to the high power battery, while the other output connected to the auxiliary battery that feeds low power loads. In conventional battery chargers, the auxiliary battery is powered by the high power battery. In the proposed operation, the auxiliary battery is charged by the PV system. Thus, the high power battery has more energy to power the electric motor and allows the electric vehicle to travel more miles with a single charge process. In addition, the proposed architecture can save energy costs demanded from the grid in the long term. Another advantage of the proposed battery charge architecture is creating a compact structure to save extra cable cost. The proposed two-stage battery charger architecture is shown in Figure 5.1.

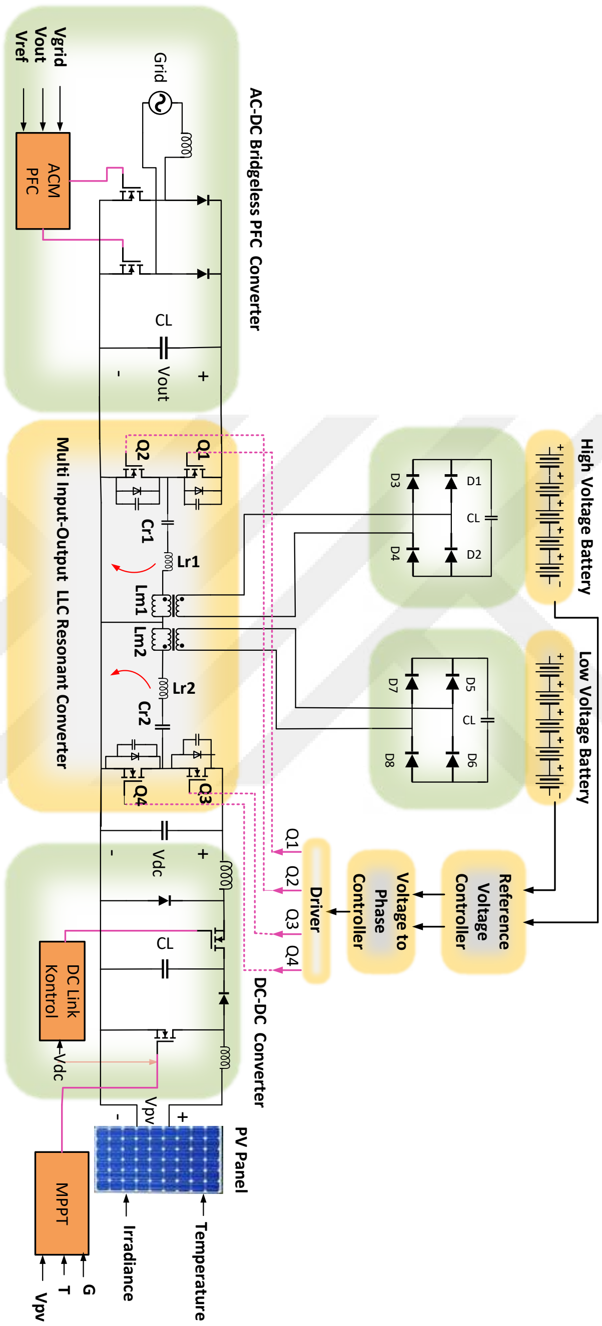


Figure 5.1 Proposed two stage battery charger architecture

## 5.1. PV Systems

The first stage of the proposed battery charging unit consists of the PV-fed LLC resonant converter with the developed MPPT method. PV panels are renewable energy sources created by connecting solar cells in series and parallel. The single-diode equivalent circuit of the solar cell, which is used most in the literature, is shown in Figure 5.2.

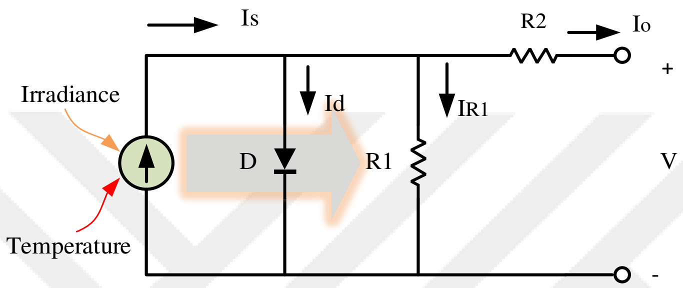


Figure 5.2 Single diode equivalent circuit of the solar cell.

The first resistance ($R_1$) seen in the solar cell equivalent circuit represents the loss of the small leakage current (High-value kΩ), the second resistance ($R_2$) represents the metal losses in the solar cell (about 1Ω) (Yilmaz et al., 2019).

$$I_o = I_s - I_d - I_{R1} \tag{5.1}$$

$$I_d = I_0 \cdot \left( e^{q \cdot \frac{(V + IR_S)}{nKT}} - 1 \right) \tag{5.2}$$

In order tor represent the electrical characteristics; the electron charge value *q*, the Boltzmann constant $K$ ($1.38 \times 10^{-23} J/K$), reverse saturation current $I_o$, and diode factor *n*.

$$I_{ph} = \frac{G}{G_{stc}} \left( I_{sc,ref} + \mu_{sc} \cdot \left( T - T_{stc} \right) \right) \tag{5.3}$$

Where $\mu_{sc}$ is the temperature coefficient (short-circuit current), $I_{sc,ref}$ is the reference short circuit current, $T$ is p-n junction temperature (Yilmaz et al., 2019).

DC electric power obtained from PV panels is affected by environmental conditions such as temperature and radiation. The effect of radiation and temperature on the electrical characteristics of PV panels is shown in detail in Figure 5.3.

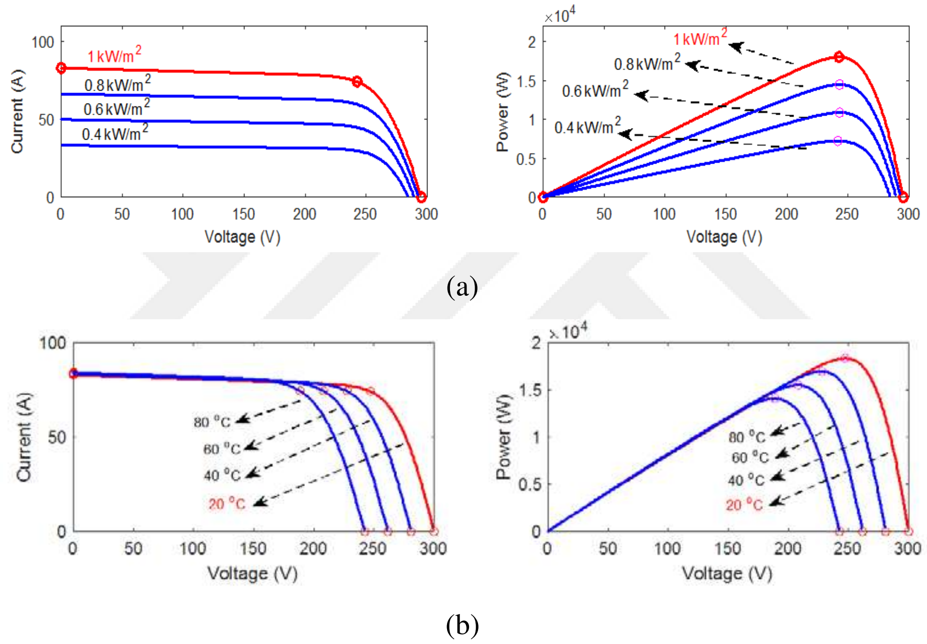


Figure 5.3 (a) Power-voltage and current-voltage characteristics of PV array (variable temperature ˚C), (b) Power-voltage and current-voltage characteristics of PV array (variable irradiance, W/m2).

### 5.1.1. MPPT Methods and Proposed Model

There are many MPPT methods developed in the literature to obtain maximum power from PV panels under different radiation and temperature conditions. These methods are; differ in accuracy rate, easy applicability, convergence rate and cost. One of the most widely used MPPT methods in the literature is the P&O method. Although the P&O method has important features such as easy applicability and low cost, it remains unstable to react under different environmental conditions, as it releases continuously around the maximum power point, resulting in loss of power and hence efficiency. The following equations form the basis of the P&O method (Ahmed et al., 2015, Abdelsalam et al., 2011, Elgendy et al., 2012)

$$\begin{aligned} \mathrm{V_{new}} &= \mathrm{V_{old}} + \Delta\mathrm{V} \times \mathrm{Slope} \Rightarrow if\,(P > P_{old}) \\ \mathrm{V_{new}} &= \mathrm{V_{old}} - \Delta\mathrm{V} \times \mathrm{Slope} \Rightarrow if\,(P < P_{old}) \end{aligned} \tag{5.4}$$

Another traditional MPPT method is the Incremental conductance algorithm. The Incremental conductance algorithm, just like the P&O method, is easy to install and cost-effective. However, as it is oscillating around the maximum power point, as in the P&O algorithm, it causes loss of power and decrease in efficiency. However, many researchers state that the Incremental conductance method gives better results under variable environmental conditions than P&O algorithm. The following equations form the basis of the incremental conductance algorithm (Tey et al., 2014, Elgendy et al., 2013, Yilmaz et al., 2020)

$$\begin{bmatrix} \dfrac{dP}{dV} > 0 \Leftrightarrow \dfrac{dI}{dV} > \dfrac{-I}{V} \Rightarrow \textit{left side of MPP} \\ \dfrac{dP}{dV} < 0 \Leftrightarrow \dfrac{dI}{dV} < \dfrac{-I}{V} \Rightarrow \textit{right side of MPP} \\ \dfrac{dP}{dV} = 0 \Leftrightarrow \dfrac{dI}{dV} = \dfrac{-I}{V} \Rightarrow \textit{ at the MPP} \end{bmatrix} \tag{5.5}$$

where $V$ is the PV terminal voltage, $P$ represents the PV generated power and $I$ represents PV panel current.

The fuzzy logic MPPT (FLC) method has a high convergence rate and there is no oscillation problem at the maximum power point. However, the cost is higher than the other traditional methods because of the need for high speed microprocessors. The following equations form the basis of the FLC method (Guenounou et al., 2011, Salah et al., 2011, Bendib et al., 2014).

$$\begin{bmatrix} E_{(k)} = \dfrac{\Delta P}{\Delta V} = \dfrac{P_{(k)} - P_{(k-1)}}{V_{(k)} - V_{(k-1)}} \\ CE = E_{(k)} - E_{(k-1)} \end{bmatrix} \tag{5.6}$$

where $E_{(k)}$ represents an error (the slope of P-V characteristics) and *CE* represents the change of error.

In the proposed MPPT method, the MPP voltage of the PV panel varies according to the variable environmental conditions, this amount of change was calculated by making use of the PV panel characteristic equations. In addition, the method was created by taking advantage of the speed of the fuzzy logic algorithm. Thus, a faster and higher accuracy MPPT method was developed than traditional methods. The operation principle of the proposed MPPT method is shown in detail in Figure 5.4.

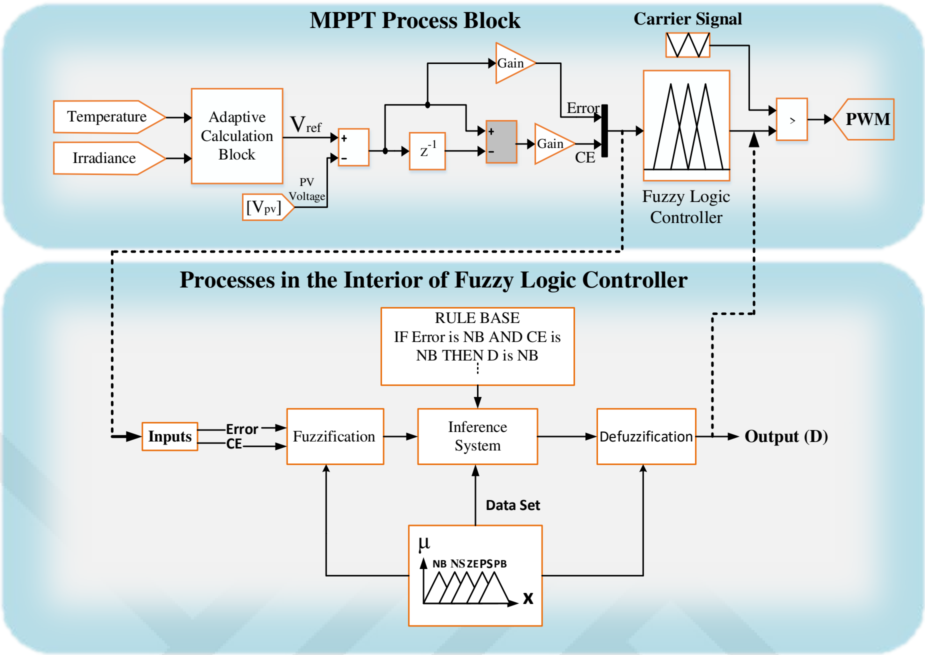


Figure 5.4 The operation process of the proposed method

The input data for the adaptive soft calculation part are given as temperature and radiation and the reference voltage value at the MPP point is calculated using the basic equations below. In the fuzzy logic block, the error rate between the voltage at the MPP point ($E_k$) and the calculated voltage of the PV panel and the change of the error over time ($CE_k$) are used as input values. At the output of the fuzzy logic, the duty cycle of the PWM signal generated for the switching element is set (Yilmaz et al., 2019).

$$\left\{\begin{bmatrix} I_{SC}^{\bullet} = I_{SC} \cdot \dfrac{G}{G_{STC}} \cdot (1 + a \cdot \Delta T) \\ V_{OC}^{\bullet} = V_{OC} \cdot (1 + K \cdot a \cdot \Delta T) \cdot \ln(e + b \cdot \Delta G) \\ V_{mpp}^{\bullet} = V_{mpp} \cdot (1 + K \cdot a \cdot \Delta T) \cdot \ln(e + b \cdot \Delta G) \\ I_{mpp}^{\bullet} = I_{mpp} \cdot \dfrac{G}{G_{STC}} \cdot (1 + a \cdot \Delta T) \\ \text{In case } \Delta G = 0 \text{ and } \Delta T \neq 0 \\ V_{mpp}^{\bullet} = V_{mpp} \cdot (1 + K \cdot a \cdot \Delta T) \\ \text{In case } \Delta G \neq 0 \text{ and } \Delta T = 0 \\ V_{mpp}^{\bullet} = V_{mpp} \cdot \ln(e + b * \Delta G) \end{bmatrix}\right\} \tag{5.7}$$

Where *K*=-0.32398, temperature coefficient, a=1.17*$10^{-1}$, Thermal coefficient. *G* is irradiance, $G_{STC}$ (1000W/$m^{2}$, in STC), $V_{MPP}$ is the PV panel MPP voltage, *T* is ambient temperature, $T_{STC}$ (25°C, in STC), b=0.0005 (Ruo-li et al., 2016).

The flowchart of the proposed MPPT method is presented in detail in Figure 5.5.

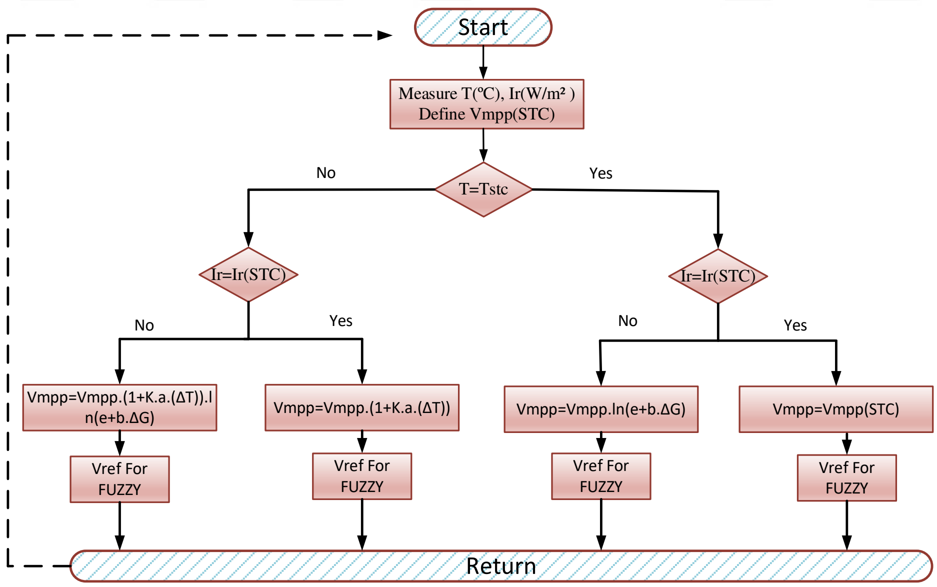


Figure 5.5 The flowchart of the proposed MPPT method.

The FLC algorithm's output values are calculated in the inference process section using the membership functions presented in Figure 5.7 and the rule table shown in Table 1. In the de-fuzzification process section, Centroid, center of gravity (CoG) method (Shown in Figure 5.6) was used. mathematically, the CoG method is defined as follows (Samanta, 2018).

$$\left[ X^* = \frac{\int x \cdot \mu_C(x)dx}{\int \mu_C(x)dx} \right] \tag{5.8}$$

Graphically;

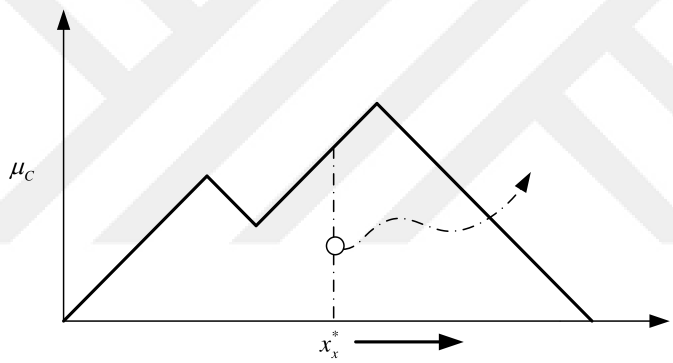


Figure 5.6 Center of gravity de-fuzzification method

Where x* is the x-coordinate of center of gravity, $\int \mu_C(x)dx$ represents the area of the region bounded by the curve $\mu_C$

If $\mu_C$ defined with a discrete membership function;

$$\left[ X^* = \frac{\sum_{i=1}^{n} x_i \mu_C(x_i)}{\sum_{i=1}^{n} \mu_C(x_i)} \right] \tag{5.9}$$

$x_i$ is the sample element and n represents the number of samples in fuzzy (Samanta, 2018).

the outputs of all rules are summed to produce a numerical crisp output value. Abbreviations specified in membership functions are as follows; NB is negative big, NS is negative small, ZE is zero, PS is positive small and PB is positive big.

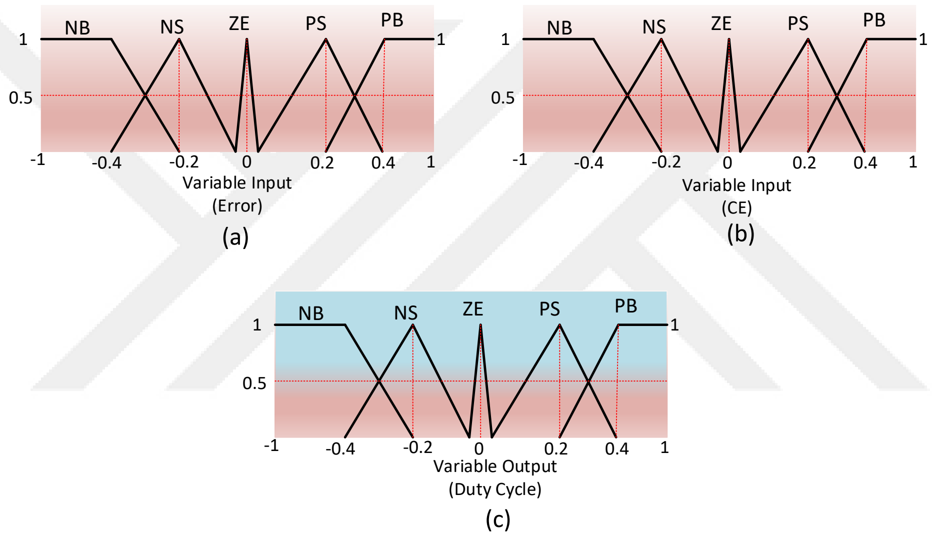


Figure 5.7 Error (a), CE (b), Duty (c).

Table 5.1 MPPT method fuzzy logic rule bases

| E/CE | PB | PS | ZE | NS | NB |
|---|---|---|---|---|---|
| PB | PB | PS | ZE | PB | PB |
| PS | PB | PS | PS | PS | PB |
| ZE | PS | PS | ZE | ZE | NS |
| NS | NS | NS | ZE | NS | NB |
| NB | NS | NS | NS | NB | NB |

The proposed method and traditional methods are compared under six different environmental conditions (Variable environmental conditions are shown in Table 5.2 and also detailed model of weather signals are shown in Figure 5.8). The result signals and convergence time analysis are given in Figure 5.9 and 5.10.

Table 5.2 Variable operation states for MPPT methods

| **States** | State 1 | State 2 | State 3 | State 4 | State 5 | State 6 |
|---|---|---|---|---|---|---|
| **Irradiance** | 1000 W/$m^2$ | 1000 W/$m^2$ | 800 W/$m^2$ | 800 W/$m^2$ | 600 W/$m^2$ | 600 W/$m^2$ |
| **Temperature** | 25$^o$C | 35$^o$C | 25$^o$C | 35$^o$C | 25$^o$C | 35$^o$C |

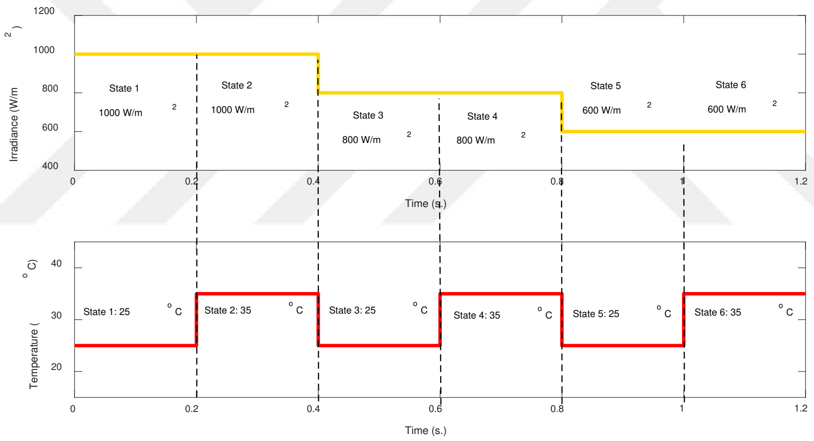


Figure 5.8 PV system operated states (variable irradiance and temperature

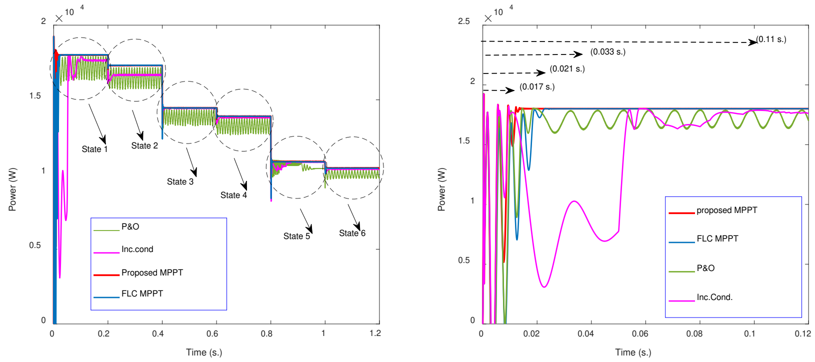


(a) (b)

Figure 5.9 Power analysis of four MPPT methods under variable environmental conditions

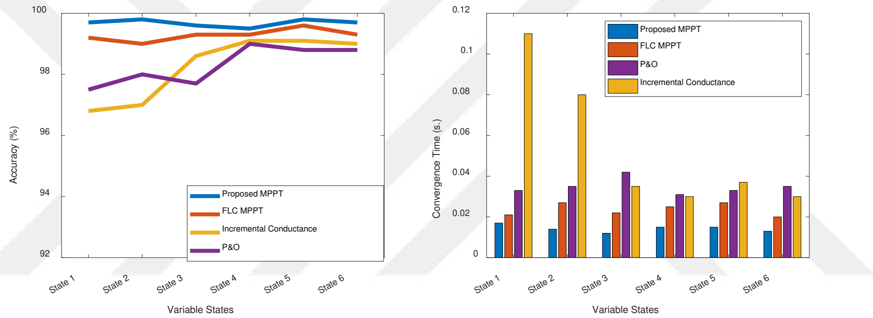


(a) (b)

Figure 5.10 Comparison of efficiency and convergence time for MPPT methods under variable environmental conditions

### 5.2. AC-DC Bridgeless PFC Converter

Research to reduce transmission losses in circuits with power semiconductors is an important issue for the design and implementation of power electronics topologies. Many topologies are available in the literature to reduce transmission and switching losses in AC-DC rectifier topologies. Due to its low THD, high power factor, low transmission loss and high efficiency, the bridgeless PFC rectifier topology is highly preferred. In addition, the bridgeless PFC topology has fewer semiconductor devices than conventional boost topology on the current path (Kararslan et al., 2009., Cheng et al., 2018., Lee et al., 2016, Yilmaz et al., 2020). The bridgeless rectifier topology with average current mode control structure is shown in Figure 5.11.

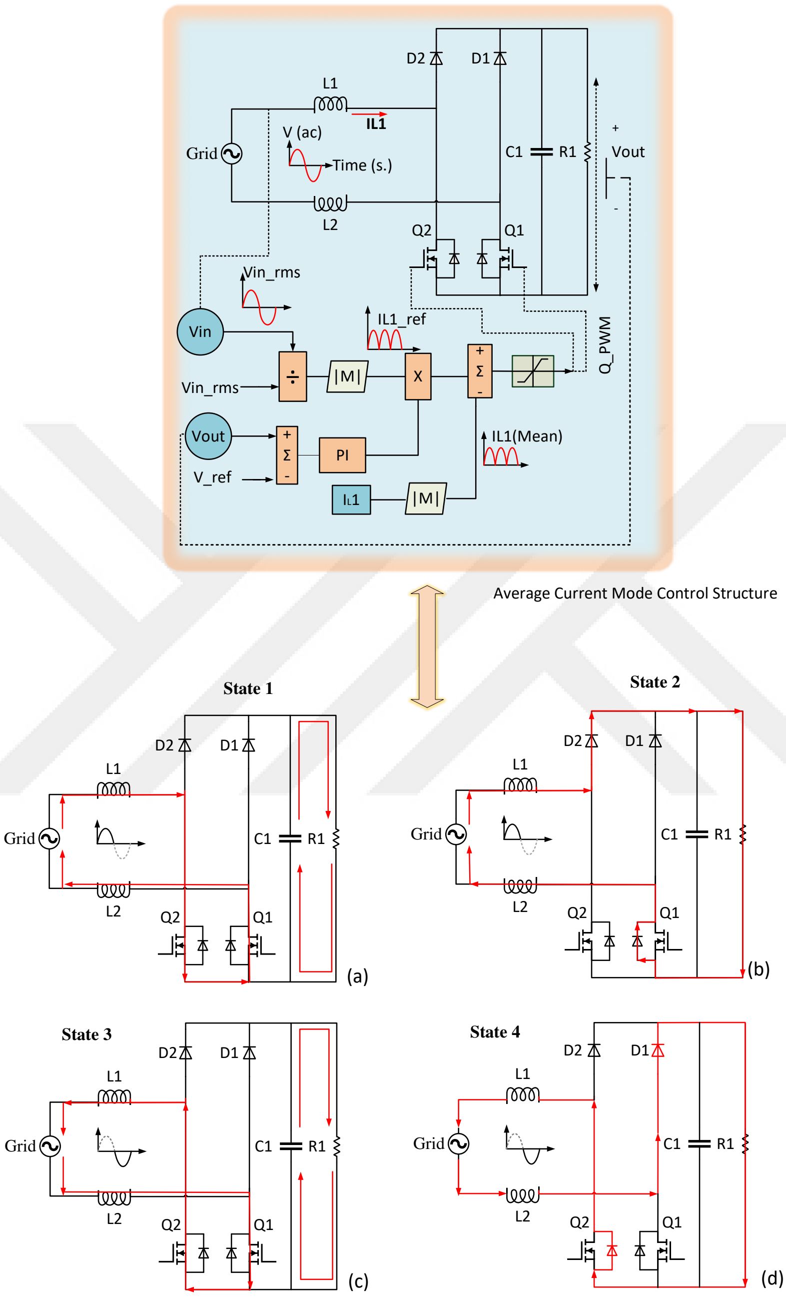


Figure 5.11 AC-DC bridgeless rectifiers with ACM control

The grid voltage ($V_{in}$) is divided by the RMS value then absolute operation applied to the created signal. At the same time, the output voltage ($V_{out}$) is compared with the reference voltage ($V_{outref}$) and an error signal is obtained. After applying PI controller, this error signal is multiplied by the absolute value obtained from the input voltage (|Vin|) and the reference signal for the inductor current ($I_{L1ref}$) is created. By comparing the inductor current and reference value, the PWM signal is created for the switching elements (Shown in Figure 5.11). In order to clarify the operation process of the bridgeless rectifier, the system was operated in four different situations. Switching elements (Q1) and (Q2) are operated synchronously on and off (synchronous control method) (Kararslan et al., 2009., Cheng et al., 2018., Lee et al., 2016, Yilmaz et al., 2020).

$$\left\{\begin{array}{l} V_{grid} = V_m \sin(wt) \\ V_{grid} = L \cdot \dfrac{diL}{dt} \Rightarrow \ 0 < t_{on} < DT \\ V_{grid} - V_{out} = L \cdot \dfrac{diL}{dt} \Rightarrow \ DT < t_{off} < T \\ V_{in} \cdot t_{on} = (V_{in} - V_{out}) \cdot t_{off} \Rightarrow \dfrac{t_{off}}{T} = \dfrac{V_{out}}{V_{in}} \end{array}\right\} \tag{5.10}$$

where $D$ is duty cycle, $V_{in}$ is grid voltage, $V_{out}$ is load voltage $C$ is load capacitor, $L$ is equivalent inductor

Performance results of the AC-DC PFC converter for THD, power factor, phase angle and current-voltage characteristics are shown in Figure 5.12.

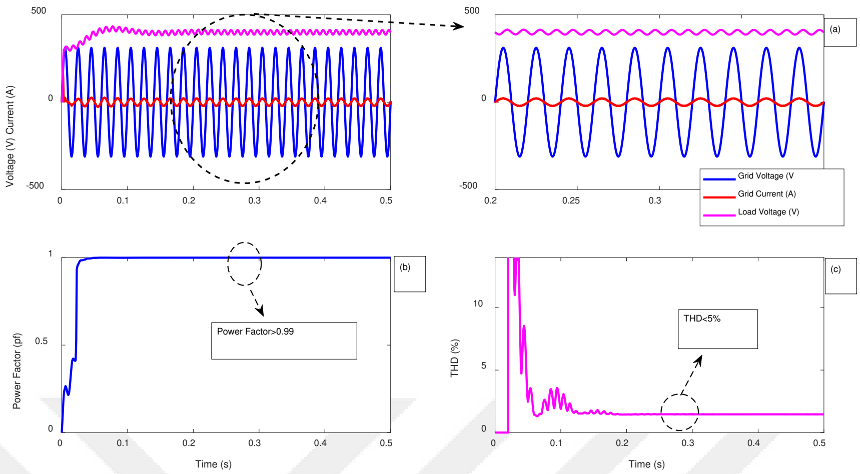


Figure 5.12 Voltage and current signals for designed bridgeless rectifier

### 5.3. Multi-Input Output LLC Resonance Converter

Due to its high efficiency low electromagnetic interference (EMI) and its ability to operate in a wide load range, LLC resonance converter was preferred in the proposed battery charging architecture. The proposed LLC resonance converter has two inputs to provide power flow from the grid and PV panel, while the output of the LLC resonance converter has a high-power battery connection as well as an auxiliary battery connection for feeding low power loads. The LLC resonant converter for proposed architecture is shown in Figure 5.13.

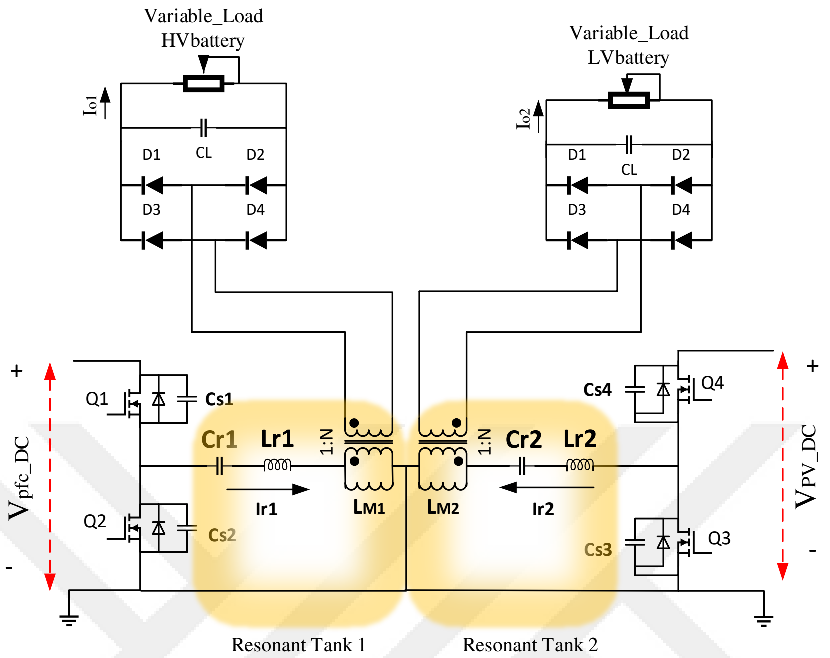


Figure 5.13 Designed LLC resonance converter for proposed battery charger architecture

Current and voltage signals of the LLC resonance converter are shown in Figure 5.14.

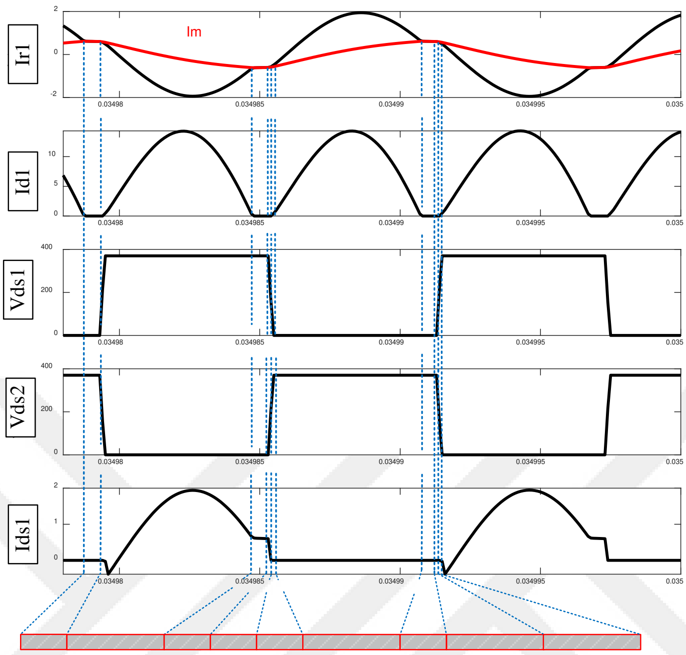


Figure 5.14 Voltage-current signal of HBLLC converter.

The switching period of the dc-dc converter can be examined in 8 different time intervals.

**State 1 (t0<t<t1):** While switching elements $Q_1$ and $Q_3$ are in transmission state, switches $Q_2$ and $Q_4$ will be off state. $D_1$, $D_4$, $D_5$, $D_8$ will be forward bias and variable loads are fed by $I_{o1}$ and $I_{o2}$ currents. In addition, the magnetizing currents $I_{m1}$ and $I_{m2}$ decreases linearly.

**State 2 (t1<t<t2):** The magnetizing current ($I_m$) and the resonance current ($I_r$) become equal in size, all the diodes in the secondary part are in reverse bias state and the filter capacitors ($C_o$) are discharged through variable loads. Magnetic inductance ($L_m$) acts as resonance inductance, so resonance occurs between $L_r$, $L_m$ and $C_r$.

**State 3 (t2<t<t3):** The switching elements $Q_1$ and $Q_3$ are switching off. While $I_{r1}$ and $I_{r2}$ charge the $C_{s1}$ and $C_{s3}$ parasitic capacitors, $C_{s2}$ and $C_{s4}$ parasitic capacitors discharged. The transformer is clamped and on the secondary side, the diodes $D_2$, $D_3$, $D_6$ and $D_7$ are forward bias and variable loads are fed by the currents $I_{o1}$ and $I_{o2}$.

**State 4 (t3<t<t4):** The voltage on the $C_{s2}$ and $C_{s4}$ parasitic capacitors decreases to zero, currents circulate to through body diode of $Q_2$ and $Q_4$ that reversely increases in sinusoidal mode. On the secondary side, $D_2$, $D_3$, $D_6$ and $D_7$ forward biased and the variable loads are fed by the currents $I_{o1}$ and $I_{o2}$. In this case, $Q_2$ and $Q_4$ soft switching technique (ZVS) can be easily realized.

**State 5 (t4<t<t5):** The switches $Q_2$ and $Q_4$ are turned on, primary resonant currents are carried by $Q_2$-$Q_4$ and also gradually increases to reverse direction as sinusoid. on the secondary side, $D_2$, $D_3$, $D_6$ and $D_7$ are forward biased, secondary side of transformers are clamped by output voltage, therefore resonance occurs between ($L_{r1}$, $C_{r1}$) and ($L_{r2}$, $C_{r2}$), on the primary side the magnetizing currents $I_{m1}$ and $I_{m2}$ circulating through $L_{m1}$, $L_{m2}$ and increases linearly.

**State 6 (t5<t<t6):** The Magnetizing currents ($I_{m1}$ and $I_{m2}$) in the primary part of the transformer will be equal in size to the $I_{r1}$ and $I_{r2}$ resonance currents. The diodes in the second part of the transformer will be reverse bias and the filter capacitors ($C_o$) will be discharged through variable loads. The Magnetizing inductance ($L_m$) acts as resonance inductance, so resonance occurs between $L_r$, $L_m$ and $C_r$.

**State 7 (t6<t<t7):** The switching elements $Q_2$ and $Q_4$ are switching off. While $I_{r1}$ and $I_{r2}$ charge the $C_{s2}$ and $C_{s4}$ parasitic capacitors, $C_{s1}$ and $C_{s3}$ parasitic capacitors discharged. The transformer is clamped and on the secondary side, the diodes $D_1$, $D_4$, $D_5$ and $D_8$ are forward bias and variable loads are fed by the currents $I_{o1}$ and $I_{o2}$.

**State 8 (t7<t<t8):** The voltage on the $C_{s1}$ and $C_{s3}$ parasitic capacitors decreases to zero, currents circulate to through body diode of $Q_1$ and $Q_3$ that

reversely increases in sinusoidal mode. On the secondary side, $D_2$, $D_3$, $D_6$ and $D_7$ forward biased and the variable loads are fed by the currents $I_{o1}$ and $I_{o2}$. In this case, $Q_2$ and $Q_4$ soft switching technique (ZVS) can be easily realized. The states of the circuit elements during switching of the two input-output HBLLC resonance converter are shown in detail in Table 5.3. (Jovanovic et al., 2016, Lin et al., 2018, Vu et al., 2018, Park et al., 2016, Park et al., 2017, Wang et al., 2018, Yilmaz et al., 2020)

Table 5.3 Switching method and state of the circuit elements

| | State 1 | State 2 | State 3 | State 4 | State 5 | State 6 | State 7 | State 8 |
|---|---|---|---|---|---|---|---|---|
| Q1 | √ | √ | ○ | ○ | ○ | ○ | ○ | ○ |
| Q2 | ○ | ○ | ○ | ○ | √ | √ | ○ | ○ |
| Q3 | √ | √ | ○ | ○ | ○ | ○ | ○ | ○ |
| Q4 | ○ | ○ | ○ | ○ | √ | √ | ○ | ○ |
| D1 | √ | ○ | ○ | ○ | ○ | ○ | ○ | √ |
| D2 | ○ | ○ | ○ | √ | √ | ○ | ○ | ○ |
| D3 | ○ | ○ | ○ | √ | √ | ○ | ○ | ○ |
| D4 | √ | ○ | ○ | ○ | ○ | ○ | ○ | √ |
| D5 | √ | ○ | ○ | ○ | ○ | ○ | ○ | √ |
| D6 | ○ | ○ | ○ | √ | √ | ○ | ○ | ○ |
| D7 | ○ | ○ | ○ | √ | √ | ○ | ○ | ○ |
| D8 | √ | ○ | ○ | ○ | ○ | ○ | ○ | √ |
| Body (d1) | ○ | ○ | √ | ○ | ○ | ○ | √ | √ |
| Body (d2) | ○ | ○ | √ | √ | ○ | ○ | √ | ○ |
| Body (d3) | ○ | ○ | √ | ○ | ○ | ○ | √ | √ |
| Body (d4) | ○ | ○ | √ | √ | ○ | ○ | √ | ○ |
| Cs1 | √ | ○ | √ | ○ | ○ | ○ | √ | ○ |
| Cs2 | ○ | ○ | √ | ○ | √ | ○ | √ | ○ |
| Cs3 | √ | ○ | √ | ○ | ○ | ○ | √ | ○ |
| Cs4 | ○ | ○ | √ | ○ | √ | ○ | √ | ○ |

In order to analyze the proposed LLC resonance converter and to determine the circuit elements AC analysis of the circuit has been performed which is shown in Figure 5.15.

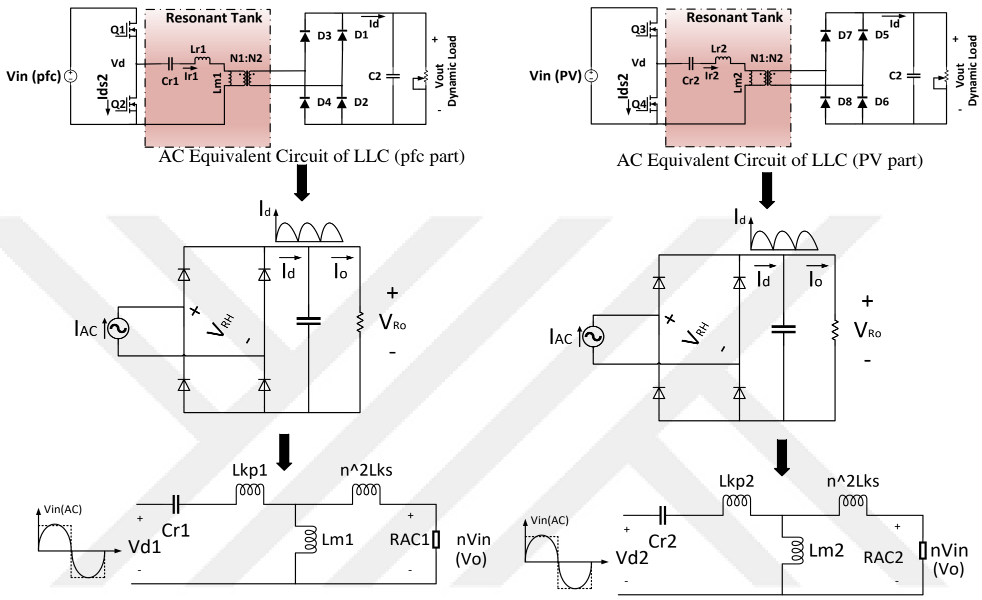


Figure 5.15 The AC equivalent circuit of LLC resonant converter.

Current and voltage calculation of AC equivalent circuit is specified in the following equations;

$$\begin{bmatrix} \mathrm{I}_{\mathrm{AC}} = \dfrac{\Pi \cdot I_0}{2}\sin(wt) \\ \mathrm{VR}_{\mathrm{H}} = +V_0 \Rightarrow if\ \sin(wt) > 0 \\ \mathrm{VR}_{\mathrm{H}} = -V_0 \Rightarrow if\ \sin(wt) < 0 \\ \mathrm{VR}_{\mathrm{H}}{}^{F} = \dfrac{4 \cdot V_0}{\Pi}\sin(wt) \end{bmatrix} \tag{5.11}$$

The calculation of the load value in the AC equivalent circuit is specified in the following equations.

$$\left[\begin{array}{l} R_{AC} = \dfrac{VR_H{}^F}{I_{AC}} = \dfrac{8}{\Pi^2}\dfrac{V_0}{I_0} = \dfrac{8}{\Pi^2}R_{LOAD} \\ n = \dfrac{N_P}{N_S}, \\ R_{AC} = \dfrac{8 \cdot n^2}{\Pi^2}R_{LOAD} \end{array}\right] \quad (5.12)$$

The mathematical expression and equation of the voltage gain are indicated by the equation below.

$$\left[\begin{array}{l} M = \dfrac{2n \cdot V_0}{V_{in}} = \left| \dfrac{w^2 L_m R_{AC} C_R}{jw(1-\dfrac{w^2}{w_0{}^2}) \cdot (L_m + n^2 L_{ks}) + R_{AC}(1-\dfrac{w^2}{w_p{}^2})} \right| \\ \text{Where}, \quad w_0 = \dfrac{1}{\sqrt{L_r C_r}}, \qquad w_p = \dfrac{1}{\sqrt{L_P C_r}} \end{array}\right] \quad (5.13)$$

When the voltage gain is regulated, the following mathematical equation can be derived.

$$\left[\begin{array}{l} M = \dfrac{2n \cdot V_0}{V_{in}} = \left| \dfrac{\dfrac{w^2}{w_p{}^2}(\dfrac{k}{k+1})}{j(\dfrac{w}{w_0}) \cdot (1-\dfrac{w^2}{w_0{}^2}) \cdot Q \cdot \dfrac{(k+1)^2}{2k+1} + (1-\dfrac{w^2}{w_p{}^2})} \right| \\ \text{Where}, \ k = \dfrac{L_m}{L_{kp}}, \qquad Q = \dfrac{\sqrt{L_r/C_r}}{R_{AC}} \end{array}\right] \quad (5.14)$$

The mathematical equations given can be explained as follows; $V_o$ is load voltage $V_{in}$ dc-link voltage, $V_{RH}$ is transformer secondary side voltage, $n$ is transformer's turn ratio, $M$ is voltage gain, $w$ is angular frequency, $f_o$ is resonant frequency, $f_p$ primary resonant frequency, $L_m$ magnetizing inductance of the transformer, $L_r$ is resonant inductance, $C_r$ is resonant capacitance, Q is quality factor (Jovanovic et al., 2016, Lin et al., 2018, Vu et al., 2018.).

The effect of changing the quality factor (Q) and k index on the gain (M) is shown in figure 5.16.

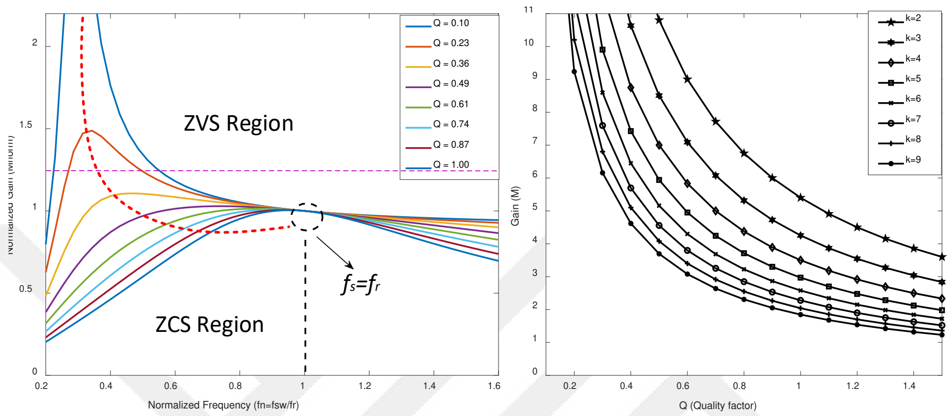


Figure 5.16 Effects of quality factor (Q) and inductance ratio (k) on the voltage gain in the LLC resonance converter.

### 5.3.1. Selection of LLC resonance Converter circuit elements

### 5.3.2. Bridgeless PFC and HV Battery side

The steps to be followed when choosing the circuit elements of the LLC resonance converter are presented below in equations.

In order to determine resonant capacitor (Cr);

$$\left[ C_r = \frac{1}{2\Pi Q \cdot f_o \cdot R_{ac}} = 302.82\text{nF} \right] \tag{5.15}$$

In order to determine resonant inductor (Lr);

$$\left[ L_r = \frac{1}{(2\Pi \cdot f_o)^2 \cdot C_r} = 11.57\,\mu H \right] \tag{5.16}$$

In order to determine Primary resonant inductor;

$$\left[ L_p = \frac{(k+1)^2}{(2k+1)} (L_r) = 37.887\,\mu H \right] \tag{5.17}$$

The relationship between primary resonant inductor, Magnetizing inductor and transformer primary side inductor is;

$$L_p = L_m + L_{pri};\ k = \frac{L_m}{L_{pri}} \Rightarrow L_p = (k+1)\cdot L_{pri}$$
$$\Rightarrow L_{pri} = 6.314\mu H \tag{5.18}$$
$$\Rightarrow L_m = 31.573\mu H$$

In order to determine the winding turn numbers of the transformer;

$$\left[ n = \frac{Np}{Ns} = \frac{V_{in\ (\max)}}{2(V_o + 2V_d)} \cdot M_{(\min)} = \frac{400}{2(120+1)} \cdot (1.18) = 1.951 \right] \tag{5.19}$$

Primary side minimum turn number can be determined as;

$$\left[ \begin{array}{l} N_{p(\min)} = \dfrac{n\cdot(V_o + 2V_d)}{2\cdot f_p \cdot \Delta B \cdot A_e} \Rightarrow \\ \Rightarrow N_p = n \cdot N_s > N_{p(\min)} \end{array} \right] \tag{5.20}$$

$$\left[ \begin{array}{l} N_{p(\min)} = \dfrac{1.951\cdot(121)}{2\cdot 4.6\cdot 10^3 \cdot 0.3\cdot 107\cdot 10^{-6}} \Rightarrow 79.937 \\ \Rightarrow N_p = n\cdot N_s > N_{p(\min)} = 79.937 \\ \Rightarrow N_p = 80 \\ \Rightarrow N_s > N_{s(\min)} = 40.972 \\ \Rightarrow N_s = 41 \end{array} \right] \tag{5.21}$$

### 5.3.3. PV Panel and Low Voltage Battery Side

The steps to be followed when choosing the circuit elements of the LLC resonance converter are presented below in equations.

In order to determine resonant capacitor (Cr);

$$\left[ C_r = \frac{1}{2\Pi Q \cdot f_o \cdot R_{ac}} = 2484\text{nF} \right] \tag{5.22}$$

In order to determine resonant inductor (Lr);

$$\left[ L_r = \frac{1}{(2\Pi \cdot f_o)^2 \cdot C_r} = 1.019\mu H \right] \tag{5.23}$$

In order to determine primary resonant inductor;

$$\left[ L_p = \frac{(k+1)^2}{(2k+1)}(L_r) = 4.384\mu H \right]$$

The relationship between primary resonant inductor, magnetizing inductor and transformer primary side inductor is;

$$\begin{aligned} & L_p = L_m + L_{pri};\ k = \frac{L_m}{L_{pri}} \Rightarrow L_p = (k+1)\cdot L_{pri} \\ & \Rightarrow L_{pri} = 0.543\mu H \\ & \Rightarrow L_m = 3.8\mu H \end{aligned} \tag{5.24}$$

In order to determine the winding turn numbers of the transformer;

$$\left[ n = \frac{Np}{Ns} = \frac{V_{in\ (\max)}}{2(V_o + 2V_d)} \cdot M_{(\min)} = \frac{65}{2(24+1)} \cdot (1.14) = 1.482 \right] \tag{5.25}$$

Primary side minimum turn number can be determined as;

$$\left[ \begin{aligned} & N_{p(\min)} = \frac{n\cdot(V_o + 2V_d)}{2\cdot f_p \cdot \Delta B \cdot A_e} \Rightarrow \\ & \Rightarrow N_p = n\cdot N_s > N_{p(\min)} \end{aligned} \right] \tag{5.26}$$

$$\left[ \begin{aligned} & N_{p(\min)} = \frac{1.482\cdot(25)}{2\cdot 4.84\cdot 10^3 \cdot 0.3\cdot 107\cdot 10^{-6}} \Rightarrow 11.916 \\ & \Rightarrow N_p = n\cdot N_s > N_{p_{(\min)}} = 11.916 \\ & \Rightarrow N_p = 12 \\ & \Rightarrow N_s > N_{s(\min)} = 8.0409 \\ & \Rightarrow N_s = 9 \end{aligned} \right] \tag{5.27}$$

For this study, the measured transformers turn number is given in Figure 5.17.

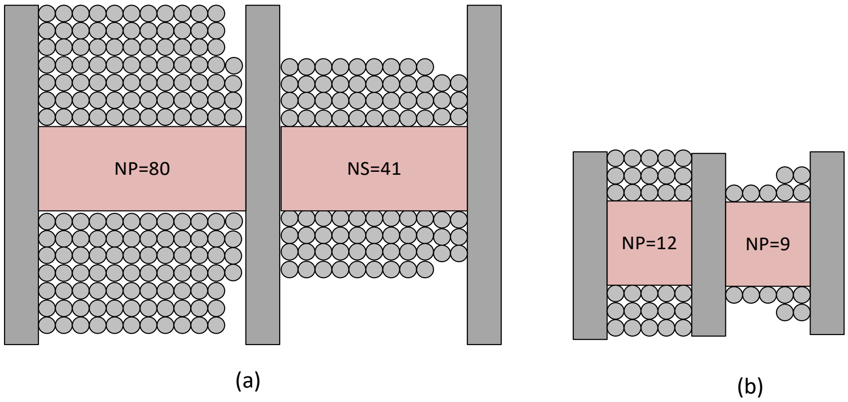


Figure 5.17 Transformer design, (a) HV battery side, (b) LV battery side.

### 5.3.4. Control Structure of LLC Resonant Converter

The feed-back loop control of the LLC resonance converter consists of the transfer function for determining the power stage, a feedback compensator to perform the power transfer appropriately, and a PWM generator for the production of PWM to the switching elements as shown Figure 5.18. Additionally, the error amplifier and compensation block are designed to compensate for the error signal, which is the difference between the reference and the output voltage. Therefore, the resulting signal transmitted to $V_{co1}$ and $V_{co2}$ blocks in order to convert the measured signal to switching frequency. The switching frequency created according to the error signal is converted into a pulse signal for the switch elements. Finally, the signals generated by the PWM generator are sent to the gate of the switches Q1, Q2, Q3, Q4 and a cycle of the feed-back control loop is realized. This process repeats throughout the operation period (Jovanovic et al., 2016, Lin et al., 2018, Vu et al., 2018, Park et al., 2016, Park et al., 2017, Wang et al., 2018).

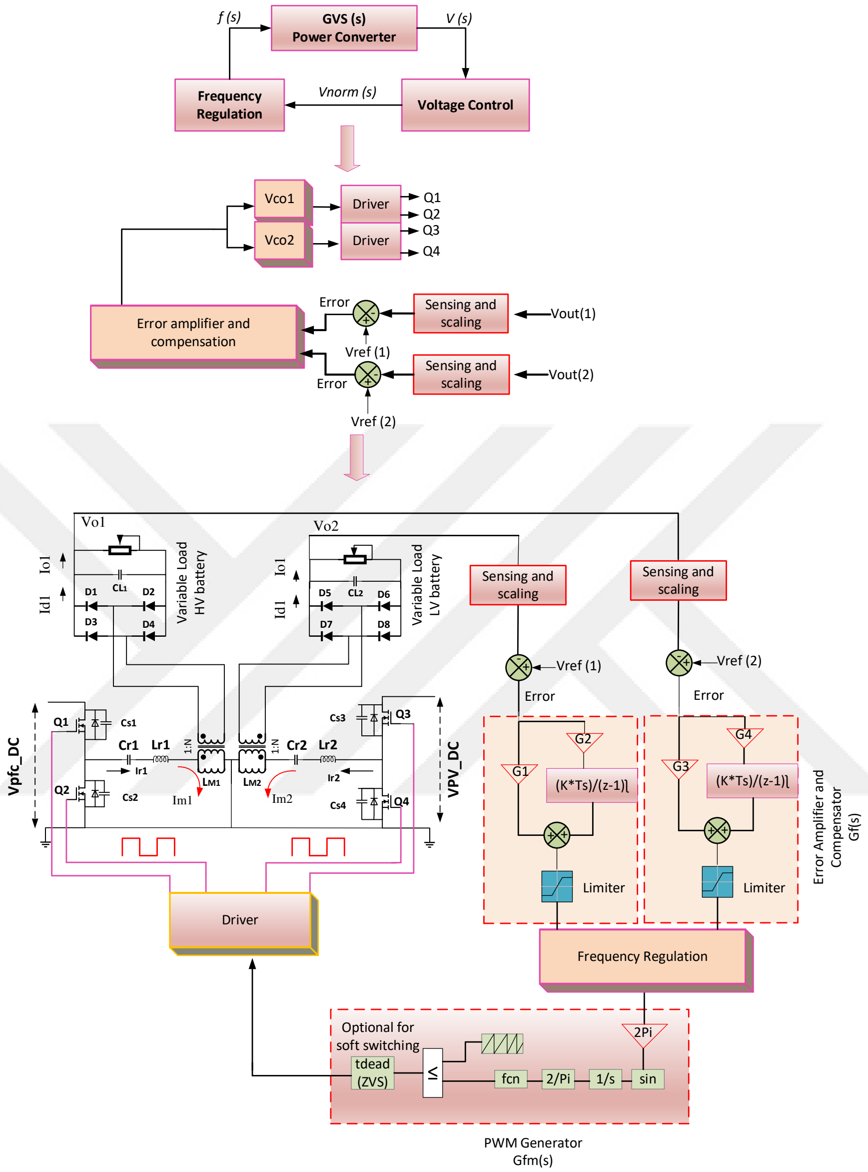


Figure 5.18 Control structure for proposed LLC resonant converter.

### 5.4. Performance Results

The grid voltage-frequency values are applied to the bridgeless converter controlled in average current mode in five different electrical situations (shown in Table 5.4) and the THD status is presented in Figure 5.19.

Table 5.4 Variable operation states for bridgeless PFC converter

| **States** | State 1 | State 2 | State 3 | State 4 | State 5 |
|---|---|---|---|---|---|
| **Voltage** | 220 V | 180 V | 245 V | 220 V | 220 V |
| **Frequency** | 50 Hz | 50 Hz | 50 Hz | 48 Hz | 65 Hz |

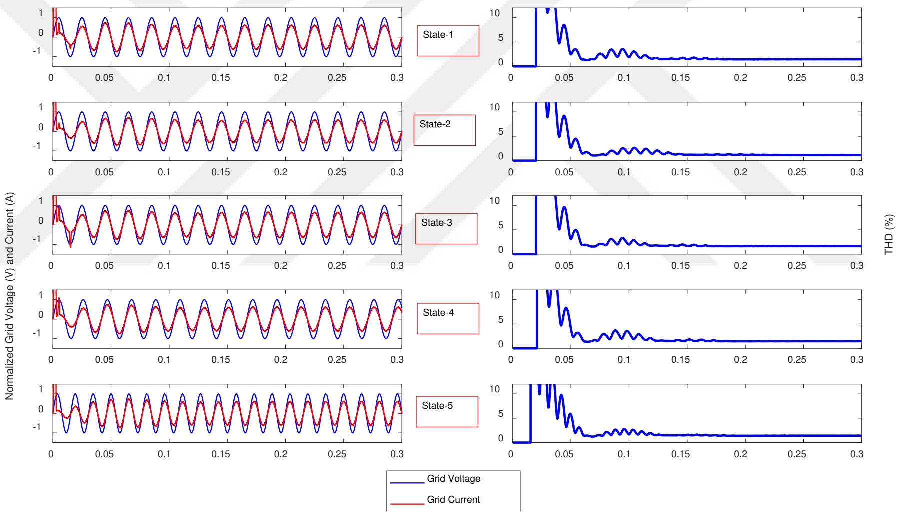


Figure 5.19 Ac-dc bridgeless PFC converter under variable operation states.

The high power battery charger unit of the proposed battery charging architecture was operated in six different load situations (From 5% load to 100% load) as shown in Table 5.5.

Table 5.5 Variable load states for proposed battery charger

| **States** | State 1 | State 2 | State 3 | State 4 | State 5 | State 6 |
|---|---|---|---|---|---|---|
| **Load** | 100% | 50% | 30% | 20% | 10% | 5% |

### 5.4.1. State 1 (100% Load):

Grid voltage and current, DC-Link voltage and current, phase angle between voltage and current, power factor are shown in Figure 5.20. Bridgeless converter side load voltage and current are shown in Figure 5.21. PV panel power-voltage characteristics, PV power, PV voltage and current, are shown in Figure 5.22. PV panel side load voltage and current are shown in Figure 5.23. Grid-side resonance capacitor and transformer magnetizing current, switch current, switch voltage, rectifier diode current are shown in Figure 5.24. PV panel side resonance capacitor and transformer magnetizing current (Icr-Im), switch current (IsQ1), switch voltage (VsQ1), rectifier diode current are shown in Figure 5.25. Comparision of bridgeless PFC side grid current harmonics and IEC 61000-3-2-Class-D standards are shown in Figure 5.26.

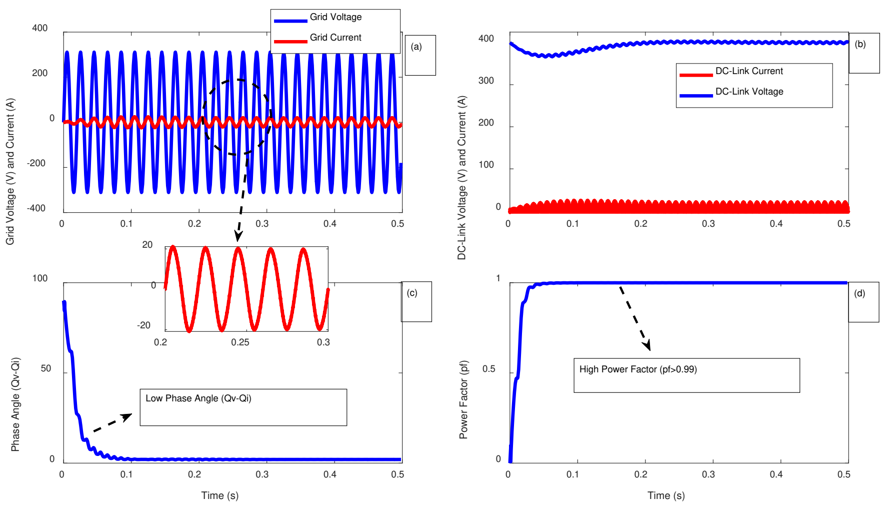


Figure 5.20 Grid voltage and current (a), DC-Link voltage and current (b), Phase angle between voltage and current (c), power factor (d)

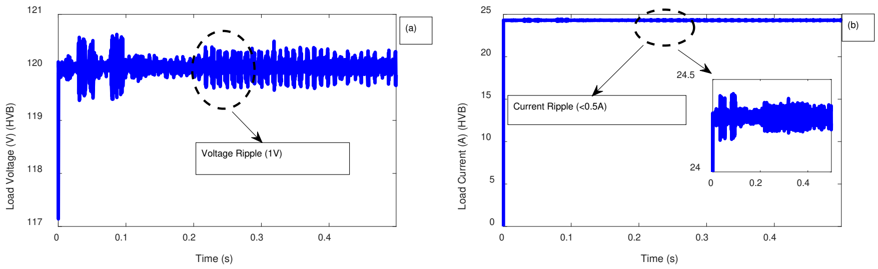


Figure 5.21 Load voltage (HV-battery side) (a), Load current (HV-battery side) (b)

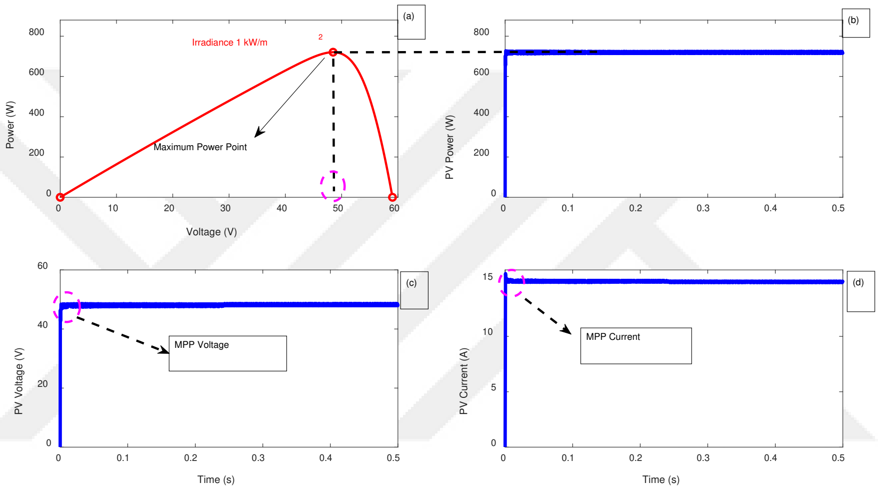


Figure 5.22 PV panel power-voltage characteristics (a), PV power (b), PV voltage (c), PV current (d)

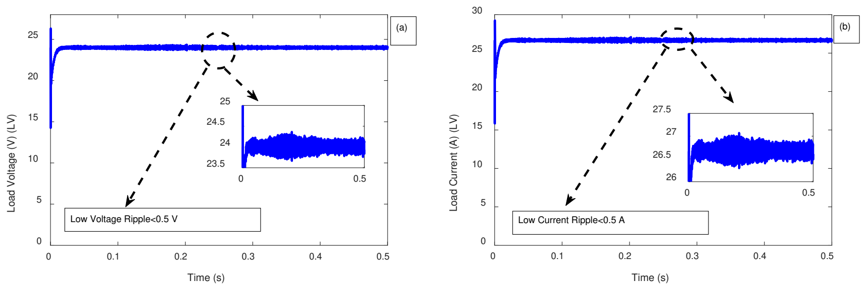


Figure 5.23 Load voltage (LV-battery side) (a), Load current (LV-battery side) (b)

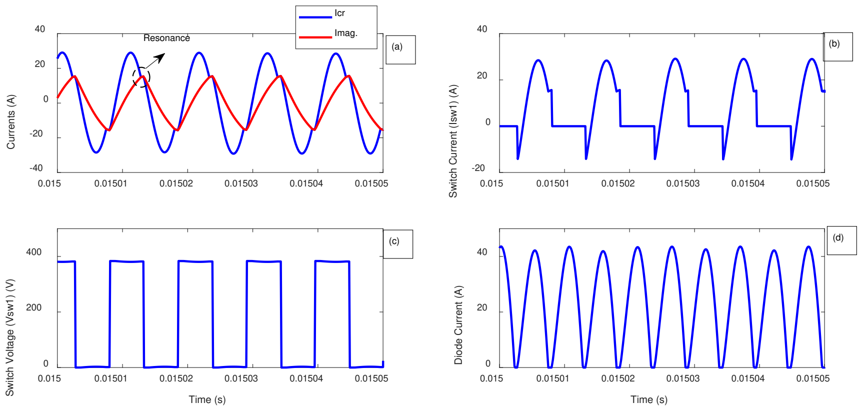


Figure 5.24 Grid-side resonance capacitor and transformer magnetizing current (Icr-Im) (a) Switch current (IsQ1) (b), Switch voltage (VsQ1) (c), Rectifier diode current (d)

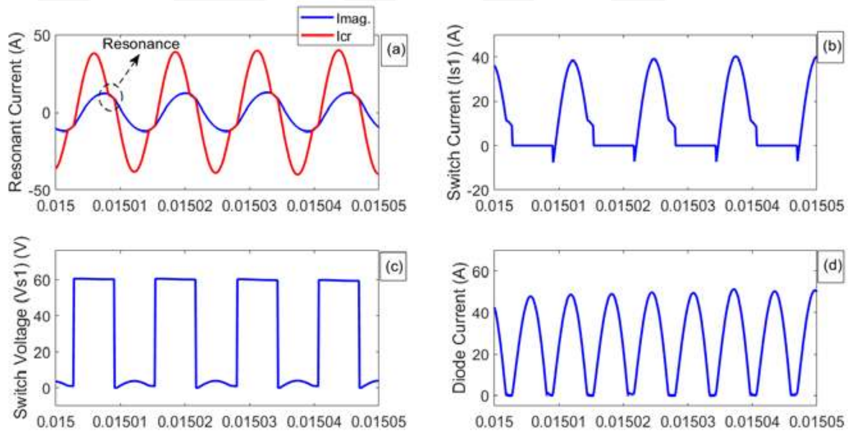


Figure 5.25 PV Panel-side resonance capacitor and transformer magnetizing current (Icr-Im) (a) Switch current (IsQ1) (b), Switch voltage (VsQ1) (c),Rectifier diode current (d)

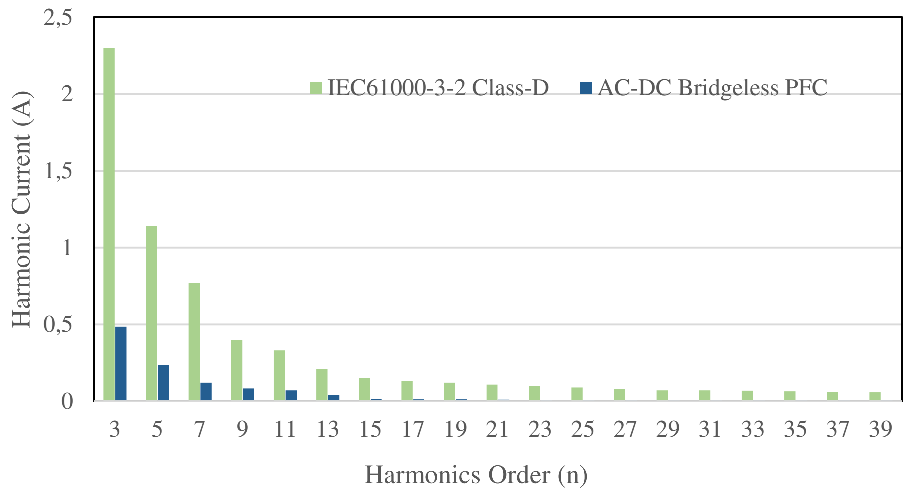


Figure 5.26. Comparison of bridgeless PFC harmonics and IEC 61000-3-2-Class-D standards.

In the case of full load, in HV battery side and LV battery side, the performance results of the proposed circuit are summarized in Table 6.

Table 5.6. Performance results in the case full load

| | Power Factor | THD | MPPT Accuracy | ΔV(ripple) |
|---|---|---|---|---|
| HV (Bat.) | >0.99 | < IEC61000-3-2-D-Class | -- | <1V |
| LV (Bat.) | -- | --- | >0.99 | <1V |

### 5.4.2. State 2 (50% Load)

Grid voltage and current, DC-Link voltage and current, phase angle between voltage and current, power factor are shown in Figure 5.27. Bridgeless converter side load voltage and current are shown in Figure 5.28. PV panel power-voltage characteristics, PV power, PV voltage and current, are shown in Figure 5.29. PV panel side load voltage and current are shown in Figure 5.30. Grid-side resonance capacitor and transformer magnetizing current, switch current, switch

voltage, rectifier diode current are shown in Figure 5.31. PV panel side resonance capacitor and transformer magnetizing current (Icr-Im), switch current (IsQ1), switch voltage (VsQ1), rectifier diode current are shown in Figure 5.32. Comparision of bridgeless PFC side grid current harmonics and IEC 61000-3-2-Class-D standards are shown in Figure 5.33.

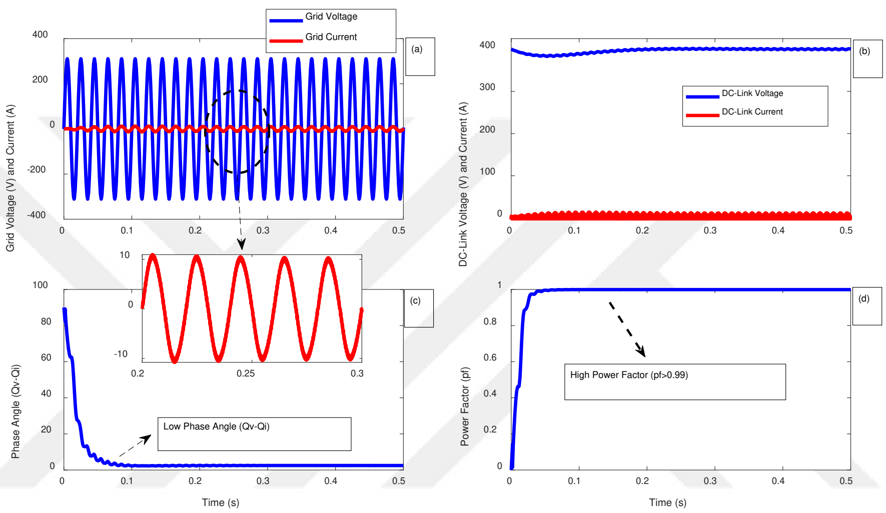


Figure 5.27 State 2, Grid voltage and current (a), DC-Link voltage and current (b), Phase angle between voltage and current (c), power factor (d)

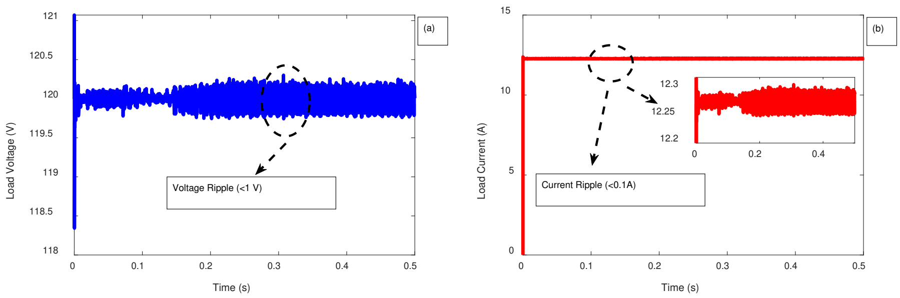


Figure 5.28 State 2, Load voltage (HV-Battery side) (a), Load current (HV-battery side) (b)

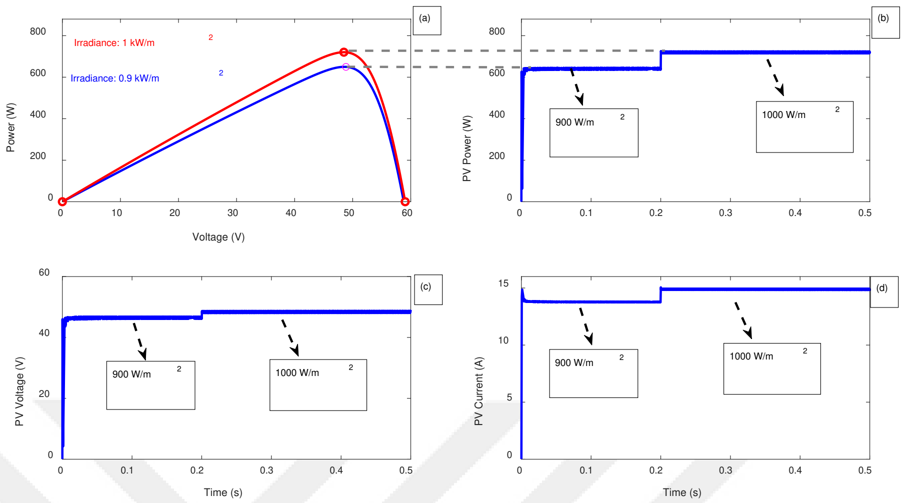


Figure 5.29 State 2, PV panel power-voltage characteristics (a), PV power (b), PV voltage (c), PV current (d)

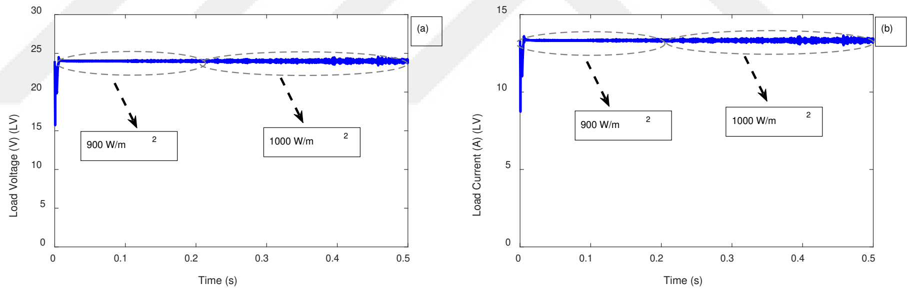


Figure 5.30 State 2, Load voltage (LV-battery side) (a), Load current (LV-battery side) (b)

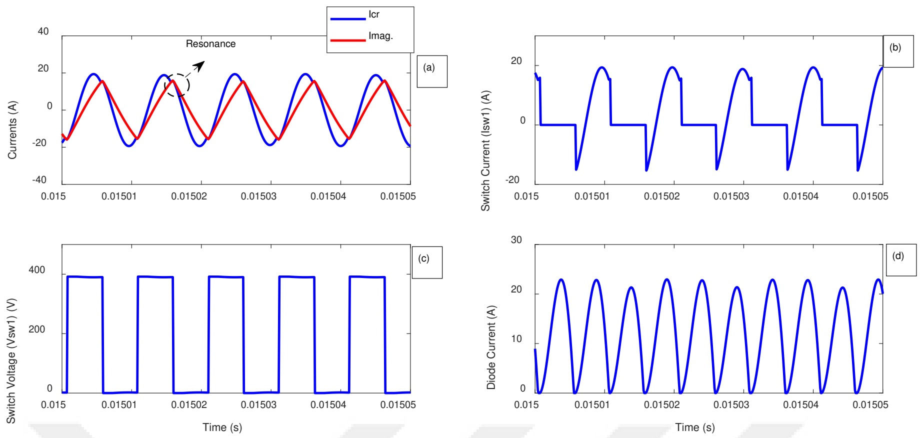


Figure 5.31 State 2, Grid-side resonance capacitor and transformer magnetizing current (Icr-Im) (a) Switch current (IsQ1) (b), Switch voltage (VsQ1) (c), Rectifier diode current (d)

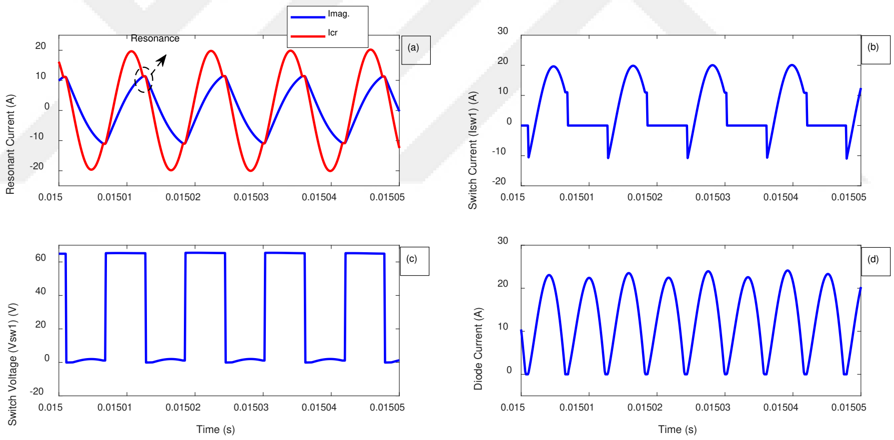


Figure 5.32 State 2, PV panel-side resonant capacitor and transformer magnetizing current (Icr-Im) (a) Switch current (IsQ1) (b), Switch voltage (VsQ1) (c), Rectifier diode current (d)

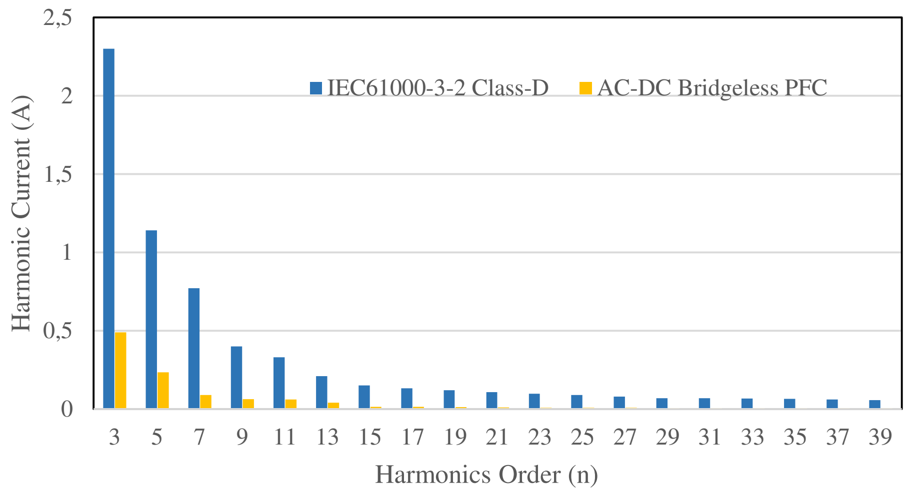


Figure 5.33 State 2, Comparison of bridgeless PFC harmonics and IEC 61000-3-2-Class-D standards.

In the case of 50% load, in HV battery side and LV battery side, the performance results of the proposed circuit are summarized in Table 5.37.

Table 5.7 Performance results in the case 50% load

| | **Power Factor** | **THD** | **MPPT Accuracy** | **ΔV(ripple)** |
|---|---|---|---|---|
| HV (Bat.) | >0.99 | <IEC61000-3-2-D-Class | -- | <1V |
| LV (Bat.) | --- | --- | >0.99 | <1V |

### 5.4.3. State 3 (30% Load)

Grid voltage and current, DC-Link voltage and current, phase angle between voltage and current, power factor are shown in Figure 5.34. Bridgeless converter side load voltage and current are shown in Figure 5.35. PV panel power-voltage characteristics, PV power, PV voltage and current, are shown in Figure 5.36. PV panel side load voltage and current are shown in Figure 5.37. Grid-side resonance capacitor and transformer magnetizing current, switch current, switch voltage, rectifier diode current are shown in Figure 5.38. PV panel side resonance capacitor and transformer magnetizing current (Icr-Im), switch current (IsQ1), switch voltage (VsQ1), rectifier diode current are shown in Figure 5.39. Comparision of bridgeless PFC side grid current harmonics and IEC 61000-3-2-Class-D standards are shown in Figure 5.40.

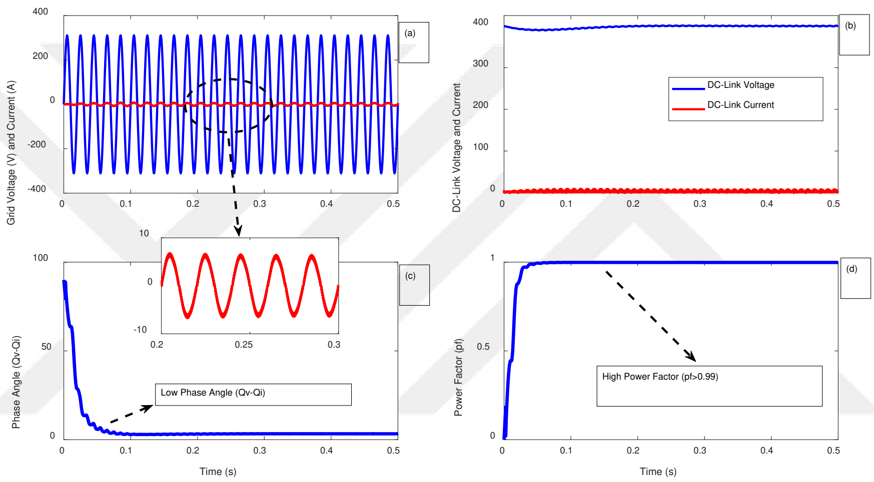


Figure 5.34 State 3, Grid voltage and current (a), DC-Link voltage and current (b), Phase angle between voltage and current (c), power factor (d)

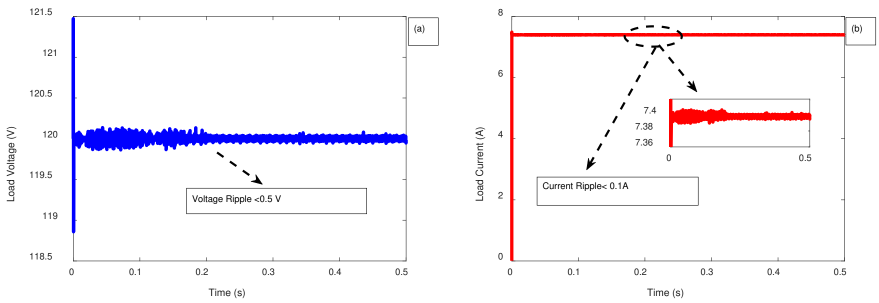


Figure 5.35 State 3, Load voltage (HV-battery side) (a), Load current (HV-battery side) (b)

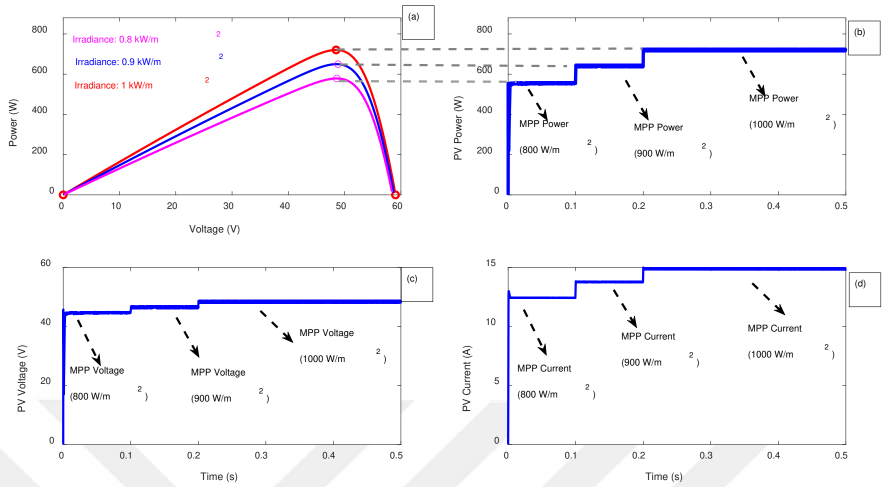


Figure 5.36 State 3, PV panel power-voltage characteristics (a), PV power (b), PV voltage (c), PV current (d)

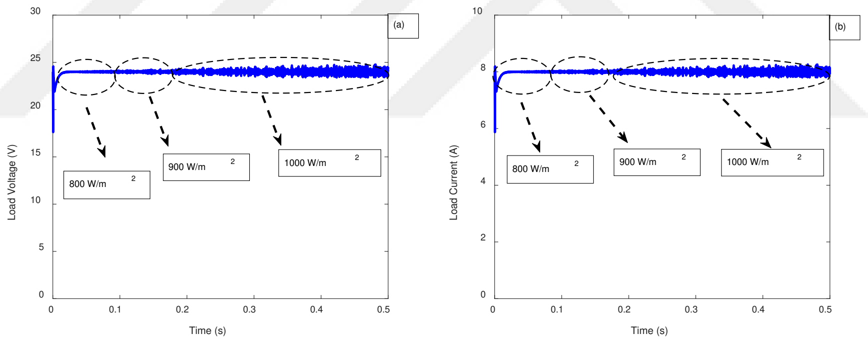


Figure 5.37 State 3, Load voltage (LV-battery side) (a), Load current (LV-battery side) (b)

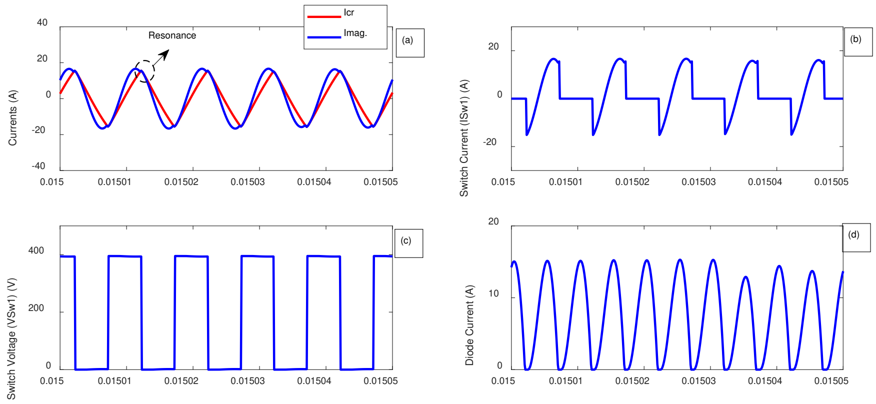


Figure 5.38 State 3, Grid side resonance capacitor and transformer magnetizing current (Icr-Im) (a) Switch current (IsQ2) (b), Switch voltage (VsQ2) (c), Rectifier diode current (d)

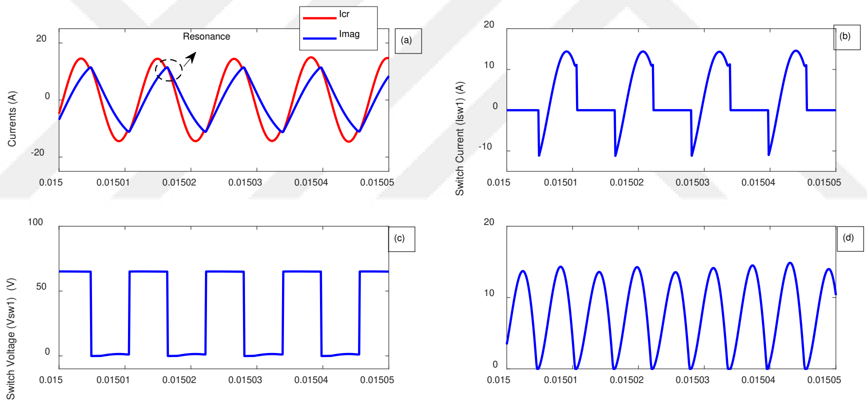


Figure 5.39 State 3, PV panel-side resonant capacitor and transformer magnetizing current (Icr-Im) (a) Switch current (IsQ1) (b), Switch voltage (VsQ1) (c), Rectifier diode current (d)

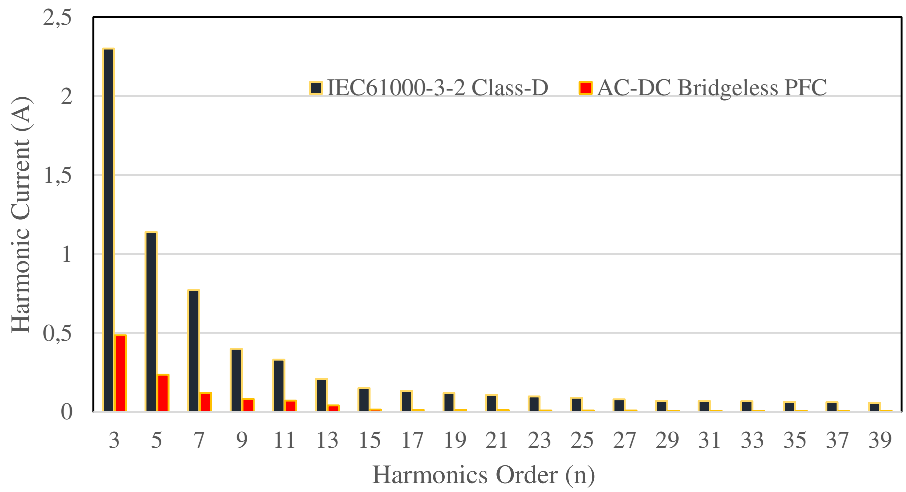


Figure 5.40 State 3, Comparison of bridgeless PFC harmonics and IEC 61000-3-2-Class-D standards.

In the case of 30% load, in HV battery side and LV battery side, the performance results of the proposed circuit are summarized in Table 5.8.

Table 5.8 Performance results in the case 30% load

| | Power Factor | THD | MPPT Accuracy | ΔV(ripple) |
|---|---|---|---|---|
| HV (Bat.) | 0.99 | < IEC61000-3-2-D-Class | -- | <1V |
| LV (Bat.) | -- | --- | >0.99 | <1V |

### 5.4.4. State 4 (20% Load)

Grid voltage and current, DC-Link voltage and current, phase angle between voltage and current, power factor are shown in Figure 5.41. Bridgeless converter side load voltage and current are shown in Figure 5.42. PV panel power-voltage characteristics, PV power, PV voltage and current, are shown in Figure 5.43. PV panel side load voltage and current are shown in Figure 5.44. Grid-side resonance capacitor and transformer magnetizing current, switch current, switch

voltage, rectifier diode current are shown in Figure 5.45. PV panel side resonance capacitor and transformer magnetizing current (Icr-Im), switch current (IsQ1), switch voltage (VsQ1), rectifier diode current are shown in Figure 5.46. Comparision of bridgeless PFC side grid current harmonics and IEC 61000-3-2-Class-D standards are shown in Figure 5.47.

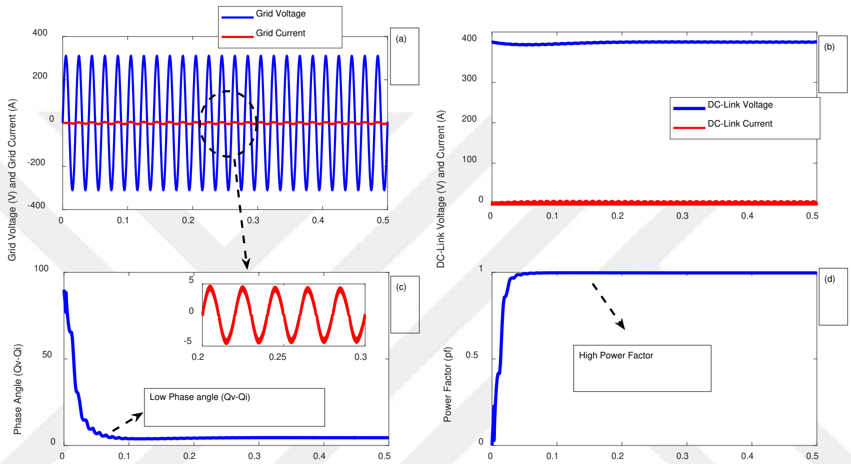


Figure 5.41 State 4, Grid voltage and current (a), DC-Link voltage and current (b), Phase angle between voltage and current (c), power factor (d)

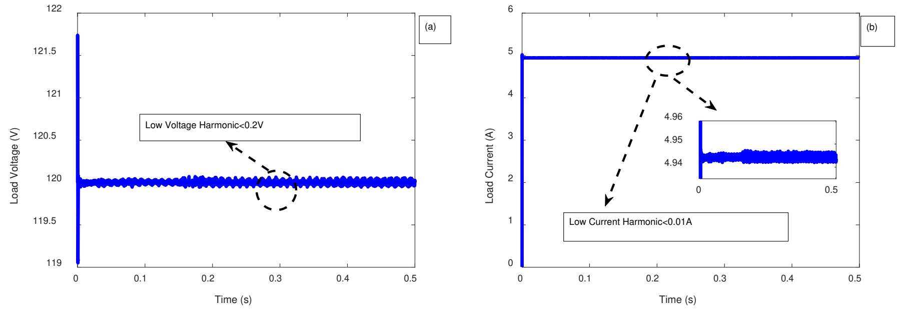


Figure 5.42 State 4, Load voltage (HV-battery side) (a), Load current (HV-battery side) (b)

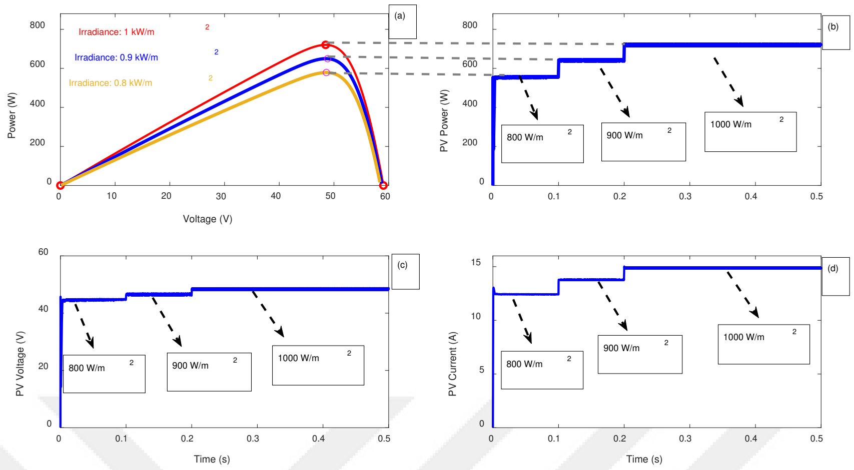


Figure 5.43 State 4, PV panel power-voltage characteristics (a), PV power (b), PV voltage (c), PV current (d)

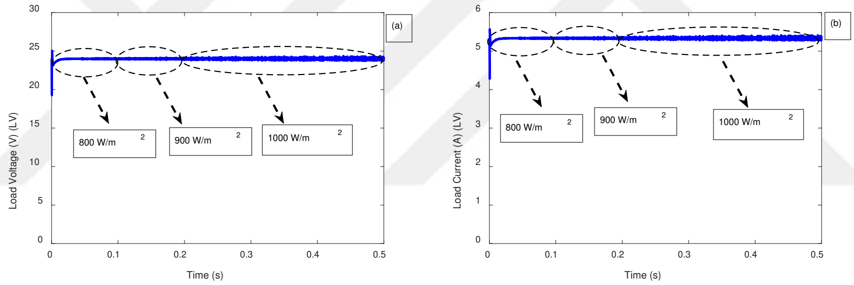


Figure 5.44 State 4, Load voltage (LV-battery side) (a), Load current (LV-battery side) (b)

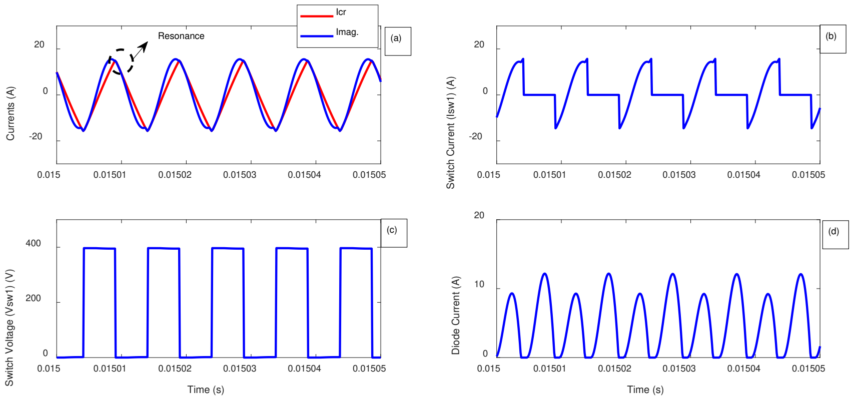

Figure 5.45 State 4, Grid side resonant capacitor and transformer magnetizing current (Icr-Im) (a) Switch current (IsQ2) (b), Switch voltage (VsQ2) (c), Rectifier diode current (d)

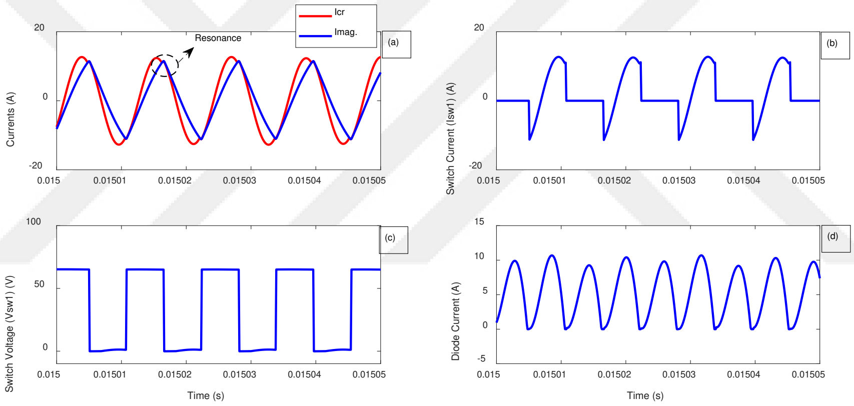

Figure 5.46 State 4, PV panel-side resonance capacitor and transformer magnetizing current (Icr-Im) (a) Switch current (IsQ1) (b), Switch voltage (VsQ1) (c), Rectifier diode current (d)

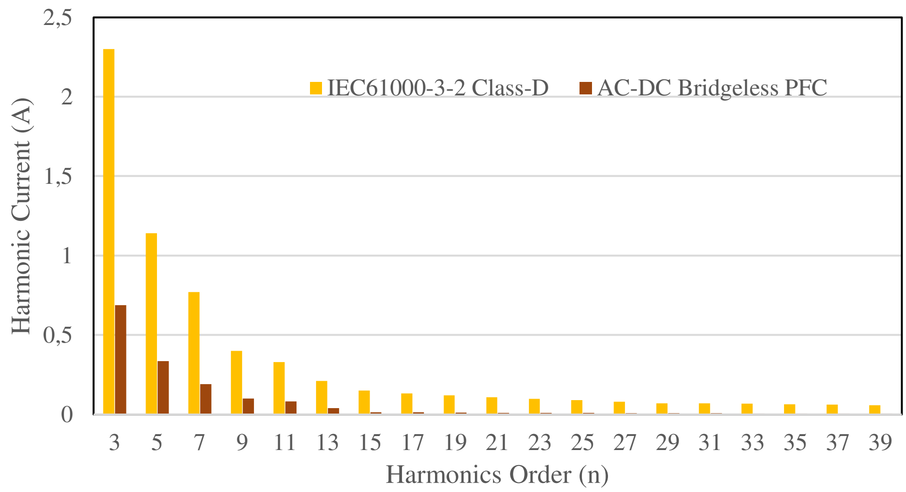


Figure 5.47 State 4, Comparison of bridgeless PFC harmonics and IEC 61000-3-2-Class-D standards.

In the case of 20% load, in HV battery side and LV battery side, the performance results of the proposed circuit are summarized in Table 5.9.

Table 5.9 Performance results in the case 20% load

| | **Power Factor** | **THD** | **MPPT Accuracy** | **ΔV(ripple)** |
|---|---|---|---|---|
| HV (Bat.) | 0.99 | < IEC61000-3-2-D-Class | -- | <0.5 V |
| LV (Bat.) | --- | --- | >0.99 | <0.5 V |

### 5.4.5. State 5 (10% Load)

Grid voltage and current, DC-Link voltage and current, phase angle between voltage and current, power factor are shown in Figure 5.48. Bridgeless converter side load voltage and current are shown in Figure 5.49. PV panel power-voltage characteristics, PV power, PV voltage and current, are shown in Figure 5.50. PV panel side load voltage and current are shown in Figure 5.51. Grid-side resonance capacitor and transformer magnetizing current, switch current, switch

voltage, rectifier diode current are shown in Figure 5.52. PV panel side resonance capacitor and transformer magnetizing current (Icr-Im), switch current (IsQ1), switch voltage (VsQ1), rectifier diode current are shown in Figure 5.53. Comparision of bridgeless PFC side grid current harmonics and IEC 61000-3-2-Class-D standards are shown in Figure 5.54.

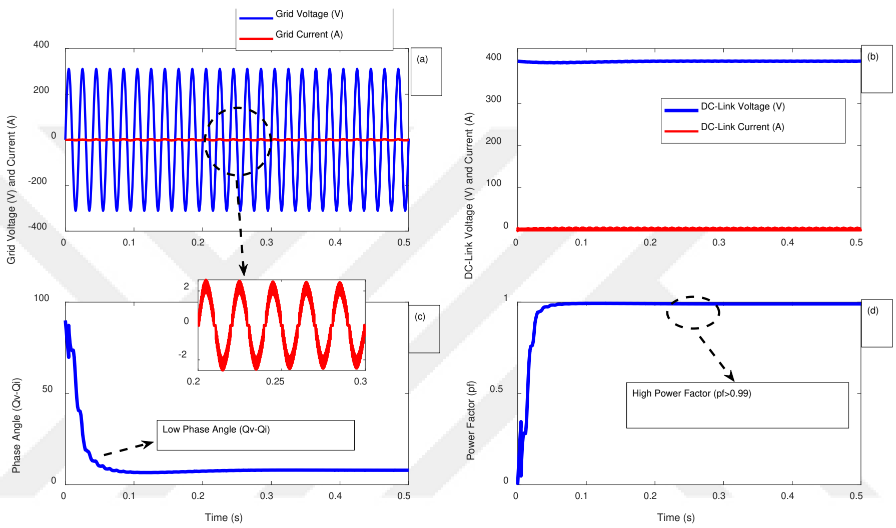


Figure 5.48 State 5, Grid voltage and current (a), DC-Link voltage and current (b), Phase angle between voltage and current (c), power factor (d)

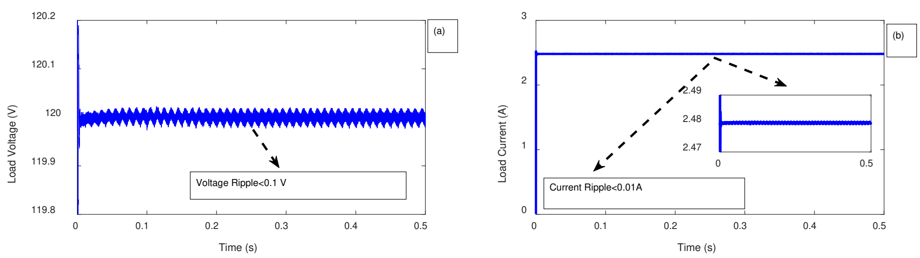


Figure 5.49 State 5, Load voltage (HV-battery side) (a), Load Current (HV-battery side) (b)

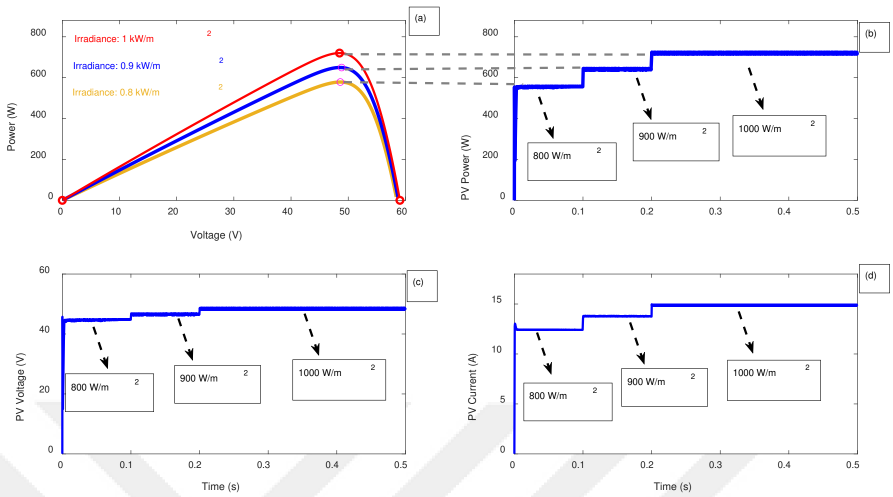


Figure 5.50 State 5, PV panel power-voltage characteristics (a), PV power (b), PV voltage (c), PV current (d)

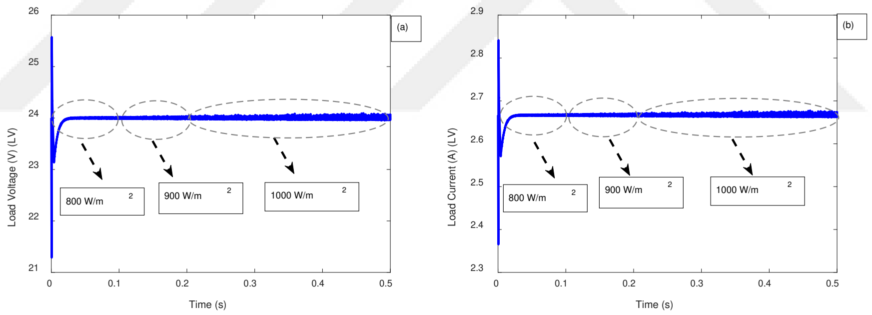


Figure 5.51 State 5, Load voltage (LV-battery side) (a), Load current (LV-battery side) (b)

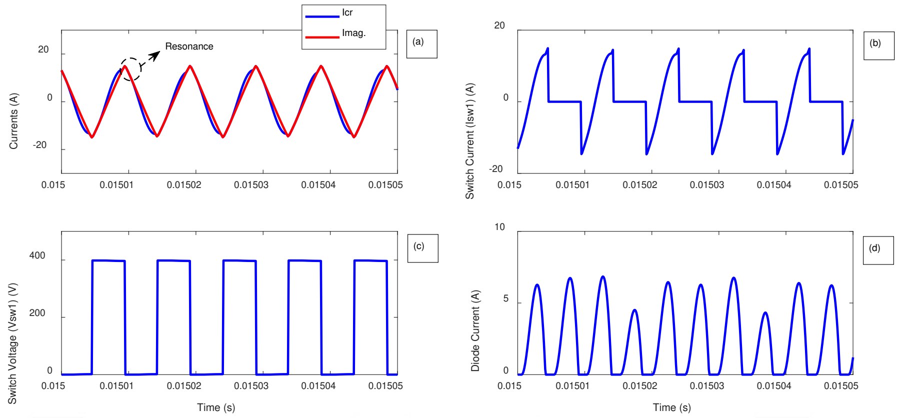


Figure 5.52 State 5, Grid-side resonance capacitor and transformer magnetizing current (Icr-Im) (a) Switch current (IsQ2) (b), Switch voltage (VsQ2) (c), Rectifier diode current (d)

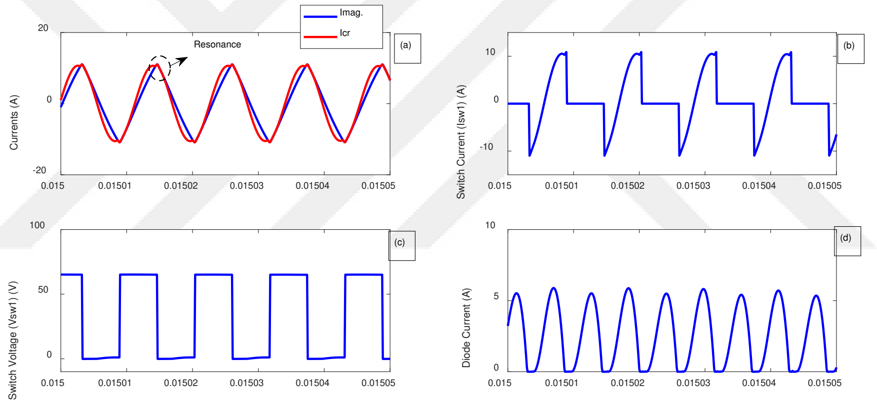


Figure 5.53 State 5, PV panel-side resonance capacitor and transformer magnetizing current (Icr-Im) (a) Switch current (IsQ1) (b), Switch Voltage (VsQ1) (c), Rectifier diode current (d)

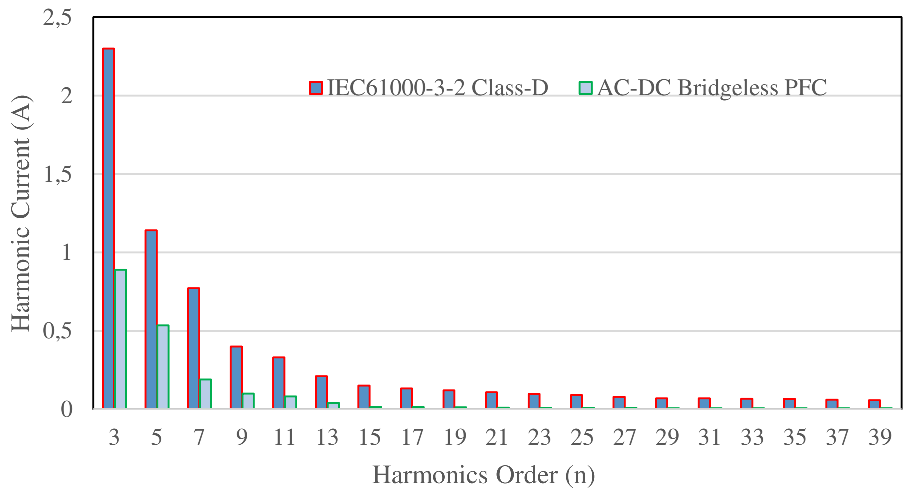


Figure 5.54 State 5, Comparison of bridgeless PFC Harmonics and IEC 61000-3-2-Class-D standards.

In the case of 10% load, in HV battery side and LV battery side, the performance results of the proposed circuit are summarized in Table 5.10.

Table 5.10 Performance results in the case 10% load

| | **Power Factor** | **THD** | **MPPT Accuracy** | **ΔV(ripple)** |
|---|---|---|---|---|
| HV (Bat.) | ≥0.99 | < IEC61000-3-2-D-Class | -- | <0.5 V |
| LV (Bat.) | --- | --- | >0.99 | <0.5 V |

### 5.4.6. State 6 (5% Load)

Grid voltage and current, DC-Link voltage and current, phase angle between voltage and current, power factor are shown in Figure 5.55. Bridgeless converter side load voltage and current are shown in Figure 5.56. PV panel power-voltage characteristics, PV power, PV voltage and current, are shown in Figure 5.57. PV panel side load voltage and current are shown in Figure 5.58. Grid-side resonance capacitor and transformer magnetizing current, switch current, switch

voltage, rectifier diode current are shown in Figure 5.59. PV panel side resonance capacitor and transformer magnetizing current (Icr-Im), switch current (IsQ1), switch voltage (VsQ1), rectifier diode current are shown in Figure 5.60. Comparision of bridgeless PFC side grid current harmonics and IEC 61000-3-2-Class-D standards are shown in Figure 5.61.

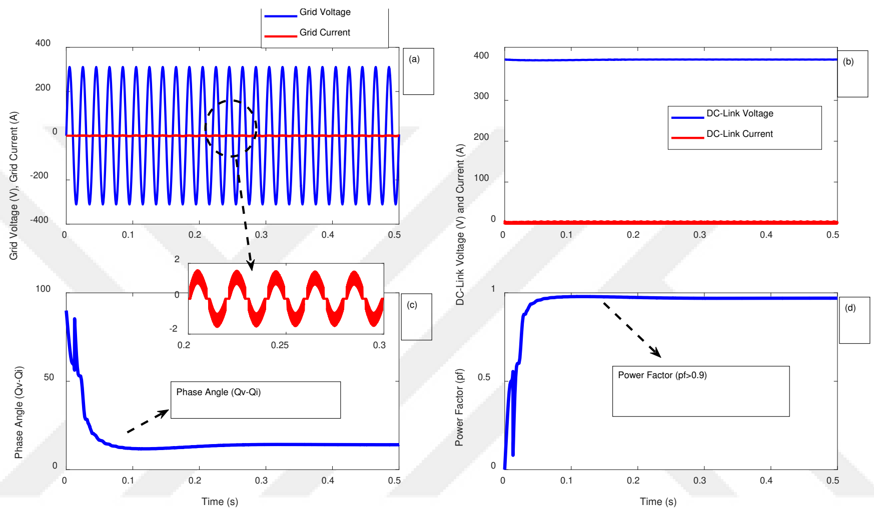


Figure 5.55 State 6, Grid voltage and current (a), DC-Link voltage and current (b), Phase angle between voltage and current (c), power factor (d)

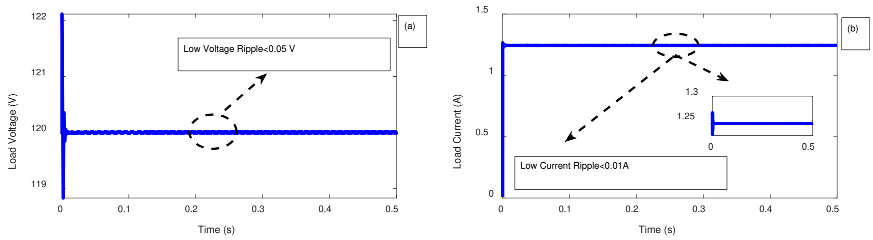


Figure 5.56 State 6, Load voltage (HV-battery side) (a), Load current (HV-battery side) (b)

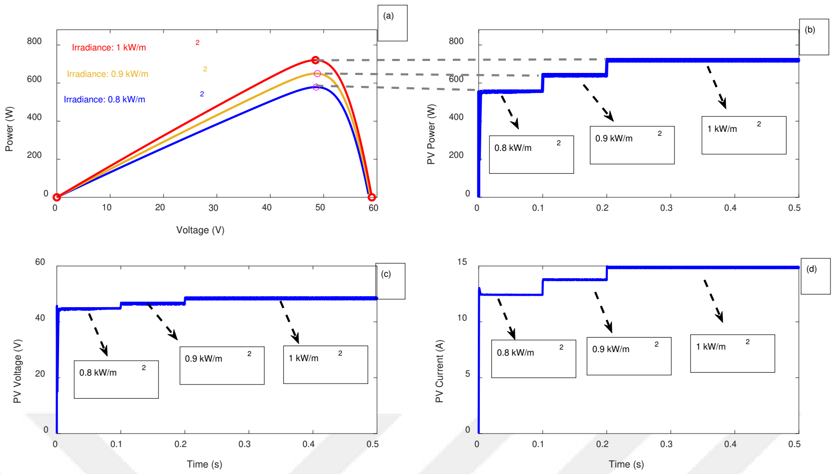


Figure 5.57 State 6, PV panel power-voltage characteristics (a), PV power (b), PV voltage (c), PV current (d)

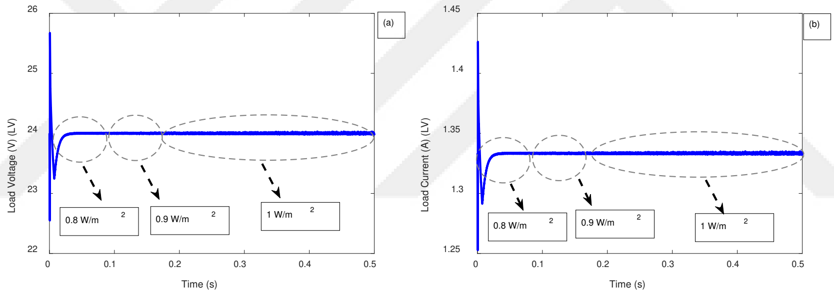


Figure 5.58 State 6, Load voltage (a), Load current (LV-battery side) (b)

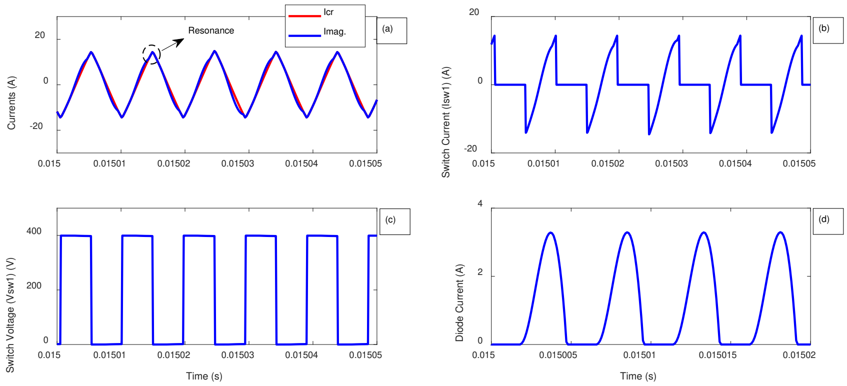


Figure 5.59 State 6, Grid-side resonance capacitor and transformer magnetizing current (Icr-Im) (a) Switch current (IsQ2) (b), Switch voltage (VsQ2) (c), Rectifier diode current (d)

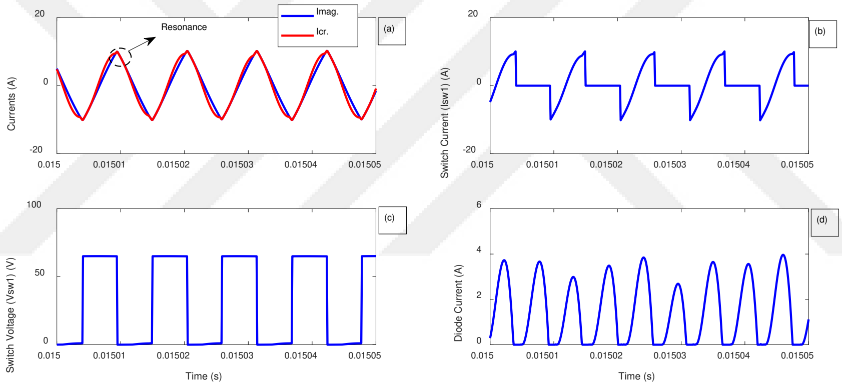


Figure 5.60 State 6, PV panel-side resonant capacitor and transformer magnetizing current (Icr-Im) (a) Switch current (IsQ1) (b), Switch voltage (VsQ1) (c), Rectifier diode current (d)

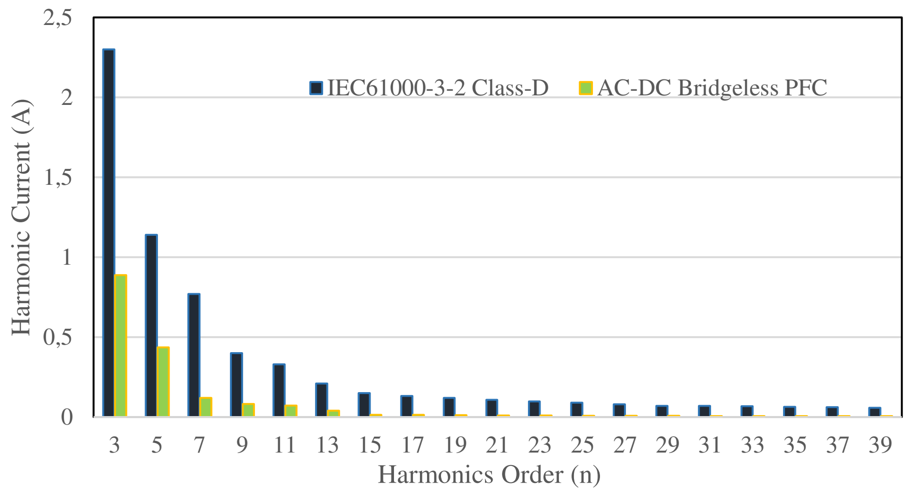

Figure 5.61 State 6, Comparison of bridgeless PFC harmonics and IEC 61000-3-2-Class-D standards.

In the case of 5% load, in HV battery side and LV battery side, the performance results of the proposed circuit are summarized in Table 5.11.

Table 5.11 Performance Results in the case 5% Load

| | **Power Factor** | **THD** | **MPPT Accuracy** | **ΔV(ripple)** |
|---|---|---|---|---|
| HV (Bat.) | ≥0.96 | <EC61000-3-2-D-Class | -- | <0.5 V |
| LV (Bat.) | --- | --- | >0.99 | <0.5 V |

Under variable load states, the efficiency, load voltage ripples (ΔV) and THD ratios of the proposed system are presented in Figure 5.62.

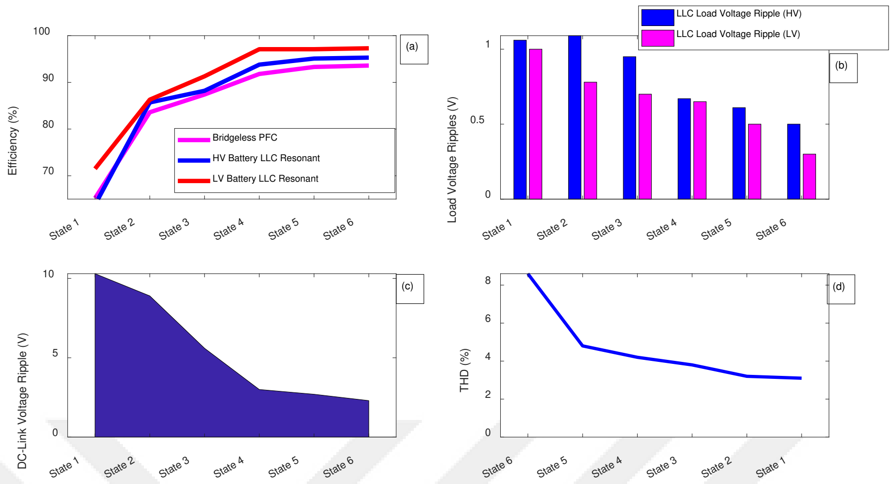


Figure 5.62 Efficiencies (a), Load voltage ripples (b), DC-Link voltage ripples (c), THD (d).

The European efficiency standards calculations for the system is shown as the following equation:

$$\begin{aligned}
&EU\eta = 0.03\eta_{\%5} + 0.06\eta_{\%10} + 0.13\eta_{\%20} + 0.1\eta_{\%30} + 0.48\eta_{\%50} + 0.2\eta_{\%100} \\
&EU\eta_{(LLC\text{-}HV)} = 92{,}041\% \\
&EU\eta_{(LLC\text{-}LV)} = 90{,}743\% \\
&EU\eta_{(AC-DC_{PFC})} = 94.48\%
\end{aligned} \tag{5.29}$$

## 5.5. Discussion

In this study, two-stage battery charging unit is proposed. The first stage of the proposed battery charger consists of a mains powered ac-dc PFC converter and half bridge LLC resonance converter. The power factor (pf) of the AC-DC pfc converter has been observed to be greater than 0.99 in most load cases. In addition, the THD of the mains current has been compliant with the IEC61000-3-2-D-Class standard in most load cases. In the second phase of the proposed battery charger, the PV powered half bridge LLC is modeled as low power battery dynamic load for auxiliaries loads with resonance converter. For the proposed battery charger, the MPPT method has also been proposed and its performance has been observed to be better than traditional methods. The aim of this study is to feed the high power battery and low power battery through the same converter, to enable the electric vehicle to take more miles with a single charge process and at the same time to reduce the electricity production cost after a certain period of time by using environmentally friendly green energy. The results obtained are enough to prove the accuracy of the proposed method Electrical characteristics and system parameters are presented in Table 5.12.

Table 5.12 System parameters in Topology-2

| Parameters | Values | Parameters | Values |
|---|---|---|---|
| Vin (PFC) | 85-265 V | $R_{Load}$ (HV) | 4.84Ω-96.96Ω |
| Frequency (PFC) | 48-65 Hz | $V_{out}$ (HV) | 120 V |
| Vdc-Link (HV) | 365-420 V | Kp | 0.35 |
| Power (kW) (HV) | 3.3 kW (Level-2) | Ki | 6.815 |
| Lr1 | 8.364 µH | *THD* | <5% |
| Cr1 | 302.82nF | *pf* | >0.99 |
| Lm1 | 31.573µH | *fp* | 57 KHz |
| *fr1* | 100 KHz | Lboost | 0.6 mH |
| C*boost* | 500µF | Cdc-link | 984 µF |
| $PV_{Power}$ (W) $_{(STC-MPP)}$ | 720,4 W | $PV_{Voltage}$ (V) $_{(STC-MPP)}$ | 24 V |
| $C_{dc-Link}$ (LV) | 250 µF | $R_{Load}$ (LV) | 0.9 Ω-18 Ω |
| $V_{out}$ (LV) | 24 V | $L_{r2}$ | 2.737 µH |

Electrical characteristics of Zhejiang Wanxiang Solar WXS180P PV panel, which is selected from the PV array simulator for the proposed two-stage on-board battery charging system, are shown in detail in Table 5.13.

Table 5.13 Electrical characteristics of PV panel

| | **PV Panel Model** | **Zhejiang Wanxiang Solar WXS180P** |
|---|---|---|
| **Module Data** | Open Circuit Voltage | 29.52 V |
| | Voltage at maximum Power Point $V_{mpp}$ | 24.24 V |
| | Temperature coefficient of Voc (%/deg.C) | -0.32398 |
| | Cells per module (Ncell) | 48 |
| | Short-circuit current Isc (A) | 8.3 A |
| | Current at maximum power point Imp (A) | 7.43 A |
| | Temperature coefficient of Isc (%/deg.C) | 0.027 |
| **Model Parameter** | Light-generated current IL (A) | 8.3808 A |
| | Diode saturation current I0 (A) | 6.972e-11 |
| | Diode ideality factor | 0.9432 |
| | Shunt resistance Rsh (ohms) | 46.97 |
| | Series resistance Rs (ohms) | 0.231 |
| **Array Data** | Parallel strings | 2 |
| | Series-connected modules per string | 2 |

# 6. CONCLUSION AND FUTURE

This section presents the results of the proposed studies, summarizes the main contributions of the thesis study to the Literature, and indicates the areas of study in which the thesis can be directed in the future.

## 6.1. Conclusion and Discussion

Electric vehicles technology has become very interesting in recent years due to its advantageous features. However, there are still aspects that need to be improved, such as improving the performance of electric vehicles, allowing them to be charged in less time and travel more with a single charge process. Power components (motor, auxiliary loads, lighting etc.) in electric vehicles are powered by batteries. Therefore, battery chargers have an important place in the research topics for electric vehicles.

During the battery charging process of electric vehicles, it is necessary to provide efficient and reliable transfer of energy. However, some problems may occur due to the design of the battery charging unit while charging is taking place. In order to eliminate these problems, DC-DC converters are of great interest due to the functional interface between the battery and the grid. In addition, DC-DC converters have a significant impact on improving efficiency, power quality and reliability.

In this thesis, two different studies are proposed for two-stage on-board battery charge topologies.

Since the internal volume of electric vehicles is limited, the on-board battery chargers recommended for Electric vehicles must meet some requirements. These requirements are described in the Literature as follows: high power density, high efficiency, good heat dissipation, low harmonic distortion and high power factor. The power density and efficiency of on-board battery chargers largely depend on the design of the isolated DC-DC converters. In addition, low total harmonic distortions (THD) occurring in the grid current during charging process improves both power conversion performance and electrical quality, the harmonic distortions occurring in the current should be within the range specified in IEC 61000-3-2 THD standards. In order to carry out charging under different load conditions, pi-based controller is used in conventional grid-connected on-board battery charging units. However, the pi based controller is generally; has problems such as slow dynamic response, steady state errors and complex structure. In the proposed Topology-I, the output voltage was controlled with artificial neural networks to eliminate the negative effects of the conventional pi-based controller. In addition, in the isolated DC-DC converters operated at high frequencies, circuit element sizes decrease while electromagnetic interference (EMI) and switching losses increase. In the proposed Topology-I, without any hardware changes, significant improvements were made in the variable load conditions, dynamic response and steady state error compared to the conventional pi control method thanks to the proposed Topology-I (shown in Figure 55). Moreover, thanks to the soft switching (ZVS) method applied to the LLC resonance converter, the efficiency of proposed topology increased 2% and 96.8% peak efficiency has been reached. In addition, the proposed study to calculate efficiency according to the European efficiency standard was operated in 6 different load situations from 5% to 100%, and efficiency was calculated as > 93%. It was observed that power factor> 0.99 and output voltage ripples <1V for all load cases. In addition, grid current harmonics for all load cases have been observed to comply with the IEC 61000-3-2 THD standard.

For the topology II, a two-stage battery charger architecture that can be powered both from the grid and a renewable energy source, was developed. A half-bridge LLC resonance (HBLLC) DC-DC converter is designed for the proposed battery charger and has been tested in a wide load range (5% load to 100% load). The first input of the HBLLC resonance converter is powered from the bridgeless PFC converter connected to the grid, while the other input is powered from the photovoltaic (PV) panel. Moreover, in the Topology-II, for PV system, a maximum power point tracking (MPPT) method with higher accuracy and lower convergence time than traditional methods, was developed. On the other hand, the first output of the HBLLC resonance converter connected to the high power battery, while the other output connected to the auxiliary battery that feeds low power loads. In conventional battery chargers, the auxiliary battery is powered by the high power battery. In the proposed operation, the auxiliary battery is charged by the PV system. Thus, the high power battery has more energy to power the electric motor and allows the electric vehicle to travel more miles with a single charge process. In addition, the proposed architecture can save energy costs demanded from the grid in the long term. Another advantage of the proposed battery charge architecture is creating a compact structure to save extra cable cost. The accuracy rate of the MPPT method proposed for Topology II was compared with conventional methods under different radiation and temperature conditions, and it was observed that in all cases it was over 99% (the results are shown in detail in figures 8, 9 and 10). In addition, the proposed study to calculate efficiency according to the European efficiency standard was run in 6 different load situations from 5% to 100%, and efficiency was calculated as > 90%. It was observed that power factor > 0.99 and output voltage ripples ≤1V for all load cases. In addition, grid current harmonics for all load cases have been observed to comply with the IEC 61000-3-2 THD standard.

### 6.2. Future Work

The studies planned for the future are presented below.

- Two-stage battery charging units (Topology-I and II) given as computer applications are planned to be carried out experimentally.
- The power circuit of the proposed topologies will be modified to reduce the size and number of components.

- For the battery charging unit proposed in Topology-II, different soft switching methods will be applied to reduce switching losses and EMI.
- In order to improve the dynamic response of the two-stage battery charging unit proposed in Topology-II at different loads, different and easily applicable control methods will be applied.

## REFERENCES


Abdelmessih G.Z., Alonso J. M., Costa M. A. D., 2018. Loss Analysis for Efficiency Improvement of the Integrated Buck–Flyback LED Driver. IEEE Transactions On Industry Applications 54(6): 6543-6553.

Abdelsalam A.K., Massoud A.M., Ahmed S., Enjeti P.N., 2011. High Performance Adaptive Perturb and Observe MPPT Technique for Photovoltaic-Based Microgrids. IEEE Transactions on Power Electronics 26(4): 1010-1021.

Ahmed J., Salam Z., 2015. An improved perturb and observe (P&O) maximum power point tracking (MPPT) algorithm for higher efficiency. Applied Energy 150: 97–108

Akamatsu K., Mishima T., Nakaoka M., 2012. A secondary-side phase-shifted zero voltage and zero current full-range soft-switching PWM DC-DC converter for EV battery chargers. International Conference on Renewable Energy Research and Applications (ICRERA), Nagasaki, 2012, pp. 1-6.

Alam M.U. Investigation of Bridgeless Single-Phase Solutions for AC-DC Power Factor Corrected Converters. PhD Thesis, University of British Columbia, Okanagan, Canada, 2017.

Alemdar Ö. Ş. Design And Implementation of an Unregulated DC-DC Transformer Module Using LLC Resonant Converter. MSc Thesis, Middle East Technical University. Turkey, 2016.

Alhamrouni I., Hanis W.I., Salem M., Albatsh F. M., B. Ismail B., 2016. Application of DC-DC converter for E.V battery charger using PWM technique and hybrid resonant. IEEE International Conference on Power and Energy (PECon), Melaka, pp. 133-138.

Ali K., Das P., Panda S.K., 2017. Analysis and Design of APWM Half-Bridge Series Resonant Converter With Magnetizing Current Assisted ZVS. IEEE Transactions on Industrial Electronics, 64(3): 1993-2003. (LOSSES)

Altıntaş N. Yumuşak Anahtarlamalı DC-DC Dönüştürücülerin İncelenmesi. Yüksek Lisans Tezi, Yıldız Teknik Üniversitesi, İstanbul, 2007.

Asa E., K. Çolak K., Czarkowski D., León F., Sefa I., 2013. PLL control technique of LLC resonant converter for EVs battery charger. 4th International Conference on Power Engineering, Energy and Electrical Drives, Istanbul, pp. 1382-1386.

Assadi S.A., Matsumoto H., Moshirvaziri M., Nasr M., Zaman M. S., Trescases O., 2018. Active Mitigation of Transformer Saturation in a Dual-Active-Bridge Converter for Electric Vehicle Chargers. 20th European Conference on Power Electronics and Applications (EPE'18 ECCE Europe), Riga: pp. 1-10

Baek J.I., Kim C.-E., Lee J.B., Youn H.-S., Moon G.-W., 2018. A Simple SR Gate Driving Circuit with Reduced Gate Driving Loss for Phase-Shifted Full-Bridge Converter. IEEE Transactions On Power Electronics, 33(11): 9310-9317.

Bai H., Taylor A., Guo W., Szatmari-Voicu G., Wang N., Patterson J., Kane J., 2012. Design of an 11 kW power factor correction and 10 kW ZVS DC/DC converter for a high-efficiency battery charger in electric vehicles. IET Power Electronics 5(9): 1714-1722.

Bendib B., Krim F., Belmili H., Almi M.F., Boulouma S., 2014. Advanced Fuzzy MPPT Controller for a stand-alone PV system. Energy Procedia 50: 383 – 392.

Büyük M. Design and Experimental Verification of Resonance Damping Methods for A Shunt Active Power Filter With LCL Filter. PhD Thesis, University of Cukurova, Turkey, 2019.

Çelik Ö. Controller Design and Experimental Verification of Grid-Connected Micro Inverters for Photovoltaic Applications. PhD Thesis, University of Çukurova, Turkey, 2019.

Çelik O., Teke A., Yıldırım H.B., 2016. The optimized artificial neural network model with Levenberge-Marquardt algorithm for Global solar radiation estimation in Eastern Mediterranean Region of Turkey. Journal of Cleaner Production, 116:1-12.

Chamjangali M. A., Beglari M., Bagherian G., 2007. Prediction of cytotoxicity data (CC50) of anti-HIV 5-pheny-l-phenylamino-1H-imidazole derivatives by artificial neural network trained with Levenberge-Marquardt algorithm. J Mol Graph, Model 26(1):360-367.

Chen Z., Zhou Q., Xu J., 2015. Coupled-inductor boost integrated flyback converter with high-voltage gain and ripple-free input current" IET Power Electron 8(2): 213–220.

Cheng H., Chen W., Wang C., Deng J., 2018. Open Circuit Fault Diagnosis and Fault Tolerance of Three-Phase Bridgeless Rectifier. Electronics *7*(11): 1-15.

Choi J-Y., Choi S-W., Lee J-Y., 2018. Hybrid PWM DC/DC converter for EV on-board charger with single transformer. EPE Journal, 28 (2): 63–74.

Choi W., Yang M., Cho H., 2014. High-Frequency-Link Soft-Switching PWM DC–DC Converter for EV On-Board Battery Chargers. IEEE Transactions on Power Electronics, 29(8): 4136-4145.

Connaughton A., Talei A. P., Leong K. K., Krischan K., Muetze A. 2019. Variable On-Time Control Scheme for the Secondary-Side Controlled Flyback Converter. IEEE Transactions On Power Electronics 34(3): 2416-2426.

Cunha V. A. G., Neto A. O. C., Lima G.B., Freitas L. C. G., 2019. A Bridgeless Boost Half Bridge DC-DC Converter for Electrical and Hybrid Vehicle Applications," 2019 IEEE PES Innovative Smart Grid Technologies Conference - Latin America (ISGT Latin America), Gramado, Brazil, pp. 1-6.

Das P., Pahlevaninezhad M., Drobnik J., Moschopoulos G., Jain P. K., 2013. A Nonlinear Controller Based on a Discrete Energy Function for an AC/DC Boost PFC Converter. IEEE Transactions on Power Electronics 28(12): 5458-5476.

Daş Y., Tekin A., Boztepe M., Tarhan C., 2019. A Robust Voltage Control Method for Universal EV Battery Charger LLC Resonant Converters. IEEE International Conference on Sustainable Energy Technologies and Systems (ICSETS), Bhubaneswar, India, pp. 120-125, doi: 10.1109/ICSETS.2019.8744865.

De Gusseme K., Van de Sype D.M., Van den Bossche A. P. M., Melkebeek, J. A., 2007. Input-Current Distortion of CCM Boost PFC Converters Operated in DCM. IEEE Transactions on Industrial Electronics 54(2):858-865.

Deng J., Li S., Hu S., Mi C.C., Ma R., 2014. Design Methodology of LLC Resonant Converters for Electric Vehicle Battery Chargers. IEEE Transactions On Vehicular Technology, 63(4): 1581-1592.

Dobi A-H. M., Sahid, M. R., Sutikno T., 2018. Overview of Soft-switching DC-DC Converters. International Journal of Power Electronics and Drive System (IJPEDS), 9(4): 2006-2018

Duan C., Bai H., Guo W., Nie Z., 2015. Design of a 2.5-kW 400/12-V High-Efficiency DC/DC Converter Using a Novel Synchronous Rectification Control for Electric Vehicles. IEEE Transactions on Transportation Electrification 1(1):106-114.

Elgendy M.A., Zahawi B., and D. J. Atkinson D.J., 2013. Assessment of the Incremental Conductance Maximum Power Point Tracking Algorithm. IEEE Transactions On Sustainable Energy 4(1): 108-117.

Elgendy, M.A., Zahawi B., Atkinson D.J., 2012. Assessment of Perturb and Observe MPPT Algorithm Implementation Techniques for PV Pumping Applications. IEEE Transactions on Sustainable Energy 3(1): 21-33.

Emrani A., Adib E., Farzanehfard H., 2012. Single-Switch Soft-Switched Isolated DC–DC Converter" IEEE Transactıons On Power Electronıcs, 27(4): 1952-1957.

Feizi M., Beiranvand R., 2020. An Improved Phase-Shifted Full-Bridge Converter with Extended ZVS Operation Range for EV Battery Charger Applications. 11th Power Electronics, Drive Systems, and Technologies Conference (PEDSTC), Tehran, Iran, pp. 1-6.

Frivaldsky ́ I. M., Drgon ˇa P., Špánik P., 2013. Experimental analysis and optimization of key parameters of ZVS mode and its application in the proposed LLC converter designed for distributed power system application. Electrical Power and Energy Systems 47 (2013) 448–456 (LOSSES)

Gautam D. S., Musavi F., Eberle W., Dunford W. G., 2013. A Zero-Voltage Switching Full-Bridge DC–DC Converter with Capacitive Output Filter for Plug-In Hybrid Electric Vehicle Battery Charging. IEEE Transactions on Power Electronics, 28(12): 5728-5735.

Golahmar-Zavare A., Mohamadian M., Beiranvand R., 2015. High efficiency, low size, and low weight vehicle battery charger," The 6th Power Electronics, Drive Systems & Technologies Conference (PEDSTC2015), pp. 96-102.

Guenounou O., Dahhou B., Chabour F., 2011. Adaptive fuzzy controller based MPPT for photovoltaic systems. Energy Conversion and Management 78: 843–850

Gumera X.D., Caberos A., Huang S., 2017. Design and Implementation of a High Efficiency Cost Effective EV Charger Using LLC Resonant Converter. Asian Conference on Energy, Power and Transportation Electrification (ACEPT), Singapore, 2017, pp. 1-6.

He P., Khaligh A., 2017. Comprehensive Analyses and Comparison of 1 kW Isolated DC–DC Converters for Bidirectional EV Charging Systems. IEEE Transactions On Transportation Electrification 3(1):147-156.

Hou N., Song W., Wu M., 2016. Minimum-Current-Stress Scheme of Dual Active Bridge DC–DC Converter with Unified Phase-Shift Control. IEEE Transactions On Power Electronics, 31(12): 8552-8561

Hsieh Y.-C., Huang C.-S., 2011. Li-ion battery charger based on digitally controlled phase-shifted full-bridge converter. IET Power Electronics 4(2): 242–247.

Hua C.C., Deng Y.-L., 2019. A Novel Dual-Bridge LLC Resonant Converter with Wide Range of Low Input Voltage. Energy Procedia 156: 361-365.

IEA (2020), Global EV Outlook 2020, IEA, Paris https://www.iea.org/reports/global-ev-outlook-2020

Iyer V. M., Gulur S., Bhattacharya S., 2017. Optimal design methodology for dual active bridge converter under wide voltage variation. 2017 IEEE Transportation Electrification Conference and Expo (ITEC), Chicago, IL, 2017, pp. 413-420.

Iyer V.M., Gulur S., Bhattacharya S., 2019. Small-Signal Stability Assessment and Active Stabilization of a Bidirectional Battery Charger. IEEE Transactions on Industry Applications. 55(1): 563-574.

Jeong S-G., , Jeong Y-S., Kwon J-M., Kwon B-H.,2019. A Soft-Switching Single-Stage Converter With High Efficiency for a 3.3-kW On-Board Charger. IEEE Transactions On Industrial Electronics, 66(9):6959-6967.

Jovanovic ́ M.M., Irving B. T., 2016. On-the-Fly Topology-Morphing Control—Efficiency Optimization Method for LLC Resonant Converters Operating in Wide Input- and/or Output-Voltage Range. IEEE Transactions On Power Electronics, 31(3): 2596-2608.

Jung J-H., Kwon J-G., 2007. Theoretical analysis and optimal design of LLC resonant converter. European Conference on Power Electronics and Applications, Aalborg, pp. 1-10, doi: 10.1109/EPE.2007.4417639.

Kanamarlapudi V. R. K., Wang B., Kandasamy N. K., So P. L., 2018. A New ZVS Full-Bridge DC–DC Converter for Battery Charging with Reduced Losses Over Full-Load Range. IEEE Transactions on Industry Applications, 54(1): 571-579.

Kanamarlapudi V. R. K., Wang B., So P. L., Wang Z., 2017. Analysis, Design, and Implementation of an APWM ZVZCS Full-Bridge DC–DC Converter for Battery Charging in Electric Vehicles" IEEE Transactions On Power Electronics 32(8): 6145-6160.

Kang S. H., Maksimovic ´ D., Cohen I., 2012. Efficiency Optimization in Digitally Controlled Flyback DC–DC Converters Over Wide Ranges of Operating Conditions. IEEE Transactions on Power Electronics, 27(8): 3734-3748.

Kang S.-W., Kim H.-J., Cho B.-H., 2016. Adaptive Voltage-Controlled Oscillator for Improved Dynamic Performance in LLC Resonant Converter. IEEE Transactions On Industry Applications, 52(2): 1652-1659.

Karaarslan A., Iskender I., 2011. The analysis of AC-DC boost PFC converter based on peak and hysteresis current control techniques. Int J Tech Phys Prob Eng (IJTPE) 3(2):100-105.

Karaarslan A., İskender İ., **2009.** Pure Sinusoidal Input Voltage Based Bridgeless PFC Converter Using TMS320F2812 Digital Signal Processor. International Conference on Electrical and Electronics Engineering - ELECO **: 234-238.**

Kathiresan R., Das P., Reindl T., Panda S. K., 2017. A Novel ZVS DC–DC Full-Bridge Converter with Hold-Up Time Operation. IEEE Transactions on Industrial Electronics, 64(6): 4491-4500.

Kim S., Kang, F-S., 2015. Multifunctional Onboard Battery Charger for Plug-in Electric Vehicles. IEEE Transactions On Industrial Electronics 62(6); 3460-3472.

Kim Y., Oh C., Sung W., Lee B.K., 2017. Topology and Control Scheme of OBC–LDC Integrated Power Unit for Electric Vehicles. IEEE Transactions on Power Electronics 32(3): 1731-1743.

Kondo R., Y. Higaki Y., Yamada M., 2016. Proposition and experimental verification of a bi-directional isolated DC/DC converter for battery charger-discharger of electric vehicle. IEEE Applied Power Electronics Conference and Exposition (APEC), Long Beach, CA, 2016, pp. 1713-1720.

Kongjeen Y., Bhumkittipich K., 2018. Impact of Plug-in Electric Vehicles Integrated into Power Distribution System Based on Voltage-Dependent Power Flow Analysis. Energies 2018, 11, 1571; pp. 1-16. doi:10.3390/en11061571

Koroglu T., Tan A., Savrun M. M., Cuma M.U., Bayindir K.C., Tumay M., 2019. Implementation of a novel Hybrid UPQC topology endowed with an Isolated Bi-Directional DC-DC Converter at DC link. in IEEE Journal of Emerging and Selected Topics in Power Electronics 8(3):2733-2746

Kumar S.S., Panda A.K., Ramesh T., 2014. A ZVT–ZCT PWM synchronous buck converter with a simple passive auxiliary circuit for reduction of losses and efficiency enhancement. Ain Shams Engineering Journal (2015) 6, 491–500.

Kundu U., Sensarma P., 2017. A Unified Approach for Automatic Resonant Frequency Tracking in LLC DC–DC Converter. IEEE Transactions On Industrial Electronics, 64(12): 9311-9321.

Kupati S.K,, Chavan M., Bhattad S., Arun N., 2015. Average current mode controlled power factor correction converter. Indian J Sci Technol 8(S2):53-57.

Kushwaha R., Singh B., 2018. An Improved Battery Charger for Electric Vehicle with High Power Factor. IEEE Industry Applications Society Annual Meeting (IAS), Portland, OR, pp. 1-8.

Lai Y.-S., Chen B.-Y., 2013. New Random PWM Technique for a Full-Bridge DC/DC Converter with Harmonics Intensity Reduction and Considering Efficiency. IEEE Transactions On Power Electronics, 28(11): 5013-5023.

Lee B-K., Kim J-P., Kim S-G., J-Y., 2017. An Isolated/Bidirectional PWM Resonant Converter for V2G(H) EV On-Board Charger. IEEE Transactions On Vehicular Technology, 66(9) :7741 -7750

Lee B-K., Kim J-P., Kim S-G., Lee J-Y., 2016. A PWM SRT DC/DC Converter for 6.6-kW EV Onboard Charger. IEEE Transactions on Industrial Electronics 63(2): 894-902.

Lee I., Kim J., 2017. A high-power DC-DC converter for electric vehicle battery charger. IEEE 3rd International Future Energy Electronics Conference and ECCE Asia (IFEEC 2017 - ECCE Asia), Kaohsiung, pp. 1861-1866.

Lee M., Lim C., Kim K., Park M., Moon G., 2019. A Phase-Shift Full-Bridge Converter with Novel Voltage Oscillation Clamping Circuit for Electric Vehicle On-Board Charger. 10th International Conference on Power Electronics and ECCE Asia (ICPE 2019 - ECCE Asia), Busan, Korea (South), pp. 2040-2045.

Lee S., Yi J., Kim W., Cho B.H., 2013. A parallel-series connected four-transformer half bridge DC-DC converter for electric vehicle application. IEEE ECCE Asia Downunder, Melbourne, VIC, pp. 711-715.

Lee S.-H., Park C.-Y., Kwon J.-M., Kwon B.-H., 2015. Hybrid-Type Full-Bridge DC/DC Converter with High Efficiency. IEEE Transactions on Industrial Electronics, 30(8): 4156-4164.

Lee S.-W., Do H.-L., 2016. Single-Stage Bridgeless AC–DC PFC Converter Using a Lossless Passive Snubber and Valley Switching. IEEE Transactions on Industrial Electronics 63(10): 6055-6063

Li H., Wang S., Zhang Z., Tang J., Ren X., Chen Q., 2019. A SiC Bidirectional LLC On-Board Charger. IEEE Applied Power Electronics Conference and Exposition (APEC), Anaheim, CA, USA, pp. 3353-3360.

Li S., Deng J., Mi C.C., 2013. Single-Stage Resonant Battery Charger with Inherent Power Factor Correction for Electric Vehicles. IEEE Transactions On Vehicular Technology 62(9):4336-4344.

Li S., Nam K. H., 2012. Design and analysis of a DC-DC converter for EVs battery charger," Proceedings of The 7th International Power Electronics and Motion Control Conference, Harbin, 2012, pp. 2981-2986.

Li S., Xiangli K., Smedley K. M., 2017. A Control Map for a Bidirectional PWM Plus Phase-Shift-Modulated Push–Pull DC–DC Converter. IEEE Transactions On Industrial Electronics, 64(11) :8514-8524.

Li W., Jiang Q., Mei Y., Li C., Deng Y., He X., 2015. Modular Multilevel DC/DC Converters with Phase-Shift Control Scheme for High-Voltage DC-Based Systems. IEEE Transactions on Power Electronics, 30(1): 99-107

Lim C., Jeong Y., Moon G., 2019. Phase-Shifted Full-Bridge DC–DC Converter with High Efficiency and High Power Density Using Center-Tapped Clamp Circuit for Battery Charging in Electric Vehicles. IEEE Transactions on Power Electronics 34(11). 10945-10959.

Lin R.-L., Huang L.-H., 2018. Efficiency Improvement on LLC Resonant Converter Using Integrated LCLC Resonant Transformer. IEEE Transactions On Industry Applications, 54(2): 1756-1764.

Liu F., Wang Z., Mao Y., Ruan X., 2014. Asymmetrical Half-Bridge Double-Input DC/DC Converters Adopting Pulsating Voltage Source Cells for Low Power Applications. IEEE Transactions on Power Electronics, 29(9): 4741-4751.

Liu G., Jang Y., Jovanovic M.M., Zhang J.O., 2017. Implementation of a 3.3-kW DC–DC Converter for EV On-Board Charger Employing the Series Resonant Converter with Reduced Frequency-Range Control. IEEE Transactions On Power Electronics, 32 (6): 4168-4184.

Liu G., Li D., Zhang J.Q., Jia M.L., 2014. High efficiency wide range bidirectional DC/DC converter for OBCM application. 2014 International Power Electronics and Application Conference and Exposition, Shanghai, pp. 1434-1438.

Liu X., Zhu Z. Q.,Stone D. A., Foster M. P., Chu W. Q., Urquhart I., Greenough J., 2017. Novel Dual-Phase-Shift Control with Bidirectional Inner Phase Shifts for a Dual-Active-Bridge Converter Having Low Surge Current and Stable Power Control. IEEE Transactions On Power Electronics, 32(5): 4095-4106

Lo Y.-K., Lin C.-Y., Hsieh M.-T., Lin C.-Y., 2011. Phase-Shifted Full-Bridge Series-Resonant DC-DC Converters for Wide Load Variations. IEEE Transactions On Industrial Electronics, 58(6): 2572-2575.

Lu J., Liu G., Bai H., Brown A., Johnson P.M., McAmmond M., Taylor A.R., 2017. Applying Variable-Switching-Frequency Variable-Phase-Shift Control and E-Mode GaN HEMTs to an Indirect Matrix Converter-Based EV Battery Charger. IEEE Transactions on Transportation Electrification, 3(3): 554-564.

Mallik A., Khaligh A., 2017. Variable-Switching-Frequency State-Feedback Control of a Phase-Shifted Full-Bridge DC/DC Converter. IEEE Transactions on Power Electronics, 32(8): 6523-6531.

Mehdipour A., Farhangi S., 2011. Comparison of three isolated bi-directional DC/DC converter topologies for a backup photovoltaic application. 2nd International Conference on Electric Power and Energy Conversion Systems (EPECS), 1-5.

Mehedy M.H., Zoardar Md. A. H., Islam S. A., Ahmed S., 2018. Implementation of Soft Switching in Resonant Converters. A Thesis Submitted to the Department of Electrical & Electronic Engineering of BRAC University, Bangladesh, pp. 1-43.

Mishima T., Nakaoka M., 2009. A Novel High-Frequency Transformer-Linked Soft-Switching Half-Bridge DC–DC Converter with Constant-Frequency Asymmetrical PWM Scheme. IEEE Transactions On Industrial Electronics, 56(8): 2961-2969.

Mishra D., Singh B., Panigrahi B.K., 2018. Modified Phase Shift Control for DAB Based Bidirectional Onboard EV Charger. IEEE International Conference on Power Electronics, Drives and Energy Systems (PEDES), Chennai, India, pp. 1-6.

Moghaddam S. H. A., Ayatollahi A., Rahmati A., 2012. Modeling and Current Programmed Control of a Bidirectional Full Bridge DC-DC Converter. Energy and Power Engineering, 4: 107-116

Musavi F., Eberle W., Dunford W. G., 2010. Efficiency evaluation of single-phase solutions for AC-DC PFC boost converters for plug-in-hybrid electric vehicle battery chargers. IEEE Vehicle Power and Propulsion Conference, 1-6.

Musavi F., Eberle, W., William G. Dunford W. G., 2011. A High-Performance Single-Phase Bridgeless Interleaved PFC Converter for Plug-in Hybrid Electric Vehicle Battery Chargers. IEEE Transactions On Industry Applications, 47(4): 1833-1843.

Noah M., Endo S., Ishibashi H., Nanamori K., Imaoka J., Umetani K., Yamamoto M., 2018. A Current Sharing Method Utilizing Single Balancing Transformer for a Multiphase LLC Resonant Converter with Integrated Magnetics. IEEE Journal of Emerging and Selected Topics in Power Electronics, 6(2): 977-992.

Oh C-Y., Kim D-H., Woo D-G., Sung W-Y., Kim Y-S., Lee B-K., 2013. A High-Efficient Nonisolated Single-Stage On-Board Battery Charger for Electric Vehicles. IEEE Transactions On Power Electronics 28(12): 5746-5757.

Oun Lee O., 2015. A Hybrid PWM-Resonant DC-DC Converter for Electric Vehicle Battery Charger Applications. Journal of Power Electronics, 15(5): 1158-1167.

Özbay H.,, Közkurt C., Dalcalı A., Tektaş M., 2020. Geleceğin ulaşım tercihi: Elektrikli araçlar. Akıllı Ulaşım Sistemleri ve Uygulamaları Dergisi 3(1):35-50.

Pandey R., Singh B., 2019. A Power-Factor-Corrected LLC Resonant Converter for Electric Vehicle Charger Using Cuk Converter. IEEE Transactions on Industry Applications, 55(6): 6278-6286.

Park H.-P., Jung J.-H, 2016. Modeling and Feedback Control of LLC Resonant Converters at High Switching Frequency. Journal of Power Electronics, 16(3): 849-860.

Park HP., Jung J.H., 2017. Power stage and feedback loop design for LLC resonant converter in high-switching frequency operation. IEEE Trans Power Electron. 32(10):7770-7782.

Park H-P., Ryu Y., Han K. J., Jung J-H., 2016. Design considerations of resonant network and transformer magnetics for high frequency LLC resonant converter. J Electr Eng Technol. 11 (2):383-392.

Polat Ö., Yumak K., Sezgin M.S., Yumurtacı G., Gül Ö., 2015. Elektrikli Araç Ve Şarj İstasyonlarının Türkiye'deki Güncel Durumu. Enerji Verimliliği ve Kalitesi, pp. 1-6.

Praneeth A.V.J.S., Vincent D., Williamson S.S., 2019. An Universal On-board Battery Charger with Wide Output Voltage Range for Electric Transportation. IEEE Energy Conversion Congress and Exposition (ECCE), Baltimore, MD, USA, pp. 1159-1165,

Rathore A. K., Prasanna U. R., 2013. Analysis, Design, and Experimental Results of Novel Snubberless Bidirectional Naturally Clamped ZCS/ZVS Current-Fed Half-Bridge DC/DC Converter for Fuel Cell Vehicles. IEEE Transactions On Industrial Electronics, 60(10): 4482-4491.

Restrepo, M., Morris J., Kazerani M., Cañizares C.A., Modeling and Testing of a Bidirectional Smart Charger for Distribution System EV Integration. IEEE transactions on smart grid, 9(1):152-162

Ronanki D., Apoorva Kelkar A., Williamson S.S.,2019. Extreme Fast Charging Technology—Prospects to Enhance Sustainable Electric Transportation. Energies, 12, 3721: 1-17.

Ruo-li T., Wu Z., Fang Y-J., 2016. Maximum power point tracking of large-scale photovoltaic array. Solar Energy 134: 503–514.

Saeed J., Hasan A., 2018. Unit Prediction Horizon Binary Search-Based Model Predictive Control of Full-Bridge DC–DC Converter. IEEE Transactions On Control Systems Technology 26(2): 463-474.

Safaee A., Ghartemani M.K, Jain P. K., Bakhshai A., 2016. Time-Domain Analysis of a Phase-Shift-Modulated Series Resonant Converter with an Adaptive Passive Auxiliary Circuit. IEEE Transactions On Power Electronics, 31(11): 7714-7734.

Safaee A., Jain P. K., Bakhshai A., 2015. An Adaptive ZVS Full Bridge DC–DC Converter with Reduced Conduction Losses and Frequency Variation Range. IEEE Transactions On Power Electronics, 30(8): 4107-4118.

Safaee A., Jain P., Bakhshai A., 2016. A ZVS Pulse width Modulation Full-Bridge Converter with a Low-RMS-Current Resonant Auxiliary Circuit" IEEE Transactions on Power Electronics, 31(6): 4031-4047.

Saket M.A., Shafiei N., Ordonez M., Craciun M., Botting C., 2016. Low parasitics planar transformer for LLC resonant battery chargers. IEEE Applied Power Electronics Conference and Exposition (APEC), Long Beach, pp. 854-858.

Salah C.B., Ouali M., 2011. Comparison of fuzzy logic and neural network in maximum power point tracker for PV systems. Electric Power Systems Research 81: 43–50.

Samanta D., 2018. Defuzzification Techniques. Application Notes. Pp: 1-55. https://cse.iitkgp.ac.in/~dsamanta/courses/sca/resources/slides/FL-03%20Defuzzification.pdf

Sayed K., Ali Z. M., Aldhaifallah M., 2020. Phase-Shift PWM-Controlled DC–DC Converter with Secondary-Side Current Doubler Rectifier for On-Board Charger Application. Energies 2020, 13, 2298: 1-22.

Saygı A.S., Beşer E., Ünlü M., 2017. Comparative Study of Soft Switching Methods Used in DC-DC Converters. Journal of Naval Science and Engineering 13(1): 1-22

Shi C., Khaligh A., 2018. A Two-Stage Three-Phase Integrated Charger for Electric Vehicles with Dual Cascaded Control Strategy. IEEE Journal of Emerging and Selected Topics in Power Electronics 6(2): 898-909.

Shi C., Khaligh A., Wang H., 2016. Interleaved SEPIC Power Factor Preregulator Using Coupled Inductors in Discontinuous Conduction Mode with Wide Output Voltage. IEEE Transactions on Industry Applications, 52(4): 3461-3471.

Shi C., Wang H., Dusmez S., Khaligh A., 2017. A SiC-Based High-Efficiency Isolated Onboard PEV Charger with Ultrawide DC-Link Voltage Range. IEEE Transactions on Industry Applications 53(1): 501-511.

Shi Y., Yang X., 2013. Zero-Voltage Switching PWM Three-Level Full-Bridge DC–DC Converter with Wide ZVS Load Range" IEEE Transactions On Power Electronics, 28(10): 4511-4524.

Shitole A. B., Sathyan S., Suryawanshi H. M., Talapur G. G., Chaturvedi P., 2018. Soft-Switched High Voltage Gain Boost-Integrated Flyback Converter Interfaced Single-Phase Grid-Tied Inverter for SPV Integration. IEEE Transactions On Industry Applications 54(1):482-493

Singh B., Kushwaha R., 2019. EV battery charger with non-inverting output voltage-based bridgeless PFC Cuk converter. IET Power Electronics 12(13): 3359-3368.

Singh V., Gupta I., Gupta H.O., 2007. ANN-based estimator for distillation using Levenberge Marquardt approach. Engineering Applications of Artificial Intelligence, 20(2):249-259.

Tao H., Zhang G., Zheng Z., 2019. Onboard Charging DC/DC Converter of Electric Vehicle Based on Synchronous Rectification and Characteristic Analysis. Hindawi Journal of Advanced Transportation Volume 2019, Article ID 2613893, pp. 1-10

Tarzamni H., Babaei E., Gharehkoushan A. Z., 2017. A Full Soft-Switching ZVZCS Flyback Converter Using an Active Auxiliary Cell. IEEE Transactions on Industrial Electronics 64(2): 1123-1129

Tey K.S., Mekhilef S., 2014. Modified incremental conductance MPPT algorithm to mitigate inaccurate responses under fast-changing solar irradiation level. Solar Energy 101: 333–342

Thangavelu A., Senthilkumar V., Parvathyshankar D., 2016. Zero voltage switching-pulse width modulation technique-based interleaved flyback converter for remote power solutions. IET Power Electron 9(7): 1381–1390

Toshiba Electronic Devices & Storage Corporation. 2019. Resonant Circuits and Soft Switching (LLC Resonant Converter and Resonant Inverter). pp.1-32.

Vu H.-N., Choi W., 2018. A Novel Dual Full-Bridge LLC Resonant Converter for CC and CV Charges of Batteries for Electric Vehicles. IEEE Transactions On Industrial Electronics, 65(3): 2212-2225.

Wang C.-M., 2008. A Novel ZCS - PWM Flyback Converter with a Simple ZCS-PWM Commutation Cell. IEEE Transactions on Industrial Electronics, 55(2): 749-757.

Wang H., Dusmez S., Khaligh A., 2014. Design and Analysis of a Full-Bridge LLC-Based PEV Charger Optimized for Wide Battery Voltage Range. IEEE Transactions on Vehicular Technology, 63(4): 1603-1613.

Wang H., Dusmez S., Khaligh A., 2014. A novel approach to design EV battery chargers using SEPIC PFC stage and optimal operating point tracking technique for LLC converter. IEEE Applied Power Electronics Conference and Exposition - APEC 2014, pp. 1683-1689.

Wang H., Z. Li Z., 2018. A PWM LLC Type Resonant Converter Adapted to Wide Output Range in PEV Charging Applications. IEEE Transactions On Power Electronics, 33(5): 3791-3901.

Wang R., Wu Y., He G, Lv Y., Du J., Li Y., 2018. Impedance modeling and stability analysis for cascade system of three-phase PWM rectifier and LLC resonant converter. Energies. 11(3050):1-15.

Wang Y., Wu Y., Lee T., 2013. Design and implementation of a bidirectional isolated dual-active-bridge-based DC/DC converter with dual-phase-shift control for electric vehicle battery. IEEE Energy Conversion Congress and Exposition, Denver, CO, pp. 5468-5475.

Whitaker B., Barkley A., Cole Z., Brandon Passmore B., Martin D.,, McNutt T.R., Lostetter A.B., Lee J.S., Shiozaki K., 2014. A High-Density, High-Efficiency, Isolated On-Board Vehicle Battery Charger Utilizing Silicon Carbide Power Devices. IEEE Transactions on Power Electronics, 29(5): 2606-2617.

Wi S-M., Kim M., 2019. Precise control strategy of dual-mode flyback DC/DC converter. IET Power Electron 12(2): 220-227.

Wirtz J., 2011. On-Board vs. Off Board Charging, Electrical Transportation of Infrastructure Eaton Corporation. 1-10.

Xie M., Huangfu Y., Zhang Q., Li Q., Zhao D., Liu Y., 2018. Small Signal Analysis and Control Design of Snubberless Naturally Clamped ZCS/ZVS Current-Fed Half-Bridge DC/DC Converter for EV. IECON 2018 - 44th Annual Conference of the IEEE Industrial Electronics Society, Washington, DC, pp. 4998-5004.

Yang M., Cho H., Lee S., Choi W., 2013. High-efficiency soft-switching PWM DC-DC converter for electric vehicle battery chargers. IEEE Energy Conversion Congress and Exposition, Denver, CO, 2013, pp. 1092-1095.

Yang M., Cho H., Lee S., Choi W., 2015. High-efficiency low-cost soft-swtiching DC-DC converter for EV on-board battery chargers. IEEE Applied Power Electronics Conference and Exposition (APEC), Charlotte, pp. 2050-2055.

Ye Z., 2013. Dual Half-Bridge DC–DC Converter with Wide-Range ZVS and Zero Circulating Current. IEEE Transactions on Power Electronics, 28(7): 3276-3286.

Yeon C.-O., Lee J.-B., Lee I.-O., Moon G.-W., 2016. Wide ZVS Range Asymmetric Half-Bridge Converter with Clamp Switch and Diode for High Conversion Efficiency. IEEE Transactions On Industrial Electronics, 63(5): 2862-2870.

Yilmaz U., Turksoy O., A. Teke A. 2019. Improved MPPT method to increase accuracy and speed in photovoltaic systems under variable atmospheric conditions. International Journal of Electrical Power Energy Systems (113): 634–651.

Yilmaz U., Turksoy O., Teke A., 2019. Intelligent control of high energy efficient two-stage battery charger topology for electric vehicles. Energy 186:1-11

Yilmaz U., Turksoy O., Teke A., 2020. Improving a battery charger architecture for electric vehicles with photovoltaic system. Int J Energy Res. 2020;44: 4376–4394.

Zhao B., Yu Q., Sun W. 2012. Extended-Phase-Shift Control of Isolated Bidirectional DC–DC Converter for Power Distribution in Microgrid. IEEE Transactions on Power Electronics 27(11): 4667-4680.

Zuk P., Havanur H., 2014. Zero-Voltage Switching Full-Bridge Converter: Operation, FOM, and Guidelines for MOSFET Selection. System Application Note AN847. Vishay Siliconix, pp. 1-6.

## CURRICULUM VITAE

Ünal YILMAZ was born in Diyarbakır, Turkey in 1986. He received his BSc from Electrical and Electronics Engineering Department of Çukurova University in 2013. He received his MSc from Electrical and Electronics Engineering Department of Harran University in 2016. Now, he has been working as research assistant in Electrical and Electronics Engineering Department of Harran University since 2014. His research interests include power quality, photovoltaic systems and DC-DC Converters.

### SCI/SCI-Expanded Publications

**Yilmaz, U.,** Turksoy, O., Teke, A., "Improving a battery charger architecture for electric vehicles with photovoltaic system." Int J Energy Res. 2020;44: 4376–4394. May, 2020.

**Yilmaz, U.,** Turksoy, O., Teke, A., “Intelligent control of high energy efficient two stage battery charger topology for electric vehicles,” Energy, vol. 186, no. 1, pp. 1–11, November 2019.

**Yilmaz, U.,** Turksoy, O., Teke, A., “Improved MPPT method to increase accuracy and speed in photovoltaic systems under variable atmospheric conditions,” International Journal of Electrical Power Energy Systems, vol. 113, pp. 634–651, December 2019.

Turksoy, O., **Yilmaz, U.,** Teke, A., “Minimizing Capacitance Value of Interleaved Power Factor Corrected Boost Converter for Battery Charger in Electric Vehicles,” Elektronika Ir Elektrotechnika, vol. 25, no. 5, pp. 11–17, October 2019.